This item was submitted to Loughborough's Research Repository by the author.
Items in Figshare are protected by copyright, with all rights reserved, unless otherwise indicated.

Radiation from curved (conical) frequency selective surfaces

PLEASE CITE THE PUBLISHED VERSION

PUBLISHER

© Y.W. Chia

LICENCE

CC BY-NC-ND 4.0

REPOSITORY RECORD

Chia, Yan Wah. 2019. “Radiation from Curved (conical) Frequency Selective Surfaces”. figshare. https://hdl.handle.net/2134/7200.

Loughborough University

This item is held in Loughborough University's Institutional Repository (https://dspace.lboro.ac.uk/) and was harvested from the British Library's EThOS service (http://www.ethos.bl.uk/). It is made available under the following Creative Commons Licence conditions.

creative commons

COMMONS DEED

Attribution-NonCommercial-NoDerivs 2.5

You are free:

- to copy, distribute, display, and perform the work

Under the following conditions:

Attribution. You must attribute the work in the manner specified by the author or licensor.

Noncommercial. You may not use this work for commercial purposes.

No Derivative Works. You may not alter, transform, or build upon this work.

- For any reuse or distribution, you must make clear to others the license terms of this work.
- Any of these conditions can be waived if you get permission from the copyright holder.

Your fair use and other rights are in no way affected by the above.

This is a human-readable summary of the Legal Code (the full license).

Disclaimer

For the full text of this licence, please go to:
http://creativecommons.org/licenses/by-nc-nd/2.5/

RADIATION FROM CURVED (CONICAL) FREQUENCY SELECTIVE SURFACES

by

Yan Wah Chia (Michael), BSc.

A Doctoral Thesis

Submitted in partial fulfilment for the requirements for the award of
the degree of Doctor of Philosophy of the
Loughborough University of Technology

November 1993

Supervisor: Dr. J.C. Vardaxoglou, B.Sc., Ph.D, MIEEE

Department of Electronic and Electrical Engineering
Loughborough University of Technology
United Kingdom

© Y.W.Chia, 1993

The fear of the Lord is the
beginning of knowledge.

Proverb 1 Verse 7

ABSTRACT

The thesis deals with the analysis of a microwave Frequency Selective Surface (FSS) on a conical dielectric radome illuminated by a feed horn located at the base. Two approaches have been adopted to solve this problem. The first approach is to calculate the element currents under the assumption that the surface is locally flat. Consequently, the element current at that locality can be determined by employing Floquet modal analysis. The local incidence has been modelled from the radiation pattern of the source or the aperture fields of the feed. Three types of feed model were used to account for the field illumination on the radome. The transmitted fields from the curved surface are obtained from the sum of the radiated fields due to the equivalent magnetic and electric current sources distributed in each local unit cell of the conical surface. This method treats the interaction of neighbouring FSS elements only. In the second approach the curvature is taken into account by dividing the each element into segments which conform to the curved surface. An integral formulation is used to take into account the interaction of all the elements. The current source in each FSS element from the formulation is solved using the method of moments (MOM) technique. A linear system of simultaneous equations is obtained from the MOM and has been solved using elimination method and an iterative method which employs conjugate gradients. The performance of both methods has been compared with regard to the speed of computations and the memory storage capability. New formulations using quasi static approximations have been derived to account for thin dielectric backing in the curved aperture FSS analysis. Computer models have been developed to predict the radiation performance of the curved (conical) FSS. Experiments were performed in an anechoic chamber where the FSS cone was mounted on a jig resting on a turntable. The measuring setup contained a sweep oscillator that supplied power to a transmitting feed placed at the base of the cone. Amplitude and phase values of the far field radiation pattern of the cone were measured with the aid of a vector network analyser. Cones with different dimensions and FSS element geometries were constructed and the measured transmission losses and radiation patterns compared with predictions.

ACKNOWLEDGEMENTS

I would like to thank Dr. J.C. Vardaxoglou for his supervision and constructive criticisms throughout these three years of studies, especially for his support in writing the thesis.

I would like to acknowledge the receipt of the O.R.S. award and the funding by British Aerospace, RMP. Particularly like to thank Mr. R. Simpkin for his useful comments and discussions.

I wish also to thank my colleagues in the LUT Antenna and Microwave Lab., especially A. Stylianou and A. Hozzaindesh for their help. Also like to thank R. Ball for much of his technical assistance.

I am very grateful to my parents and family for much of their love, encouragement and prayers. I also appreciate the prayers of my brothers and sisters in Christ especially those from LCCF.

Most of all, I would like to thank God for providing the opportunity and his grace to do this Ph.D. He has been my counsellor and friend especially in time of need.

TABLES OF UNITS AND DEFINITIONS

Table of Units

GHz	Gigahertz
m	metre
cm	centimetre
mm	millimetre

Table of definitions

ω (=$2\pi f$)	angular frequency
λ	wavelength
f	frequency
ε	permittivity
μ	permeability
ε_o (= 8.854X10^{-12} Farad/metre)	permittivity of free space
μ_o (= 4πX10^{-7} Henry/metre)	permeability of free space
H	magnetic field intensity
E	electric field intensity

Table for the definitions of acronyms

FSS	Frequency Selective Surface
TIA	Tangential Infinite Array model
FC	Finite Current model
FN	Far to Near field feed model
PB	Parallel Beam feed model
SPS	Superposition of Point Sources feed model
MOM	Method Of Moments
EFIE	Electric Field Integral Equation
MFIE	Magnetic Field Integral Equation
CG	Conjugate Gradient method

TABLE OF CONTENTS

Page

ABSTRACT i
ACKNOWLEDGEMENTS ii
TABLES OF UNITS AND DEFINITIONS iii
TABLE OF CONTENTS iv

CHAPTER 1.0
INTRODUCTION 1
References 5

CHAPTER 2.0
MODAL ANALYSIS OF PLANAR APERTURE FSS
2.1 Introduction 8
2.2 Theory 10
2.2.1 Infinite Array Configuration 10
2.2.2 Floquet modal representations of fields 11
2.2.3 Integral Equation formulation 13
2.2.4 Method of Moments solution 18
2.3 Transmission and Reflection for Arbitrary Incidence 20
2.3.1 TE and TM incident components 20
2.3.2 Transmission and Reflection coefficients 22
2.4 Conclusions 24
References 26

CHAPTER 3.0
Tangential Infinite Array (TIA) approximation 27
3.1 Introduction 27
3.2 Geometry of the conical FSS 28
3.2.1 Relationship between the local and surface coordinates of the conical FSS 28
3.2.2 Construction of the conical FSS from the planar surface 30
3.3 Analysis of FSS and feed system 33
3.3.1 Feed to surface co-ordinate transformation 34
3.3.2 Feed modelling 36
3.3.3 Surface currents from modal analysis 39
3.3.4 Scattered fields using the radiation integral 41

3.4 Experiments 47
3.4.1 Construction and dimensions of conical FSS 47
3.4.2 Experimental set-up 49
3.5 Results and Discussions 54
3.5.1 Predictions from a planar infinite array of slotted rings 54
3.5.2 Results from the Dielectric cone 56
3.5.3 Results using the FN feed model 57
3.5.4 Results using the SPS feed model 57
3.5.5 Results using the PB feed model 58
3.6 Conclusions 58
References 71

Chapter 4.0
CURVED FINITE METALLIC FSS 72
4.1 Introduction 72
4.2 Free standing finite FSS 73
4.2.1 Integral Equation Formulation 73
4.2.2 Method of Moments solution 76
4.2.3 Elimination method 82
4.2.4 Iterative CG method 82
4.2.5 Radiated and scattered fields 87
4.3 Dielectric and ferrite coated metallic FSS dipole 88
4.3.1 Quasi-static equivalent of dielectric backed FSS 89
4.3.2 Quasi-static equivalent of ferrite backed FSS 92
4.4 Results 97
4.4.1 Transmission response 98
4.4.2 Radiation patterns 102
4.5 Conclusions 104
References 115

CHAPTER 5.0
CURVED FINITE APERTURE FSS 117
5.1 Introduction 117
5.2 Free standing finite aperture FSS 118
5.2.1 Aperture in screen formulation 118
5.2.2 MOM using pulses testing and basis functions 123
5.2.3 Radiated fields 126
5.3 Magnetic charge and current: theory of static fields 127

5.3.1 Magnetic charge in ferrite medium 128
5.3.2 Magnetic current in dielectric medium 132
5.4 Dielectric and ferrite coated FSS slot 137
5.4.1 Quasi static equivalent of dielectric coated slot 140
5.4.2 Quasi static equivalent of ferrite coated slot 143
5.5 Results 149
5.5.1 Transmission response 150
5.5.2 Radiation patterns 153
5.6 Comparing the tangential infinite array and finite current models 161
5.6.1 Current and modal recipe for a planar array of dipoles 161
5.6.2 Transmission response 163
5.6.3 Radiation patterns 164
5.7 Conclusions 170
References 172

CHAPTER 6.0
CONCLUSIONS AND SUGGESTIONS FOR FURTHER WORK 173
References 177

APPENDICES
Appendix 1
Coefficients from the modal analysis I
Appendix 2
Feed to surface co-ordinate transformations III
Appendix 3
FN feed model IV
Appendix 4
Aperture fields of a narrow flare circular conical corrugated horn VI
Appendix 5
Parallel Beam (PB) feed model VIII
Appendix 6
Scattered fields using Stratton and Chu's formulation X

CHAPTER 1.0

INTRODUCTION

Frequency Selective Surfaces (FSS) or Dichroic surfaces are usually periodic array of metallic elements or apertures that exhibit bandstop or bandpass properties [1] when excited by incident electromagnetic waves. These properties have been exploited as subreflectors in microwave reflector antennas[2] and optical laser systems [3]. There has also been an increasing interest in using them in radomes for aerospace applications [4,5]. In general, FSS have the advantage of increasing the frequency band capacity and lightening the weight of antenna systems, especially in satellite payloads, and reducing the radar cross section (RCS) of aerospace radomes [5]. The FSS performance depends mainly on the element and lattice geometry [6-8] but can be altered by a multi-layer structure [9]. Due to the periodic nature of the FSS, a large enough surface can be approximated as an infinite array so that Floquet's theorem with modal analysis [10] can be used to find the current of each element in the local unit cell. As a subreflector, gentle curvature has been used in previous studies by Mok and others [11,12]. They have adopted a locally infinite planar approach with modal analysis on the curved surface to approximate the currents induced by far field illumination of an antenna feed. Recently, Carloglanian [13] has assessed this approach for various curvatures of hyperboloid radome fitted with arrays of aperture FSS. It was found that the curvature of the FSS can alter the radiation performance of the array substantially. Therefore, it plays an important part in the overall design. When a radome is placed in front of an antenna, it distorts the wave front of the incident electromagnetic radiation from the feed and degrades its radiation pattern. In general, the performance of a radome is usually judged by the transmission loss, radiation pattern and polarisation distortions and errors in boresight [14]. Only the first two aspects are investigated in this thesis but information about the others can be obtained.

This thesis deals with the analysis of a conical dielectric radome enclosing a feed horn antenna located at the base of the cone. Unlike the previous example [13], the antenna feed here is illuminating the radome in the near field, so the non-planar incident field on the inner wall is more acute and mutual coupling with the radome is inevitable. This simple model simulates the performance of a streamlined radome [4] which is normally encountered in the nose of an aircraft and missile. A passband is required in such applications so aperture FSS elements with inductive properties are used in the conical array. Two methods have been used to tackle this problem, without considering complications of near field coupling. The first method is to calculate the element currents assuming that the surface is locally flat. Consequently, the element current at

that locality could be determined by employing modal analysis, which assumes a tangential infinite array (TIA) [15]. The computation time would depend mainly on the number of elements and associated current basis functions.

In the second method the surface curvature is defined by dividing each element into linear segments which conform to the conical surface. An integral equation formulation is used to account for mutual coupling among the FSS elements on the entire surface. This has been called the finite current (FC) model [16] here because the interactions of all the FSS elements are treated in a finite geometrical sense. The performance of both approaches to the conical FSS radome problem are compared with regard to the accuracy, speed of computations and memory storage capability. Computer models have been developed with a view to predict the radiation performance of the curved (conical) FSS. Cones with different dimensions and FSS element geometries were constructed and the measured transmission losses and radiation patterns have been compared with predictions.

This thesis is organised in the following manner:
The main objective in Chapter 2 is to derive certain equations and quantities for the analysis of the tangential infinite array (TIA) approximation of the conical FSS. Based on the infinite array assumption, aspects of the modal analysis are discussed with the view of calculating the magnetic currents of each local aperture FSS element. The tangential fields of the array are expressed as Floquet expansions [17] and solved using the boundary conditions in the aperture. As a result, a magnetic field integral equation (MFIE) is formed with the induced elemental currents represented by full domain basis functions and the associated unknown coefficients. Using a suitable method of solution, such as the method of moments (MOM) [18], this equation is reduced to a system of matrices and solved by an elimination method [19] to determine these current coefficients. Plane wave transmission and reflection coefficients are computed using the transmitted, reflected and incident fields. These allow the computer model to be verified with existing software for conducting elements using Babinet's principle. The subroutine for computing the current coefficients has also been modified to find the tangential fields in the centre unit cell. This is incorporated into the software for the curved FSS which uses the TIA approximation as discussed in the next chapter.

In Chapter 3 the analysis of the conical FSS and feed system are derived taking into account the geometry of the curved surface and the non-planar illumination of the feed. The geometrical feature of the cone requires the relationship between certain co-ordinate systems which help to locate the position of each FSS element on the curved

surface. Due to the size of the cone, the conical FSS is constructed from two planar surfaces laid symmetrically on this dielectric former. This is illuminated by a corrugated conical circular feed at the base pointing toward the tip and aligned along the axis. The incident near fields are modelled using three feed models. The first is called the far to near field (FN) feed model which is based on the far field pattern but weighted according to the distance from the centre of the feed to the FSS surface [11]. The second uses a parallel beam (PB) from the feed aperture [16]. A more rigorous definition of the near field is to use a superposition of radiated fields from point sources (SPS) in the feed aperture. The local incidences using these feed models provide input data to the modal analysis subroutine, as described in Chapter 2, to compute the current coefficients and hence the tangential fields of a local unit cell tangential to the curved surface. These fields become the current sources for the radiated fields of each cell. The total transmitted field of the cone is computed using a summation of such far fields from all the unit cell distributed on the cone. Experiments were performed in an anechoic chamber where the FSS cone was mounted in a jig which rests on a turntable. The measuring setup contained a sweep oscillator that supplied power to a transmitting feed which illuminated the cone at its base. Amplitude and phase of the far field radiation pattern of the cone were measured with the aid of a vector network analyser. The prototype cone using slotted ring element geometries, was constructed and its performance was compared with predictions from the computer model.

Work on finite FSS in the past tends to concentrate on small planar arrays of metallic elements [20]. Since the metallic element and aperture are complementary electromagnetic structures, the electric field integral equation (EFIE) formulation [21] for the former is similar in form to the MFIE of the aperture. In order to understand the coupling of the FSS on a dielectric conical array, a quasi static EFIE was used for metallic elements in this thesis. The EFIE is firstly assessed to see if it is viable to use a quasi-static approximation for dielectric backing so that subsequent work can be developed on aperture elements using an integral equation approach. In order to model curved FSS of metallic elements supported by such substrate, the quasi-static approach has been used in Chapter 4. This was first formulated by Popovic [22] for modelling a thin dielectric coated antenna but is developed here for the conical FSS radome case with thin metallic elements. Since the main objective here is to investigate the performance of surface curvature on a finite FSS radome, the dielectric support is assumed to be much thinner than the operating wavelength in order to reduce the shift in resonant frequency and undesirable effects like surface waves [23]. This formulation is a modified version of the EFIE but coupled with dielectric/ferrite loading feature. In

contrast to Popovic's point matching MOM procedure, sub-domain basis pulse functions with Galerkin's testing is adopted to define the curvature of FSS elements into linear segments on the conical surface. Each pulse is weighted at the junction of the segments [24]. The latter MOM procedure has been shown to produce a complex symmetric matrix which can be exploited to reduce computer memory size and increase the speed of the solution for the original EFIE [25]. It also yields a system of matrices which can be solved by the elimination method [19] or the iterative conjugate gradients (CG) [26] method. Both mathematical methods were compared with regard to computation time and memory. The transmitted fields were calculated using the sum of radiated fields from the feed aperture and the electric current source on each linear segment. Since the FSS is now considered in a finite geometrical sense (which accounts for the coupling between all the array elements), it is called a finite current (FC) model. Due to the limitation in computer memory, a smaller FSS cone was modelled. Hence, a prototype was constructed from planar FSS, which consisted of two symmetrical lattices etched on a single sheet. Measurements are compared with predictions from the FC model.

A tutorial review of solving general aperture problems have been presented by several authors [27] but there is no published work that takes into account the dielectric effects for a curved aperture screen geometry. Using a similar quasi-static concept for aperture structures, a novel formulation has been developed for slotted FSS supported by a thin curved dielectric radome. This is discussed in Chapter 5, where a MFIE for a free standing aperture screen [27] was enhanced to include dielectric and ferrite loading features [16]. The general MFIE was originally derived using the equivalence principle for an aperture in a infinite conducting screen separated by semi-half spaces [28]. However, equations for static fields due to magnetic current sources in a dielectric medium and magnetic charge sources in a ferrite medium are not explicit enough in current literature to account for a quasi-static approximation of the MFIE. So, these equations were expanded here with the help of the complementary forms of Gauss' and Ampere's laws for magnetic charge and current sources. These are fundamental to the derivation of a modified MFIE with both dielectric and ferrite loading effects. The resulting MFIE can be treated in the same manner as the EFIE in Chapter 4 using the MOM to define the curvature of elements on a conical surface. A small dielectric conical array of thin slotted dipoles was constructed and the radiation patterns were measured. The experimental results are compared with predictions from the present FC model using the novel MFIE. The performance of this FC model is also compared with the TIA model with regard to computation time, memory and accuracy. General conclusions and suggestions for further work are presented in Chapter 6.

References

[1] Chen, C.C. :'Transmission through a conducting screen perforated with apertures', IEEE Trans., MTT-18, 1970, pp.627-632.

[2] Lee, C.K. and Langley, R.J. :' Performance of a dual-band reflector antenna incorporating a frequency selective subreflector', Int. J. Electron., Vol. 61, 1986, pp.607-616.

[3] Urlich, R., Bridges, J.J. and Pollack, M.A. :'Variable mesh coupler for I.R. lasers', Appl. Opt., 1970, Vol.9, pp.2511-2516.

[4] Pelton, E.L. and Munk, B. A. :'A streamlined metallic radome', IEEE Trans., AP-22, 1974, pp.799-803.

[5] Ousbeck, J.O. and Pettersson, L. :'Frequency selective radomes', 3rd Int. Conf. on Electomag. in Aerosp. Appl. and 7th Europ. Electromag. Struct. Conf. 1993,.pp115-117.

[6] Parker, E.A., Hamdy S.M.A. and Langley R.J. :'Arrays of concentric rings as frequency selective surfaces', Electron. Lett., 1981, Vol.17, pp.880-881.

[7] Hamdy S.M.A. and Parker, E.A. :'Current distribution on the elements of a square loop frequency selective surfaces', Electron. Lett., 1982, Vol.18, pp.624-626.

[8] Parker, E.A., Hamdy S.M.A. and Langley R.J. :'Modes of resonance of the Jerusalem Cross in frequency selective surfaces', IEE Proc.,Vol.130, 1983, pp.203-208.

[9] Vardaxoglou, J.C. and Parker, E.A. :' Modal analysis of scattering from two layer frequency selective surfaces', Int. J. Electron., Vol.58, No.5, 1985, pp.827-830.

[10] Montgometry, J.P. :'Scattering by an infinite periodic array of thin conductors on a dielectric sheet', IEEE Trans., AP-23, 1975, pp.70-75.

[11] Mok,.K., Allam, M.A.M., Vardaxoglou, J.C. and Parker, E.A. :' Curved and plane frequency selective surfaces: a study of two offset subreflectors', Journ. Inst. of Electric. and Radio Eng., Vol.58, No.6, 1988, pp.284-290.

[12] Rahmat-Samii, Y. and Tulintseff, A.N. :'Diffraction analysis of frequency selective reflector antennas', IEEE Trans., AP-41, 1993, pp.476-487.

[13] Caroglanian, A. and Webb, K. :'Study of curved and planar frequency-selective surfaces with nonplanar illumination ', IEEE Trans., AP-39, 1991, pp 211-217

[14] Rudge A.W., Milne K., Olver, A.D. and Knight P. (Ed.). :'The handbook of antenna design', IEE Electromagnetic Wave Series:16, Vol. 2, Peter Peregrinus Ltd., 1983, Chapter 14, pp.457-550.

[15] Chia, Y.W., Simpkin, R. and Vardaxoglou, J.C. :'A study of a conical frequency selective surface', 7th International Symposium on Antennas, JINA'92, Nice, France, Nov. 1992, pp 321-324.

[16] Chia, Y.W., Simpkin, R. and Vardaxoglou, J.C. :'Scattering from conical frequency selective surface using a Finite Current model', 3rd Int. Conf. on Electromag. in Aerosp. Appl. and 7th Europ. Electromag. Struct. Conf. 1993, pp.119-122.

[17] Amitay, N., Galindo, V. and Wu, C.P. :' Theory and analysis of phased array antennas', New York:Wiley-Interscience, 1972, pp.37-74.

[18] Harrington, R.F. :'Matrix methods for field problems', IEEE Proc.,1967, pp.136-149.

[19] Jennings, A. :'Matrix computation for engineers and scientists', John Wiley & Sons, 1977,pp.100-141.

[20] Stylianou, A.S. :'Scattering from finite and multilayer FSS using iterative schemes Loughborough Univ. Tech., Ph.D. thesis, 1992.

[21] Balanis C.A. :'Advanced engineering electromagnetics', John Wiley & Sons, Inc., 1989,.pp.696

[22] Popovic, B.D., Dragovic, M.B. and Djordjevic, A.R. :'Analysis and synthesis of wire antennas', Research Studies Press,1982, pp.100-104.

[23] Luebbers, R.J. and Munk, B.A. :' Some effects of dielectric loading on periodic slot arrays', IEEE Trans.,1978, AP-26, pp.536-542.

[24] Glisson, A.W. and Wilton, D.R. :'Simple and efficient numerical methods for problems of electromagnetic radiation and scattering from surfaces', IEEE Trans., 1980, AP-28, pp. 593-603

[25] Canning, F.X. :'Direct solution of the EFIE with half the computation', IEEE Trans. ,1991, AP-1, pp.118-119

[26] Hestenes, M. and Stiefel, E. :'Methods of conjugate gradients for solving linear systems', J. Res. Nat.. Bur. Stand, Vol.49,1952, pp.409-436.

[27] Butler, C.M., Rahmat-Samii and Y., Mittra, R. :'Electromagnetic penetration through apertures in conducting surfaces', IEEE Trans., 1978, AP-26, pp.82-93.

[28] Butler, C.M. and Umashankar, K.R. :'Electromagnetic penetration through an aperture in an infinite planar screen separating two half-spaces of different electromagnetic properties', Radio Science, 1976, Vol.11, No.7, pp.611-619.

CHAPTER 2.0

MODAL ANALYSIS OF PLANAR APERTURE FSS

2.1 Introduction

In this Chapter, the modal analysis for an infinite planar array of aperture FSS element in multi-dielectric substrates is presented. It forms the basis for calculating the induced magnetic currents in the aperture which is required for the source fields on the conical FSS. These radiating sources are taken to be the fields in each local unit cell on the curved surface. This is needed in the radiation pattern calculation of a conical FSS illuminated by a feed as discussed in Chapter 3. The main objective here is to derive certain equations and quantities required for the work in Chapter 3. The formulation of the modal analysis here is to facilitate the case when a feed is illuminating from inside the conical radome with the metallic FSS screen wrapped around the exterior of the curved surface. The dielectric layers facing the feed consist of the radome wall and the FSS substrates. In addition, there are four dielectric layers on the other side of the aperture screen to accommodate for an embedded FSS. This aperture array sandwiched in a total of seven dielectric layers is illustrated in Fig.2.1.

Modal analysis of rectangular apertures was first treated by Chen [1] for thin metallic screens with a single dielectric backing. Here the analysis is modified for a FSS screen sandwiched in multi-layer dielectrics. Arbitrary oriented thin slotted elements have also been analysed recently by Singh [2] using a subdomain approach instead of the full domain functions. Only slotted ring and dipole FSS elements will be investigated here because these are used for the curved FSS analysis in later chapters. Results have shown that the FSS ring elements give low crosspolarisation and few current functions are required in the modal analysis [3]. The dipole element is simple to model and has also been used in the finite current model in Chapter 5 for comparison. More complicated element geometries like tripoles, crosses and squaree have been studied by others [4,5,6] for metallic elements. Some aspects of theory in modal analysis are discussed in Sec.2.2. This Section shows how the theory exploits the periodicity of the FSS and provides a vector formulation which includes coupling between the array element. The electromagnetic boundary conditions for the aperture and Floquet expansions of the fields were used to derive an integral equation with unknown induced aperture electric fields. The aperture field was expressed as magnetic currents for computation purposes. A suitable method of solution, like the Method of Moments(MOM) [7] was used to reduce the equation into a system of linear equations and solved by the elimination method which is availiable as a NAG routine [8]. In Sec.2.3, the plane wave transmission and reflection coefficients are calculated using the

transmitted, reflected and incident fields. Conclusions to this chapter are given in Sec.2.4.

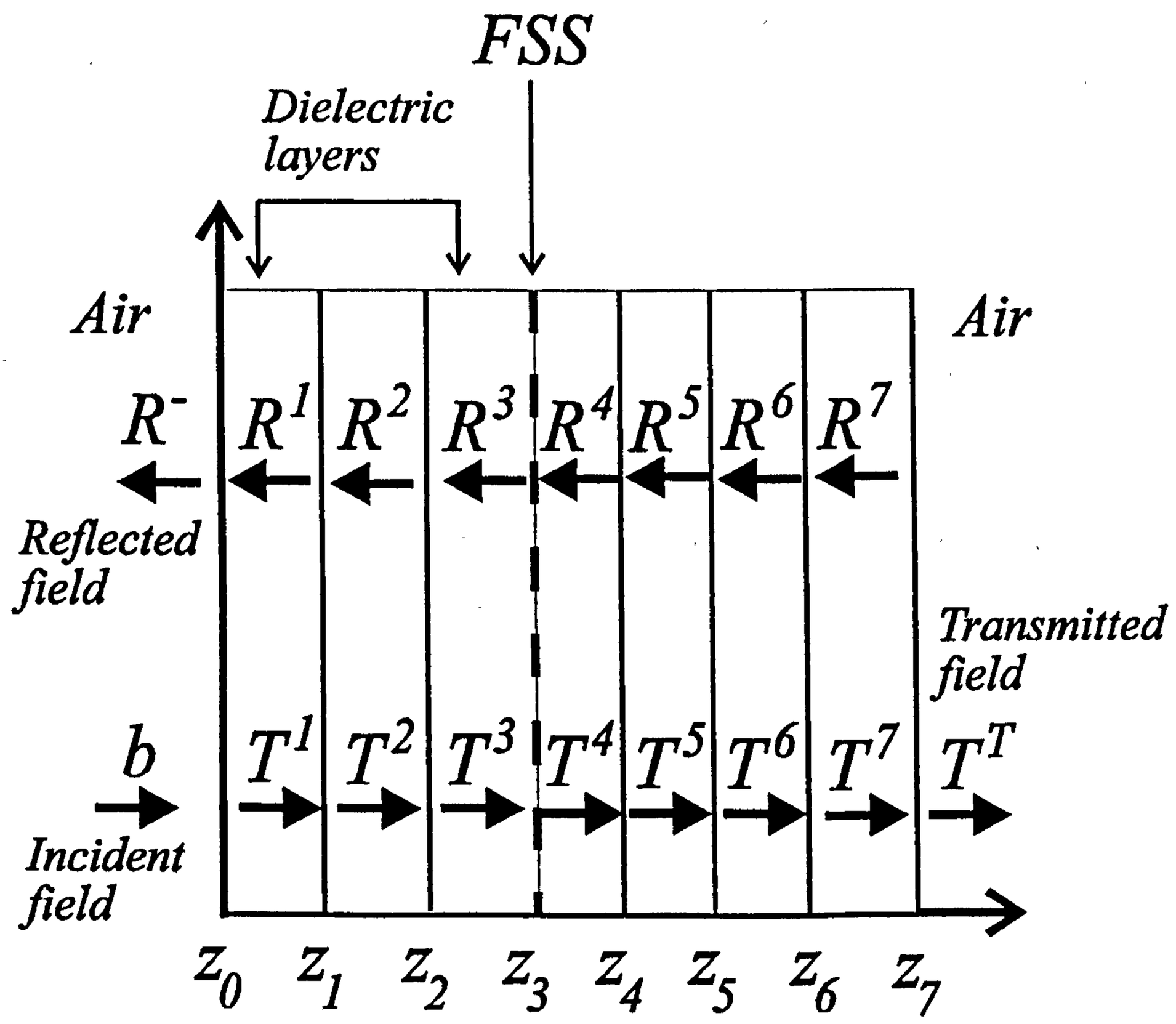

Fig.2.1 Transmitted and reflected fields in modal analysis.

2.2 Theory

In an infinite array configuration, each FSS element is located in a unit cell which is distributed in a periodic fashion. The modal theory exploits the periodicity so that the fields can be expanded in terms of Floquet modes. When the array is excited by an incident field, current will be induced in each element. After enforcing the boundary conditions, an integral equation is obtained in terms of the unknown current in the element as shown in Eq.(2.37). The Method of Moments (MOM) can be used to reduce the integral equation into a system of linear equations. Here the current is expressed in terms of full domain basis functions which span the entire area of the element or domain. The unknown coefficients were solved conveniently using Crout's factorisation which is available as a NAG routine [8].

2.2.1 Infinite Array Configuration

In practice, a large planar FSS array can be approximated as an infinite array. Consider an arbitrary FSS element in a unit cell area which is arranged periodically so as to form a infinite planar array as shown in Fig.2.2. The array could also be sandwiched between several dielectric layers. These may represent the dielectric substrate and radome covering often encountered in antenna systems. The skewed cell lattice is related to its next nearest neighbour by the vectors $\vec{d}_1$ and $\vec{d}_2$ respectively in the *x-y* plane.

They are expressed as,

$$\vec{d}_1 = d_1(\cos\alpha_1\hat{x} + \sin\alpha_1\hat{y}) \tag{2.1}$$

$$\vec{d}_2 = d_2(\cos\alpha_2\hat{x} + \sin\alpha_2\hat{y}) \tag{2.2}$$

These lattice vectors are skewed by the angles α_1 and α_2. The unit cell area is defined by:

$$A = \left|\vec{d}_1 \times \vec{d}_2\right| \tag{2.3}$$

The incident plane wave can be represented as a linear combination of a transverse electric (TE) polarisation and a transverse magnetic (TM) component. The TE wave has no component of the electric (E) field in the direction of propagation whereas the TM wave has no component of magnetic (H) field in the direction of propagation.

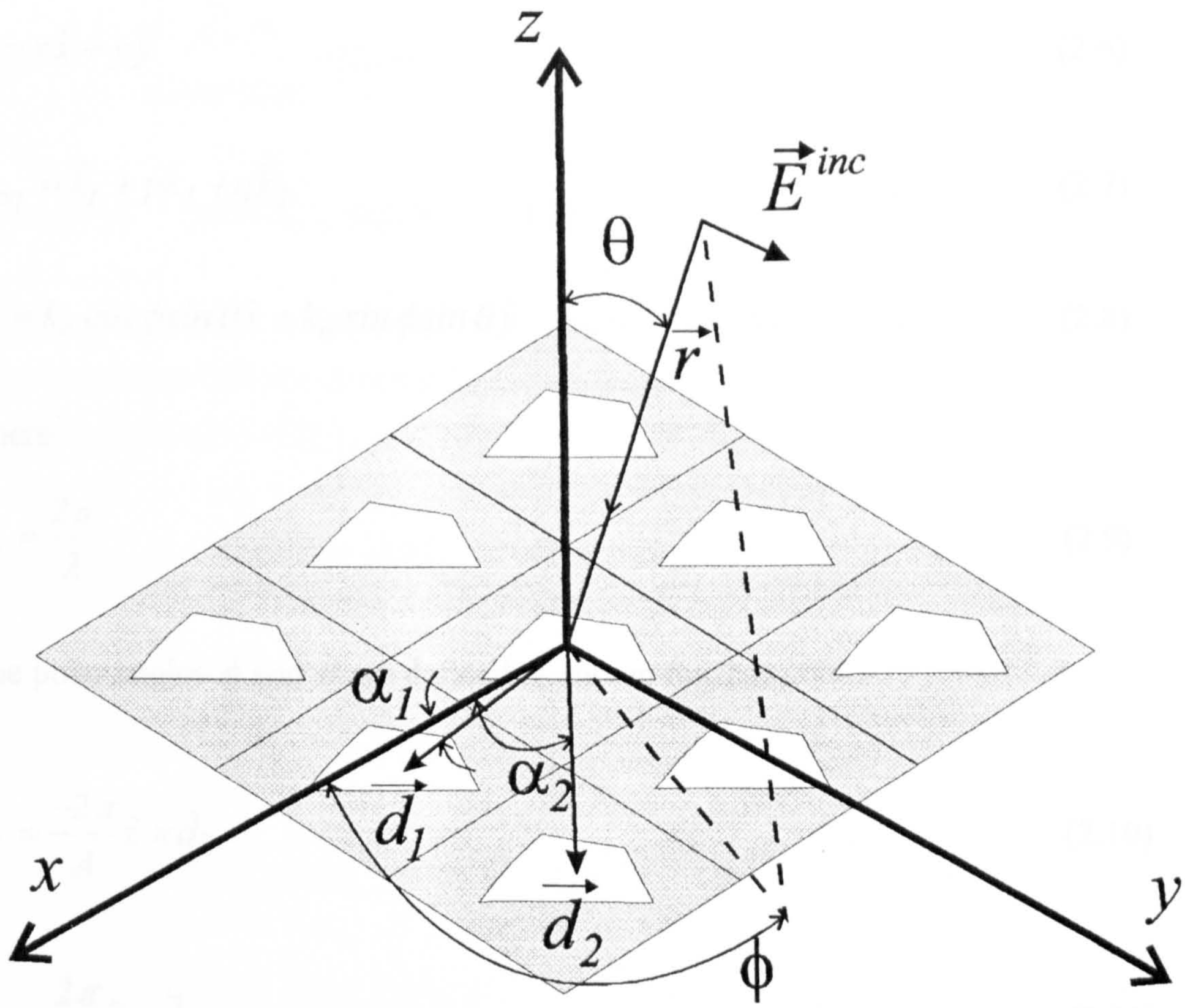

Fig.2.2 Incident plane wave on a FSS array.

2.2.2 Floquet modal representations of fields

The tangential fields in the infinite array can be expressed in terms of Floquet modes [9] which are given by:

$$\Psi_{pq}(x,y,z) = \psi_{pq}(x,y)e^{-j\gamma_{pq}z} \tag{2.4}$$

where the Floquet numbers $p,q = 0, \pm 1, \pm 2, \ldots..$

and $\psi_{pq}(x,y) = \psi_{pq}(\vec{r}_t) = e^{-j\vec{k}_{tpq}.\vec{r}_t}$ (2.5)

The time variation $e^{-j\omega t}$ has been assumed. The position of the fields is located at,

$$\vec{r}_t = x\hat{x} + y\hat{y} \tag{2.6}$$

$$\vec{k}_{tpq} = \vec{k}_t + p\vec{k}_1 + q\vec{k}_2 \tag{2.7}$$

$$\vec{k}_t = k_o \cos\phi \sin\theta \hat{x} + k_o \sin\phi \sin\theta \hat{y} \tag{2.8}$$

where

$$k_o = \frac{2\pi}{\lambda} \tag{2.9}$$

The polar angles ϕ and θ are defined as shown Fig.2.2.

$$\vec{k}_1 = \frac{-2\pi}{A}\hat{z} \times \vec{d}_2 \tag{2.10}$$

$$\vec{k}_2 = \frac{2\pi}{A}\hat{z} \times \vec{d}_1 \tag{2.11}$$

The propagation constant is given by:

$$\gamma_{pq} = \sqrt{\left(k^2 - \vec{k}_{tpq}.\vec{k}_{tpq}\right)} \tag{2.12}$$

where

$k = k_o\sqrt{\varepsilon_r}$ (valid only in the dielectric, otherwise $k = k_o$) (2.13)

For propagating waves, $k^2 \geq \vec{k}_{tpq}.\vec{k}_{tpq}$ and γ_{pq} is real and positive (or zero).

For evanescent waves, $k^2 < \vec{k}_{tpq}.\vec{k}_{tpq}$ and γ_{pq} is negative and imaginary.

The orthogonality condition for the Floquet modes is given by,

$$\int_{\substack{unit\ cell \\ area}} \psi_{pq}(\vec{r}_t)\psi^*_{p'q'}(\vec{r}_t)dr_t = A\delta_{pp'}\delta_{qq'} \tag{2.14}$$

$$\delta_{\alpha\beta} = \begin{cases} 1 & if\ \alpha = \beta \\ 0 & elsewhere \end{cases} \quad \text{(Knonecker delta)}$$

The asterisk * indicates complex conjugation.

The tangential fields in the array can be expressed in terms of both TM and TE vector Floquet modes which are denoted by the subscript 1 and 2 respectively.. The TM vector mode is given by:

$$\vec{\Omega}_{1pq}(x,y,z) = \Psi_{pq}(x,y,z)\vec{\kappa}_{1pq} \tag{2.15}$$

$$\text{where } \vec{\kappa}_{1pq} = \frac{\vec{k}_{tpq}}{\left|\vec{k}_{tpq}\right|} \tag{2.16}$$

and the TE mode is given:

$$\vec{\Omega}_{2pq}(x,y,z) = \Psi_{pq}(x,y,z)\vec{\kappa}_{2pq} \tag{2.17}$$

$$\text{where } \vec{\kappa}_{2pq} = \hat{z} \times \vec{\kappa}_{1pq} \tag{2.18}$$

The TM and TE modal admittances are defined as,

$$\eta_{1pq} = \frac{k}{\gamma_{pq}}\eta \tag{2.19}$$

and

$$\eta_{2pq} = \frac{\gamma_{pq}}{k}\eta \quad \text{respectively.} \tag{2.20}$$

$$\text{where } \eta = \sqrt{\frac{\varepsilon}{\mu}} \tag{2.21}$$

ε and μ are the permittivity and permeability of the medium.

2.2.3 Integral Equation formulation

The following modal analysis is formulated for an aperture FSS with three dielectric layers on the illumination side. This is to facilitate the case when a feed is illuminating from inside the conical radome with the FSS screen wrapped around exterior of the curved surface. These three layers represent the radome and the FSS substrates. In addition, four dielectric layers are used at the rear of the aperture screen to accommodate the cases where FSS is embedded within the radome. This aperture array, sandwiched in a total of seven dielectric layers, is illustrated in Fig.2.1

The tangential electromagnetic field in each respective medium can be expressed as TM and TE Floquet modes as follows:

For $z \leq z_0$,

$$\vec{E}_t^-(x,y,z) = \vec{E}_t^i(x,y,z) + \sum_{mpq} R_{mpq}^- e^{j\gamma_{pq}^{air} z} \psi_{pq}(x,y)\vec{\kappa}_{mpq} \tag{2.22}$$

$$\vec{H}_t^-(x,y,z) = \vec{H}_t^i(x,y,z) - \sum_{mpq} \eta_{mpq}^{air} R_{mpq}^- e^{j\gamma_{pq}^{air} z} \psi_{pq}(x,y)\hat{z} \times \vec{\kappa}_{mpq} \tag{2.23}$$

For $z_\alpha \leq z \leq z_{\alpha+1}$, (where $\alpha = 0,1,2,3,4,5,6$)

$$\vec{E}_t^\alpha(x,y,z) = \sum_{mpq} \left(T_{mpq}^\alpha e^{-j\gamma_{pq}^\alpha z} + R_{mpq}^\alpha e^{j\gamma_{pq}^\alpha z} \right) \psi_{pq}(x,y)\vec{\kappa}_{mpq} \tag{2.24}$$

$$\vec{H}_t^\alpha(x,y,z) = \sum_{mpq} \eta_{mpq}^\alpha \left(T_{mpq}^\alpha e^{-j\gamma_{pq}^\alpha z} - R_{mpq}^\alpha e^{j\gamma_{pq}^\alpha z} \right) \psi_{pq}(x,y)\hat{z} \times \vec{\kappa}_{mpq} \tag{2.25}$$

For $z \geq z_7$

$$\vec{E}_t^T(x,y,z) = \sum_{mpq} T_{mpq}^T e^{-j\gamma_{pq}^{air} z} \psi_{pq}(x,y)\vec{\kappa}_{mpq} \tag{2.26}$$

$$\vec{H}_t^T(x,y,z) = \sum_{mpq} \eta_{mpq}^{air} T_{mpq}^T e^{-j\gamma_{pq}^{air} z} \psi_{pq}(x,y)\hat{z} \times \vec{\kappa}_{mpq} \tag{2.27}$$

where T and R denote the field amplitudes for the forward and the backward waves respectively.

The incident field for $z \leq 0$ is given by,

$$\vec{E}_t^i(x,y,z) = \sum_m b_{m00} e^{-j\gamma_{00}^{air} z} \psi_{00}(x,y) \vec{\kappa}_{m00} \tag{2.28}$$

$$\vec{H}_t^i(x,y,z) = \sum_m \eta_{m00}^{air} b_{m00} e^{-j\gamma_{00}^{air} z} \psi_{00}(x,y) \hat{z} \times \vec{\kappa}_{m00} \tag{2.29}$$

where b_{m00} denotes the incident field amplitude in free space.

The MFIE is obtained by applying the following boundary conditions.

(1) The tangential fields electric and magnetic fields are continuous at all the dielectric/dielectric and dielectric/air interface.

(2) The tangential electric field must be zero on the conducting portion of the screen but the electric and magnetic fields must be continuous across the aperture regions.

The field amplitudes at $z = z_3$ must be expressed in terms of the unknown electric fields using the mode orthogonality condition in Eq.(2.14). Therefore, Eq.(2.24) becomes,

$$T_{mpq}^3 e^{-j\gamma_{pq}^3 z_3} + R_{mpq}^3 e^{j\gamma_{pq}^3 z_3} = \int_{A'} \vec{E}_t^3(x',y',z_3).\vec{\kappa}_{mpq} \psi_{pq}^*(x',y') dr_t' = \tilde{E}_3 \tag{2.30}$$

$$\overline{A}$$

The prime indicates that the electric field is located in the aperture area A' of the unit cell area A, such that $\vec{r}_t \in A'$.

Similarly,

$$T_{mpq}^4 e^{-j\gamma_{pq}^4 z_3} + R_{mpq}^4 e^{j\gamma_{pq}^4 z_3} = \tilde{E}_4 \tag{2.31}$$

The continuity of the electric field from **(2)** ensures that the electric fields are the same in the aperture on both sides, therefore equating (2.30) and (2.31) yields,

$$\tilde{E}_3 = \tilde{E}_4 = \tilde{E} \tag{2.32}$$

Since the magnetic field is also continuous across the aperture portions at $z = z_3$, then

$$\vec{H}_t^3(x',y',z_3) = \vec{H}_t^4(x',y',z_3) \tag{2.33}$$

Using boundary condition **(1)**, the electric and magnetic fields from Eq.(2.26) and Eq.(2.27) are solved at $z = z_7$. This is to find the relationship between field amplitudes in medium 7 and air. This relationship is required for subsequent boundaries, so that the process is repeated by solving for $z = z_6$, $z = z_5$ until $z = z_4$. It can be shown that,

$$\vec{H}_t^4(x,y,z_3) = \sum_{mpq} \tilde{E}\sigma_3^4(m,p,q)\eta_{mpq}^4 \psi_{pq}(x,y)\hat{z} \times \vec{\kappa}_{mpq} \tag{2.34}$$

where the coefficient σ_3^4 shows the relationships between the media at the rear of the screen. Details of the derivation of this coefficient can be found in Appendix 1

Applying the same reasoning for the fields from $z = z_2$ to $z = z_0 = 0$ with the boundary condition **(1)** and then using the boundary condition **(2)** at $z = z_3$ gives the following,

$$\begin{aligned}\vec{H}_t^3(x,y,z_3) = &\sum_m \eta_{m00}^3 2e^{-j\gamma_{00}^3 z_3} b_{m00} V_{123}(m,0,0)\psi_{00}(x,y)\hat{z} \times \vec{\kappa}_{m00} \\ &+ \sum_{mpq} \eta_{mpq}^3 \left(2e^{-j\gamma_{pq}^3 z_3}\tilde{E}U_{123}(m,p,q) - \tilde{E}\right)\psi_{pq}(x,y)\hat{z} \times \vec{\kappa}_{mpq}\end{aligned} \tag{2.35}$$

where the coefficients $U_{123}(m,p,q)$ and $V_{123}(m,p,q)$ shows the relationship between the media on the illumination side (Appendix 1).

Equating the magnetic fields, using Eqs.(2.33), (2.34) and (2.35), gives the required MFIE as,

$$\sum_m \eta_{m00}^3 2e^{-j\gamma_{00}^3 z_3} b_{m00} V_{123}(m,0,0)\psi_{00}(x,y)\hat{z}\times\vec{\kappa}_{m00}$$

$$=\sum_{mpq}\tilde{E}\left(\sigma_3^4(m,p,q)\eta_{mpq}^4+\eta_{mpq}^3-\eta_{mpq}^3 2e^{-j\gamma_{pq}^3 z_3}U_{123}(m,p,q)\right)\psi_{pq}(x,y)\hat{z}\times\vec{\kappa}_{mpq} \tag{2.37}$$

In order to solve Eq.(2.37), the aperture electric field can be expressed in terms of equivalent magnetic current $\vec{M}$. The relationship is given by,

$$\vec{E}(x',y',z_3)=\hat{z}\times\vec{M}(x',y',z_3)$$

$$\Rightarrow\vec{E}(x',y')=\hat{z}\times\vec{M}(x',y') \tag{2.38}$$

where

$$\vec{M}(x',y')=M_x\hat{x}+M_y\hat{y} \tag{2.39}$$

The variable z_3 indicates that the aperture electric field or magnetic current is valid only in the plane where the planar FSS is located. This has been neglected in the following equations for simplicity.

Substituting Eq.(2.38) into Eq.(2.30) yields,

$$\tilde{E}=\int_{A'}\vec{E}(x',y').\vec{\kappa}_{mpq}\psi_{pq}^*(x',y')dr_t'$$

$$=\int_{A'}\vec{M}(x',y').\left(-\hat{z}\times\vec{\kappa}_{mpq}\right)\psi_{pq}^*(x',y')dr_t' \tag{2.40}$$

Substituting Eq.(2.40) into Eq.(2.37) gives,

$$\sum_m \eta_{m00}^3 2e^{-j\gamma_{00}^3 z_3} b_{m00} V_{123}(m,0,0)\psi_{00}(x,y)\hat{z}\times\vec{\kappa}_{m00}$$

$$= \sum_{mpq}\left(\sigma_3^4(m,p,q)\,\eta_{mpq}^4 + \eta_{mpq}^3 - \eta_{mpq}^3\, 2e^{-j\gamma_{pq}^3 z_3} U_{123}(m,p,q)\right)\psi_{pq}(x,y)$$

$$\int_{A'} \vec{M}(x',y').\left(-\hat{z}\times\vec{\kappa}_{mpq}\right)\psi_{pq}^*(x',y')\,\hat{z}\times\vec{\kappa}_{mpq}\,dr_t' \qquad (2.41)$$

$$\overline{A}$$

2.2.4 Method of Moments solution

A suitable method that is frequently used to solve integral equations is the method of moments (MOM). The MOM uses testing and basis functions to convert the integral equation to a linear system of equations. The unknown magnetic current induced in the aperture FSS can be expanded in terms of an infinite series of basis functions. These are defined only on the non-conducting part of the unit cell A' which is given by :

$$\vec{M}(x,y) = \sum_{n=1}^{n=N} c_n \vec{h}_n(x,y) \quad r_t \in A' \qquad (2.42)$$

c_n is the complex amplitude of the nth basis function.

In practice, only a finite set of basis functions is required to approximate the actual current induced. The total number of functions is denoted by N.

Substituting Eq.(2.42) into Eq.(2.41) and taking the inner product with a testing function $\vec{h}_s(x,y)$ yields a linear system of equations which can be expressed in the following matrix form,

$$[A_s] = [B_{sn}][C_n] \qquad (2.43)$$

where

$[A_s]$ is a column vector of dimension N:

$$A_s = \sum_m \left(\eta_{m00}^3\, 2e^{-j\gamma_{00}^3 z_3} b_{m00} V_{123}(m,0,0)\right)\left(\tilde{h}_s^*(k_{t00}).\hat{z}\times\vec{\kappa}_{m00}\right) \qquad (2.44)$$

and

$[B_{sn}]$ is a square matrix of dimensions $N \times N$, given by:

$$B_{sn} = \sum_{mpq}\left(\sigma_3^4(m,p,q)\eta_{mpq}^4 + \eta_{mpq}^3 - \eta_{mpq}^3 2e^{-j\gamma_{pq}^3 z_3} U_{123}(m,p,q) \right)$$

$$\left(\tilde{h}_s^*\left(\vec{k}_{tpq}\right).\hat{z} \times \vec{\kappa}_{mpq}\right)\left(-\tilde{h}_n\left(\vec{k}_{tpq}\right).\hat{z} \times \vec{\kappa}_{mpq}\right) \qquad (2.45)$$

$$\overline{A}$$

where

$$\vec{h}_s\left(\vec{k}_{tpq}\right) = \left\langle \vec{h}_s(x',y'), \psi_{pq}^*(x',y') \right\rangle$$

$$= \int_{A'} \vec{h}_s(r_t')e^{jk_{tpq}.r_t'} dr_t' \qquad (2.46)$$

The above expression can be regarded as the Fourier transform of the testing function. The basis function can be easily integrated in closed form. Notice that the testing function in the inner product is same as the basis function. This is a special case, called the Galerkin's method.

The unknown current amplitude coefficients in the column matrix $[C_n]$ of dimension N can be solved by matrix inversion as follows:

$$[C_n] = [B_{sn}]^{-1}[A_s] \qquad (2.47)$$

where $[B_{sn}]^{-1}$ denotes the inverse of $[B_{sn}]$

This matrix inversion however, is solved here using the elimination method. This is availiable as Crout's factorisation in the NAG library [8]. Further descriptions of this method are given in Sec.4.2.3 where this method has been compared with the iterative method in terms of computational speed and memory for a large matrix system.

In theory, an infinite set of Floquet modes are required to solve the integral equations. In practice however, a finite number is used. Experimental validation is normally a reliable way to check the accuracy.

2.3 Transmission and Reflection for Arbitrary Incidence

Plane wave transmission and reflection coefficients are often used as a measure to quantify the transmitted and reflected field from a planar FSS. These are computed along a ray path which is in the direction of the boresight from an illuminating feed. The planar FSS is positioned in the far field of the transmitting feed so that the incidence produces a near planar wave front on the surface. Similarly, the receiving feed is aligned along the boresight direction in the far field of the FSS in order to measure the transmission or reflection coefficients. The predicted transmission and reflection coefficients are computed by normalising the transmitted or reflected field with respect to the incident field. These were used to verify the computer subroutines for calculating the current coefficients, before implementing the computer model for curved FSS. For the curved FSS analysis, however, the transmitted fields are computed from the sum of contributions of radiated fields from field sources of each local unit cell on the curved surface as discussed in Chapter 3. The transmission coefficient is also calculated in the similar manner as discussed above except that the field in this case is not planar.

In order to use the modal analysis, it is required to resolve the incident fields into the tangential TE and TM components with amplitudes b_{100} and b_{200} in the direction of $\hat{k}_{100}$ and $\hat{k}_{200}$. Ludwig's third definition [10] is used here to find the reference direction of the electric field vector with respect to its copolar and crosspolar component.

2.3.1 TE and TM incident components

Assume a plane wave is propagating in the direction $\vec{r}$ as shown in Fig.2.2.

$$\vec{r} = \sin\theta\cos\phi\hat{x} + \sin\theta\sin\phi\hat{y} + \cos\theta\hat{z} \tag{2.48}$$

Its total electric incident field is $\vec{E}^{inc}$ given as:

$$\vec{E} = E_x\hat{x} + E_y\hat{y} + E_z\hat{z} \tag{2.49}$$

The subscripts and superscripts for $\vec{E}$ have been neglected for simplicity.

Using Ludwig's third definition on the $\vec{E}$, gives:

$$\vec{E}.\hat{i}_{co} = 1 \tag{2.50}$$

$$\vec{E}.\hat{i}_{cross} = 0 \tag{2.51}$$

$$\vec{E}.\vec{r} = 0 \tag{2.52}$$

Where,

$$\hat{i}_{co} = -(1-\cos\theta)\sin\phi\cos\phi\hat{x} + \left[1-\sin^2\phi(1-\cos\theta)\right]\hat{y} - \sin\theta\sin\phi\hat{z} \tag{2.53}$$

$$\hat{i}_{cross} = \left[1-\cos^2\phi(1-\cos\theta)\right]\hat{x} - (1-\cos\theta)\sin\phi\cos\phi\hat{y} - \sin\theta\cos\phi\hat{z} \tag{2.54}$$

Solving the above equations yields the components of $\vec{E}$ as:

$$E_x = \frac{\sin\phi\cos\phi(\cos\theta-1)E_y}{\cos\theta-\cos^2\phi(\cos\theta-1)} \tag{2.55}$$

$$E_y = \cos\theta-\cos^2\phi(\cos\theta-1) \tag{2.56}$$

$$E_z = -\sin\theta\sin\phi \tag{2.57}$$

Eq.(2.52) is also the result of the divergence equation $\vec{\nabla}.\vec{E} = 0$ which gives:

$$E_z = \frac{-\left(\sin\theta\cos\phi E_x + \sin\theta\sin\phi E_y\right)}{\cos\theta} \tag{2.58}$$

$\vec{E}$ can be resolved into the other orthogonal directions in the modal analysis given by,

$$\vec{E} = b_{100}\hat{k}_{100} + b_{200}\hat{k}_{200} + E_z\hat{z} \tag{2.59}$$

By solving Eq.(2.49) and Eq.(2.59), the amplitudes can be found:

$$b_{100} = E_x \cos\phi + E_y \sin\phi \tag{2.60}$$

$$b_{200} = E_y \cos\phi - E_x \sin\phi \tag{2.61}$$

The amplitudes b_{100} and b_{200} will be used in the modal analysis for the incident fields.

Notice, that for pure TE incidence, i.e. $\phi = 0^o$, $\vec{E} = \hat{y}$, then

$b_{100} = 0$ and $b_{200} = 1$

And for pure TM incidence, i.e. $\phi = 90^o$, $\vec{E} = \cos\theta\hat{y} - \sin\theta\hat{z}$, then

$b_{100} = \cos\theta$ and $b_{200} = 0$

2.3.2 Transmission and Reflection coefficients

The transmission coefficient is defined as the ratio of the complex amplitudes of the transmitted and incident waves with zero order propagating Floquet modes.

The expression for the transmitted field is derived from Eq.(2.26) for the zero order mode as:

$$\vec{E}_t^T(x,y,z) = \sum_{m00} T_{m00}^T e^{-j\gamma_{00}^{air} z} \psi_{00}(x,y)\vec{\kappa}_{m00}$$

$$= \sum_{m00} \omega_6^7 \omega_5^6 \omega_4^5 \omega_3^4 \tilde{E} \psi_{00}(x,y)\vec{\kappa}_{m00}$$

$$= E_x^T \hat{x} + E_y^T \hat{y} \tag{2.62}$$

The coefficient $\omega_\alpha^{\alpha+1}$ shows the relationship between the interfaces on the rear of the FSS screen (Appendix 1).

The total transmitted field is given by:

$$\vec{E}^T = E_x^T \hat{x} + E_y^T \hat{y} + E_z^T \hat{z} \tag{2.63}$$

where the z component is derived from Eq.(2.59) is written as:

$$E_z^T = \frac{-\left(\sin\theta\cos\phi E_x^T + \sin\theta\sin\phi E_y^T\right)}{\cos\theta} \tag{2.64}$$

Therefore, the complex transmission coefficient for the copolar component is given by:

$$T_{co} = \frac{\vec{E}^T.\hat{i}_{co}}{\vec{E}^i.\hat{i}_{co}} \tag{2.65}$$

The transmission coefficient for the crosspolar components can be calculated by replacing the Ludwig's vector $\hat{i}_{co}$ in the numerator by $\hat{i}_{cross}$

In the same way, the reflection coefficient is defined by the ratio of the complex amplitudes of the reflected and incident waves with zero order propagating Floquet modes.

It can be shown that the reflected field for the zero order mode from Eq.(2.22) is:

$$\vec{E}_t^-(x,y,z) = \sum_{m00} R_{m00}^- e^{j\gamma_{00}^{air} z} \psi_{00}(x,y)\vec{\kappa}_{m00}$$

$$= \sum_{m00}\left(\tilde{E}.G_0 - b_{m00}F_0\right)\psi_{00}(x,y)\vec{\kappa}_{m00}$$

$$= E_x^R \hat{x} + E_y^R \hat{y} \tag{2.66}$$

The coefficients G_0 and F_0 represents the relationship between the interfaces on the front of the FSS screen (Appendix 1).

The total reflected field is given by:

$$\vec{E}^R = E_x^R \hat{x} + E_y^R \hat{y} + E_z^R \hat{z} \tag{2.67}$$

where the z component is derived from Eq.(2.59) can be written as:

$$E_z^R = \frac{-\left(\sin\theta\cos\phi E_x^R + \sin\theta\sin\phi E_y^R\right)}{\cos\theta} \tag{2.68}$$

Therefore, the complex reflection coefficient for the copolar component is given by:

$$R_{co} = \frac{\vec{E}^R . \hat{i}_{co}}{\vec{E}^i . \hat{i}_{co}} \tag{2.69}$$

Representative predictions of the transmission and reflection coefficients for a slotted ring planar array can be found in Fig.2.3. These have been verified with known results for arrays of metallic rings [11] using Babinet's principle. The predictions show that the transmission coefficents predicted a passband with resonance at about 14 GHz. This is also confirmed by the reflection coefficients. The preliminary predictions of the plane wave transmission coefficients can be used as a guide for locating the pass band of the curved FSS.

2.4 Conclusions

In this Chapter, modal analysis has been used to solve for the infinite planar array of aperture FSS elements. The formulation of the modal analysis facilitates the case when a feed is illuminating from inside the conical radome with the metallic FSS screen wrapped around the exterior of the curved surface. The inner layers facing the feed take into account the radome and the FSS substrates. In addition, four dielectric layers on the other side of the aperture screen can accommodate the cases where the FSS is embedded within the radome. This Chapter has derived certain equations and quantities required for the curved FSS analysis in Chapter 3. A computer model was developed to compute the current, reflection and transmission coefficients for this work. The predicted transmission and reflection coefficients for a slotted ring planar FSS are used as a guide to the likely resonance of the passband location for the conical FSS. The software was written in FORTRAN 77 and run on a SUN SPARC 2

workstation. The computer subroutine for calculating the current coefficients will be implemented in the software for curved FSS analysis in the next chapter.

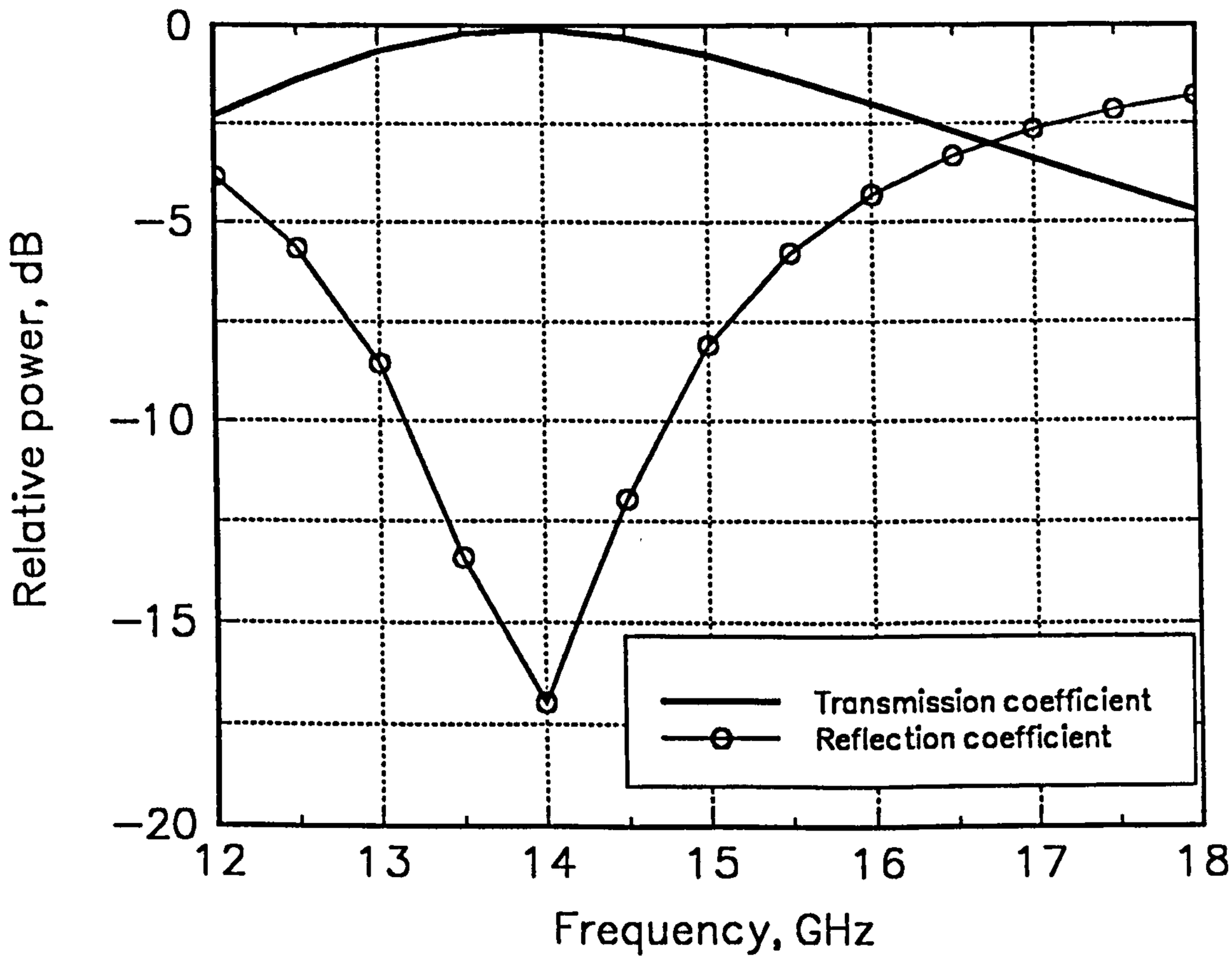

Fig.2.3 Passband response of a infinite planar array of slotted rings.

References

[1] Chen, C.C. :'Transmission through a conducting screen perforated periodically with apertures', IEEE Trans., MTT-18, pp.627-632.

[2] Singh, S. and Wilton, D.R. :'Analysis of an infinite periodic array of slot radiators with dielectric loading', IEEE Trans., AP-39, 1991, pp.190-196.

[3] Cahill, R., and Parker, E.A. :'Concentric ring and Jerusalem cross arrays as frequency selective surfaces for a 45^0 incidence diplexer', Electronic. Lett., 1982, 18, pp.313-314.

[4] Vardaxoglou, J.C. and Parker, E.A. :'Performance of two tripole arrays as frequency selective surfaces', Electron. Lett., 1983, 19, pp.709-710.

[5] Hamdy, S.M.A. and Parker, E.A. :'Influence of lattice geometry on transmission of electromagnetic waves through arrays of crossed dipole', IEE Proc.H, 1982,129, pp.7-10.

[6] Vardaxoglou, J.C. and Stylianou, A. :'Modal analysis of double square frequency selective surface', Int. Conf. Electromag. in Aerosp. Appl. (ICEAA), 1989, pp.355-358.

[7] Harrington, R.F. :'Matrix methods for field problems', IEEE Proc.,1967, pp.136-149.

[8] 'Subroutine F04ADF', Numerical Algorithm Group (NAG) Mk.13.

[9] Amitay, N., Galindo, V. and Wu, C.P. :'Theory and analysis of phased array antennas', New York, Interscience, 1972, pp.310-313.

[10] Ludwig, A.C. :'The definition of cross polarisation', IEEE Trans., AP-21, 1973, pp.116-119.

[11] Parker, E.A. and Hamdy, S.M.A. :'Rings as elements for frequency selective surfaces', Electron. Lett., 1981, 17, pp.612-614.

CHAPTER 3.0

TANGENTIAL INFINITE ARRAY (TIA) APPROXIMATION

3.1 Introduction

This Chapter involves a theoretical and experimental assessment of a symmetrical conical frequency selective surface (FSS), which could, for example, represent a radome housing antennas or other radiating structures [1]. Dielectric radomes have been readily employed in aircraft applications, especially in the nose. For a single layer dielectric, either a thin or multiple half-wavelength thick layer is often required. The half-wavelength criteria is to avoid reflections and so minimise the attenuation of the electromagnetic energy through the dielectric material.

The choice of the curvature in this study has been partly dictated by the ease of producing a conical FSS by wrapping a flat FSS around a pre-formed (dielectric) cone. The computational requirements and numerical complexities together with the intricacies in the feeding (excitation) mechanisms can sometimes be a restricting factor in the understanding as well as the design of curved array structures. Owing to the lack of available analyses in existing literature on conical FSS and for the reasons given above, an approximate approach to the scattering from the curved surface has been adopted [2]. It is assumed that each element on the surface is part of an infinite array arranged tangentially at that locality. The surface currents are obtained from the modal analysis using the tangential infinite array (TIA). The same principle has been applied to FSS with gentle curvatures, for example, representing subreflectors for multiband antenna systems, [3, 4]. The transmitted far fields from the conical FSS have been calculated from an integration over the surface using both electric and magnetic currents which in turn have been calculated using a plane wave modal formulation.

A rigorous formulation of the geometry of the curved surface is presented in Sec.3.2. In Sec.3.3, the analysis of the FSS and feed system is discussed in detail. The feed illumination in the near field is modelled using three types of feed model. The surface currents obtained from the modal analysis are used in the surface radiation integral to find the radiated field from the cone. Sec.3.4 describes the experimental set-up and construction of the conical FSS. In Sec.3.5, the predictions are compared with measurements performed on a conical FSS prototype having elements of ring apertures. The effect of each feed model on the radiation patterns is discussed. A general conclusion to this Chapter is given in Sec.3.6.

3.2 Geometry of the conical FSS

This section defines certain co-ordinate systems for the conical FSS that forms the basis for further analysis of the FSS and feed system in Sec.3.3. The relationship between the local and surface co-ordinate system of the conical FSS is required in order to use a tangential infinite array (TIA) approximation locally with the modal analysis. Since the conical FSS is produced by wrapping a flat FSS around the cone, the position of each FSS element on the conical surface are determined from a planar surface using simple transformation of geometry .

3.2.1 Relationship between the local and surface coordinates of the conical FSS

Although the conical geometry is well defined in terms of the standard conic section equations, here the analytical steps utilised and adapted to the conical FSS prototype as used in the measurements are described. Fig.3.1 shows the FSS cone and array geometries. Using the surface co-ordinates, (x_s, y_s, z_s), the conical surface is described by

$$x_s^2 + y_s^2 = (z_s + z_h)^2 \tan^2 \alpha_c \tag{3.1}$$

where $\tan \alpha_c = \frac{r_c}{z_h}$. α_c, z_h and r_c are the half-angle, height and base radius of the cone respectively. The parametric equation of the cone is given by

$$\vec{r}_s = x_s \hat{x}_s + y_s \hat{y}_s + z_s \hat{z}_s \tag{3.2}$$

where

$$x_s = u \cos \theta_s \tan \alpha_c \tag{3.3}$$

$$y_s = u \sin \theta_s \tan \alpha_c \tag{3.4}$$

and

$$z_s = u - z_h \tag{3.5}$$

u is in the range $0 \le u \le z_h$.

u is an arbitrary constant. $\theta_s = \tan^{-1}\left(\frac{y_s}{x_s}\right)$.

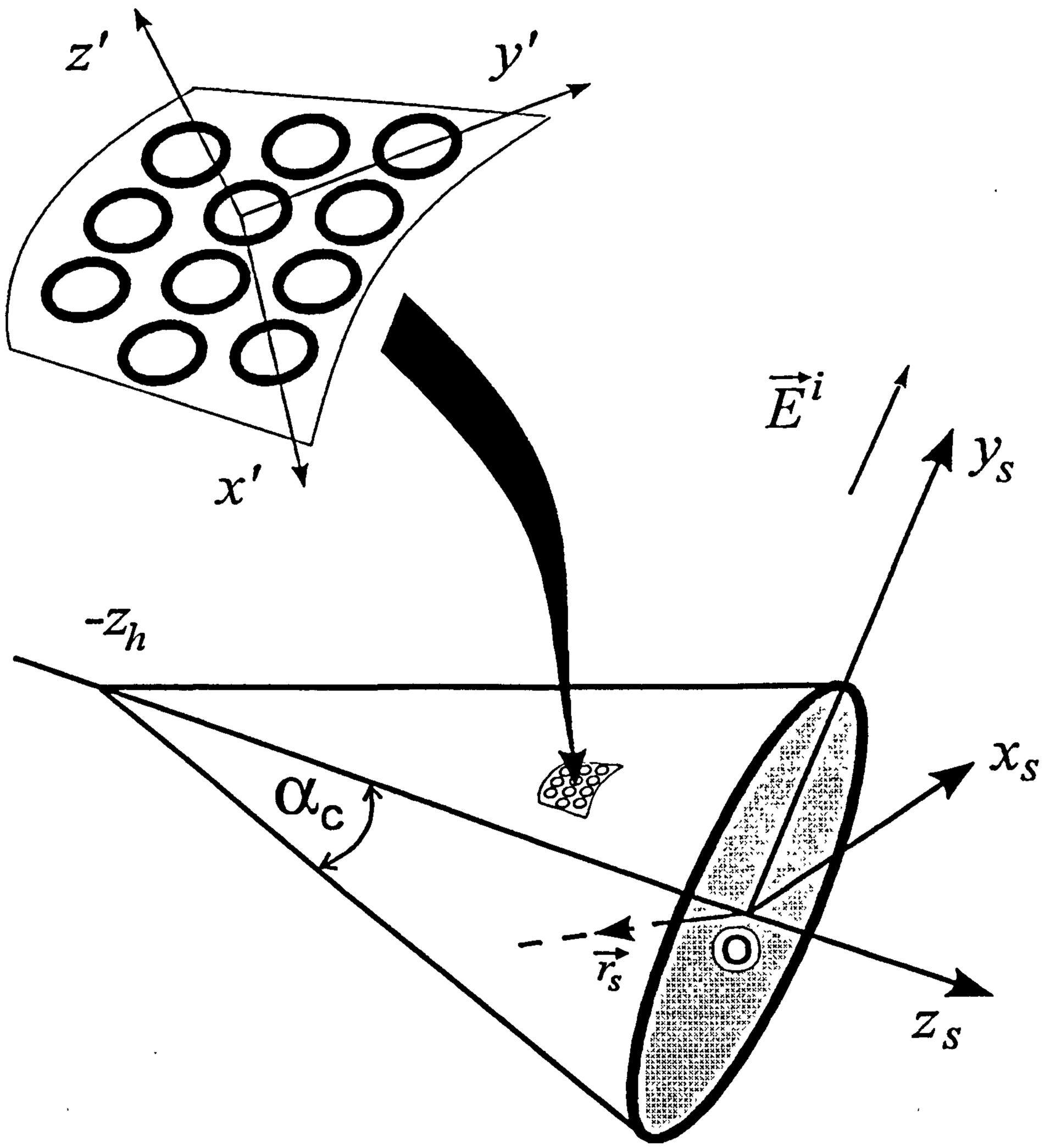

Fig.3.1. Geometry of the conical FSS. The inset shows the array elements.

In order to evaluate the surface currents, the FSS element positions, in terms of the local (primed) co-ordinates, are needed. The local normal is found from the following expression

$$\hat{z}' = \frac{\frac{\partial \vec{r}_s}{\partial u} \times \frac{\partial \vec{r}_s}{\partial \theta_s}}{\left| \frac{\partial \vec{r}_s}{\partial u} \times \frac{\partial \vec{r}_s}{\partial \theta_s} \right|} = \cos\alpha_c(\cos\theta_s \hat{x}_s + \sin\theta_s \hat{y}_s - \tan\alpha_c \hat{z}_s) \tag{3.6}$$

The y' co-ordinate was chosen to follow the rotation of a vector tangential to the cone's cross section, namely

$$\hat{y}' = \frac{\frac{\partial \vec{r}_s}{\partial \theta_s}}{u \tan\alpha_c} = -\sin\theta_s \hat{x}_s + \cos\theta_s \hat{y}_s \tag{3.7}$$

and

$$\hat{x}' = \hat{y}' \times \hat{z}' = -\sin\alpha_c \cos\theta_s \hat{x}_s - \sin\alpha_c \sin\theta_s \hat{y}_s - \cos\alpha_c \hat{z}_s \tag{3.8}$$

The above co-ordinate expressions will be used in the surface current calculations in the Sec.3.3.3

3.2.2 Construction of the conical FSS from the planar surface

The construction of the conical FSS (Sec.3.4) is based on covering a conical former with two flexible sectors, top and bottom halves. The array elements have been etched from these sectors whilst planar. In order to identify the location of the elements and subsequently their positions on the curved surface, the sector's geometry has been used in the analysis.

Fig. 3.2a shows the lattice and co-ordinate axis of the planar sector which is spanned by the following vector

$$\vec{r}_l = x_l \hat{x}_l + y_l \hat{y}_l \tag{3.9}$$

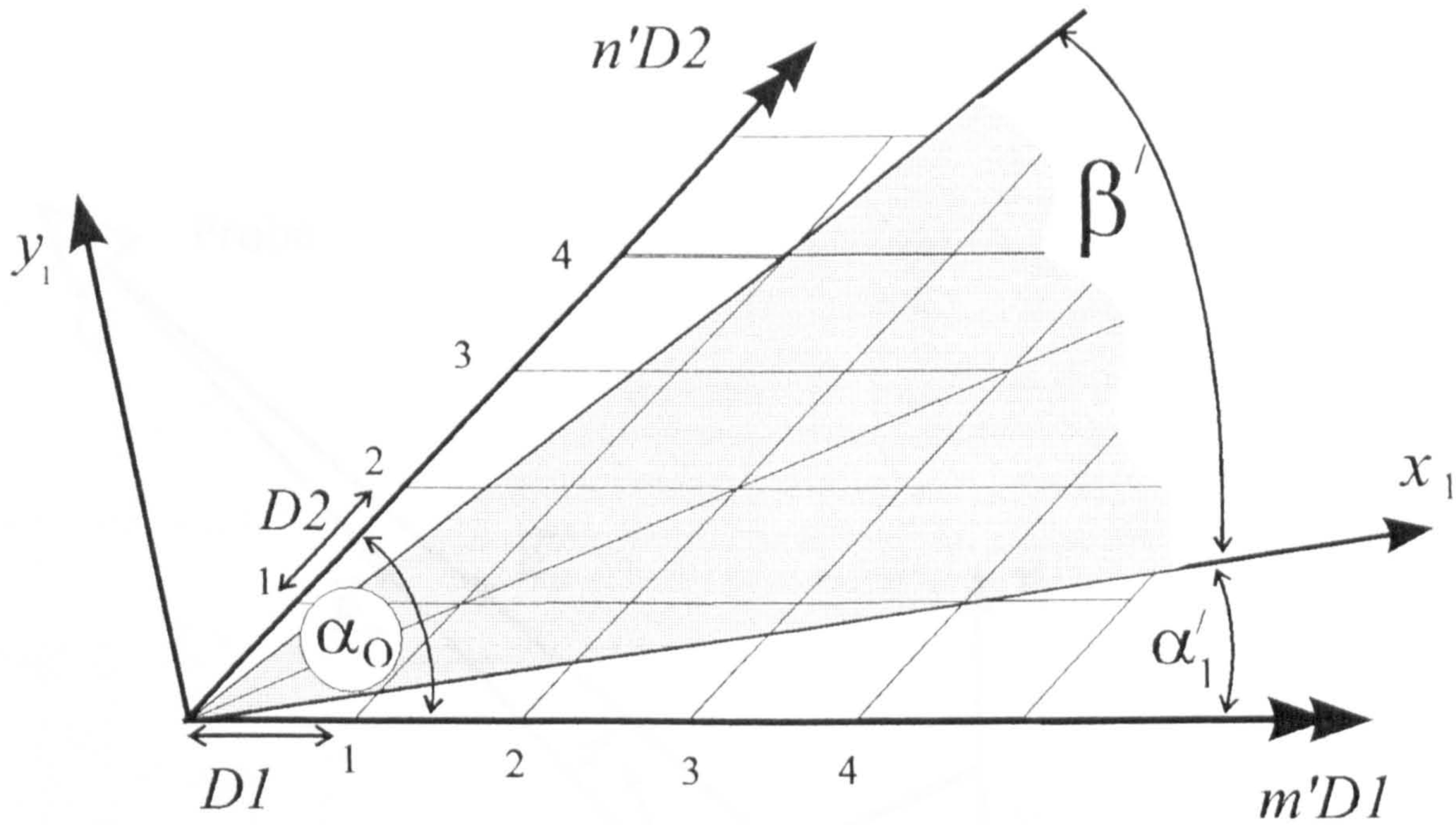

Fig.3.2a Lattice geometry of planar sector.
Shaded portion shows begining of FSS area.

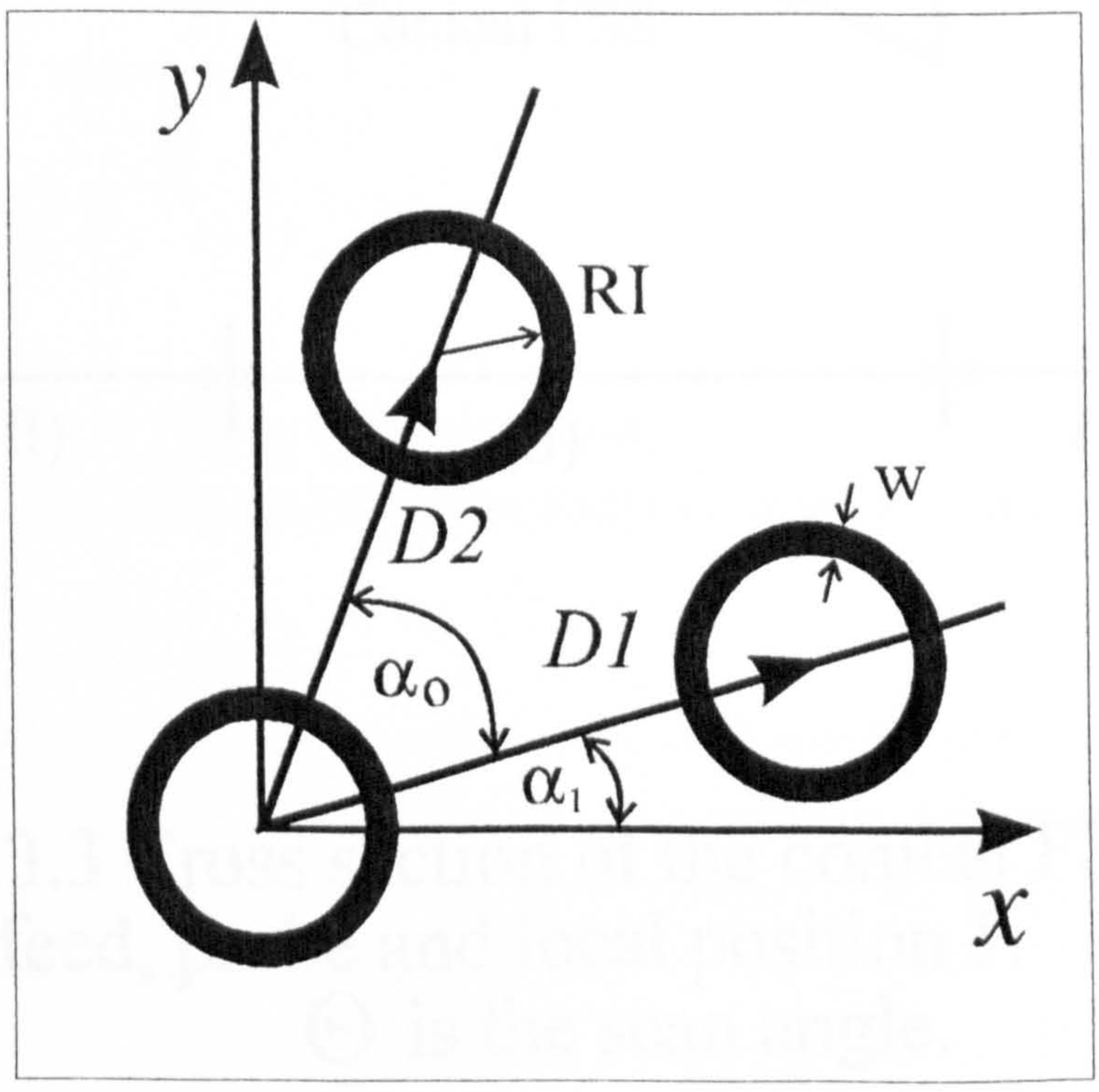

Fig.3.2b Local unit cell showing
the array element geometry.

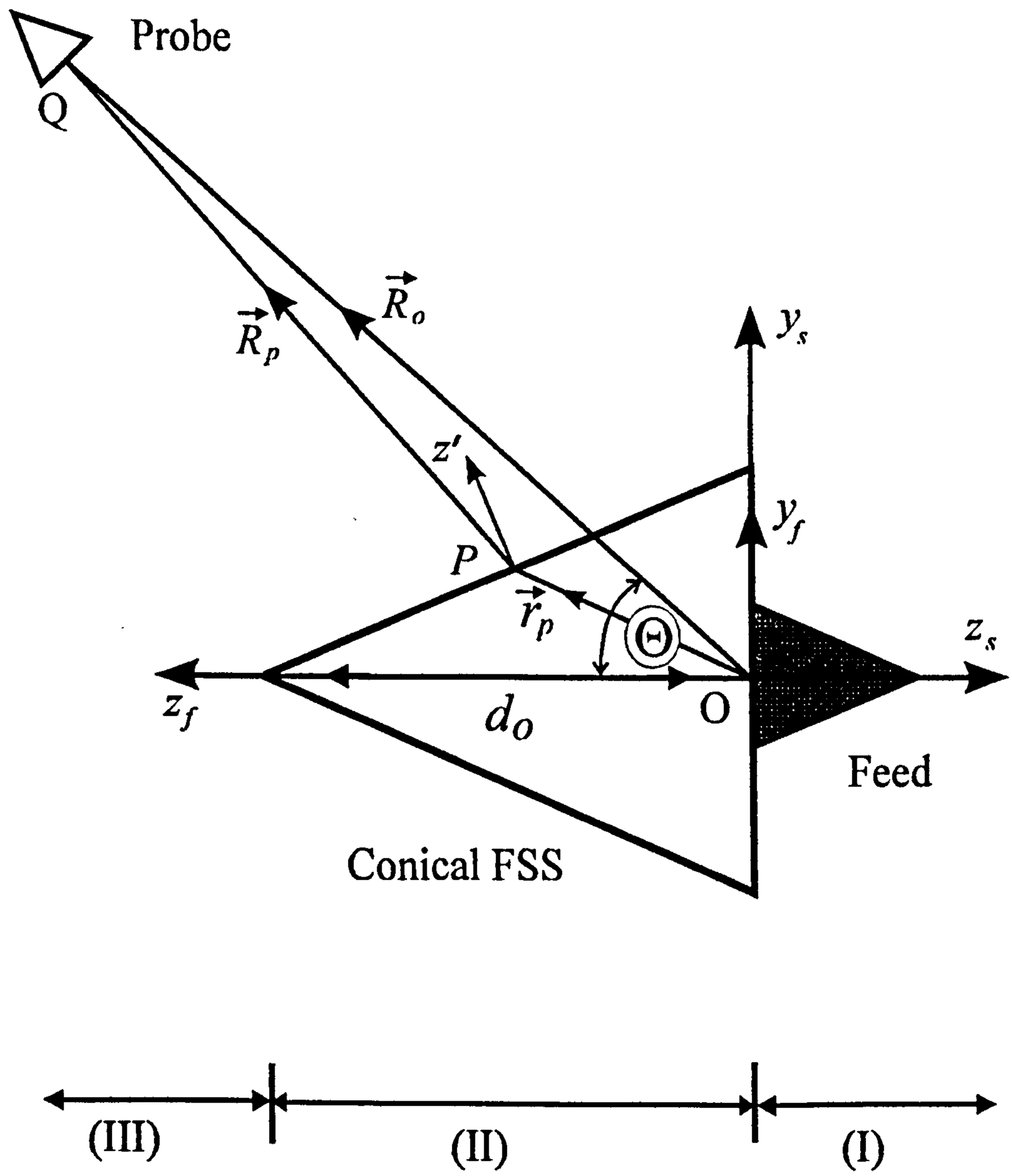

Fig. 3.3 Cross section of the conical FSS showing the feed, probe and local position P.
Θ is the scan angle.

where

$$x_1 = m'D1\cos\alpha_1' + n'D2\cos\alpha_2' + t_0\cos\left(\frac{\beta'}{2}\right) \tag{3.10}$$

$$y_1 = m'D1\sin\alpha_1' + n'D2\sin\alpha_2' + t_0\sin\left(\frac{\beta'}{2}\right) \tag{3.11}$$

$$\alpha_1' = \frac{\beta' - \alpha_0}{2} \tag{3.12}$$

$$\alpha_2' = \alpha_0 + \alpha_1' \tag{3.13}$$

and $\beta' = \dfrac{r_c\pi}{s_c}$ (3.14)

m', n' are the location indices and t_0 is the distance between the tip of the sector and the actual tip of the cone. The (x_1, y_1) co-ordinate system is transformed into the surface co-ordinate system using the following set of equations

$$x_s = \sqrt{x_1^2 + y_1^2}\,\sin\alpha_c\cos\left(\frac{\pi}{\beta'}\tan^{-1}\left(\frac{y_1}{x_1}\right)\right) \tag{3.15}$$

$$y_s = \sqrt{x_1^2 + y_1^2}\,\sin\alpha_c\sin\left(\frac{\pi}{\beta'}\tan^{-1}\left(\frac{y_1}{x_1}\right)\right) \tag{3.16}$$

and $z_s = \sqrt{x_1^2 + y_1^2}\,\cos\alpha_c - z_h$ (3.17)

3.3 Analysis of FSS and feed system

The description of the analysis of the scattering from the FSS cone can be divided into three parts:

(I) The illumination on the inner side of the cone according to the radiation of the feed.
(II) The determination of the total fields on the surface of the cone.
(III) The transformation of the equivalent currents of the conical surface to obtain the overall radiation patterns.

In step I the excitation on each aperture is found using an appropriate feed model. In step II the surface currents are computed from a modal (Floquet's) analysis [2, 6], assuming an infinite array of apertures, shown in Fig.3.2b, which is tangential to the local point P. Fig.3.3 shows a cross section of the surface, depicting the three steps,

and the position of the feed and receiving probe in relation to it. Part III deals with the integration of the equivalent currents, achieved using the Stratton and Chu formulation [6]. Throughout these steps a number of transformations take place, starting from the feed co-ordinates to the local co-ordinates. It is imperative to allow the normal vector to vary according to the curvature whilst choosing a suitable local lattice geometry orientation in relation to the tangential co-ordinate components. This choice stems from the difficulty in defining a periodic array on a curved surface. However, by careful examination of neighbouring array elements on the surface a local lattice can be found, and is simple to compute.

3.3.1 Feed to surface co-ordinate transformation

In a radome and feed system, the feed is sometimes required to scan across the radome surface. Therefore, the feed could be directed away the tip of the cone. In the computer model here, the feed is allowed to tilt in either the y_f-z_f or x_f-z_f planes as illustrated in Fig.3.4a and Fig.3.4b. These two cases would also facilitate situations where orthogonal polarisations are required in the incidence. The mode of incidence is defined according to electric(E) field vector polarisation with respect to the two halves of the FSS cone.

(i) TE incidence is for the E field vector orthogonal to the line dividing cutting the left and right halves of the FSS cone.

(i) TM incidence is for the E field vector parallel to the dividing line.

For tilting of the feed in the y_f-z_f and x_f-z_f planes, details of the co-ordinate transformations are found in Appendix 2.
The feed can be made to move along the cone axis (z_S axis), say, $d_{zo}\hat{z}_s$, by translating z_S to z'_S co-ordinate such that,

$$z'_S = z_S - d_{zo} \tag{3.18}$$

This provides addition flexibility for adjusting the feed according to the size of the FSS cone. In this study, the work is devoted to the case where the feed is located at the base of the cone and looking towards its tip.

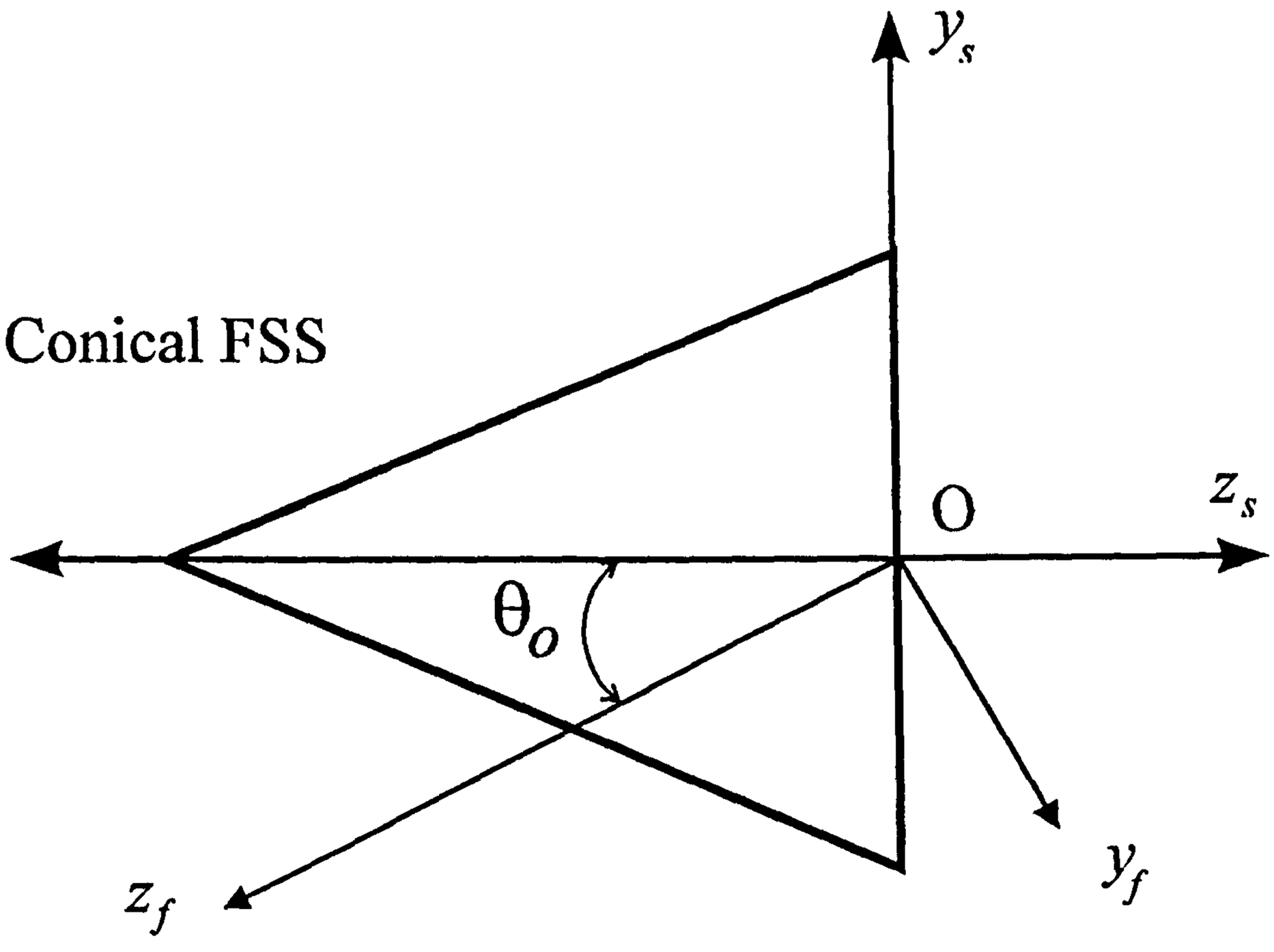

Fig. 3.4a Conical FSS tilted in the plane of $y_f - z_f$.

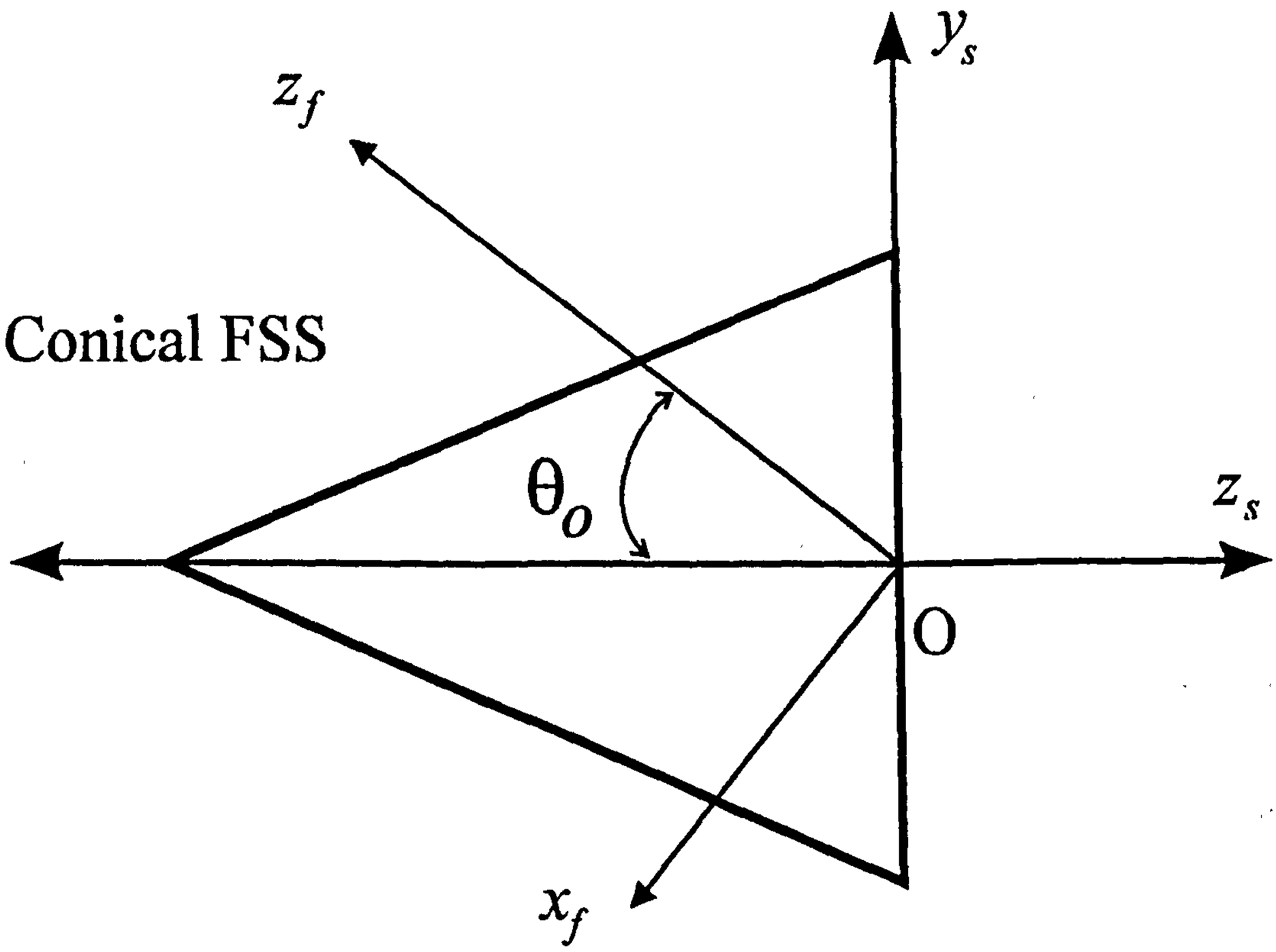

Fig. 3.4b Conical FSS tilted in the plane of $x_f - z_f$.

3.3.2 Feed modelling

In order to model the feed in terms of the surface co-ordinates a three dimensional transformation is required (Appendix 2). In addition, a further transformation takes place between the local primed co-ordinate system (Eqs 3.6, 3.7 and 3.8) and the one required for the modal (Floquet's expansion) analysis, say (x,y,z), of the currents (infinite array calculations, step (II)). The latter is important since it accounts for the lattice orientations on the curved surface. With regard to the modal analysis both the incident fields and wave vectors need to be written in terms of (x,y,z). The incident electric field can be expressed as

$$\vec{E}^i = E_x^i \hat{x} + E_y^i \hat{y} + E_z^i \hat{z} \tag{3.19}$$

where $$\begin{bmatrix} \hat{x} \\ \hat{y} \end{bmatrix} = \begin{bmatrix} cos(\alpha_l'' - \alpha_1) & sin(\alpha_l'' - \alpha_1) \\ -sin(\alpha_l'' - \alpha_1) & cos(\alpha_l'' - \alpha_1) \end{bmatrix} \begin{bmatrix} \hat{x}' \\ \hat{y}' \end{bmatrix} \tag{3.20}$$

and $$tan\,\alpha_l'' = \frac{\hat{y}' \cdot \vec{D}1}{\hat{x}' \cdot \vec{D}1} \tag{3.21}$$

The incident wave vector angles (θ, ϕ) are computed from the following projections:

$$cos\,\theta = \vec{r}_p \cdot \hat{z}' \tag{3.22}$$

and $$tan\,\phi = \frac{\hat{y} \cdot \vec{r}_p}{\hat{x} \cdot \vec{r}_p} \tag{3.23}$$

where $\vec{r}_p$ is the distance between the feed origin and the surface.

The unit normal is identical to both primed and unprimed co-ordinate systems. The components of the incident fields in Eq.(3.19) are calculated by transforming the incident fields from the feed co-ordinate system (x_f, y_f, z_f) into the one required by the modal analysis, (x,y,z). The b_1 (TM) and b_2 (TE) components of $\vec{E}^i$ are subsequently calculated and used in the Floquet's field expansion. This enables both electric and magnetic surface currents to be found. It can be shown from Eq.2.60 and Eq.2.61 that the incident plane wave can be decomposed into b_1 and b_2 components where:

$$b_1 = E_x^i cos\,\phi + E_y^i sin\,\phi \tag{3.24}$$

$$b_2 = E_y^i cos\,\phi - E_x^i sin\,\phi \tag{3.25}$$

A circular conical corrugated horn has been used as a feed because it gives a symmetric beam and low cross polarisation. The near field feed illumination is modelled in three different ways here because of their relative advantages in computation time, memory and accuracy. The first is based on a far field pattern of the feed to approximate the near fields and it will be denoted as FN. This approximation produces a local plane wave incident field at each element on the cone which is a prerequisite in using the modal analysis method for an infinite planar array. The amplitude of the illuminating field was modelled as a Gaussian distribution fitted to the measured far field pattern of the feed. Details of the FN feed model can be found in Appendix 3.

The second uses a parallel beam (PB) approximation emanating from the feed aperture. The parallel rays are compensated by a phase term due to the ray path differences at the curved surface. It can be shown that the incident field is given by:

$$\vec{E}^i = e^{-jk_o z_f} \vec{E}^a \tag{3.26}$$

The parallel rays depend on the aperture fields of the corrugated conical feed which is given in Appendix 4. Derivation of the PB feed model is described in Appendix 5. With regard to the local incidence, Eq.(3.22) and Eq.(3.23) apply to both FN and PB feed models. In the latter, the parallel beam is constructed by replacing $\vec{r}_p$ with a vector normal to the feed aperture.

A more rigorous evaluation approximates the near fields of the horn using a superposition of point sources (SPS) from its aperture fields. Since the feed has a circular aperture the aperture fields were divided into small patches in a polar grid co-ordinate system, as shown in Fig.3.5. Assuming that the aperture fields do not vary within each patch, the electric field at a point due to a source at the $m_s n_s$th patch can be written in the following form as

$$\vec{E}^i_{m_s n_s} = \frac{-j\omega\mu_0 e^{-jk_0\left|\vec{r}_{m_s n_s}\right|} A_{m_s n_s}}{4\pi\left|\vec{r}_{m_s n_s}\right|}\left[\vec{J}^a_{m_s n_s} - \left(\vec{J}^a_{m_s n_s} \cdot \hat{r}_{m_s n_s}\right)\hat{r}_{m_s n_s} + \sqrt{\frac{\varepsilon_o}{\mu_o}}\vec{M}^a_{m_s n_s} \times \hat{r}_{m_s n_s}\right] \tag{3.27}$$

where the $m_s n_s$th electric and magnetic current sources are,

$$\vec{J}^a_{m_s n_s} = \hat{z}_f \times \vec{H}^a_{m_s n_s} \text{ and } \vec{M}^a_{m_s n_s} = -\hat{z}_f \times \vec{E}^a_{m_s n_s} \text{ , respectively} \tag{3.28}$$

A is the patch area and $\vec{E}^a$ and $\vec{H}^a$ are the feed's electric and magnetic aperture fields respectively [7], expressed in terms of the feed co-ordinate system. Details of the derivations of Eq.(3.27) for a point source can be found in Appendix 6. The summation of all these contributions establishes the local field at each FSS element.

For the SPS case, the incident wave vector angles, now denoted as $\left(\theta_{m_s n_s}, \phi_{m_s n_s}\right)$, are computed from the following projections:

$$\cos\theta_{m_s n_s} = \vec{r}_{m_s n_s} \cdot \hat{z}' \tag{3.29}$$

and $$\tan\phi_{m_s n_s} = \frac{\hat{y} \cdot \vec{r}_{m_s n_s}}{\hat{x} \cdot \vec{r}_{m_s n_s}} \tag{3.30}$$

Unlike the FN or the PB feed modelling, the SPS model produces a more realistic inner cone illumination at the expense of memory storage and computation time.

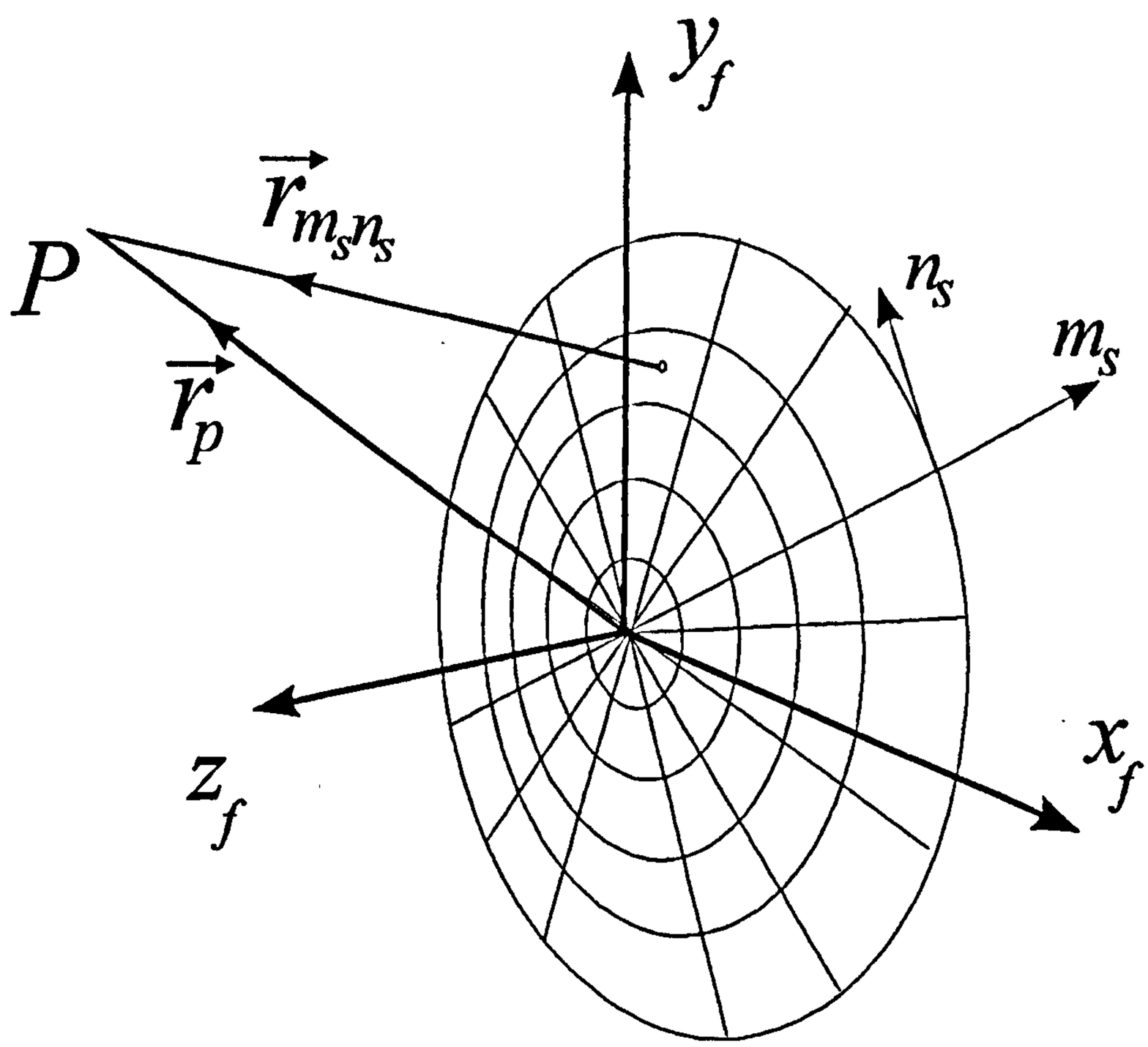

Fig. 3.5 Polar position of point sources in the feed aperture for SPS model.

3.3.3 Surface currents from modal analysis

An advantage of using the modal analysis is that it enables the calculation of both electric and magnetic surface currents. With regard to the scattered field computation (Sec.3.3.4) these currents now represent the source excitation. Both sources are computed over each entire unit cell using a summation over the Floquet modes (p,q). Here use has been made of an array of apertures having multiple dielectric superstrates and substrates. Locally the electric current source $\vec{J}$ and magnetic source $\vec{M}$ can be expressed in terms of magnetic and electric fields respectively. For the element located at point P (Fig. 3.3),

$$\vec{J}_P = \hat{z} \times \vec{H}_P \quad \text{and} \tag{3.31}$$

$$\vec{M}_P = -\hat{z} \times \vec{E}_P \tag{3.32}$$

where

$$\vec{E}(x,y,z) = \sum_{mpq} \tilde{E}_{mpq} \psi_{pq} \hat{\kappa}_{mpq} \tag{3.33}$$

$$\vec{H}(x,y,z) = \sum_{mpq} \eta_4 \sigma_3^4(m,p,q) \tilde{E}_{mpq} \psi_{pq} \hat{z} \times \hat{\kappa}_{mpq} \tag{3.34}$$

The subscript that denotes the Pth element has been ignored here for clarity.

The above Floquet expansions have been discussed in Sec.2.2.3. ψ_{pq} is the Floquet mode and the modal index m denotes either the TE or TM modes.

η is the modal admittance and the coefficient σ involves components from the dielectric media. The subscript *3* and superscript *4* denotes the interface at the FSS plane sandwich by the *3*rd dielectric layer in front and *4*th layer behind as shown in Fig.2.1 for a general case. Here Eq.(3.33) and Eq.(3.34) are expressions for the fields when the FSS screen is wrapped on the exterior of the cone i.e. no dielectric layers denoted by 4, 5, 6 and 7 in Fig.2.1 (Please refer to Sec.3.4.1 for further descriptions of the construction of the experimental FSS). By enforcing the boundary conditions on the unit cell and expanding the electric field as a set of basis functions in the aperture, their coefficients are found using the Galerkin's procedure. It can be shown that $\tilde{E}_{mpq}$ is derived as follows.

$$\tilde{E}_{mpq} = \iint_{aperture} \vec{E}(x,y,z)\,\psi^*_{pq}dxdy.\vec{\kappa}_{mpq}$$

$$= \iint_{aperture} -\vec{M}\psi^*_{pq}dxdy.\hat{z}\times\vec{\kappa}_{mpq}$$

$$= \iint_{aperture} -\sum_{n=1}^{n=N} c_n h_n \hat{\alpha}\psi^*_{pq}dxdy.\hat{z}\times\vec{\kappa}_{mpq}$$

$$= \iint_{aperture} -\sum_{n=1}^{n=N} c_n(h_{nx}\hat{x}+h_{ny}\hat{y})\psi^*_{pq}dxdy.\vec{p}_{mpq}$$

$$= -\sum_{n=1}^{n=N} c_n(g_{nx}\hat{x}+g_{ny}\hat{y}).(p_{mpqx}\hat{x}+p_{mpqy}\hat{y})$$

$$= -\sum_{n=1}^{n=N} c_n g_{nx} p_{mpqx} - \sum_{n=1}^{n=N} c_n g_{ny} p_{mpqy} \tag{3.35}$$

where

$$g_{nx} = \iint_{aperture} h_{nx}\psi^*_{pq}dxdy \tag{3.36}$$

$$g_{ny} = \iint_{aperture} h_{ny}\psi^*_{pq}dxdy \tag{3.37}$$

and $\hat{p}_{mpq} = p_{mpqx}\hat{x} + p_{mpqy}\hat{y} = \hat{z}\times\hat{\kappa}_{mpq}$ (3.38)

$$\vec{M} = \sum_{n=1}^{n=N} c_n h_n \hat{\alpha} \tag{3.39}$$

$\vec{M}$ is the magnetic current flowing in a slotted FSS element. For a ring slot it is assumed to flow around the ring circumference but remains constant across its thickness with $\hat{\alpha}$ tangential to its circumference. h_n is the nth basis function defined over the circumference with N denoting the total number of basis functions required.

In order to use these field expansions in a radiation integral as current sources, they must be expressed in a suitable co-ordinate system for computation. Expressing Eq.(3.33) and Eq.(3.34) in the x-y co-ordinates yields,

$$\vec{E}(x,y,z) = \sum_{mpq}\left(\tilde{E}_{xpq}\hat{x} + \tilde{E}_{ypq}\hat{y}\right)\psi_{pq} \tag{3.40}$$

$$\vec{H}(x,y,z) = \sum_{mpq}\left(\tilde{H}_{xpq}\hat{x} + \tilde{H}_{ypq}\hat{y}\right)\psi_{pq} \tag{3.41}$$

where

$$\tilde{E}_{xpq} = \tilde{E}_{1pq}\kappa_{1pqx} + \tilde{E}_{2pq}\kappa_{2pqx} \tag{3.42}$$

$$\tilde{E}_{ypq} = \tilde{E}_{1pq}\kappa_{1pqy} + \tilde{E}_{2pq}\kappa_{2pqy} \tag{3.43}$$

and

$$\tilde{H}_{xpq} = \eta_4\sigma_3^4(1,p,q)\tilde{E}_{1pq}p_{1pqx} + \eta_4\sigma_3^4(2,p,q)\tilde{E}_{2pq}p_{2pqx} \tag{3.44}$$

$$\tilde{H}_{ypq} = \eta_4\sigma_3^4(1,p,q)\tilde{E}_{1pq}p_{1pqy} + \eta_4\sigma_3^4(2,p,q)\tilde{E}_{2pq}p_{2pqy} \tag{3.45}$$

such that $\hat{\kappa}_{mpq} = \kappa_{mpqx}\hat{x} + \kappa_{mpqy}\hat{y}$ (3.46)

Therefore, Eq.(3.42) to Eq.(3.45) can be calculated and hence the electric and magnetic fields in Eq.(3.33) and Eq.(3.34). The inclusion of the Floquet expression in the radiation integral enables the currents to be integrated over each unit cell, as described in the following section.

3.3.4 Scattered fields using the radiation integral

With the element fields determined, the far field pattern of the feed in the presence of the FSS cone was calculated by superimposing the radiated fields from the equivalent electric and magnetic current distributions in each unit cell of the ring slot. The far field pattern due to the *P*th unit cell was determined using the following vector radiation integral [7]:

$$\vec{E}_p(\vec{R}_p) = \frac{-j\omega\mu_o}{4\pi}\frac{e^{-jk_oR_p}}{R_p}\iint_{\substack{unit\\cell}}\left(\vec{J}_P - (\vec{J}_P.\hat{R}_P)\hat{R}_P + \sqrt{\frac{\varepsilon_o}{\mu_o}}\vec{M}_P \times \hat{R}_P\right)e^{jk_o\hat{R}_P.\vec{r}_t}d\vec{r} \tag{3.47}$$

$\vec{M}_P$ and $\vec{J}_P$ are the equivalent magnetic and electric currents respectively (from Eq.(3.31) and Eq.(3.32)) , and are valid over the entire unit cell. The integration in Eq.(3.47) will be transformed into the local (unprimed) variables used in the Floquet expansions.

$\vec{R}_P$ is the vector joining the centre of the local cell to the far field point Q (in feed co-ordinates) given by:

$$\vec{R}_P = R_{Px}\hat{x}_f + R_{Py}\hat{y}_f + R_{Pz}\hat{z}_f \tag{3.48}$$

$\vec{r}_t$ is the position vector in the unit cell given by:

$$\vec{r}_t = x\hat{x} + y\hat{y} \text{ (in the local coordinates of the modal analysis) or} \tag{3.49}$$

$$\vec{r}_t = x'\hat{x}' + y'\hat{y}' \text{(in local prime coordinates)} \tag{3.50}$$

For convenience, Eq.(3.50) will be expressed in feed co-ordinates. The relationship between the local primed and surface coordinates in Eq.(3.50) can be found in Eq.(3.7) and Eq.(3.8). The surface coordinates are further converted to feed coordinates using the transformation (Appendix 2).

Thus, expressing the tangential local prime co-ordinates in feed co-ordinates yields:

$$\hat{x}' = A_1\hat{x}_f + A_2\hat{y}_f + A_3\hat{z}_f \text{ and} \tag{3.51}$$

$$\hat{y}' = B_1\hat{x}_f + B_2\hat{y}_f + B_3\hat{z}_f \tag{3.52}$$

where A_u and B_u are coefficients derived from the transformation of feed to local primed coordinates.

In order to compute the Fourier transform in the integral, the term within the exponential should be expressed in modal coordinates (x, y). Therefore,

$$\vec{r}_t.\vec{R}_p = L_x'x' + L_y'y' \text{ (using Eq.(3.47) to Eq.(3.52))} \tag{3.53}$$

where

$$L_x' = A_1R_{Px} + A_2R_{Py} + A_3R_{Pz} \tag{3.54}$$

$$L_y' = B_1R_{Px} + B_2R_{Py} + B_3R_{Pz} \tag{3.55}$$

Eq.(3.53) is expressed in (x, y) using the relationship given in Eq.(3.61). Thus,

$$\vec{r}_t.\hat{R}_P = L_x x + L_y y \tag{3.56}$$

where

$$L_x = L_x' \cos\phi_b + L_y' \sin\phi_b \tag{3.57}$$

$$L_y = L_y' \cos\phi_b - L_x' \sin\phi_b \tag{3.58}$$

The relationship between the local coordinates and the modal coordinates can be illustrated in Fig.3.6a. Assume that the Floquet expansion of FSS element C is required. If A is the next element closest to C, it is located in the infinite array as,

$$\vec{D}1 = \vec{r}_C - \vec{r}_A \tag{3.59}$$

where $\vec{r}_A$ and $\vec{r}_C$ are the position vectors of A and C with respect to the origin of the feed coordinates given by Fig.3.3 as $\vec{r}_s$.

$$\text{So, } \alpha_1' = \tan^{-1}\left(\frac{\hat{y}'.\vec{D}_1}{\hat{x}'.\vec{D}_1}\right) \tag{3.60}$$

From Fig. 3.6a, it can be shown that,

$$\phi_b = \alpha_1' - \alpha_1 \tag{3.61}$$

α_1' varies with curvature with changes in $(\hat{x}', \hat{y}')$ across the conical surface but α_1 is fixed by the lattice geometry.

Hence, the relationship between the local primed coordinates and the modal coordinates is given by the following transformation from Fig.3.6a,

$$\hat{x} = \hat{x}' \cos\phi_b + \hat{y}' \sin\phi_b \tag{3.62}$$

$$\hat{y} = \hat{y}' \cos\phi_b - \hat{x}' \sin\phi_b \tag{3.63}$$

Since the sources can be expressed in Floquet modes over the entire unit cell, they can be written in a similar form to Eq.(3.40) and Eq.(3.41) as:

$$\vec{J} = \sum_{mpq} \left(\tilde{J}_{xpq}\hat{x} + \tilde{J}_{ypq}\hat{y}\right)\psi_{pq} \tag{3.64}$$

$$\vec{M} = \sum_{mpq} \left(\tilde{M}_{xpq}\hat{x} + \tilde{M}_{ypq}\hat{y}\right)\psi_{pq} \tag{3.65}$$

the subscript P has been neglected here for clarity.

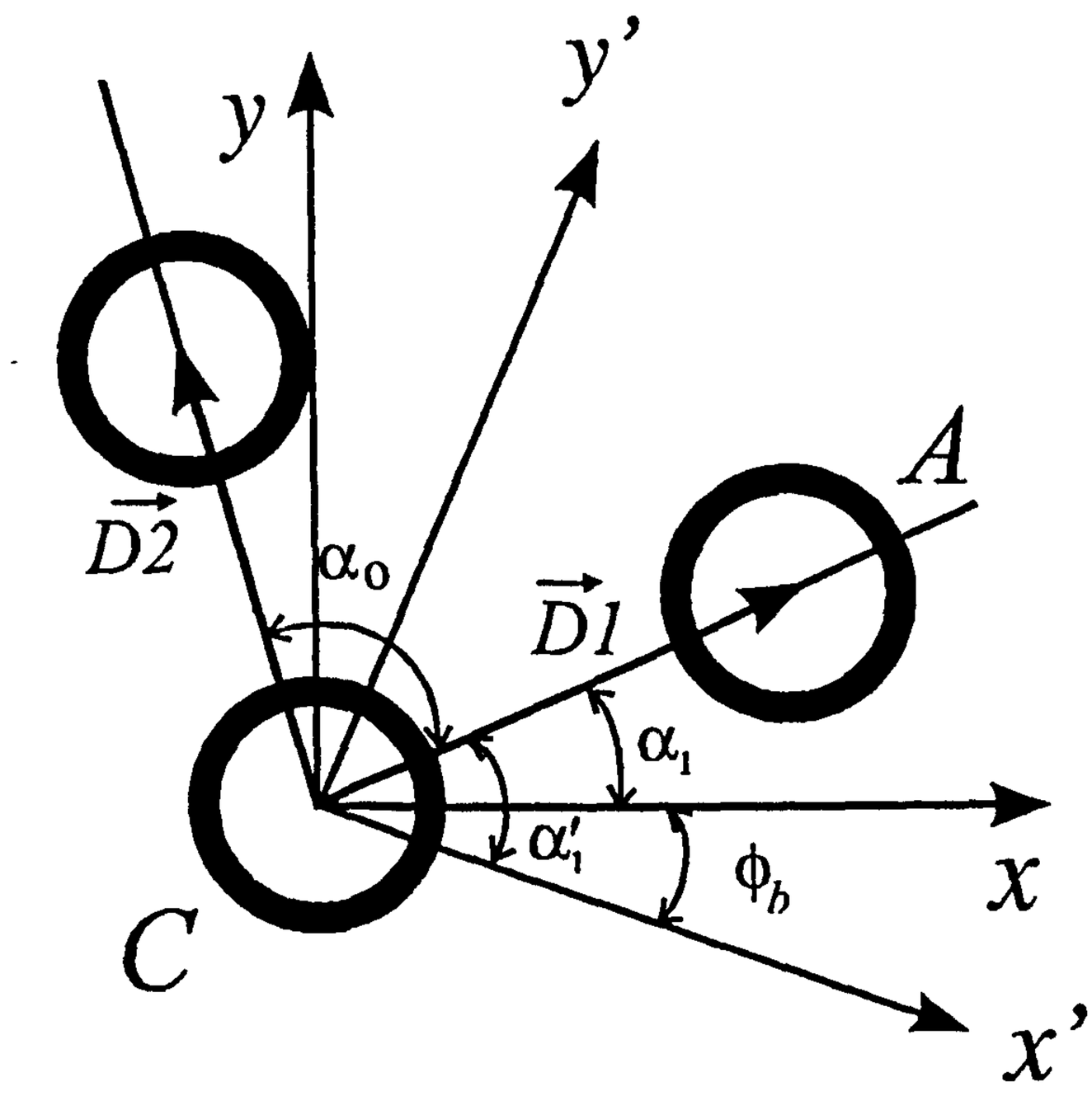

Fig.3.6a Local unit cell showing lattice array geometry.

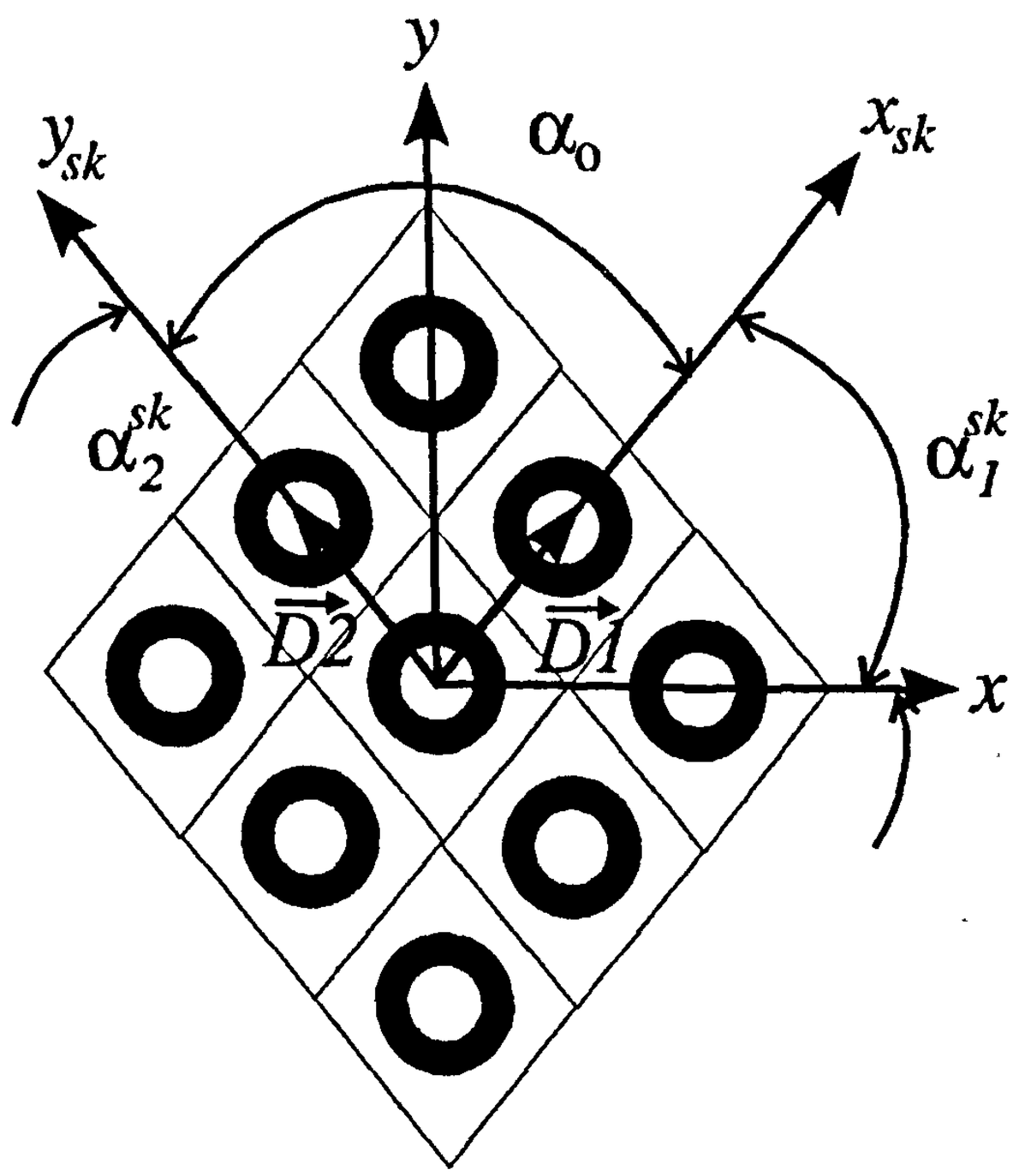

Fig.3.6b Skewed co-ordinate system for the Fourier transform.

It can be shown from Eq.(3.40) and Eq.(3.41) that,

$$\tilde{J}_{xpq} = -\tilde{H}_{ypq} \tag{3.66}$$

$$\tilde{J}_{ypq} = \tilde{H}_{xpq} \quad \text{and} \tag{3.67}$$

$$\tilde{M}_{xpq} = \tilde{E}_{ypq} \tag{3.68}$$

$$\tilde{M}_{ypq} = -\tilde{E}_{xpq} \tag{3.69}$$

The radiation integral form in Eq.(3.47) is essentially the Fourier transform of the current sources. For example the Fourier transform of the electric current source can be written as:

$$\tilde{J} = \iint_{unit\ cell} \tilde{J}\, e^{jk_o \vec{r}_t . \hat{R}_P} dxdy \tag{3.70}$$

$$= \tilde{J}_x \hat{x} + \tilde{J}_y \hat{y} \tag{3.71}$$

where, $$\tilde{J}_x = \sum_{pq} \tilde{J}_{xpq} \iint_{unit\ cell} e^{j\alpha_{pq}x} e^{j\beta_{pq}y} dxdy \tag{3.72}$$

$$\tilde{J}_y = \sum_{pq} \tilde{J}_{ypq} \iint_{unit\ cell} e^{j\alpha_{pq}x} e^{j\beta_{pq}y} dxdy \tag{3.73}$$

and $$\alpha_{pq} = k_o L_x - k_{tpqx} \tag{3.74}$$

$$\beta_{pq} = k_o L_y - k_{tpqy} \tag{3.75}$$

The above Fourier transforms also apply to the magnetic current source term.

In general, for triangular lattices the integration must be computed in terms of skewed axes (x_{sk}, y_{sk}) and converted using the determinant of the Jacobian.

So, expressing modal co-ordinates (x, y) in terms of skewed co-ordinates (x_{sk}, y_{sk}) as shown in Fig.3.6b gives,

$$x = y_{sk} \cos\alpha_2^{sk} + x_{sk} \cos\alpha_1^{sk} \tag{3.76}$$

$$y = y_{sk} \sin\alpha_2^{sk} + x_{sk} \sin\alpha_1^{sk} \tag{3.77}$$

where α_1^{sk} and α_2^{sk} are angles of the skewed lines with respect to (x,y) of the local infinite tangent plane. It can be shown that the Jacobian determinant Δ is given by,

$$\Delta = \begin{vmatrix} \dfrac{\partial x}{\partial x_{sk}} & \dfrac{\partial y}{\partial y_{sk}} \\ \dfrac{\partial y}{\partial x_{sk}} & \dfrac{\partial x}{\partial y_{sk}} \end{vmatrix} = \left| sin\left(\alpha_2^{sk} - \alpha_1^{sk}\right) \right| = sin\,\alpha_0 \tag{3.78}$$

Considering the x-component from Eq.(3.72) in the skewed co-ordinates yields,

$$\tilde{J}_x = \sum_{pq} \tilde{J}_{xpq} \iint_{unit\ cell} e^{j\alpha_{pq}x_{sk}} e^{j\beta_{pq}y_{sk}} \Delta dx_{sk} dy_{sk} \tag{3.79}$$

$$= \sum_{pq} \tilde{J}_{pq} \sin\alpha_0 D1 D2 \frac{\sin X_{pq} D1/2}{X_{pq} D1/2} \frac{\sin Y_{pq} D2/2}{Y_{pq} D2/2} \tag{3.80}$$

where

$$X_{pq} = \alpha_{pq} \cos\alpha_1^{sk} + \beta_{pq} \sin\alpha_1^{sk} \tag{3.81}$$

$$Y_{pq} = \alpha_{pq} \cos\alpha_2^{sk} + \beta_{pq} \sin\alpha_2^{sk} \tag{3.82}$$

$D1$ and $D2$ are the distances between the FSS element in the centre of the unit cell and its neighbouring elements in the local tangential infinite array as shown in Fig.3.6b.

Similar expressions can also be derived for the y component of the electric current source and x-y components of the magnetic current source.
The total radiated field is the sum of the contributions from all elements,

$$\vec{E}_Q = \sum_P \vec{E}_P(\vec{R}_P) \tag{3.83}$$

With regard to the SPS feed modelling the contribution from all the point sources at P, denoted by $\vec{E}_{m_s n_s}^P$, is summed up as follows:

$$\vec{E}_Q = \sum_P \sum_{m_s n_s} \vec{E}_{m_s n_s}^P(\vec{R}_P) \tag{3.84}$$

The predictions using the above formulation were compared against measured radiation patterns of a prototype conical frequency selective surface of ring apertures.

3.4 Experiments

The following section describes the construction of the conical FSS and the set-up used in the experiments. Amplitude and phase were measured initially to locate the phase centre of the transmitting feed so that radiation patterns could be measured accurately.

3.4.1 Construction and dimensions of conical FSS

Since a manufacturing facility is not available at LUT (Antennas and Microwave group) for printing an array of elements onto a curved surface, a pre-etched array was attached onto a rigid conical former. The FSS layer consisted of an array of ring apertures printed on a 0.037 mm thick polyester substrate with a relative permittivity $\varepsilon_r = 3$. It was etched onto two identical halves (semi-sector shaped as shown in Fig. 3.2a) and subsequently mounted on the top and bottom outer surfaces of the dielectric conical former. The former consisted of a 1 mm thick glass-reinforced plastic wall of relative permittivity 3.5 and loss tangent 0.015. This construction introduces a discontinuity in the array geometry which results from the non-conformability of the lattice at the joints between top and bottom halves. It does result, however, in two planes of symmetry being maintained on the cone surface.

A triangular lattice of ring slot elements was used for the sector array, Fig. 3.2b. The lattice and element parameters were as follows: $D1 = D2 = 6.8$ mm, $\alpha_0 = 60^o$, $\alpha_1 = -30^o$, RI = 2.4 mm and W = 0.35 mm. The array was designed to produce a passband frequency near 15 GHz. The initial design was based on the results of a modal analysis of an infinite planar FSS illuminated at an angle of incidence of 45° and was taken as a guide to the likely passband of the FSS cone. The cone height (z_h) was 554 mm and inner base radius (r_c) was 110 mm. In total there were 3,794 elements on the cone. A photograph of the actual conical FSS can be seen in Fig.3.7.

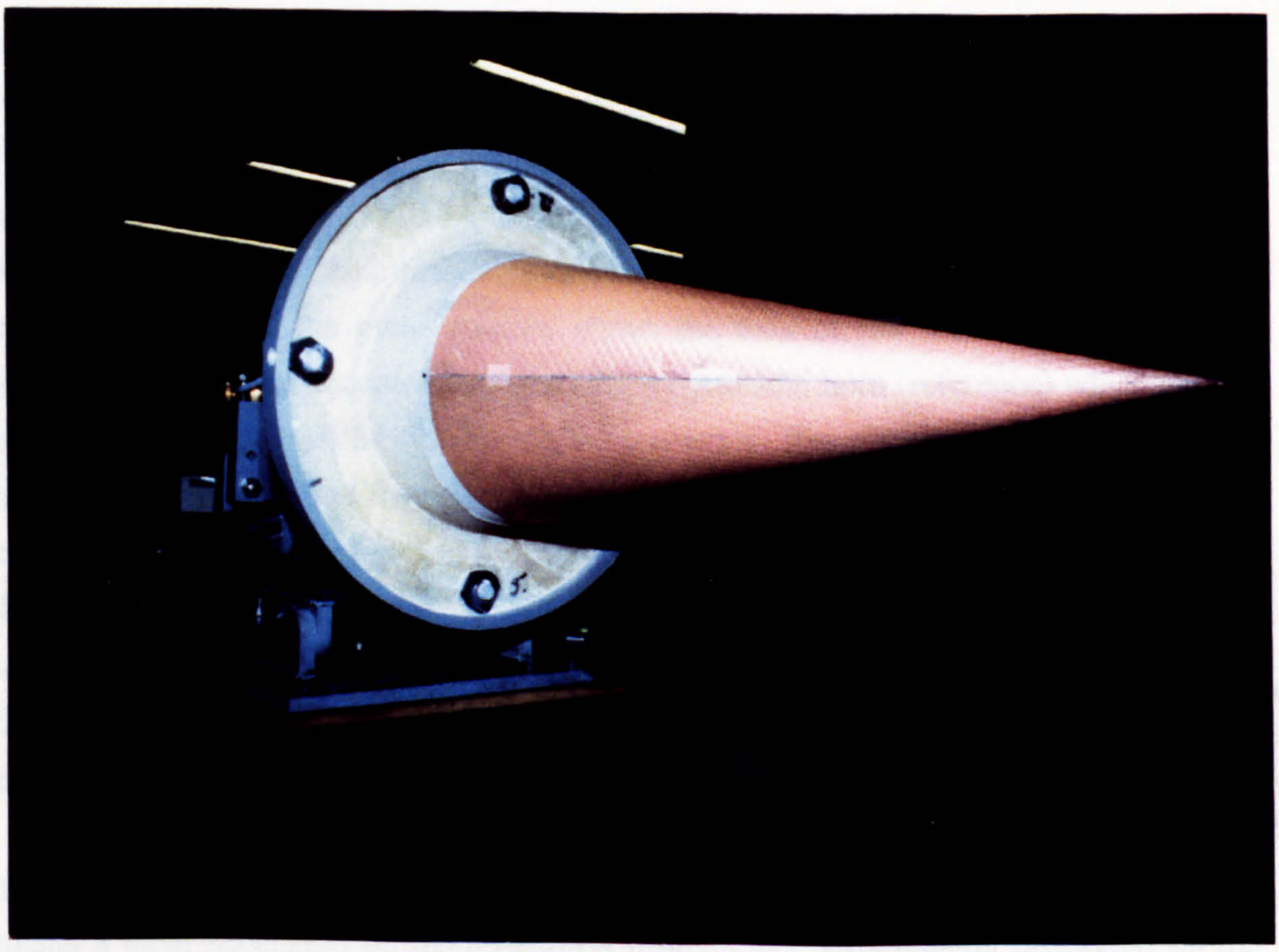

Fig.3.7 Curved FSS on a conical dielectric radome.

3.4.2 Experimental set-up

The inner surface of the conical FSS was illuminated by a conical corrugated feed horn with a circular aperture of diameter 96 mm and a semi-flare angle of 5.962^{o}, whose phase centre was measured to be about 2 cm from the aperture plane. The feed was designed to operate over the band 12-18 GHz. The FSS cone and feed horn were mounted on an azimuth turntable which provided the necessary angular scan for far field radiation pattern measurements. A fixed pyramidal horn antenna was used as a receive antenna at a distance $R_O = 1.59$ m from the origin.

The experimental set-up for both amplitude and phase measurements is illustrated in Fig.3.8. Experiments were performed in an anechoic chamber as shown in Fig.3.9. The FSS cone was mounted on a jig rested on a turn-table that contained the source which was controlled by the HP 8757A scalar network analyser. The elevation plane of the FSS is defined as the plane rotated about the phase centre of the feed. The azimuthal angle is defined as the plane rotated about the axis of the transmitting feed. The transmitted wave was received by a stationary pyramidal horn (reference) which in turn was connected to a HP8411A harmonic converter. Phase measurements required a reference signal obtained from the source, prior to attentuation, through a directional coupler which channelled part of the source signal to the receiver by a long waveguide. The waveguide was more than 1.59 metres which was also the distance between the transmit and receive horns in the measurements. A coaxial rotary joint has been used to facilitate the rotation of the source while keeping the reference receive horn in a fixed position.

The received microwave signal and reference input were mixed and down converted (using a local oscillator) by the HP8411A module and subsequently processed by the HP8410B vector network analyser. The response was viewed using a linear magnitude and phase display. A plot can be obtained now using an X-Y plotter. In the latter part of the experiments for the other conical FSS, discussed in Chapters 4 and 5, the set-up was improved by computer controlled software. An ADC card was installed in a PC to convert the analogue signal from the vector network analyser and the potentiometer (measures the angles of rotation) into digital data for storage purposes. In addition, a GPIB interface card in the PC allows computer control of the sweep oscillator (power source) so that amplitude and phase can be measured at each angle with a frequency scan as well. This enables more rapid measurements taken over a wider frequency range in contrast to the spot frequency scan without the computer control.

In order to measure the radiation pattern of the radome and feed system, the phase centre of the feed is required. The phase centre can be located when the phase pattern is almost constant at least between the angles defining the main lobe of the amplitude pattern. This is measured by recording the phase pattern for various rotation points along the axis of the transmitting horn. Fig.3.10 shows the amplitude and phase patterns of the feed at 15 GHz about the phase centre. The phase centre of the horn at 15 GHz is about 2 cm behind the feed aperture with the receiving feed 1.59 m away.

Although the conical corrugated horn is supposed to give low cross polarisation, it was necessary here to place a polariser grid at the feed aperture to reduce the peak cross polar levels. The amplitude and phase patterns were measured from 12 to 18 GHz. Crosspolar levels at these frequencies were recorded well below -40 dB.

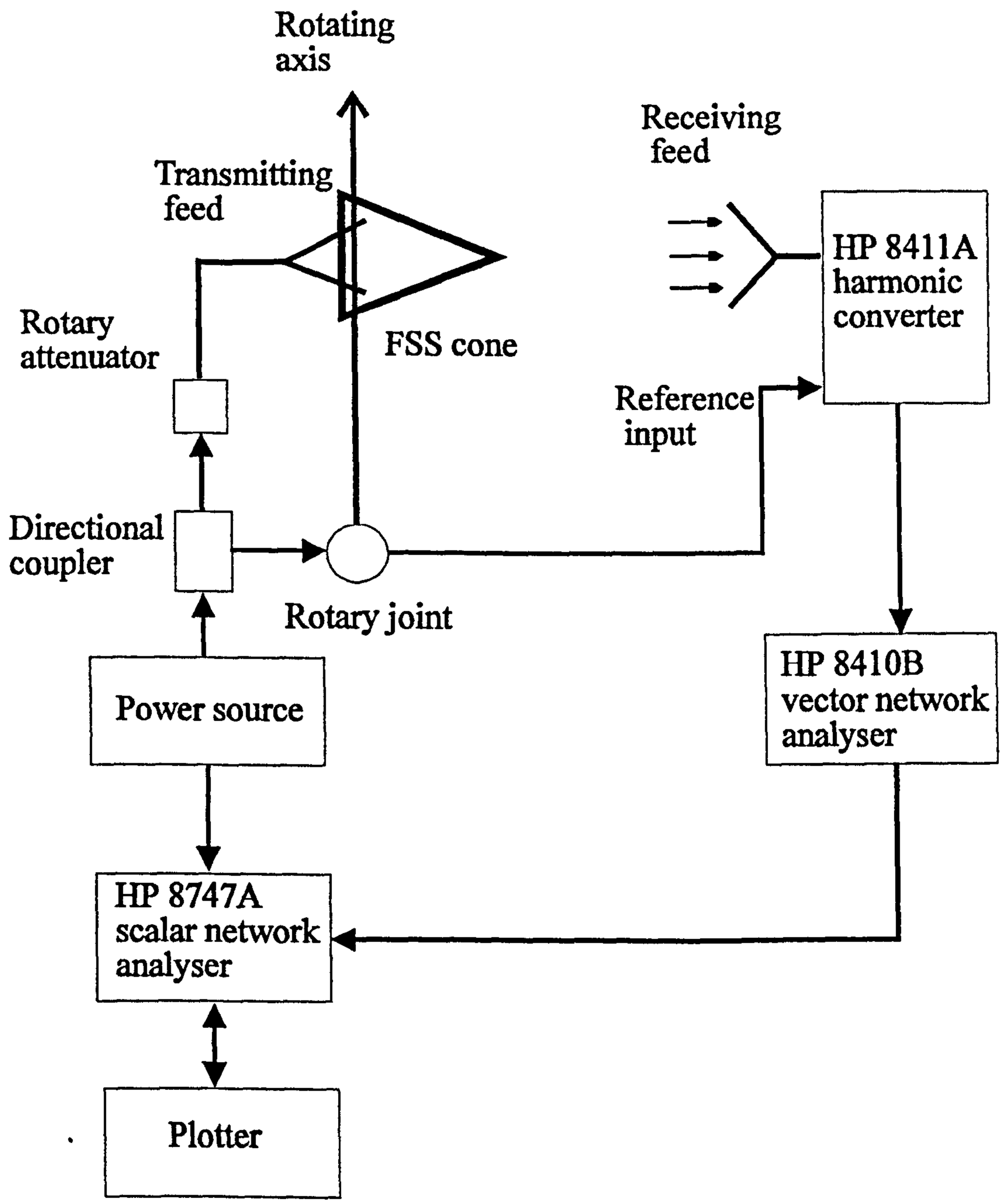

Fig.3.8 Experimental set-up for amplitude and phase measurements.

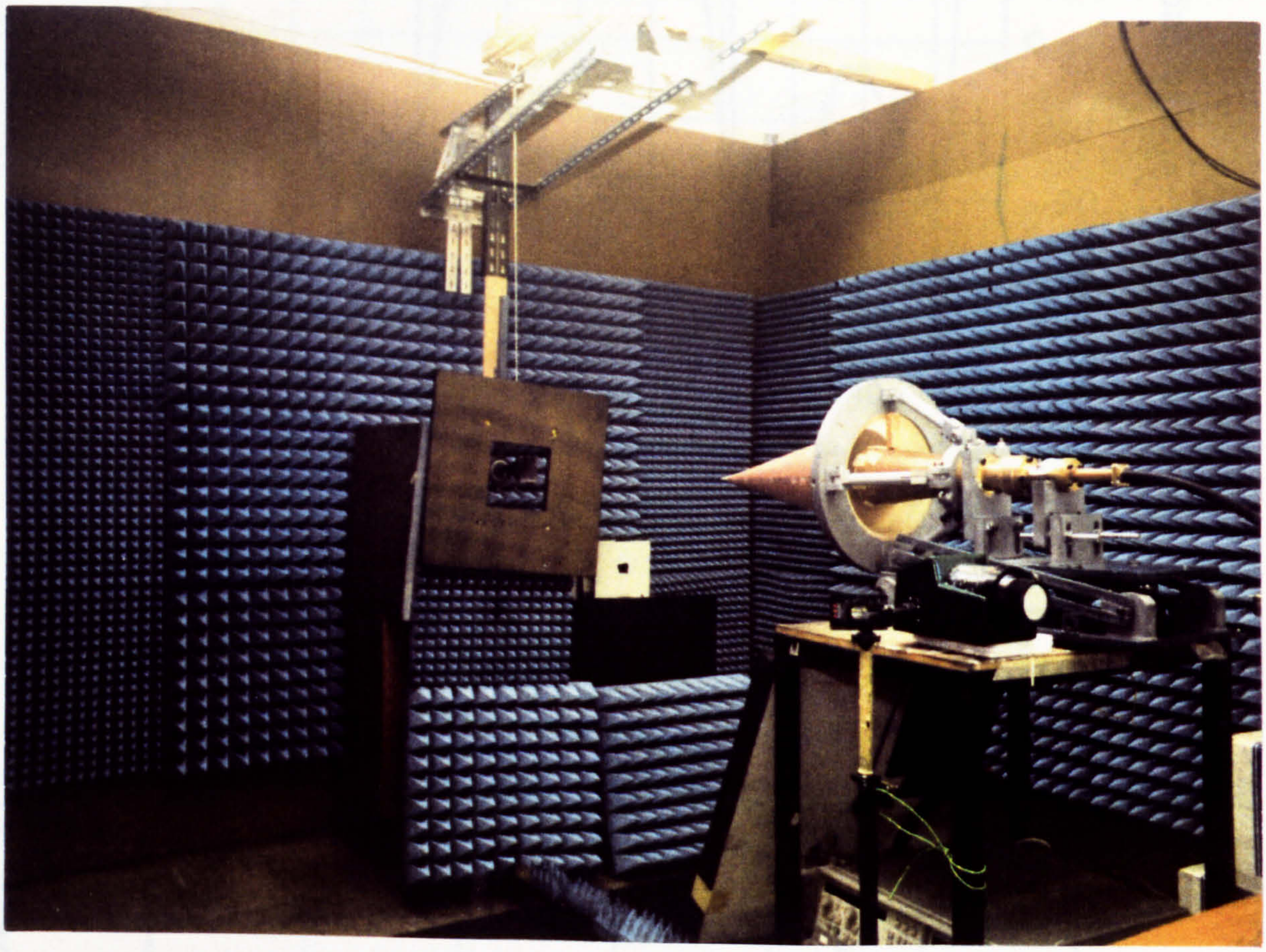

Fig.3.9 Experimental set-up in an anechoic chamber.

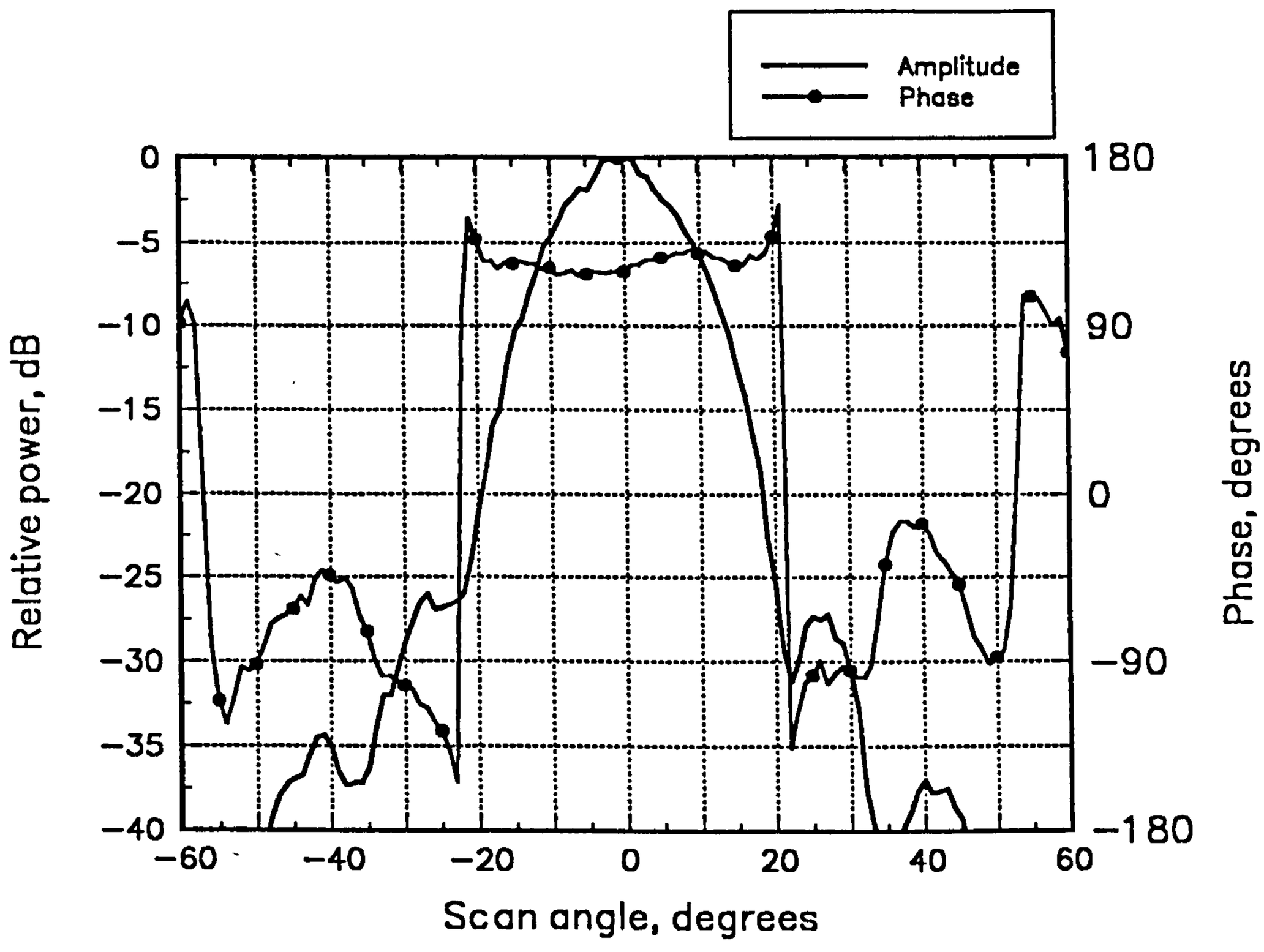

Fig.3.10 Feed pattern (45 deg. plane) at 15 GHz.

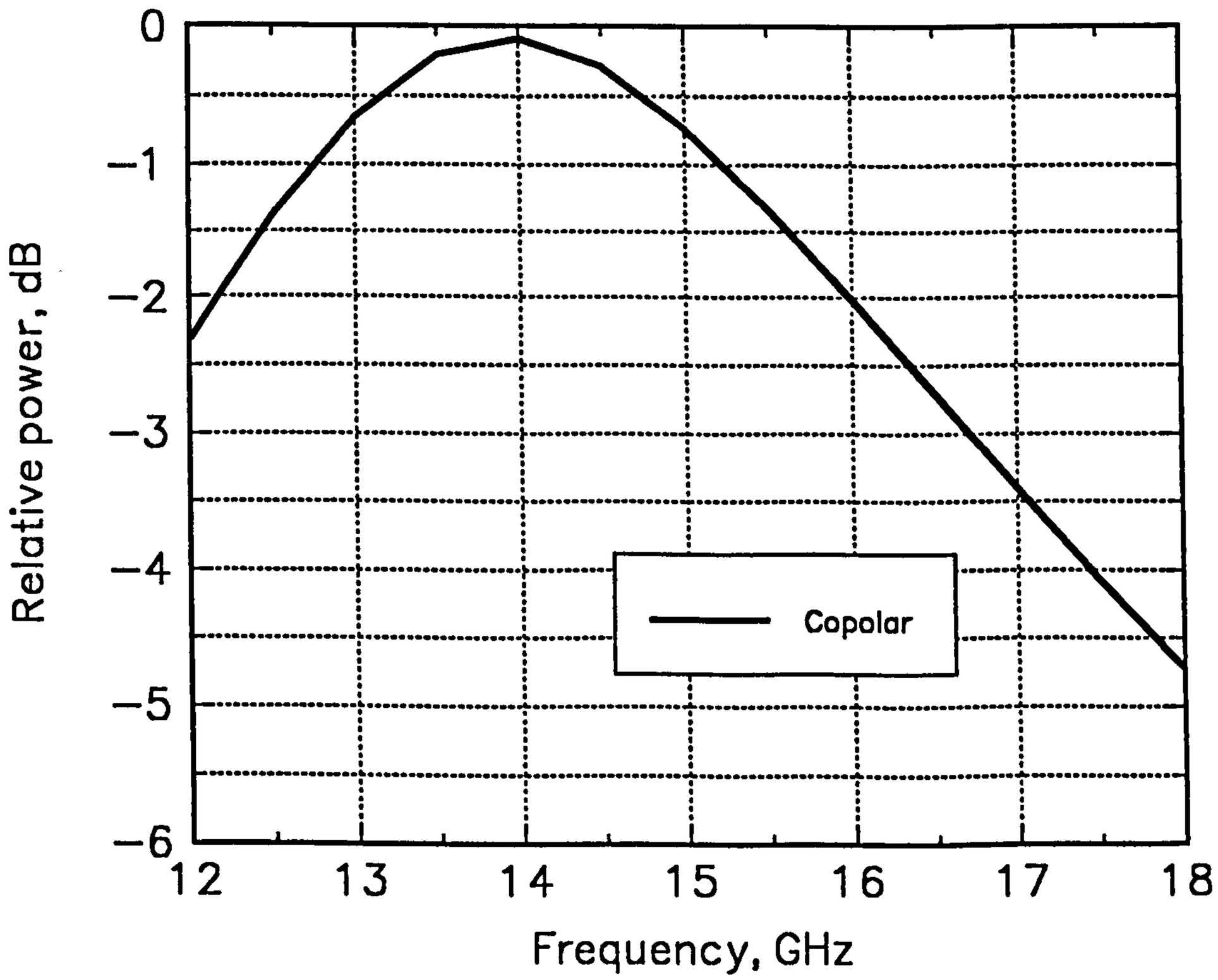

Fig.3.11 Transmission response of infinite planar array of slotted rings.

(Predicted boresight copolar levels of TE 45° incidence)

3.5 Results and Discussions

In this section, the predictions using the TIA with the three feed models (FN, PB and SPS) for a conical array of ring slots will be compared with measured results. The feed aperture is pointing towards the tip of the cone with the its axis along the axis of the cone as shown in Fig.3.8. The electric field orientation is orthogonal to the line dividing the two halves (top and bottom) of the cone and the far field power levels were normalised with respect to the peak power level of the feed alone. This normalisation was performed in both the predicted and measured results and allows the transmission loss of the FSS cone to be determined. Far field patterns of the FSS cone illuminated by the corrugated feed horn were measured over the angular range of $\pm 60^{o}$ Since the TIA approximation requires current modes of the slotted ring in an infinite array in order to compute the currents, these are estimated using predictions from the known current mode recipe of a planar infinite array of ring elements as shown in the following section.

3.5.1 Predictions from a planar infinite array of slotted rings

In order to predict the radiation patterns of the conical FSS in the TIA approach, it is required to characterise the modal currents of each local element with the modal analysis applied to an infinite planar FSS. Due to the severe curvature of the cone, large incident angles will be encountered. In order to estimate the passband of the conical FSS caused by varying incident angles, initial predictions were obtained for 0°, 45° and 75° of incidence as representatives of the range of incidences encountered in the cone. The predicted transmission response at 45° for TE plane wave incidence using the slotted rings is shown in Fig.3.11. The predicted passband is approximately 14 GHz.

The current is expanded as follows,

$$\vec{M} = \sum_{n_c=1}^{n_c=N_c} c_{n_c} h_{n_c} \hat{\alpha} + \sum_{n_s=1}^{n_s=N_s} c_{n_s} h_{n_s} \hat{\alpha} \tag{3.85}$$

where $\vec{M}$ is the magnetic current flowing in a ring. For a ring slot the current is assumed to flow around the ring circumference but remains constant across its thickness with $\hat{\alpha}$ tangential to its circumference. α is the angle measured from the x axis

where $\hat{\alpha} = -\sin\alpha\hat{x} + \cos\alpha\hat{y}$ (3.86)

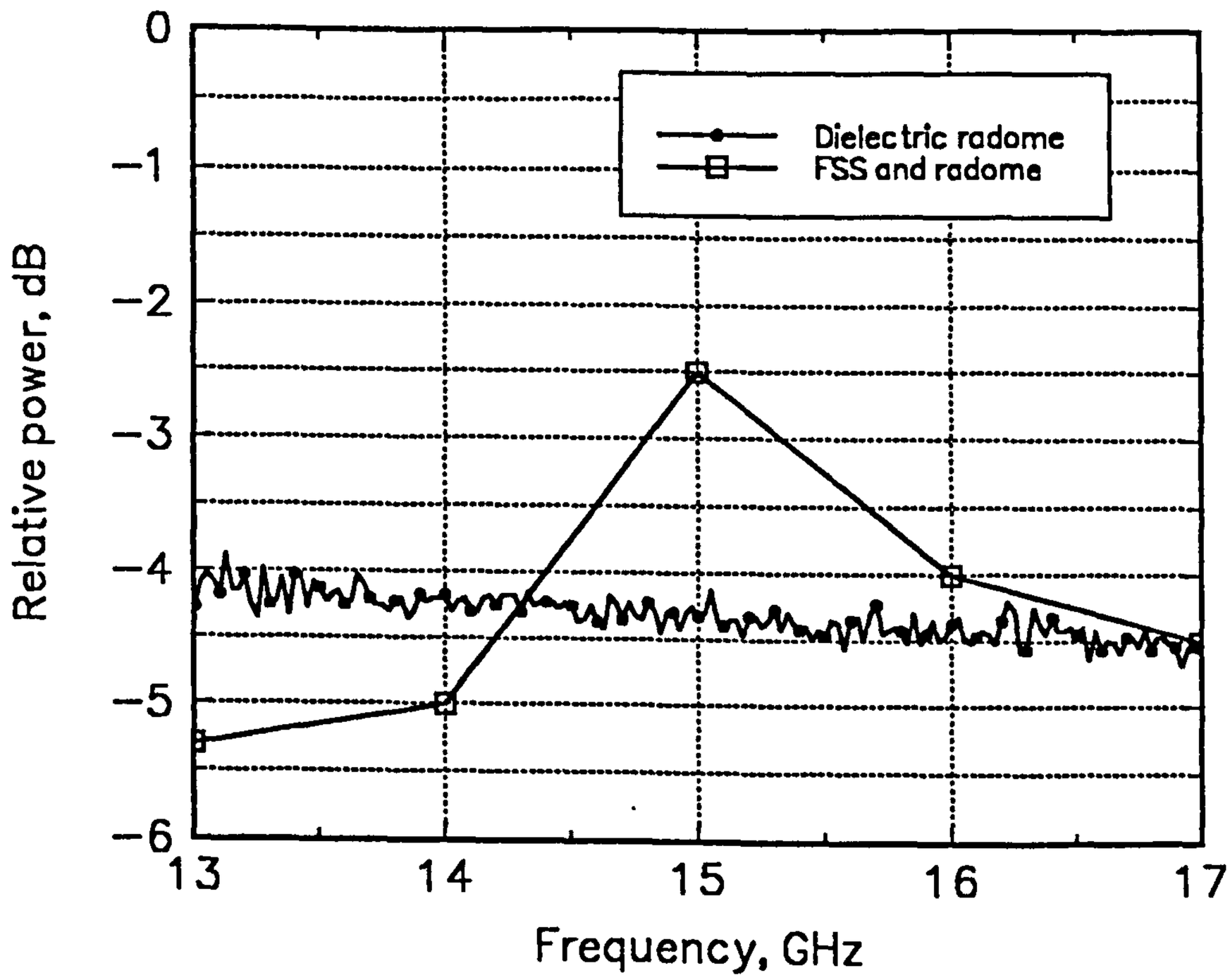

Fig.3.12 Transmission response of radomes.

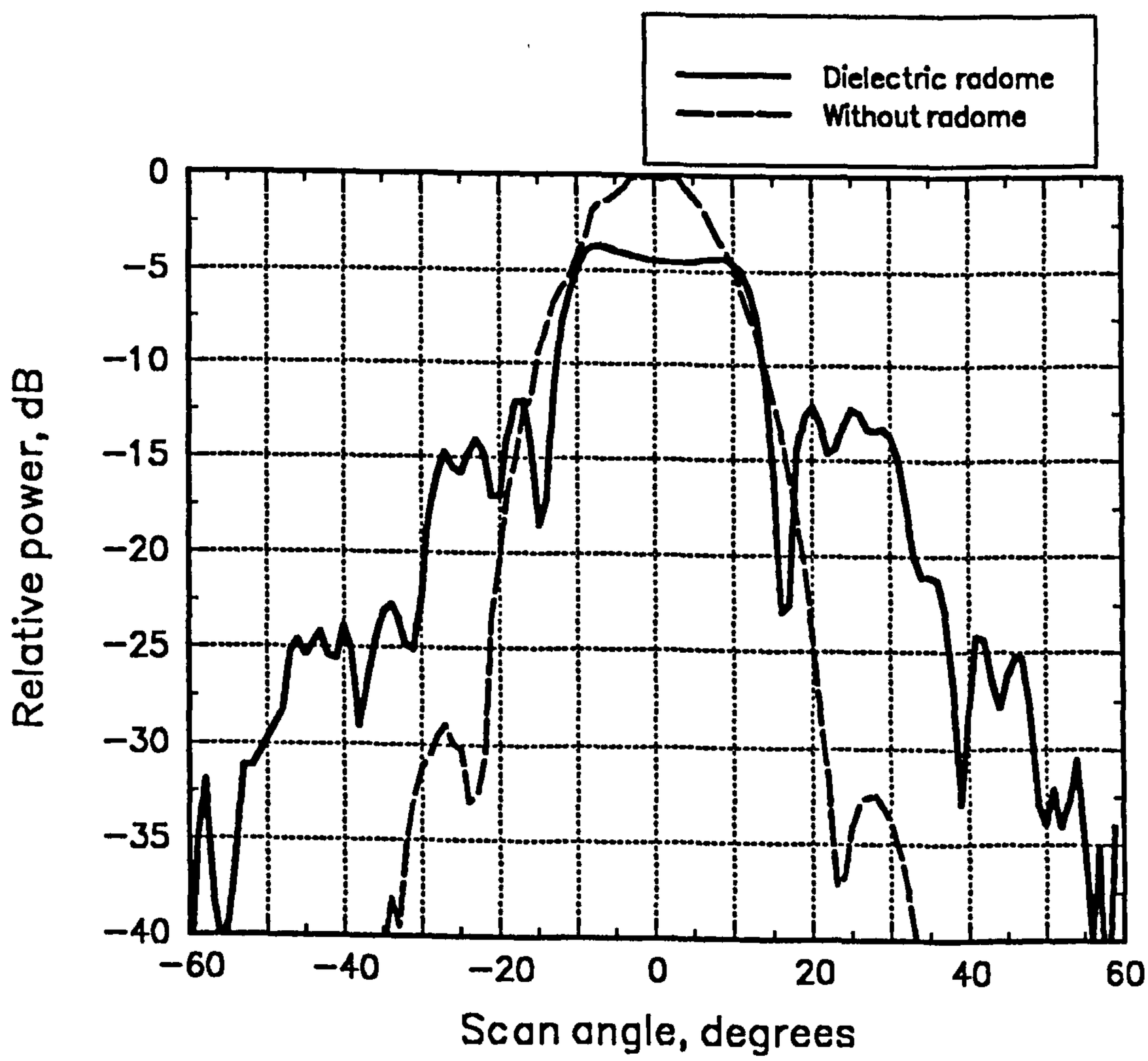

Fig.3.13 H −plane copolar pattern at 15 GHz.

The basis functions defined over the circumference are:

$$h_{n_c} = \sqrt{N_a} \cos n_c \alpha \quad n_c = 1 \text{ and } 2 \tag{3.87}$$

$$h_{n_s} = \sqrt{N_a} \sin n_s \alpha \quad n_s = 1 \text{ and } 2 \tag{3.88}$$

and N_a is a constant normalising factor given by,

$$N_a = \frac{2}{\pi W(W + 2R_{in})} = \frac{2}{A'} \text{ (} A' \text{ is the aperture area of the ring),} \tag{3.89}$$

following the mode recipe given in [8].

R_{in} is the inner radius of the ring.

121 Floquet modes was sufficient to expand the tangential fields [8]. The above current and Floquet modes are used in the predictions for the subsequent conical FSS described in the following section. It should be noted that the lattice and element geometry will inevitably deform once the planar FSS is wrapped around the cone. This deformations have not been taken into account in the TIA computer model.

3.5.2 Results from the Dielectric cone

Dielectric radomes have been readily employed in aircraft applications, especially in the the nose (the front of the aircraft) to protect the antenna. For a single layer dielectric, either a thin or multiple half-wavelength thick is often required. The half-wavelength criteria is to avoid reflections and so minimise the attenuation of the electromagnetic energy through the dielectric material. Here, the dielectric radome is only 1.0 mm thick which is not a half-wavelength in the operating frequency band (from 12 to 18 GHz), so a mismatch with free space can occur. Therefore, transmission loss can be expected in this frequency band for the conical dielectric radome (without the FSS) as shown in Fig.3.12. At 15 GHz, the transmission boresight loss of the dielectric cone without the FSS layer fitted is about -4.4 dB. With the inclusion of the slotted array, a well defined narrow passband is formed, centre at 15 GHz, with a loss about -2.5dB. Thus, it is apparent that the FSS layer is acting as a matching layer with the inductive properties of its slots. The residual losses of -2.5 dB with the FSS fitted arise principally from the mismatch with free space. The loss could potentially be improved if a half wavelength thickness is used. Further study is required to investigate the effect of the thickness on the FSS in a conical structure. For a planar FSS case, Callaghan et al [9] have already discussed the tuning of the FSS using various thickness of dielectric. However, the objective of the present study is mainly to investigate and model the effects of curved FSS in the near field region of an antenna. The presence of

the dielectric radome also distorts the feed pattern as shown in Fig.3.13. The main lobe of the copolar feed pattern in the H-plane appears to be 'chopped off' with high side lobe levels rising rapidly at $\pm 20^{o}$ to $\pm 30^{o}$ scan. This could be due to the high incident angles encountered by the rays on the inner surface, which in turn would cause internal reflections inside the cone. The next few Sections will discuss the predictions of the three feed models using the TIA approximation for the conical FSS and dielectric radome and will compare them with the measurements.

3.5.3 Results using the FN feed model

Fig.3.14 shows measured and predicted boresight loss of the FSS cone from the FN feed model over the frequency range 13-17 GHz. There is a clearly defined passband in both the measured and predicted plots. The FN model predicts a band centre 0.5 GHz lower than measured. Discrepancy is encountered in the loss with 0.37 dB at 14.5 GHz compared to measured value of -2.5 dB at 15 GHz. The predicted radiation patterns give good agreements with the measured patterns in the H-plane up to angles of $\pm 20^{o}$. Results for the normalised copolar patterns at 14, 15 and 16 GHz are shown in Fig.3.15 to 3.17. When the frequency moves away from the band centre at 15 GHz i.e.14 and 16 GHz, the measured plots show a rapid rise in side lobe levels at larger scan angles beyond $\pm 20^{o}$. The rapid oscillation of the side lobe levels in this region is thought to be due to constructive and destructive interference between the transmitted and reflected fields at the inner cone wall. There is poorer agreement in the E plane copolar pattern as shown in Fig.3.18 at 15 GHz. However, the prediction is quite reasonable in the 40° plane as shown in Fig.3.19.

As expected, the crosspolar performance induced by the conical FSS is expected to be poor because of the steep angle of the cone. Levels up to -15 dB have been recorded. The high crosspolarisation is partly due to the wide ranging incident angles and field vector orientation local to the surface. The latter stems from the lattice formation on the curved surface. The FN feed model reproduces the crosspolar pattern quite well (Fig.3.20).

3.5.4 Results using the SPS feed model

The SPS is a superposition of radiated fields from point sources in the feed aperture, as described in Sec.3.3.2. Since the modal analysis routine requires plane wave incidences, the far fields of each point source have been used. Each point is located in a patch of each polar sector. It was found that a minimum of 5 radial and 17 azimuthal divisions are required, giving a total of 85 point sources to fit the desired measured pattern. This implies that for each FSS element the modal routine is called 85 times to

compute its current sources for each incidence. This has profound implications on the storage of computer memory for the Floquet modal expansions and runtime. Therefore, only the dominant Floquet mode i.e. $p=q=0$ was used. The predicted far field feed pattern is compared with the measured one as shown in Fig.3.21.

The results for the boresight loss of the FSS cone are shown in Fig.3.22. There is a well defined predicted passband, resonating at 15 GHz as measured. The maximum loss, however, is -0.633 dB compared to the measured value at -2.5 dB. There is general agreement in predicted radiation patterns in the H-plane up to $\pm 20^{o}$. Some normalised patterns are shown in Fig.3.23 to Fig. 3.25 for frequencies near the band centre. Poorer agreement is encountered in the E-plane copolar patterns as shown in Fig.3.26. The copolar pattern at 15 GHz is predicted quite well at the 40° plane (Fig.3.27). And there is also general agreement in the crosspolar pattern except for higher peaks at $\pm 10^{o}$ scan angle at Fig.3.28.

3.5.5 Results using the PB feed model

The PB feed model is a parallel beam emanating from the feed aperture. This is compensated by the phase difference in the ray path from the aperture to the FSS surface. Although there are 3794 slotted rings on the cone, only 882 are illuminated by the PB feed model. This is because the feed aperture diameter is only 96 mm and is located at 554 mm away from the tip of the cone with a base diameter of 220 mm. In order to calculate the boresight loss of the FSS, the predicted radiated field of the FSS using the PB feed model is normalised with respect to the SPS predictions of the feed alone. The results is shown in Fig.3.29. A well defined passband is predicted with a resonant frequency at 14.5 GHz a shift of 0.5 GHz from the measured value at 15 GHz. Discrepancy in the loss is encountered with a maximum predicted value of +0.48 dB compared to -2.5 dB measured. Generally, there is agreement with the measured normalised copolar patterns only up to $\pm 10^{o}$ scan in the H-plane (Fig.3.30 to Fig.3.32). Poor agreements were encountered in the E- plane and 40° plane as shown in Fig.3.33 and Fig.3.34 at 15 GHz. The crosspolar patterns at 40° plane is not reproduced very well (Fig.3.35). However, the predicted peak crosspolar levels agree well with those measured.

3.6 Conclusions

An analysis based on a tangential infinite array approximation has been presented for predicting the far field radiation pattern of a conical frequency selective surface illuminated by a corrugated feed horn. The location of the passband was predicted fairly well by all three feeding models used, with some discrepancies in their boresight

losses. The SPS feed model could locate the measured resonant frequency better than the other two feed models. Although there are differences in the transmission boresight loss, only the SPS feed model predicted a loss at the resonant frequency, as expected in an antenna and radome system. With regard to the radiation patterns, the agreement obtained between the predicted and measured values is fairly good for SPS and FN feeding models especially at the passband centre. Nevertheless, there are descrepancies in the main lobe of the E-plane copolar pattern. At wide scan angles however the computer model did not accurately predict the fine structure of the side lobes. These may be due to inaccuracies of currents in the slotted elements and/or multiple reflections due to the internal wall of the cone and mutual coupling between the feed and FSS. In the present model only the source fields on the exterior of wall of the cone is calculated. One possible way of improving this model is to include the source fields on the interior wall of the cone as well.

The SPS model called up the modal analysis routine some 85 times for each point on the cone compared to only once per point for the FN model. This has an effect on the computer memory requirements as well as the run time. The poorer performance of the PB model is due to the larger conical FSS surface relative to the size of the feed aperture. This is because here there are 3794 elements but only 882 near the tip of the cone are illuminated. As compared to the other feed models the parallel beam depends on the size of the feed aperture which restricts the number of element illuminated. Better results have been obtained by Simpkin [11] for a larger rectangular feed relative to the FSS. It will be shown later that the PB feed model can produce fairly accurate predicted patterns in the finite current (FC) model for a smaller cone. This is demonstrated in Chapter 4. and 5. where the accuracy of the scattering from a curved FSS structure is assessed more fully. This was done by considering a finite size surface whose currents are solved using an integral equation formulation which takes into account the coupling of all the FSS elements.

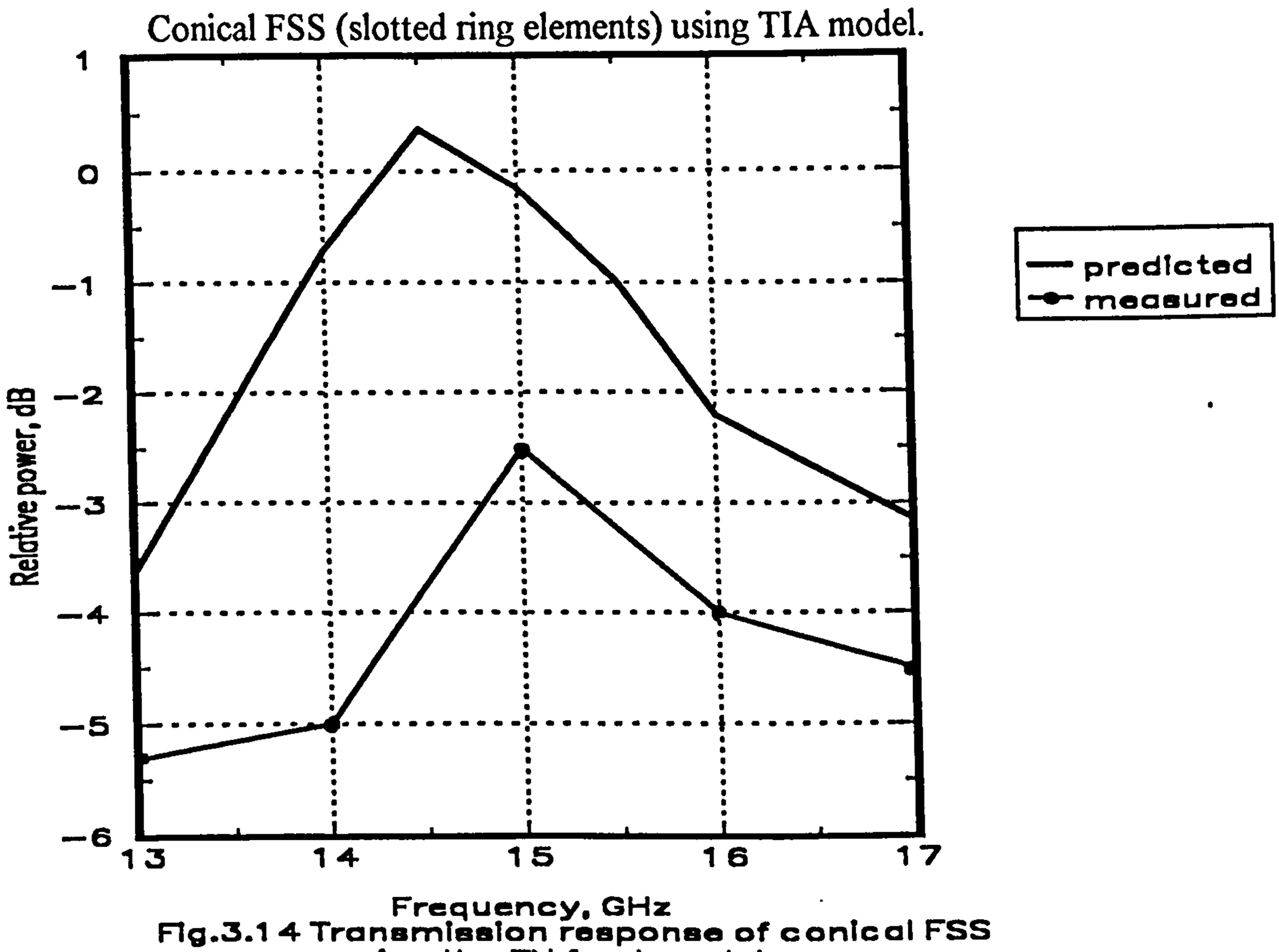

Fig.3.14 Transmission response of conical FSS using the FN feed model.

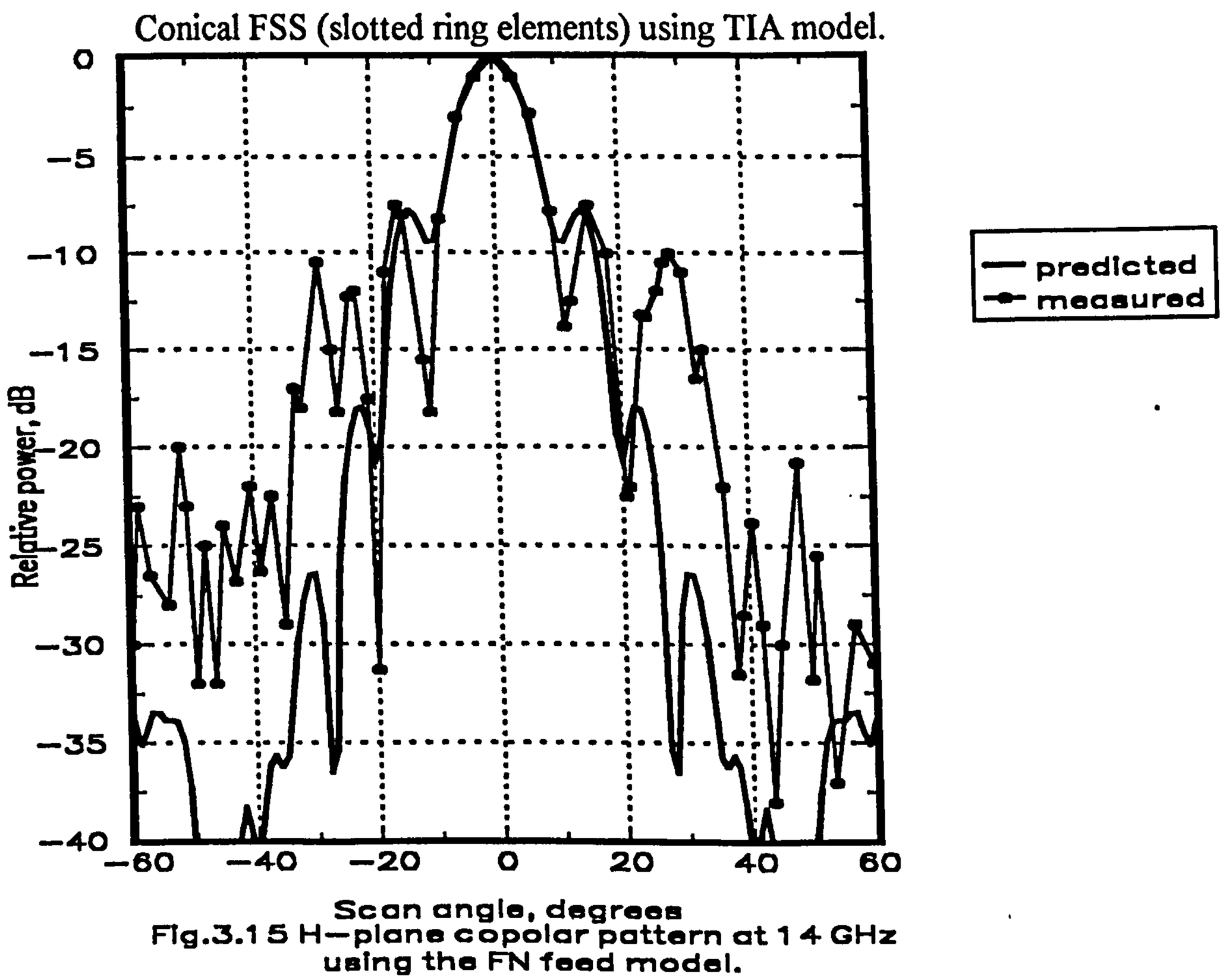

Fig.3.15 H—plane copolar pattern at 14 GHz using the FN feed model.

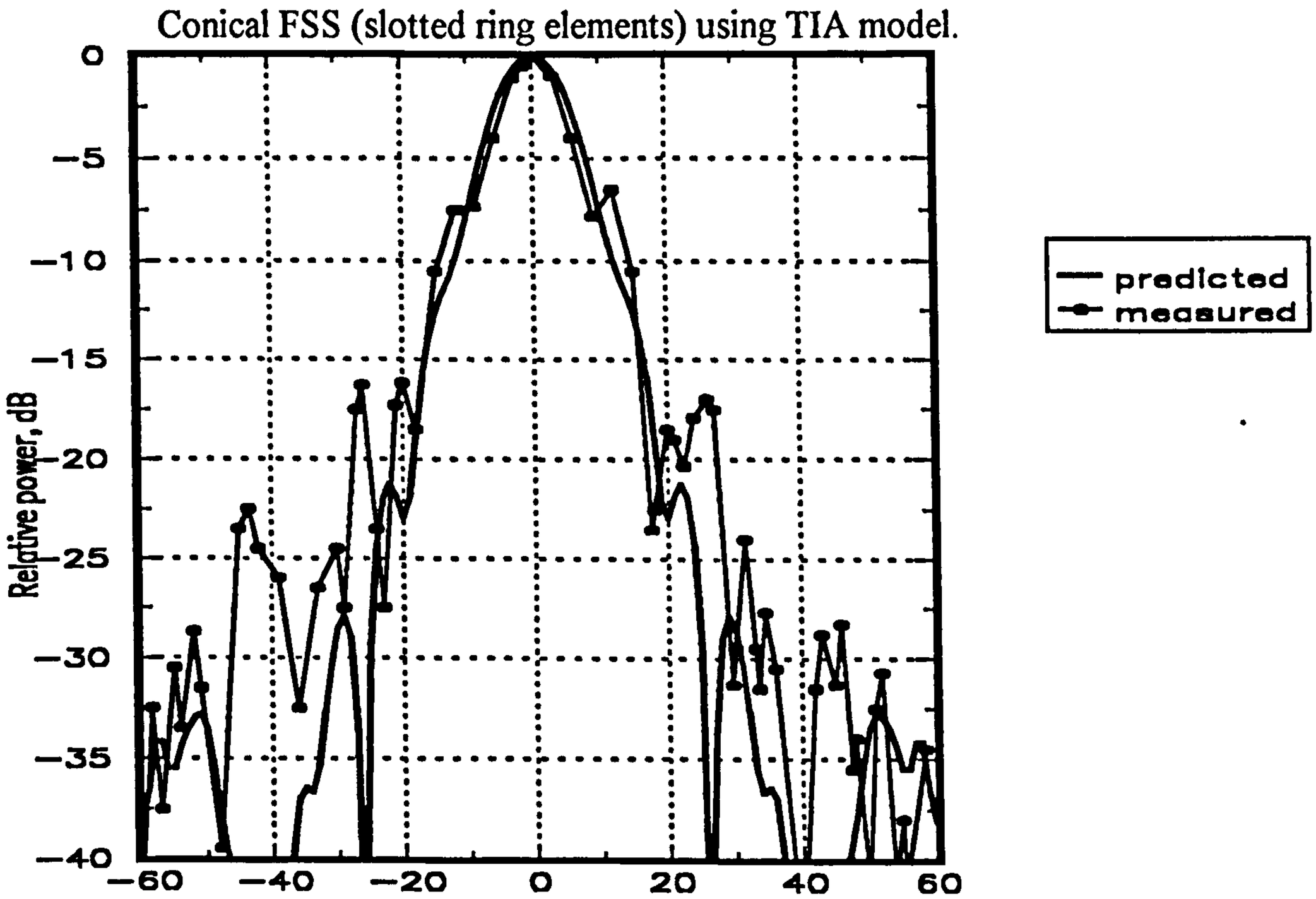

Fig.3.16 H−plane copolar pattern at 15 GHz using the FN feed model.

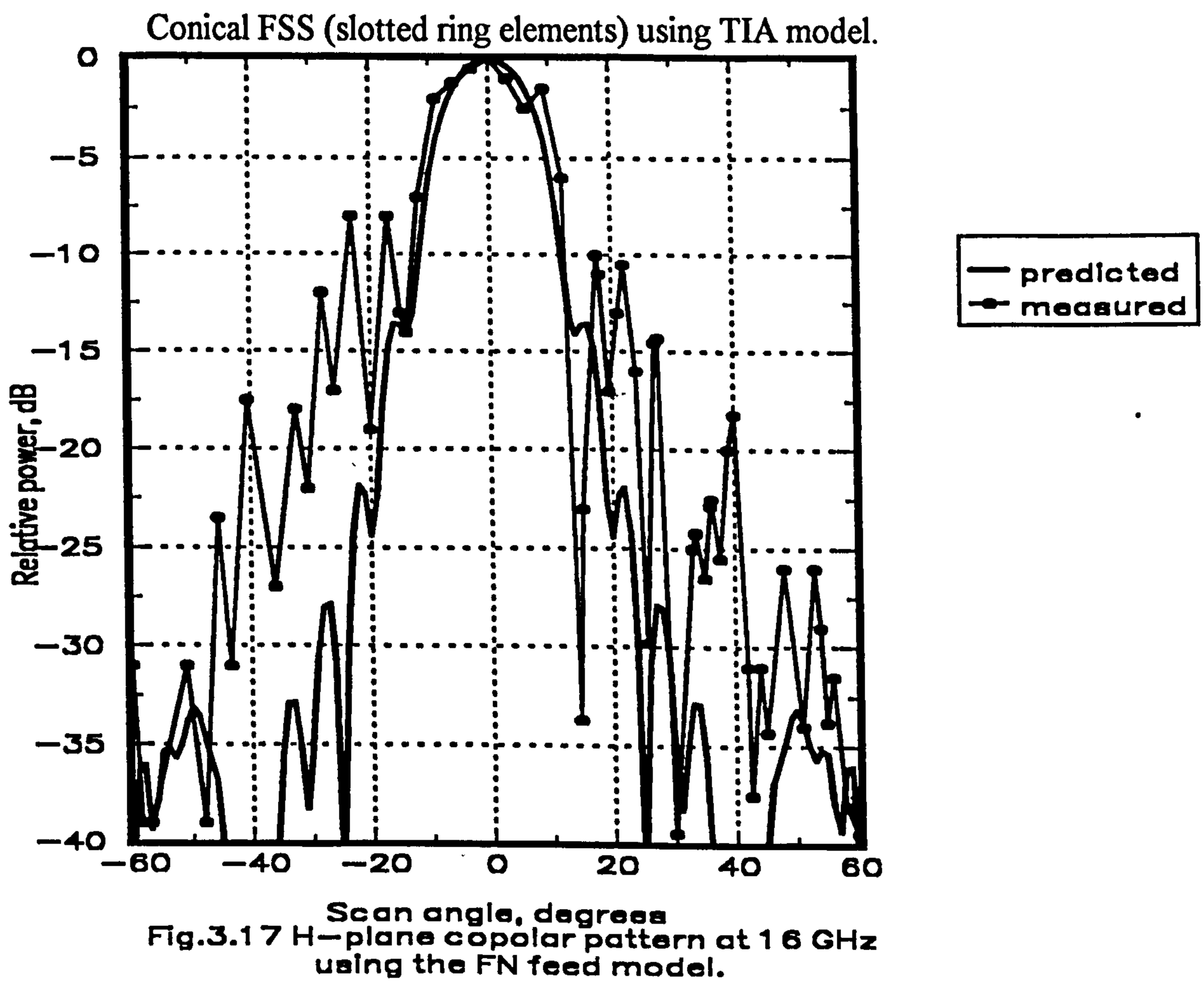

Fig.3.17 H−plane copolar pattern at 16 GHz using the FN feed model.

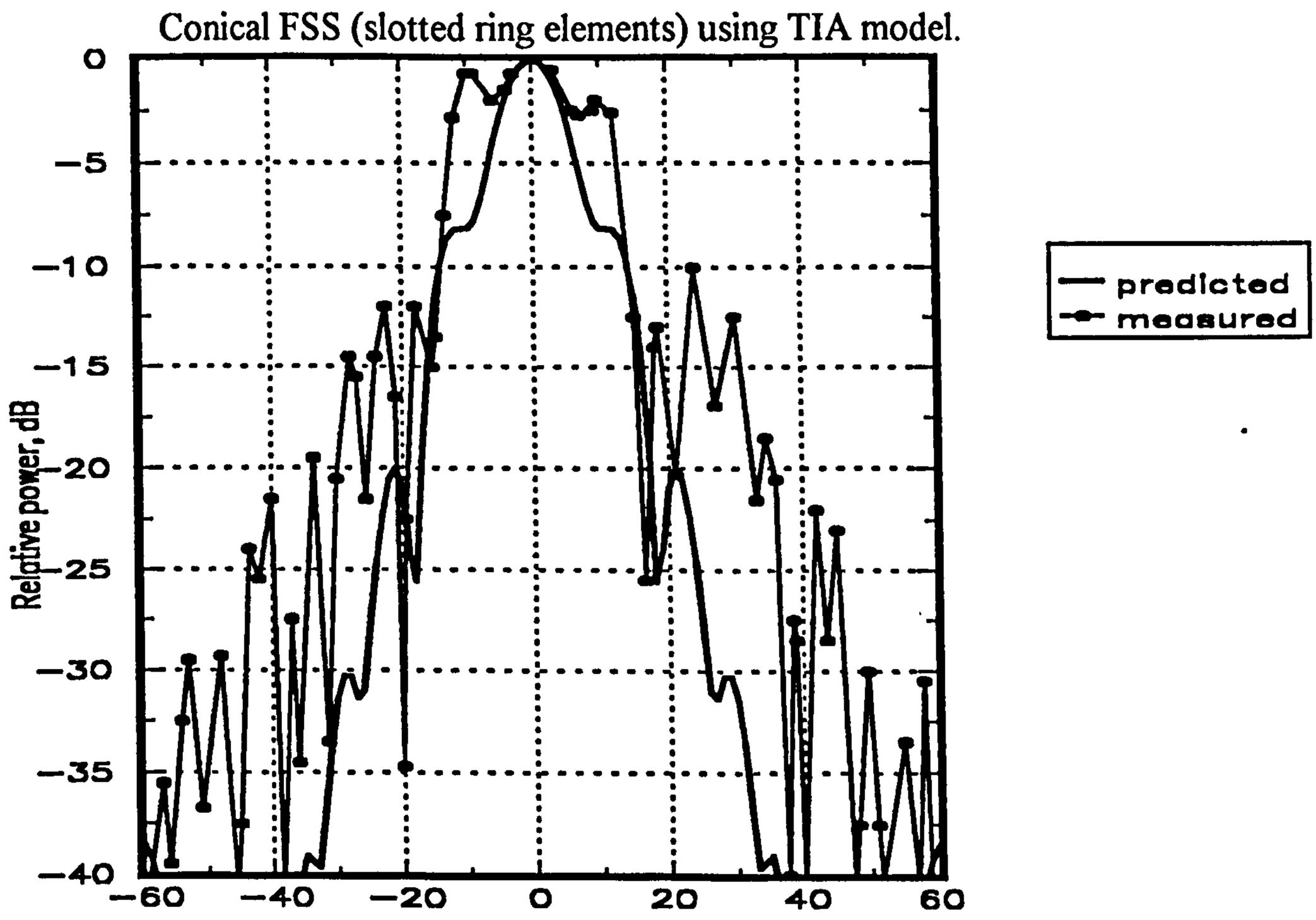

Fig.3.18 E—plane copolar pattern at 15 GHz using the FN feed model.

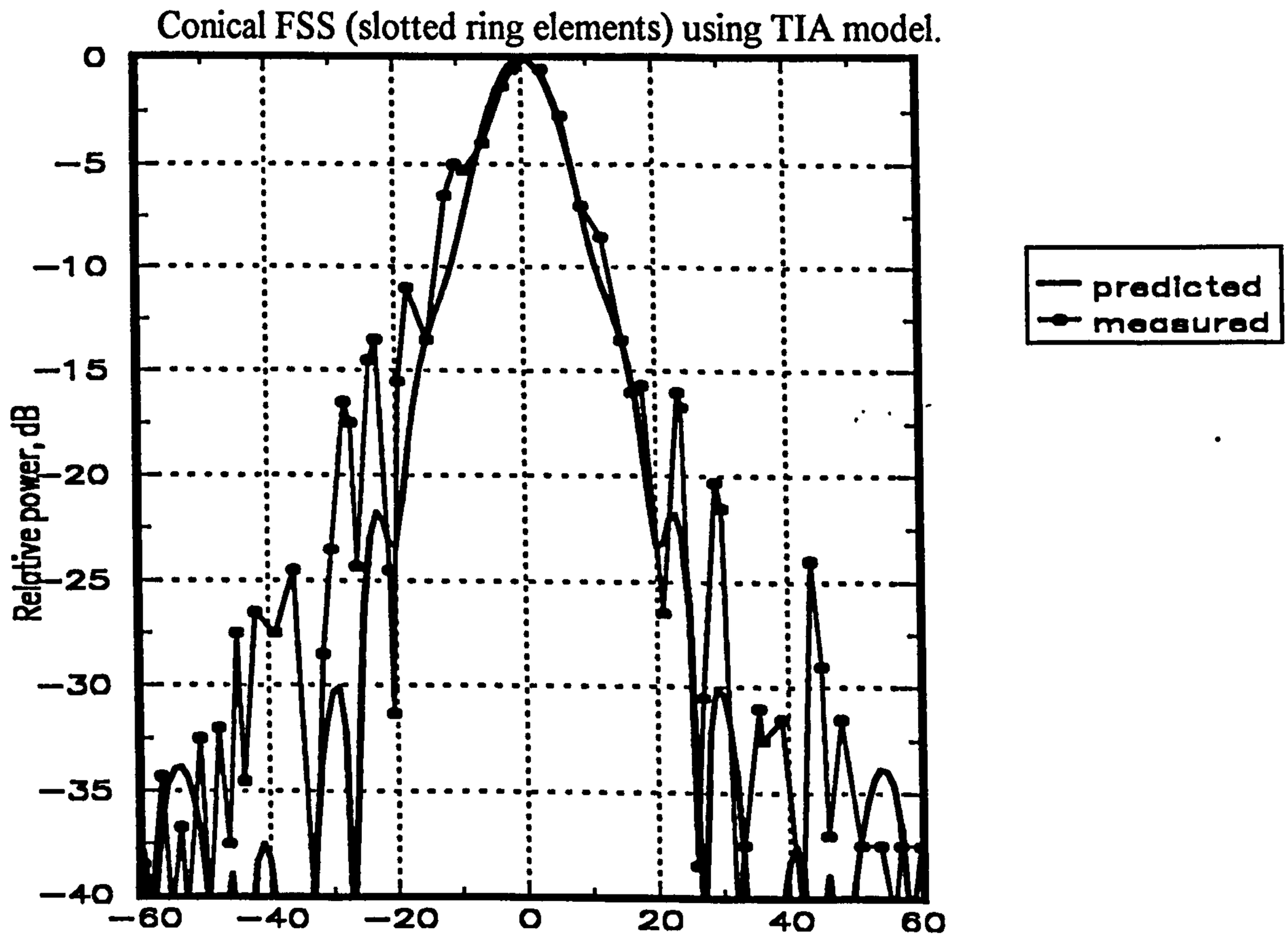

Fig.3.19 40 deg. plane copolar pattern at 15 GHz using the FN feed model.

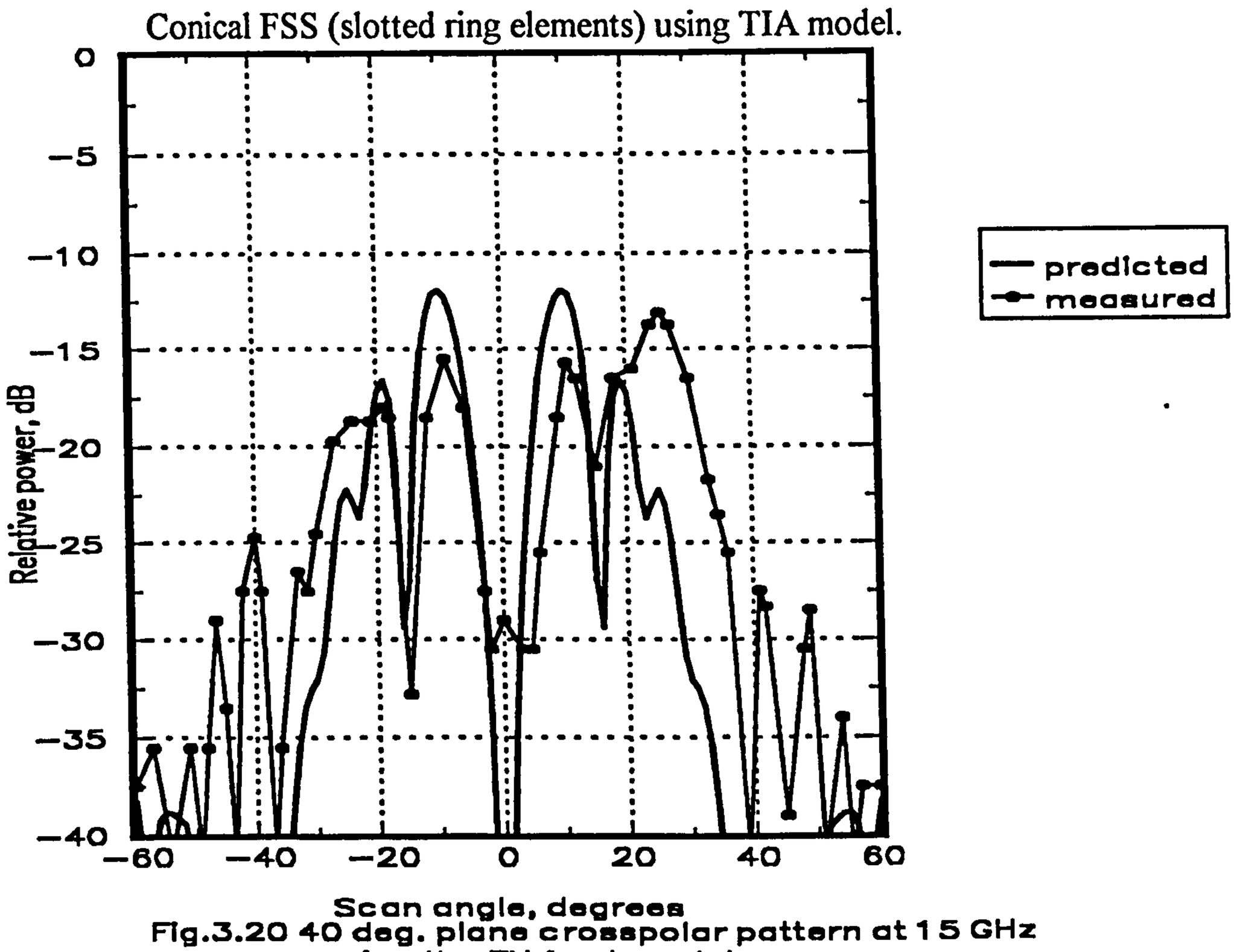

Fig.3.20 40 deg. plane crosspolar pattern at 1 5 GHz using the FN feed model.

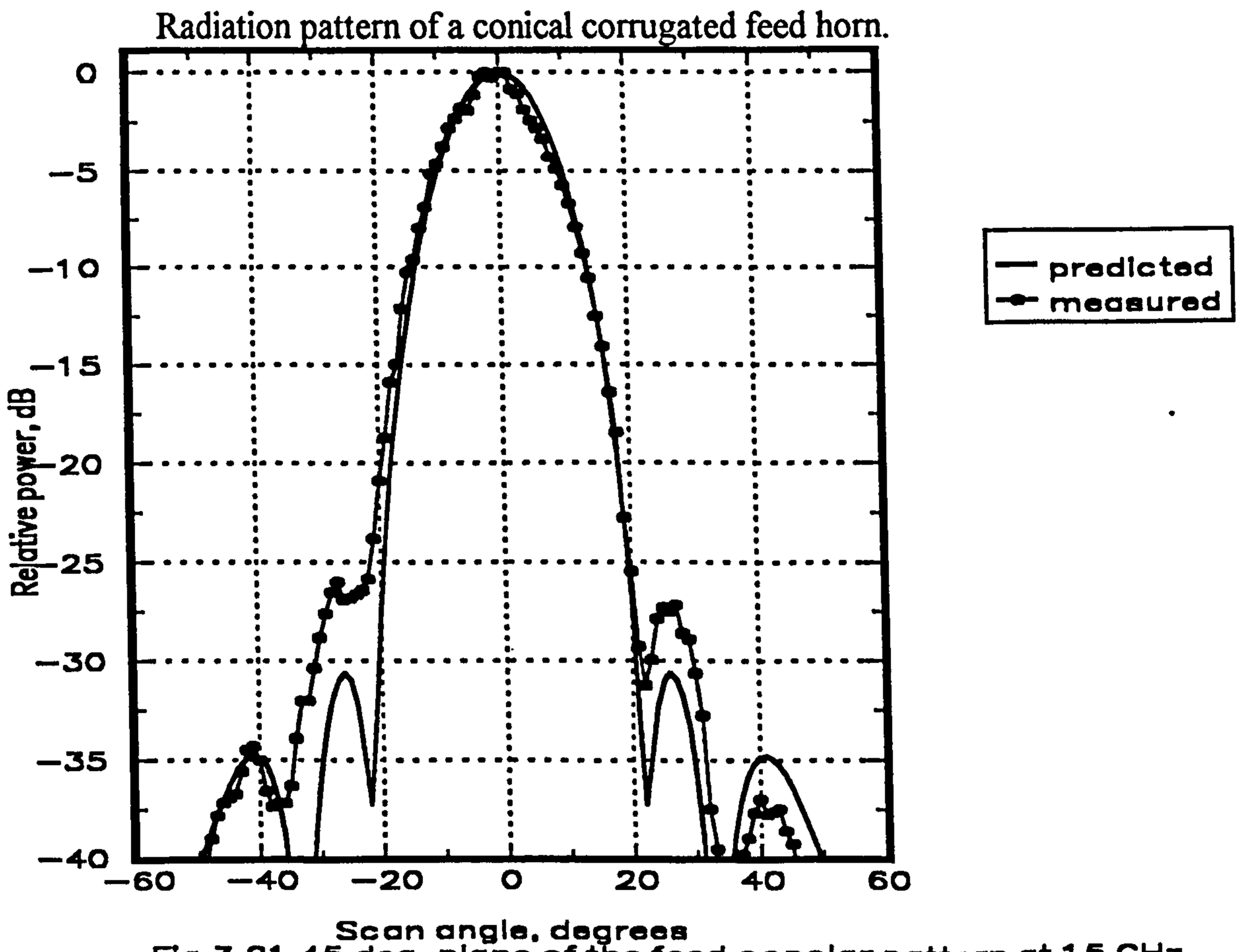

Fig.3.21 45 deg. plane of the feed copolar pattern at 1 5 GHz using the SPS feed model.

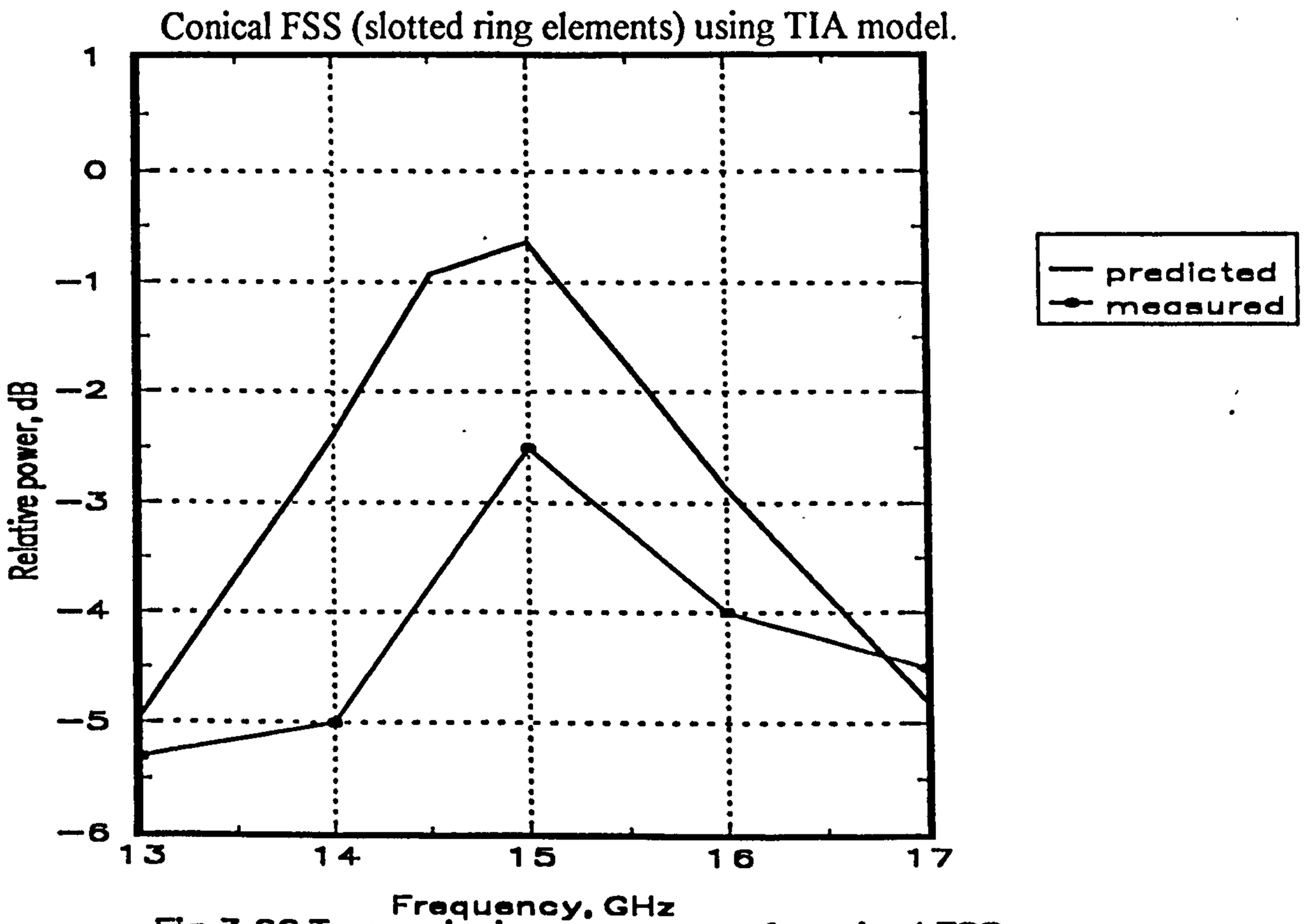

Fig.3.22 Transmission response of conical FSS using the SPS feed model.

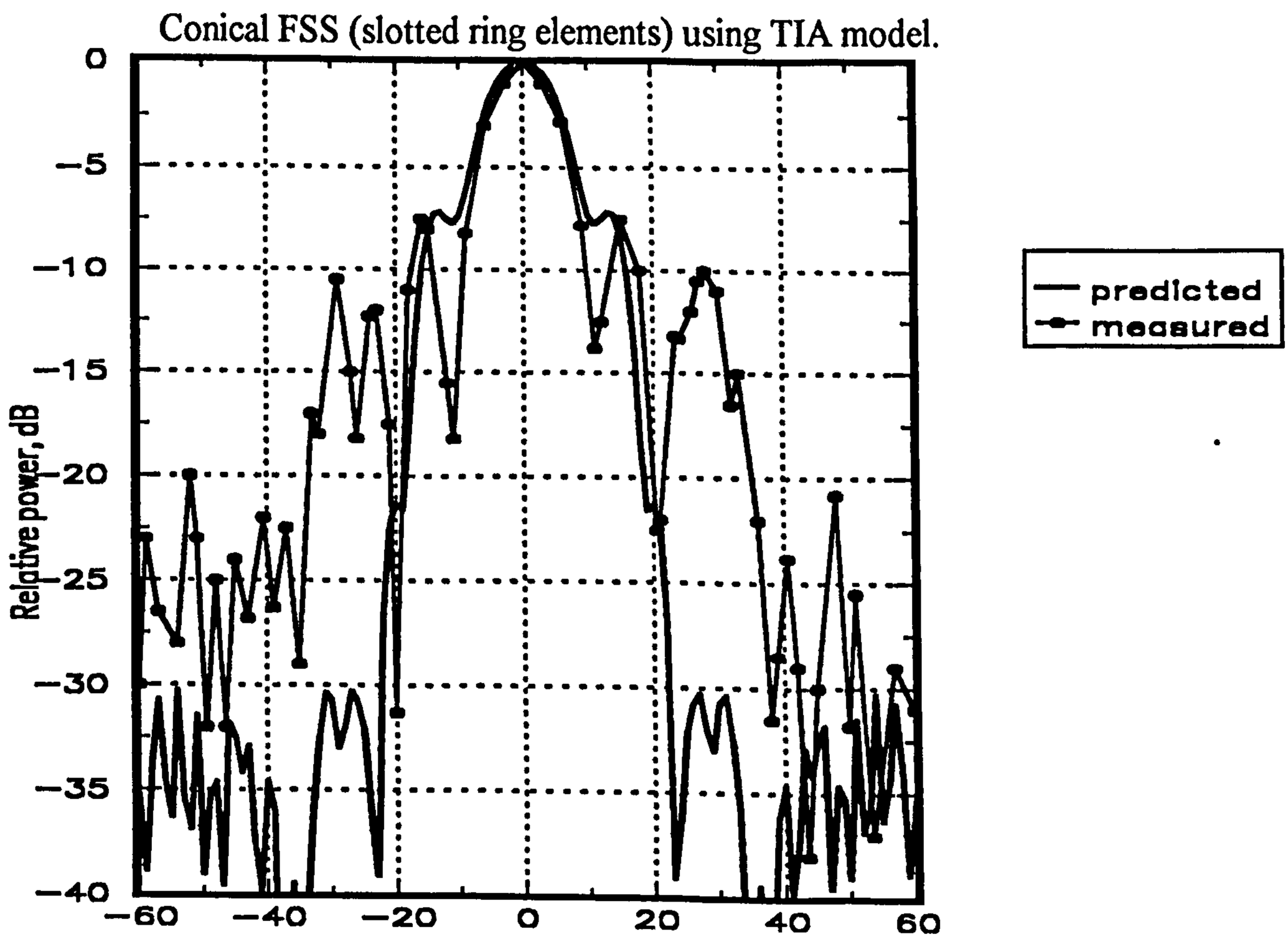

Fig.3.23 H—plane copolar pattern at 1 4 GHz using the SPS feed model.

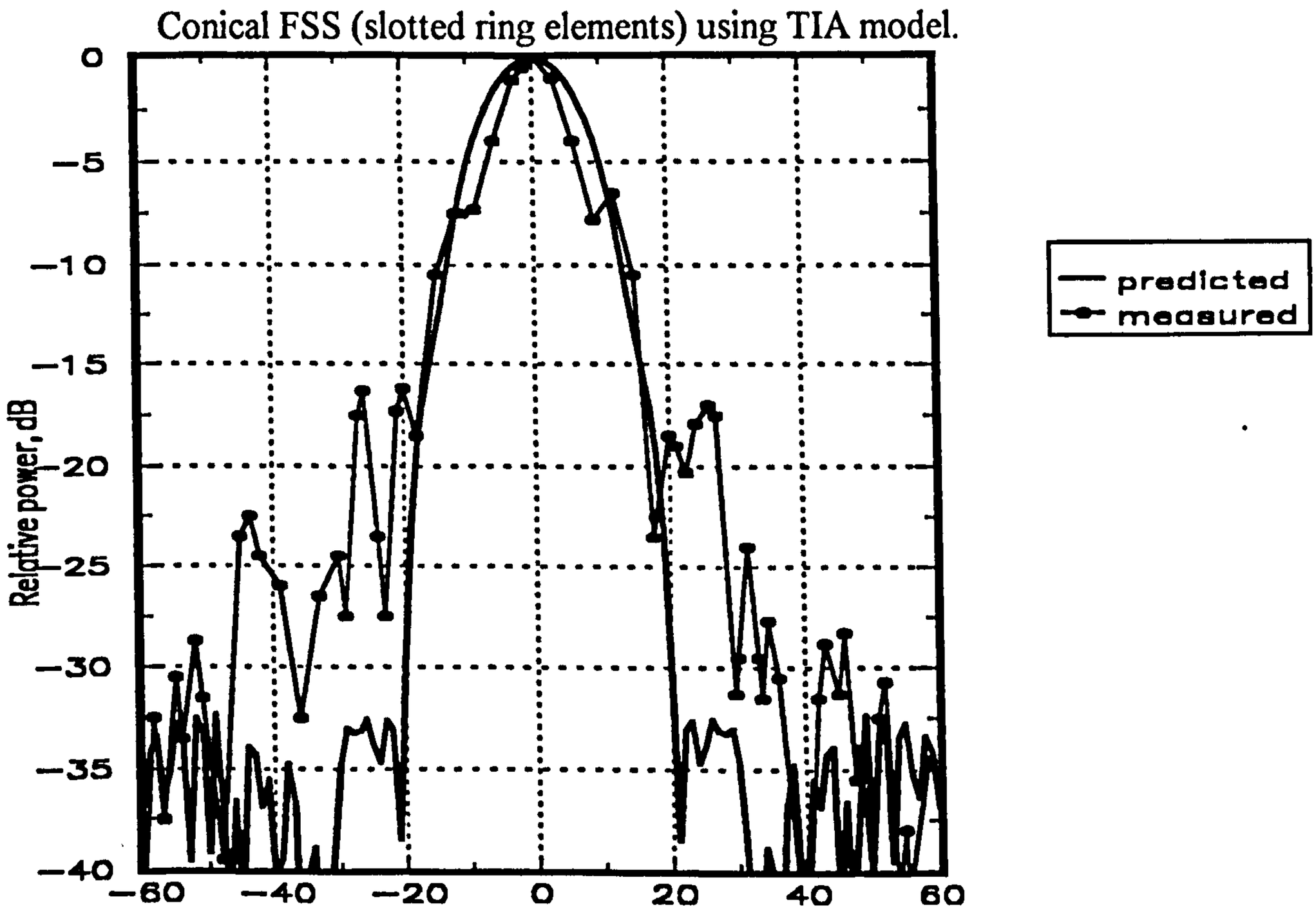

Fig.3.24 H—plane copolar pattern at 1 5 GHz using the SPS feed model.

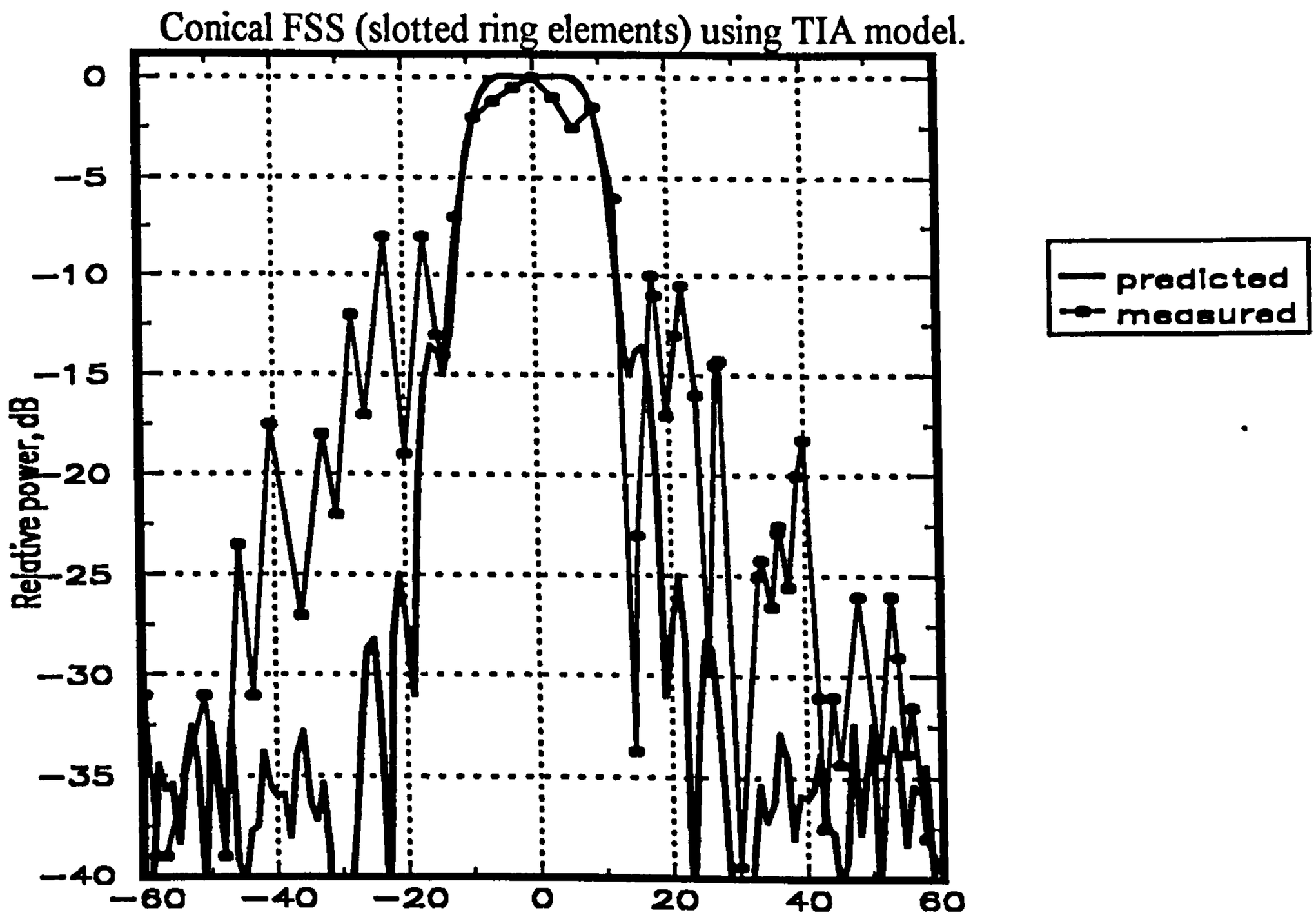

Fig.3.25 H—plane copolar pattern at 1 6 GHz using the SPS feed model.

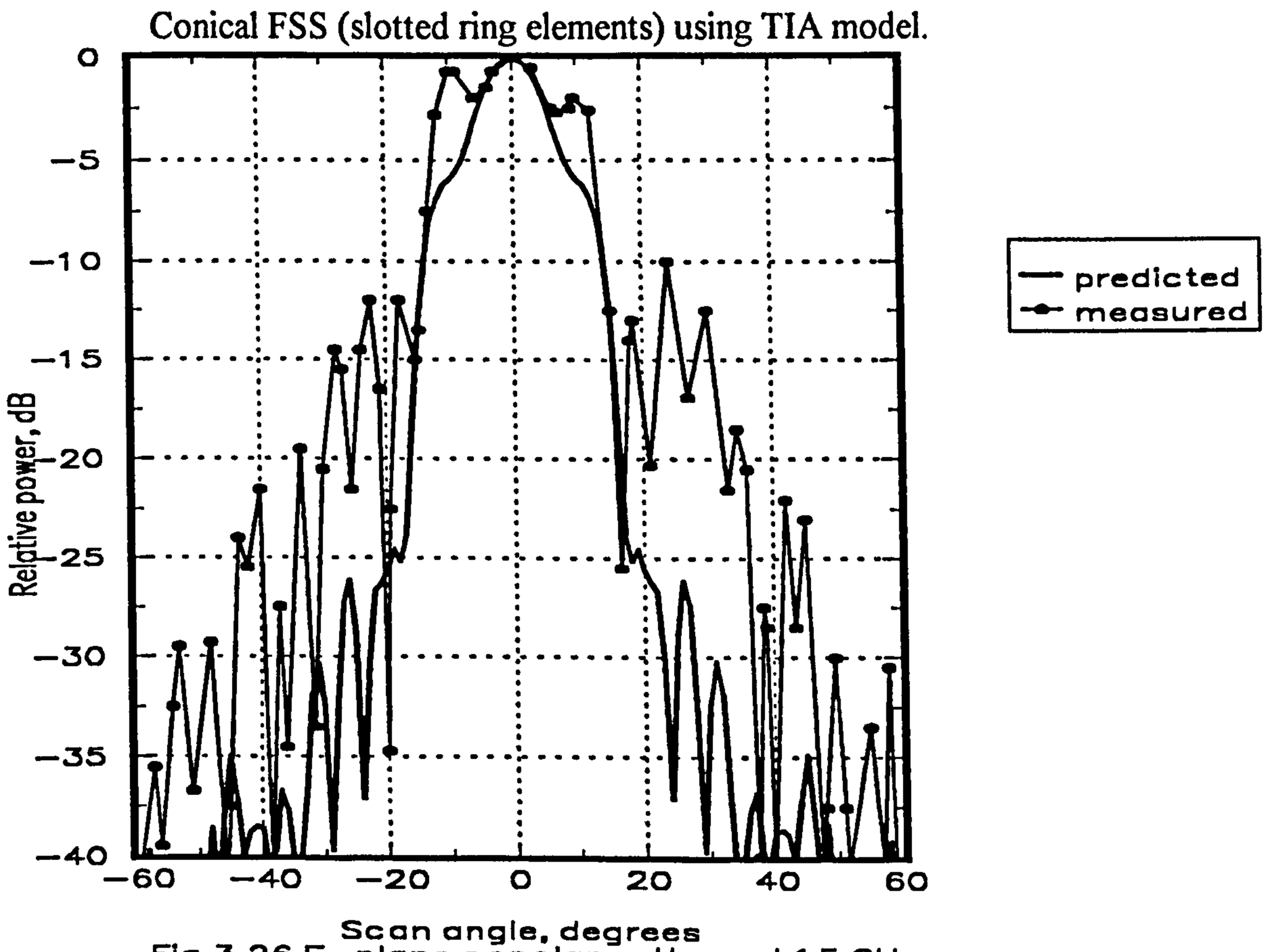

Fig.3.26 E—plane copolar pattern at 1 5 GHz using the SPS feed model.

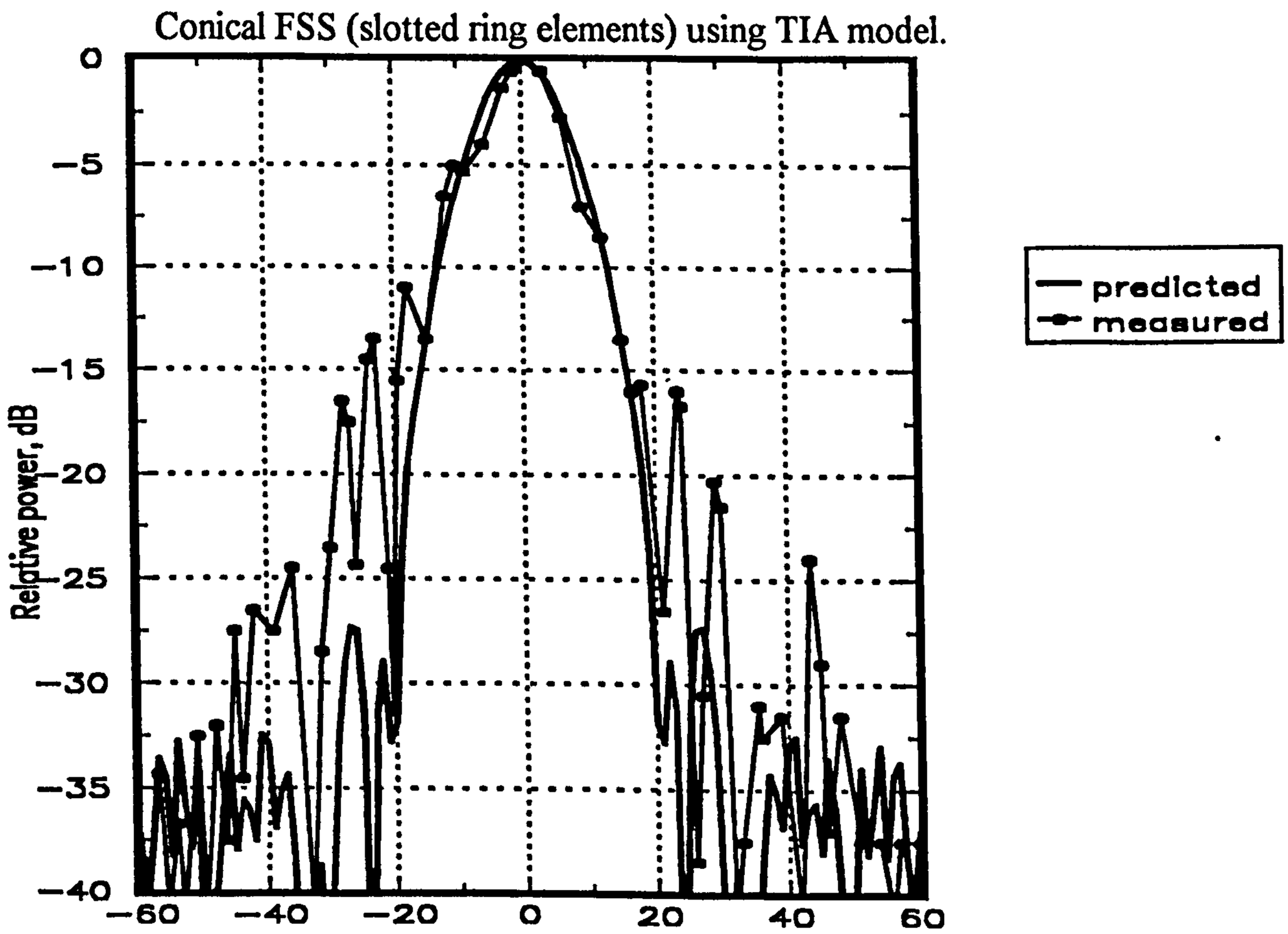

Fig.3.27 40 deg. plane copolar pattern at 1 5 GHz using the SPS feed model.

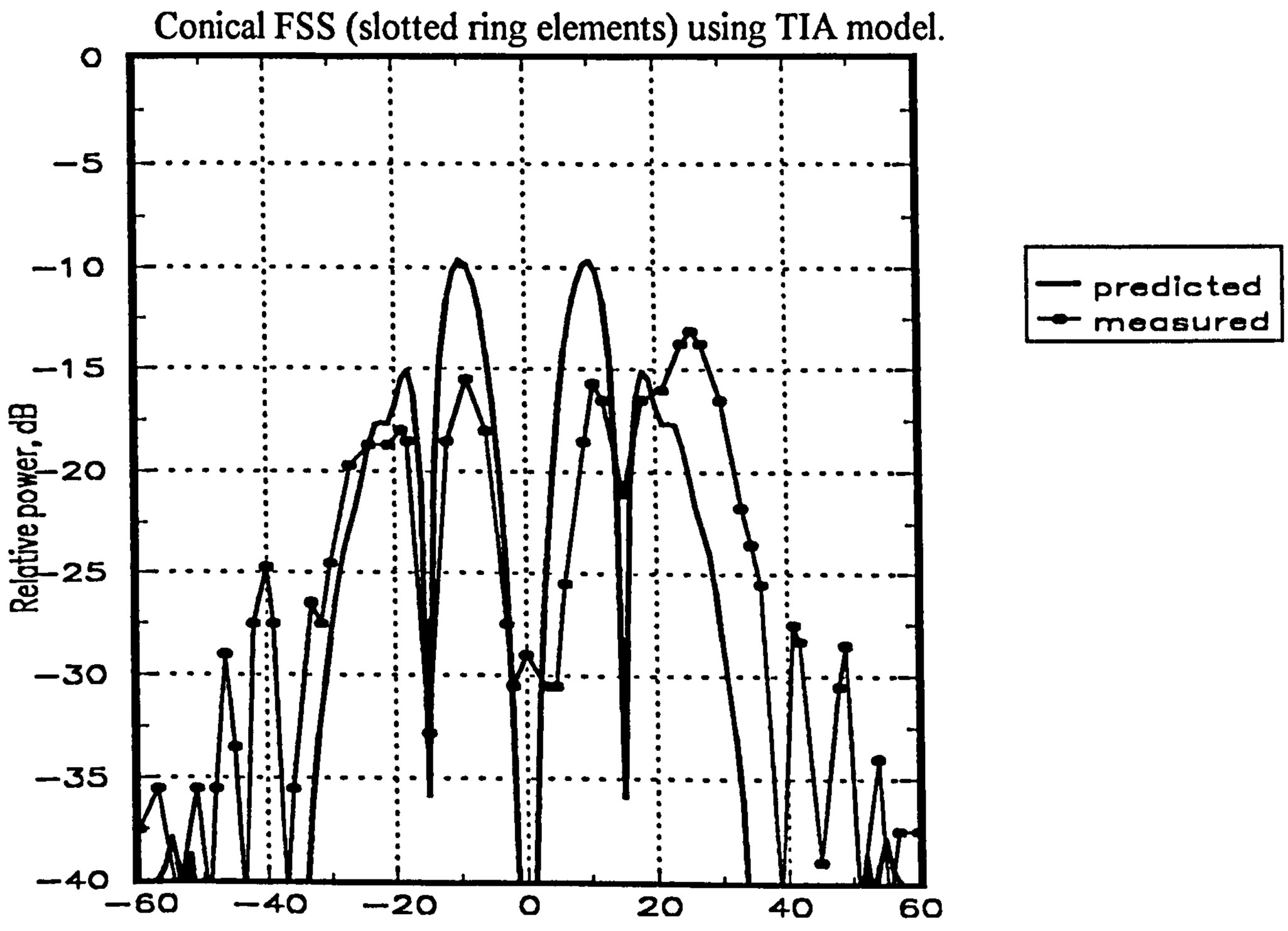

Fig.3.28 40 deg. plane crosspolar pattern at 1.5 GHz using the SPS feed model.

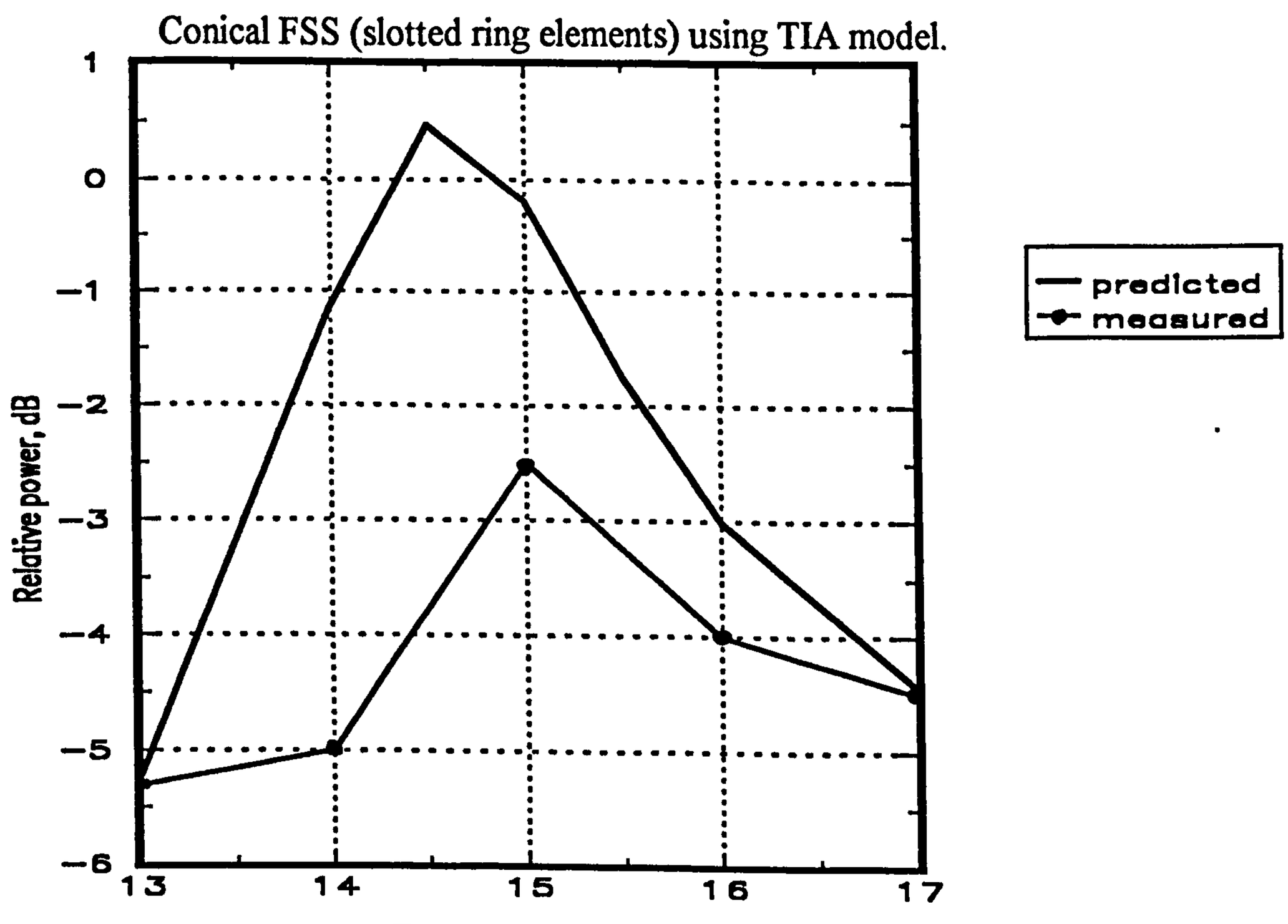

Fig.3.29 Transmission response of conical FSS using the PB feed model.

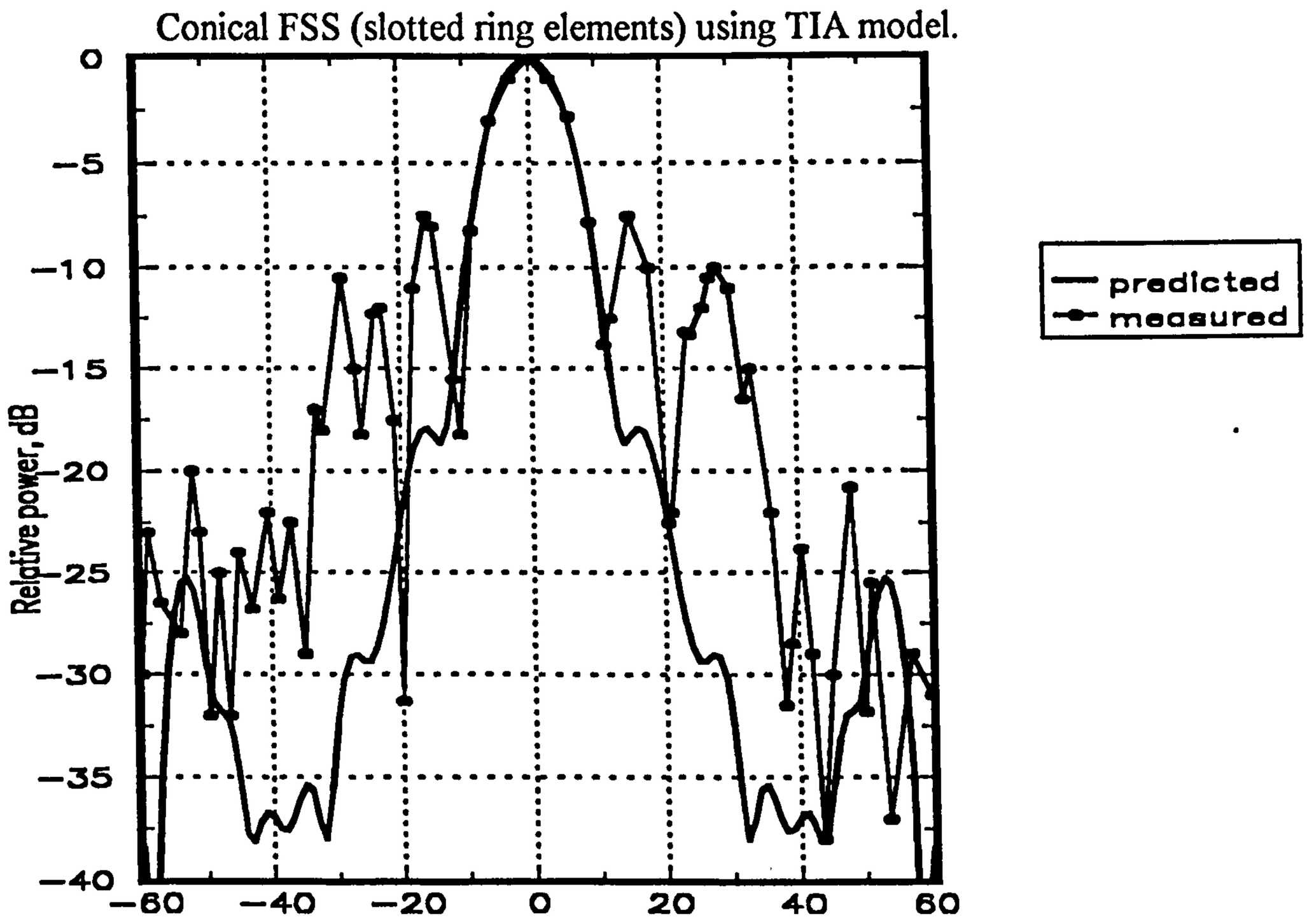

Fig.3.30 H—plane copolar pattern at 1 4 GHz using the PB feed model.

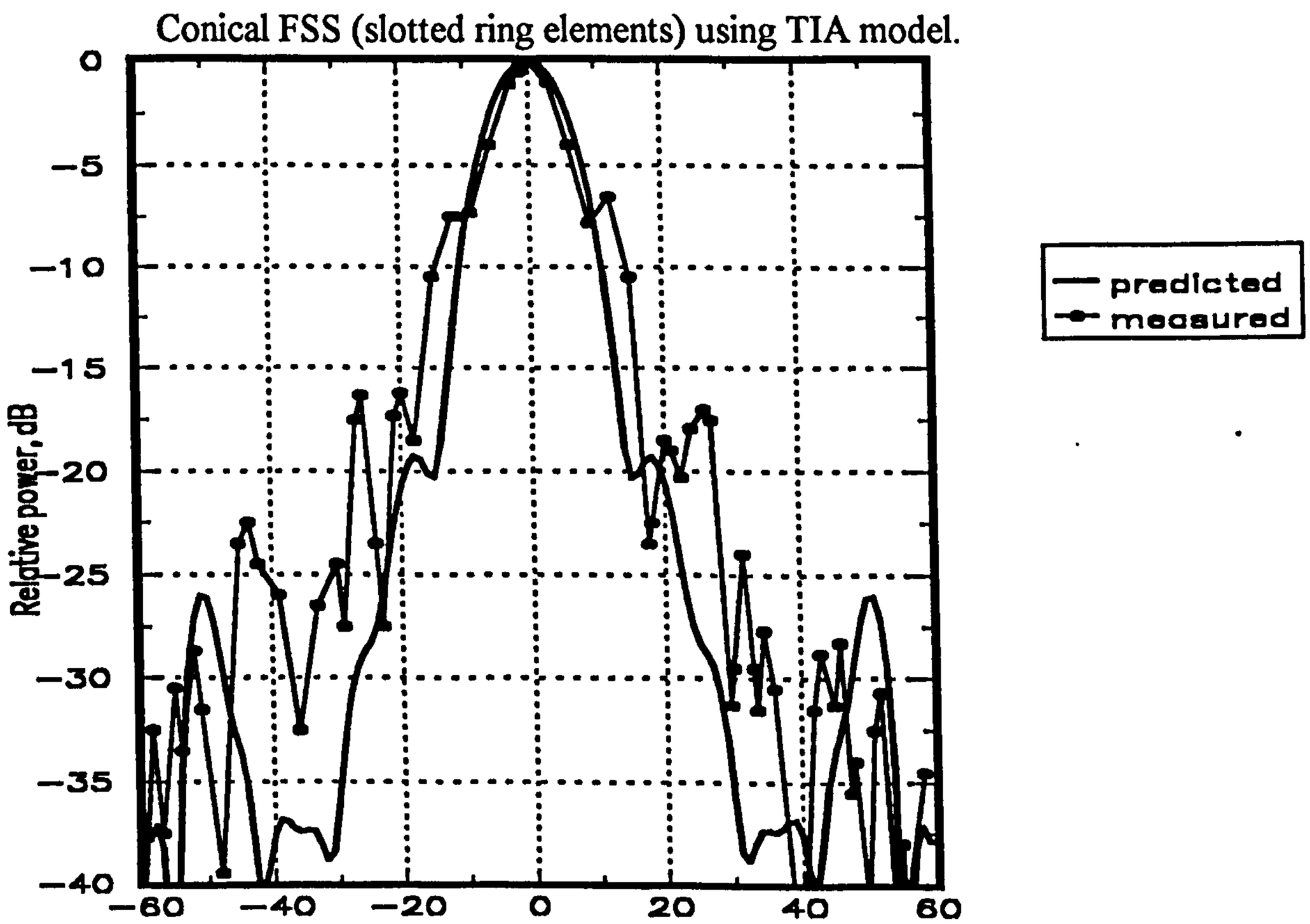

Fig.3.31 H—plane copolar pattern at 1 5 GHz using the PB feed model.

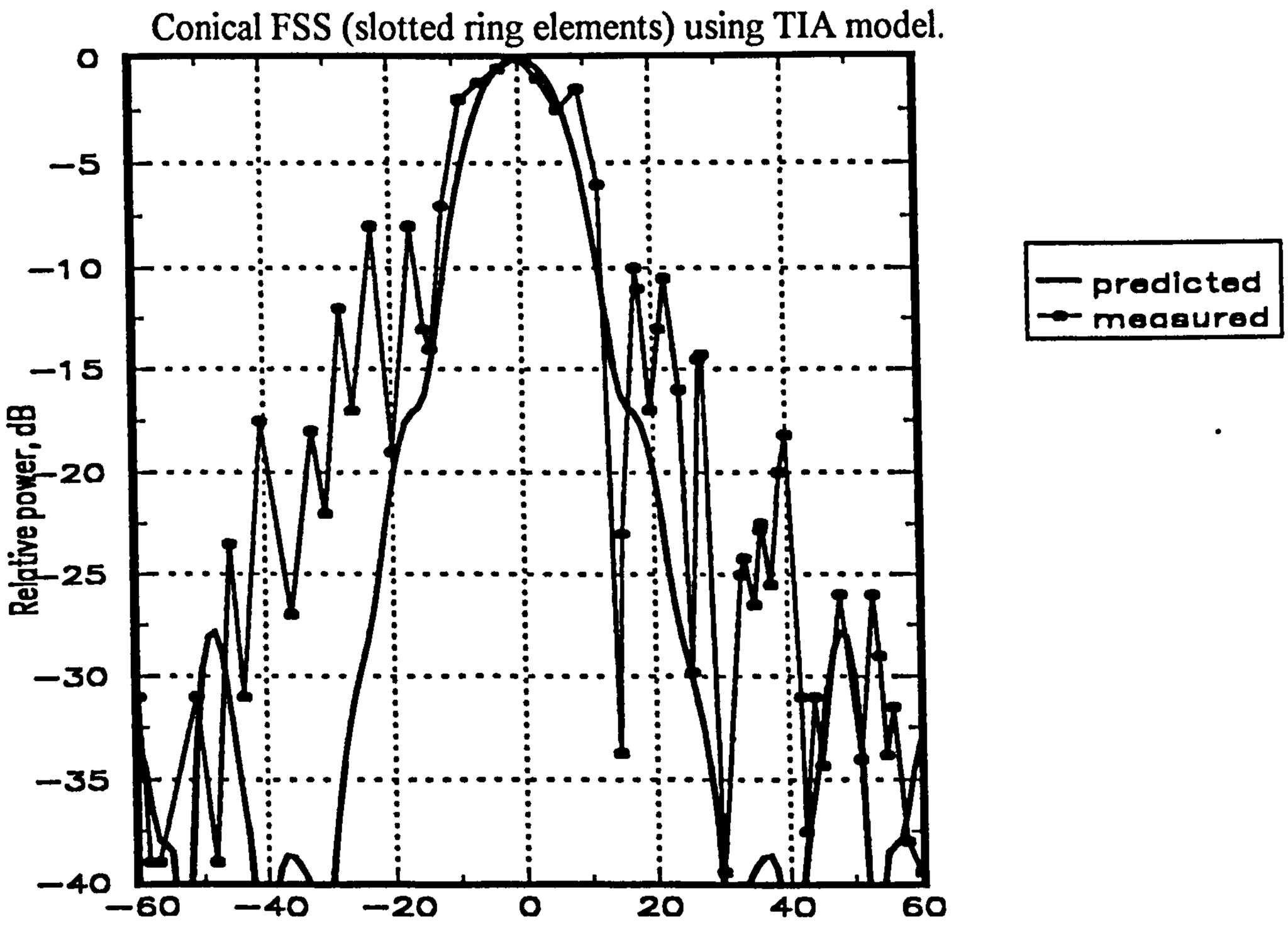

Fig.3.32 H—plane copolar pattern at 1 6 GHz using the PB feed model.

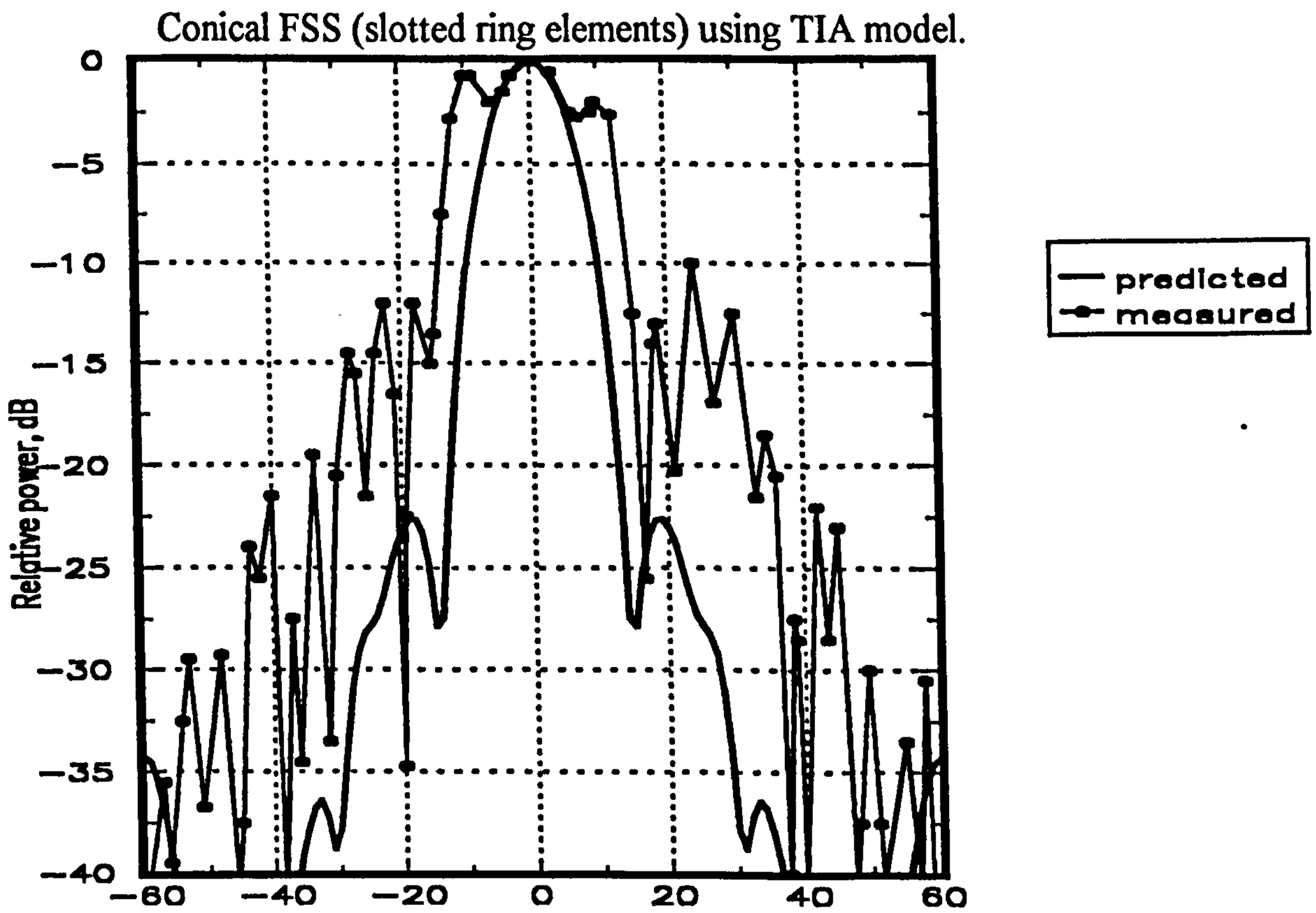

Fig.3.33 E—plane copolar pattern at 1 5 GHz using the PB feed model.

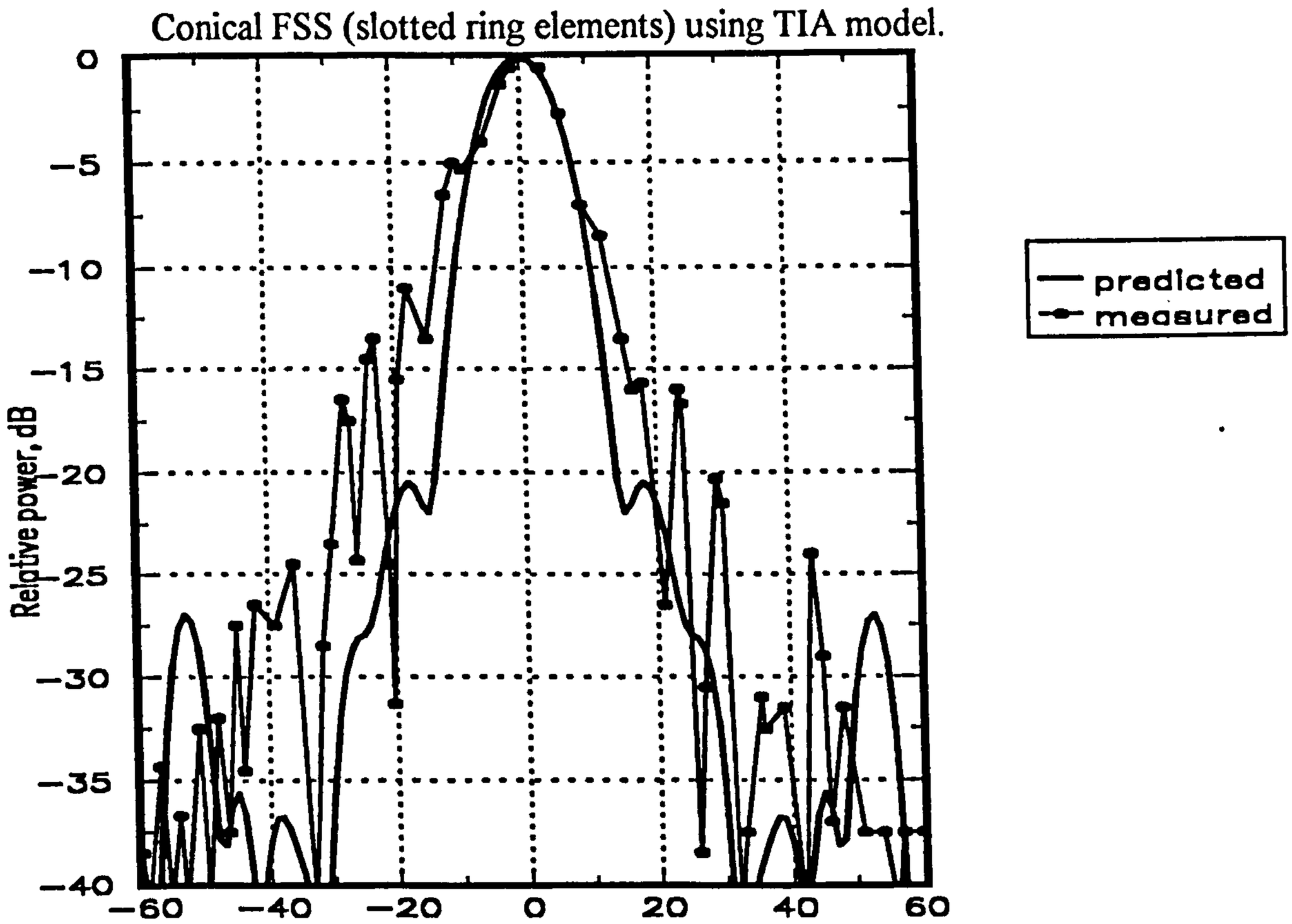

Fig.3.34 40 deg. plane copolar pattern at 1 5 GHz using the PB feed model.

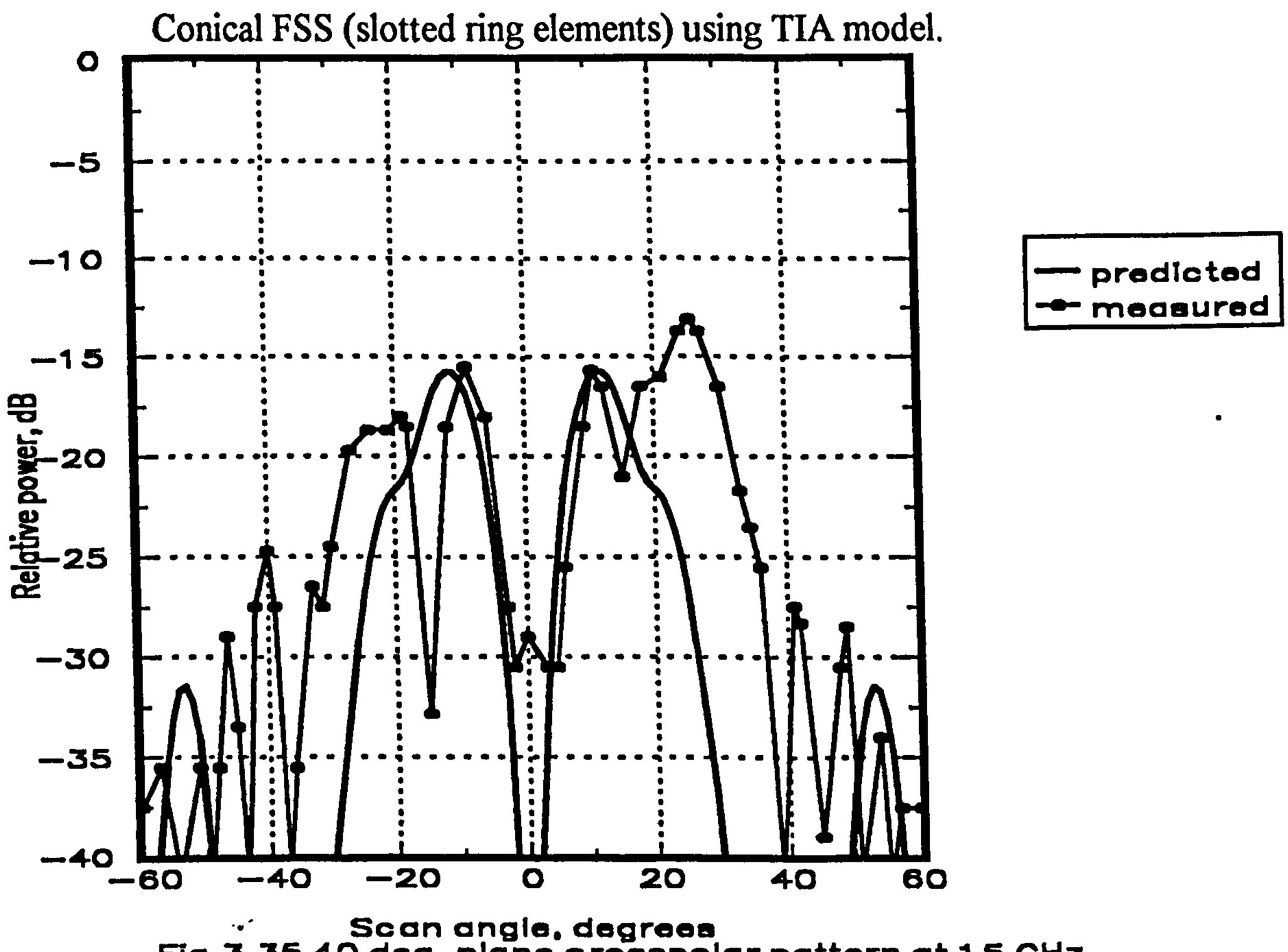

Fig.3.35 40 deg. plane crosspolar pattern at 1 5 GHz using the PB feed model.

References

[1] Pelton, E.L. and Munk, B.A. :'A Streamlined Metallic Radome', IEEE Trans. Antennas. Propagat., AP-22, 1974, pp. 174-181.

[2] Chia, Y.W., Simpkin, R. and Vardaxoglou, J.C. :'A study of a conical frequency selective surface', 7th International Symposium on Antennas, JINA'92, Nice, France, Nov. 1992, pp 321-324.

[3] Mok, K., Allam, M.A.M., Vardaxoglou, J.C., and Parker, E.A. :'Curved and Plane Frequency Selective Surfaces: A Study of Two Offset Subreflectors', J. Inst. of Electrical and Radio Eng., 58 , no.6, Sept.-Dec.1988, pp.284-290.

[4] Caroglanian, A. and Webb, K. :'Study of curved and planar frequency-selective surfaces with nonplanar illumination', IEEE Trans., AP-39, 1991, pp 211-217

[5] Chen, C.C. :'Transmission Through a Conducting Screen Perforated Periodically with Apertures', IEEE Trans. Microwave Theory and Techniques, MTT-18, 1970, pp. 627-632.

[6] Silver, S. (Ed.) :'Microwave Antenna Theory and Design', IEE Electromagnetic Wave Series 19, Peter Perregrinus Ltd, 1986, pp.80-89.

[7] Clarricoats, P.J.B. and Olver, A.D. :'Corrugated horns for microwave antennas', IEE Electromagnetic Wave Series:18, Peter Peregrinus Ltd.,1984, Chapter 3.

[8] Parker, E.A. and Vardaxoglou J.C. :'Plane wave illumination of concentric-ring frequency selective surfaces', IEE Proc., Vol.132, part H, 1985, pp.176-180.

[9] Callaghan, P., Parker, E.A. and Langley R.J. :'Influence of supporting dielectric layers on the transmission properties of frequency selective surfaces', IEE Proc., Vol.132, part H, 1991, pp.448-454.

[10] Clarricoats, P.J.B. and Olver, A.D. :'Corrugated horns for microwave antennas', IEE Electromagnetic Wave Series:18, Peter Peregrinus Ltd.,1984, Chapter 3.

[11] Simpkin .R.A. : Private communications.

CHAPTER 4.0

FINITE CURVED METALLIC FSS

4.1 Introduction

This Chapter deals with the rigorous analysis of finite curved FSS consisting of metallic elements. The FSS is a conical array which is illuminated by the near field of a circular corrugated conical feed (Fig.4.1). The problem is tackled using the electric field integral equation (EFIE) formulation for the thin cylindrical metallic structures by applying the method of moments (MOM) technique. Historically, the EFIE has often been used in electromagnetic scattering problems of aircraft and wire antennae [1]. Earlier literature on FSS has used the EFIE formulation for the two dimensional planar case using infinite array assumptions [2]. Recent research has dealt with finite but small planar arrays [3]. To the knowledge of the author, there is no published literature and data on the study of a conical FSS with dielectric substrate in a finite sense, that takes into consideration the coupling between all the FSS elements. A quasi static EFIE formulation with MOM is proposed here to account for all the interactions of elements on a small conical FSS. The near fields of the feed can be modelled as a non-planar illumination as before in the TIA model of Chapter 3. Only the SPS and PB feed models have been used in the computer model. For FSS applications, the elements are often thin compared to the wavelength, therefore they have been approximated here as cylindrical dipoles of small radius.

The proposed EFIE is derived from the original formulation for a free standing case. Section 4.2 describes how the original EFIE formulation is used after the boundary condition is enforced on a metallic conductor in free space. The curved FSS metallic elements are segmented and conformed according to their position on the cone. The equation is then weighted using the MOM technique [4] and solved by both elimination and iterative methods [5]. In practice, the FSS is supported by a dielectric substrate. If the curved FSS elements are backed by a dielectric in a finite sense, the boundary problem can become cumbersome. Although it is theoretically possible to take this into account by modelling cubes [6] or surface shaped basis functions [7], the memory storage involved would normally exceed available computing resources. Therefore, a quasi-static approach [8] has been used to account for the dielectric which is discussed in Section 4.3. The formulation is also availiable for a ferrite coating. The influence of this coating on a metallic structure is analogous to an aperture structure with dielectric coating and is discussed in Chapter 5.

Computer models were developed to predict the radiation performance of a small cone with metallic FSS dipole elements. The predictions and measurements are discussed in Sec.4.4.

4.2 Free standing finite FSS

This section describes the analysis of a free standing curved FSS using the EFIE with the method of moments (MOM) technique. The scattering problem for metallic conductors can be solved by using the electric field integral equation (EFIE) which is obtained after enforcing the boundary conditions on the conducting FSS elements. The EFIE can be reduced to a linear system of equations using the MOM. This can be solved using the elimination method [5] or the iterative method with conjugate gradients [5]. In Sec. 4.2.3 and Sec. 4.2.4, both methods have been assessed and compared for computational time and accuracy of results.

4.2.1 Integral Equation Formulation

Each conducting element on the cone can be approximated by thin cylindrical segments connected at junction points to form a certain element geometry. It is assumed that the radius and segments are small compared to the wavelength and the wire length. Therefore, the electric currents are constrained to flow along the axis of each segment with no azimuthal components. The geometry of a 'curved' dipole is segmented as shown in Fig. 4.2.

For a free standing metallic conductor, the boundary condition is given by,

$$\vec{E}^i.\hat{s} + \vec{E}^s.\hat{s} = 0 \tag{4.1}$$

where $\hat{s}$ denotes the surface tangential vector. For a thin wire, $\hat{s}$ becomes a one dimensional linear vector lying along the axis of the conductor. The incident field $\vec{E}^i$ excites the conductor to produce the scattered field, $\vec{E}^s$.

where $-\vec{E}^s = j\omega\vec{A} + \vec{\nabla}\Phi$ (4.2)

The vector potential is, $\vec{A} = \frac{\mu_o}{4\pi}\int_{segment} I(s)\hat{s}g(R)ds$ (4.3)

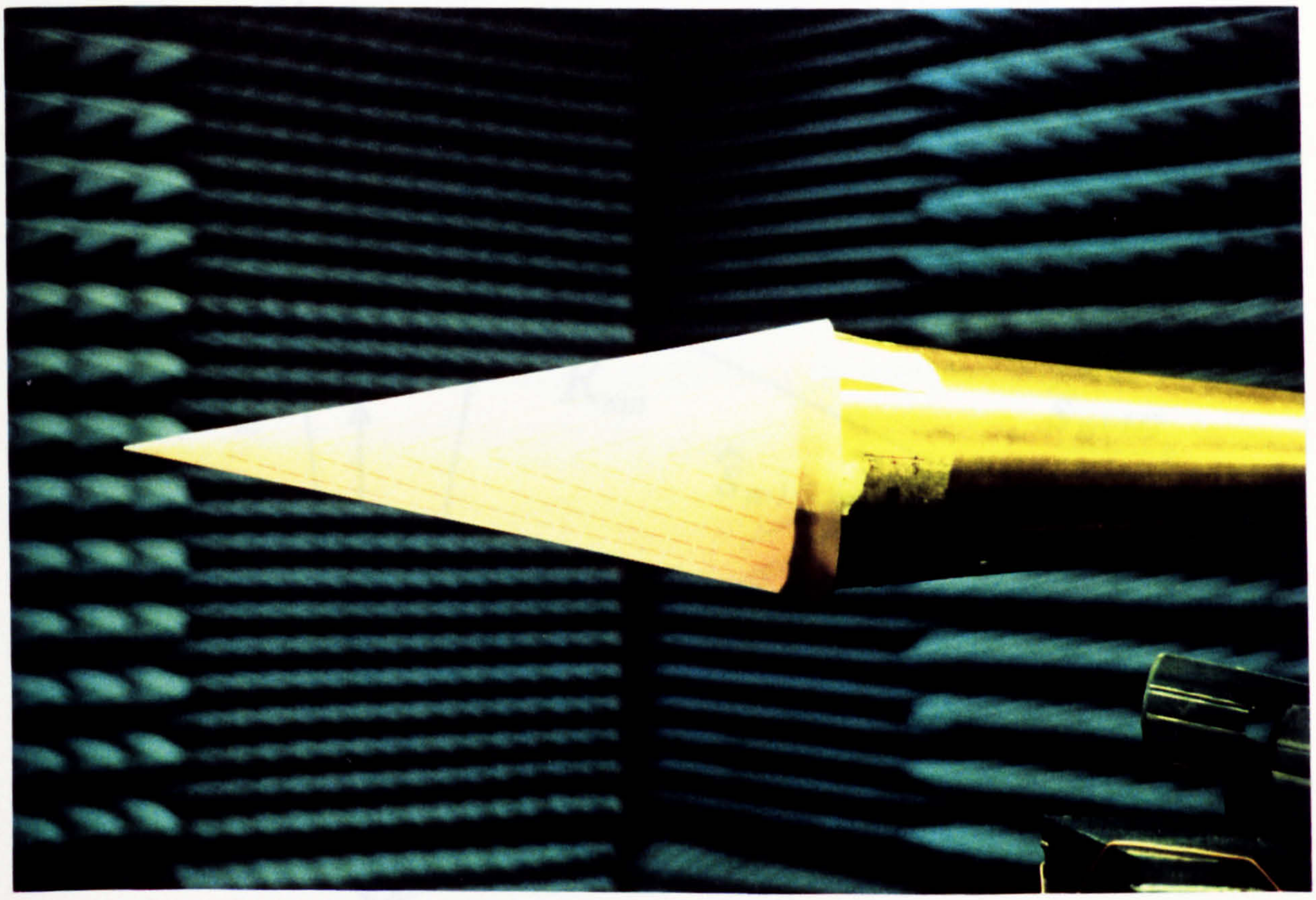

Fig.4.1 Prototype of conical FSS
(metallic dipole elements)
in the measurements.

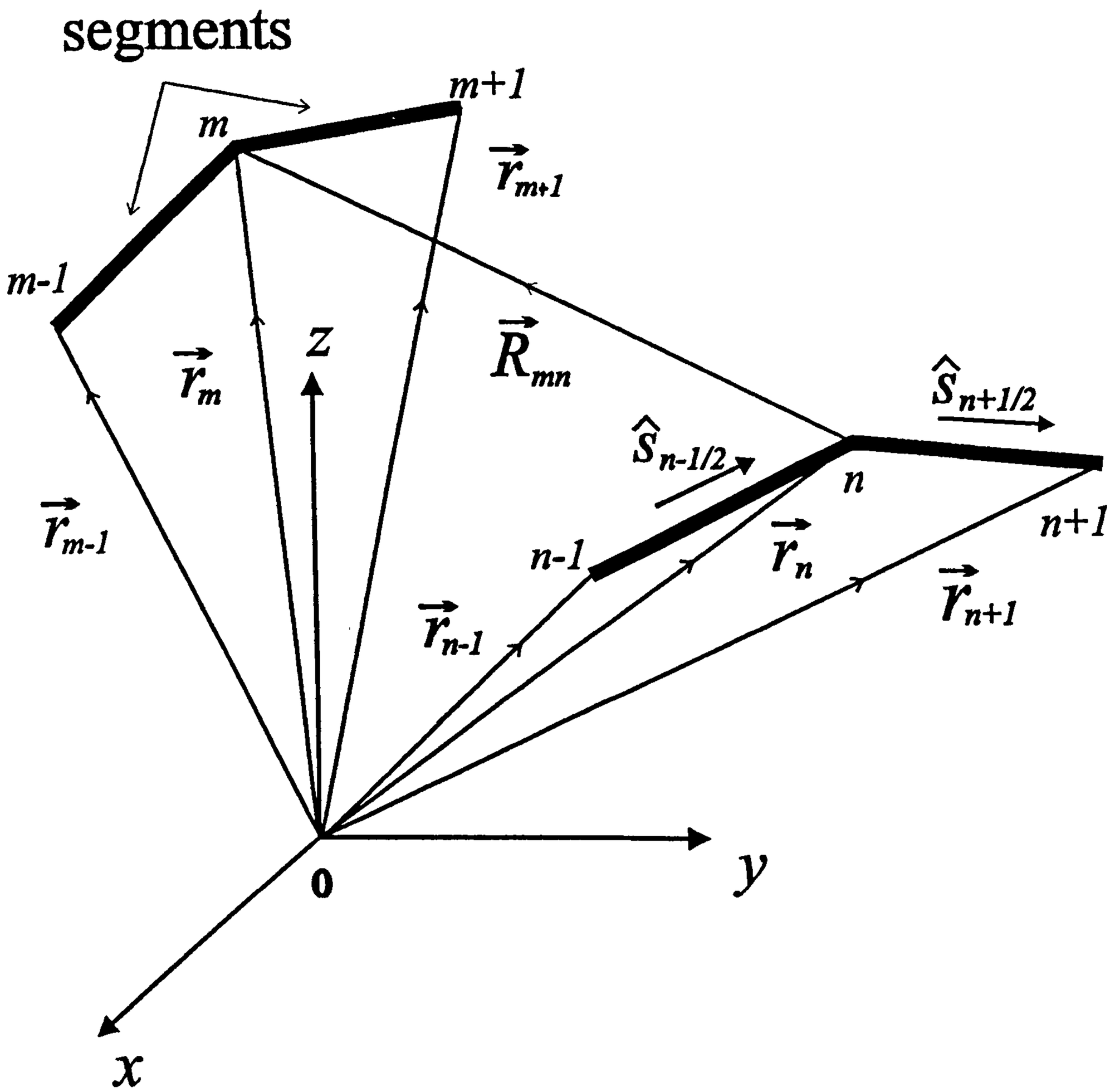

Fig.4.2 Arbitrary oriented segments of two FSS dipoles.
(For simplicity, each dipole here consists of two segments.)

and the scalar potential is, $\Phi = \frac{1}{4\pi\varepsilon_o} \int_{segment} q(s)g(R)ds$ (4.4)

where $I(s)$ and $q(s)$ are the electric current and charge per unit length on the conductor respectively.

The free space Green's function is given by,

$$g(R) = \frac{1}{2\pi} \int_{-\pi}^{\pi} \frac{e^{-jk_oR}}{R} d\phi \cong \frac{e^{-jk_oR}}{R} \tag{4.5}$$

The ϕ variation in the cross-sectional area of the conductor segment is assumed to be constant because only a one dimensional current along the axis s is considered.
and from the equation of continuity one has:

$$q(s) = \frac{-1}{j\omega} \frac{dI}{ds} \tag{4.6}$$

Substituting Eq.(4.1) into Eq.(4.2) gives the EFIE as:

$$\vec{E}^i.\hat{s} = j\omega\vec{A}.\hat{s} + \vec{\nabla}\Phi.\hat{s} \tag{4.7}$$

4.2.2 Method of Moments solution

The method of moments (MOM) was first used by Harrington [4] to analyse electromagnetic problems in the 1960's. Since then it has become a popular technique because of the accuracy and versatility in analysing arbitrary electromagnetic structures. It is a numerical technique that is frequently used to solve linear integro-differential operator equations. A typical equation is the EFIE, where the excitation from an incident field produces a current I which needs to be determined. The unknown I can be expressed as a set of basis functions over a certain domain. The domain is the area or length where the current flows. This has been represented by linear sub-domains or segments of each dipole which conformed to the curvature of the cone. The electromagnetic coupling between segments is represented as a linear system of coefficients in the form of a linear square matrix. The solution to this system has been obtained using elimination method and iterative method.

The EFIE in Eq.(4.7) is first weighted or tested using pulses as the basis functions. If the basis function of the unknown current is of the same type as the testing functions,

the MOM reduces to what is known as the Galerkin's method. This has the advantage in the EFIE case where it produces a complex symmetric matrix. Consequently, the memory storage required is about half of that in the non-symmetric case. In this study, pulse basis functions are used for representing the unknown current and weighting/testing functions. The current pulses are located across the junction of each segment [9] as shown in Fig. 4.3a. Due to the derivative dependence on the current, the charge pulse functions are shifted by half a segment length (Fig. 4.3b).

The pulse function is defined as:

$$\left.\begin{aligned} \vec{p}_m(s) &= \hat{s} \quad for \quad s_{m-1/2} < s < s_{m+1/2} \\ &= 0 \quad otherwise \end{aligned}\right\} \tag{4.8}$$

Since these segments are located on the cone which is three dimensional in nature, their positions can be defined by a vector $\vec{r}_n$ ($n=1,2,..,N$) which spans from a global origin in a Cartesian co-ordinate system to the termination of each segment, as shown in Fig.4.2. (N is the total number of position vectors to each end of a segment). The unit vector at the centre of each segment along the axis is ,

$$\hat{s}_{n+1/2} = \frac{\vec{r}_{n+1} - \vec{r}_n}{|\vec{r}_{n+1} - \vec{r}_n|} \tag{4.9}$$

The incident field $\vec{E}^i$ in Eq.(4.7) is weighted (tested) by the pulse $p_m(s)$, thus

$$\int_{s_{m-1/2}}^{s_{m+1/2}} \vec{E}^i.\vec{p}_m(s)\, ds = \int_{s_{m-1/2}}^{s_m} \vec{E}^i.\hat{s}ds + \int_{s_m}^{s_{m+1/2}} \vec{E}^i.\hat{s}ds$$

$$= \vec{E}^i.\left(\frac{s_m - s_{m-1}}{2}\hat{s}_{m-1/2} + \frac{s_{m+1} - s_m}{2}\hat{s}_{m+1/2}\right)$$

$$= \vec{E}^i.\left(\vec{r}_{m+1/2} - \vec{r}_{m-1/2}\right) \tag{4.10}$$

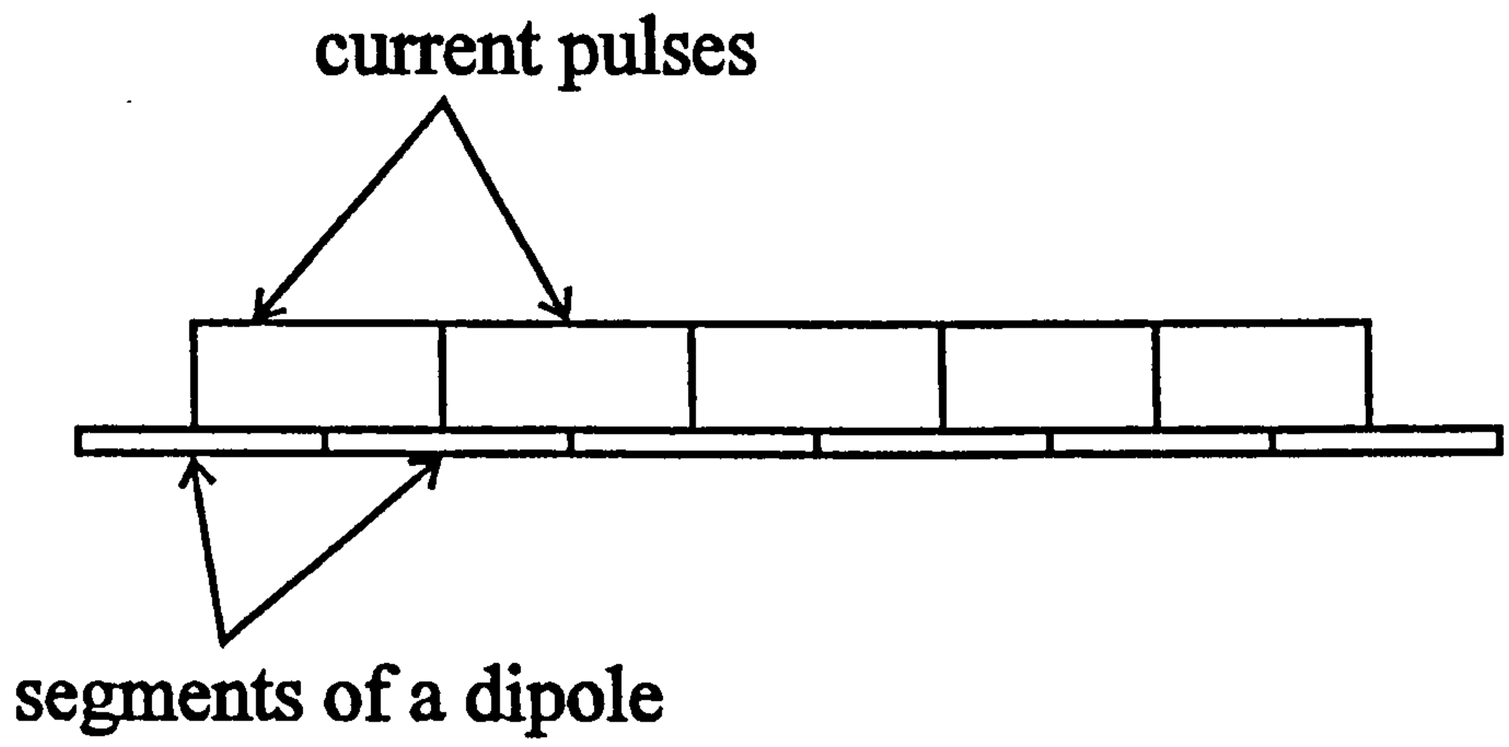

Fig. 4.3a Current pulses at the junctions of segments.

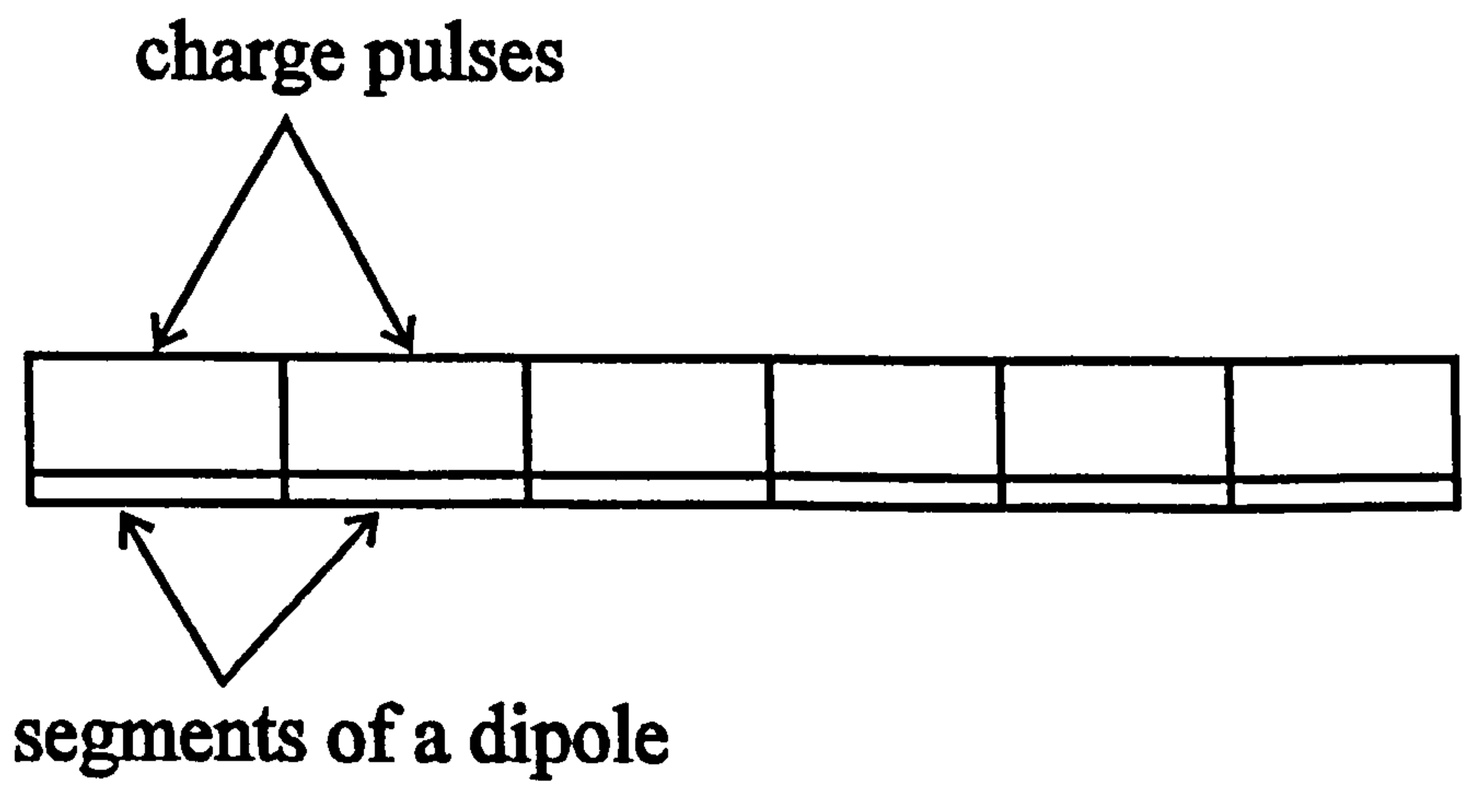

Fig.4.3b Charge pulses on segments of a dipole.

Similarly, for the vector potential term in Eq.(4.7) :

$$\int_{s_{m-1/2}}^{s_{m+1/2}} j\omega\vec{A}.p_m(s)\ ds = j\omega\vec{A}.\left(\vec{r}_{m+1/2} - \vec{r}_{m-1/2}\right) \tag{4.11}$$

Notice that centre of the pulse for the current term in the vector potential is located at m.

The scalar potential term in Eq.(4.7) is weighted as follows ,

$$\int_{s_{m-1/2}}^{s_{m+1/2}} \vec{\nabla}\Phi.\vec{p_m}(s)\ ds = \int_{s_{m-1/2}}^{s_{m+1/2}} \frac{d\Phi}{ds}\hat{s}.\hat{s}ds = \int_{s_{m-1/2}}^{s_{m+1/2}} d\Phi = \Phi\left(s_{m+1/2}\right) - \Phi\left(s_{m-1/2}\right) \tag{4.12}$$

As shown in Eq.(4.12), the derivative nature of the scalar potential has shifted the centre of the weighted charge pulse to $m + 1/2$ and $m - 1/2$.

Thus the EFIE in Eq.(4.7) becomes,

$$\vec{E}^i.\left(\vec{r}_{m+1/2} - \vec{r}_{m-1/2}\right) = j\omega\vec{A}.\left(\vec{r}_{m+1/2} - \vec{r}_{m-1/2}\right) + \Phi\left(s_{m+1/2}\right) - \Phi\left(s_{m-1/2}\right) \tag{4.13}$$

Since the current flows across the junctions of segments, the current pulse basis function is located across the nth junction. Substituting Eq.(4.8) into the vector potential term in Eq.(4.3) gives,

$$\vec{A} = \frac{\mu_o}{4\pi} I_n(s)\left[\psi(m)_{n-1/2}^{n}\hat{s}_{n-1/2} + \psi(m)_{n}^{n+1/2}\hat{s}_{n+1/2}\right] \tag{4.14}$$

where

$$\psi(m)_{n-1/2}^{n} = \int_{s_{n-1/2}}^{s_n} g(R_{mn})ds \tag{4.15a}$$

$$\psi(m)_{n}^{n+1/2} = \int_{s_n}^{s_{n+1/2}} g(R_{mn})ds \tag{4.15b}$$

This integral can be evaluated numerically or analytically. An analytical approximation given by Harrington has been chosen for convenience and simplicity. He has approximated similar terms like ψ by expanding the exponential in the Green's function g in Eq.(4.5) as a Maclaurin series so that each term in the series can be integrated analytically. Only a finite number of the terms are required to give an accuracy of 1% [4].

$$q(s) = \frac{-1}{j\omega}\frac{dI}{ds} \cong \frac{-1}{j\omega}\frac{\Delta I}{\Delta s} = \frac{-1}{j\omega}\left[\frac{I_n}{s_{n+1}-s_n} - \frac{I_n}{s_n - s_{n-1}}\right] \tag{4.16}$$

The above difference in the current pulse will shift the charge pulse by half a pulse width. Therefore, for every current pulse at the nth junction there a negative charge pulse centred at $n-\frac{1}{2}$ and a positive charge pulse at $n+\frac{1}{2}$.

Substituting Eq.(4.16) into Eq.(4.12) for one of the scalar potential terms gives,

$$\Phi\left(s_{m+1/2}\right) \cong \frac{1}{4\pi\varepsilon_o}\int \frac{-1}{j\omega}\frac{\Delta I}{\Delta s} g\left(R_{m+1/2}\right) ds$$

$$= \frac{1}{j\omega 4\pi\varepsilon_o} I_n \left[\frac{\psi\left(m+\frac{1}{2}\right)_n^{n+1}}{\left(s_{n+1}-s_n\right)} - \frac{\psi\left(m+\frac{1}{2}\right)_{n-1}^{n}}{\left(s_n - s_{n-1}\right)}\right] \tag{4.17}$$

Similarly, the other scalar potential term in Eq.(4.12) is obtained as,

$$\Phi\left(s_{m-1/2}\right) = \frac{1}{j\omega 4\pi\varepsilon_o} I_n \left[\frac{\psi\left(m-\frac{1}{2}\right)_n^{n+1}}{\left(s_{n+1}-s_n\right)} - \frac{\psi\left(m-\frac{1}{2}\right)_{n-1}^{n}}{\left(s_n - s_{n-1}\right)}\right] \tag{4.18}$$

Substituting Eqs.(4.14), (4.17) and (4.18) into the weighted EFIE in Eq.(4.13) gives,

$$\vec{E}^i.\left(\vec{r}_{m+1/2}-\vec{r}_{m-1/2}\right)$$

$$=\frac{j\omega\mu_o}{4\pi}I_n\left[\psi(m)^n_{n-1/2}\hat{s}_{n-1/2}+\psi(m)^{n+1/2}_n\hat{s}_{n+1/2}\right].\left(\vec{r}_{m+1/2}-\vec{r}_{m-1/2}\right)$$

$$+\frac{1}{j\omega 4\pi\varepsilon_o}I_n\left[\frac{\psi\left(m+1/2\right)^{n+1}_n}{\left(s_{n+1}-s_n\right)}-\frac{\psi\left(m+1/2\right)^{n}_{n-1}}{\left(s_n-s_{n-1}\right)}\right]$$

$$-\frac{1}{j\omega 4\pi\varepsilon_o}I_n\left[\frac{\psi\left(m-1/2\right)^{n+1}_n}{\left(s_{n+1}-s_n\right)}-\frac{\psi\left(m-1/2\right)^{n}_{n-1}}{\left(s_n-s_{n-1}\right)}\right] \tag{4.19}$$

Eq.(4.19) can be expressed in matrix form as,

$$\left[Y_m\right]=\left[A_{mn}\right]\left[I_n\right] \tag{4.20}$$

where

$$Y_m=\vec{E}^i\cdot\left(\vec{r}_{m+1/2}-\vec{r}_{m-1/2}\right) \tag{4.21}$$

$$A_{mn}=\frac{-1}{j\omega 4\pi\varepsilon_o}\left\{\left(k_o^2\psi(m)^n_{n-1/2}\hat{s}_{n-1/2}+k_o^2\psi(m)^{n+1/2}_n\hat{s}_{n+1/2}\right).\left(\vec{r}_{m+1/2}-\vec{r}_{m-1/2}\right)\right.$$

$$\left.\frac{\psi\left(m+1/2\right)^{n+1}_n}{\left(s_{n+1}-s_n\right)}+\frac{\psi\left(m+1/2\right)^{n}_{n-1}}{\left(s_n-s_{n-1}\right)}+\frac{\psi\left(m-1/2\right)^{n+1}_n}{\left(s_{n+1}-s_n\right)}-\frac{\psi\left(m-1/2\right)^{n}_{n-1}}{\left(s_n-s_{n-1}\right)}\right\} \tag{4.22}$$

$\left[I_n\right]$ and $\left[Y_m\right]$ are column matrices of the unknown current and excitation due to the incident fields respectively. m and $n=1,2,.....N'$, where N' is the total number of current pulses. Note that $k_o=\frac{2\pi}{\lambda}$.

$[A_{mn}]$ is a square matrix that includes the coupling between the FSS segments with the leading diagonal consisting of self coupling terms.

4.2.3 Elimination method

The matrices equation in Eq.(4.20) can be solved by the elimination method like Crout's factorisation with partial pivoting [7]. Each variable in the matrix is eliminated one at a time so that one ends up with a triangular matrix of coefficients. These coefficients are substituted back into the triangular matrix to obtain the solution. This is readily available in the NAG library Mark13 version in the subroutine F04ADF [10]. Since the Galerkins' method gives a complex symmetric matrix for the EFIE, others like Canning [11] have solved it by exploiting the symmetry with half the storage and computation time. Nevertheless, the Crout's factorisation routine was used because it was available during the development of the computer model. Sometimes, however, the elimination method can suffer from slow speed of computation and inaccuracy due to ill-conditioning problems. Therefore, another alternative is to use the iterative method, which will be discussed in the next section.

4.2.4 Iterative CG method

Recent studies have suggested that iterative methods have certain advantages over the elimination methods in three cases [12]. The former method can exploit storage reduction in the system of matrix if its elements are sparse or redundant. This kind of systems arises in differential formulations in electromagnetics. Iterative methods are preferred if the computation of the iterative algorithm is faster than the elimination method. In some cases iterative algorithms are superior to MOM solutions due to in built convergence tests and monitoring of the error. The idea behind the iterative solution is to minimise the error function after each iteration. The error function depends on the difference between the left and right hand side of the equation.

One of the more popular iterative algorithms used in solving electromagnetic problems is the conjugate gradient (CG) method. This method was first developed independently by M. Hestenes and E. Steifel for the solution of a matrix equation [13]. The novelty of this method is that the iteration converges to a solution in a finite number of steps and to a smallest minimum to the error function. But this method is slower compared to the conventional elimination method for small matrix equations.

For the integro-differential equation like the EFIE, the CG method coupled with the Fast Fourier Transform (FFT) has been quite successful in solving for planar FSS

(infinite and finite types) [3], and dielectric cylinders [14], solid 3-D metallic structures [15]. The speed of the FFT stems from being able to use multiplication in the spectra domain in place of discrete convolution in the space domain. The matrix derived from the EFIE in a regular geometry, as described above, has terms which are arranged in a cyclic convolution manner, so that the FFT can be combined with the CG method to speed up the computations. However, this is not true for multiple and arbitrarily oriented structures such as those in a conical FSS.

An alternative solution for such a problem is to apply the CG method directly to the system of matrices without using the FFT. A suitable matrix has been derived from the integral equation using MOM as in Eq.(4.20). This form of CG method has been used in the present analysis for a conical FSS. The CG performance has been compared with the elimination method with respect to computational speed and memory. No data is available in this subject of finite and curved FSS.

Details of the derivation for the CG algorithm can be obtained from [13]. However, only the version proposed by Sarkar [16] is used here because a certain amount of memory can be saved. A summary is presented here to show the order of each step of the algorithm.

To apply the CG algorithm for the weighted integral equation in Eq.(4.20), it must be rewritten with a residual column matrix $[R]_o$ introduced on the left hand side of the equation as shown here.

$$[R]_0 = [A][I]_0 - [Y] \tag{4.23}$$

The subscripts used in Eq.(4.20) have been neglected in Eq.(4.23) for convenience. The subscript of the matrix denotes the number of iteration, so 0 is the start of the algorithm.

Starting with an initial estimate $[I]_0$, new estimates $[I]_1$, $[I]_2$,..of the solution $[I]$ are calculated after each iteration. Successive estimates give a closer solution to equation Eq.(4.23) than the previous one. At each iteration, the residual $[R]_{ni}$ is computed so that the norm $\|[R]_{ni}\|$ is used as a measure of the accuracy of the estimate $[I]_{ni}$. If there is no rounding off error, one will reach an estimate $[I]_m$at

which $[R]_{ni}$ is close to zero. Computation error can arise in the calculation of these matrices (as shown in the following summary) because of numerical accuracies of the computer or mathematical routine. Such round-off errors would not allow the algorithm to converge. The CG algorithm derives its name from the fact that the search vectors $[P]_0,[P]_1,..$ are mutually conjugate i.e. $[P]_{ni}$ vector is orthogonal with respect to $[A]^*[A]$. On its own $[A]$ could be a non-singular asymmetric matrix. Therefore, it can also be multiplied by $[A]^*$ to form a new operator to ensure a symmetric and positive definite matrix. So that the CG can be universally applied to the solution of linear equations.

The CG algorithm can be summarised as follows:

An initial guess is required for the current coefficients in Eq.(4.23) and usually they are set at zeroes, so that the column matrix becomes $[I]_0 = [0]$.

The order of operation is as shown:

1. $[P]_0 = -b_{-1}[A]^*.([A][I]_0 - [Y])$

2. $t_{n_i} = \dfrac{1}{\left\|[A][P]_{n_i}\right\|^2}$

3. $[I]_{n_i+1} = [I]_{n_i} + t_{n_i}[P]_{n_i}$

4. $[R]_{n_i+1} = [R]_{n_i} + t_{n_i}[A][P]_{n_i}$

5. $b_{n_i} = \dfrac{1}{\left\|[A]^*[R]_{n_i+1}\right\|^2}$

6. $[P]_{n_i+1} = [P]_{n_i} - b_{n_i}[A]^*[R]_{n_i+1}$

7. Go to step *1*. until the error criteria $e \geq \dfrac{\left\|[R]_{n_i}\right\|}{\left\|[Y]\right\|}$

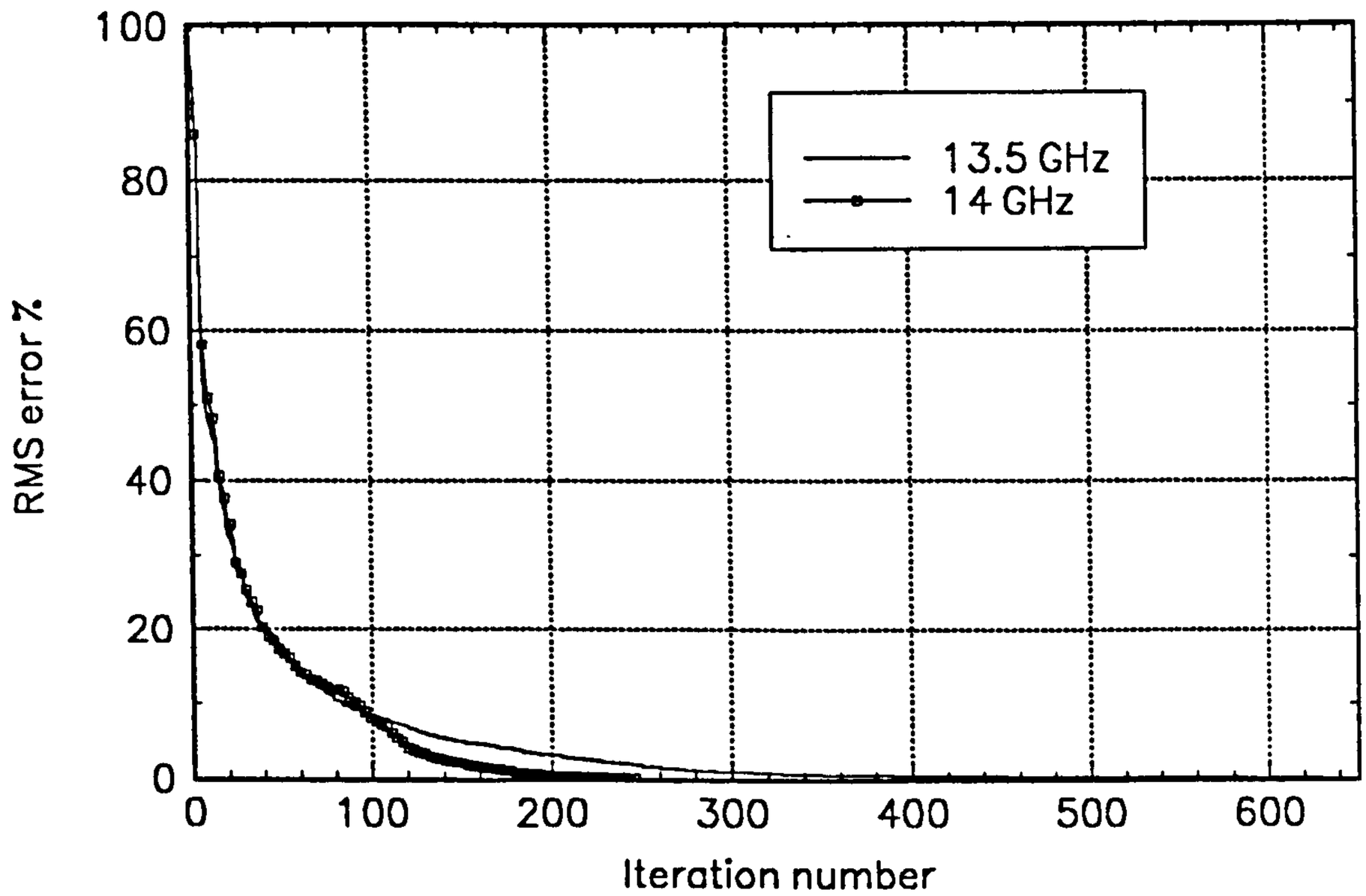

Fig.4.4 Convergence rate for a free standing conical FSS.

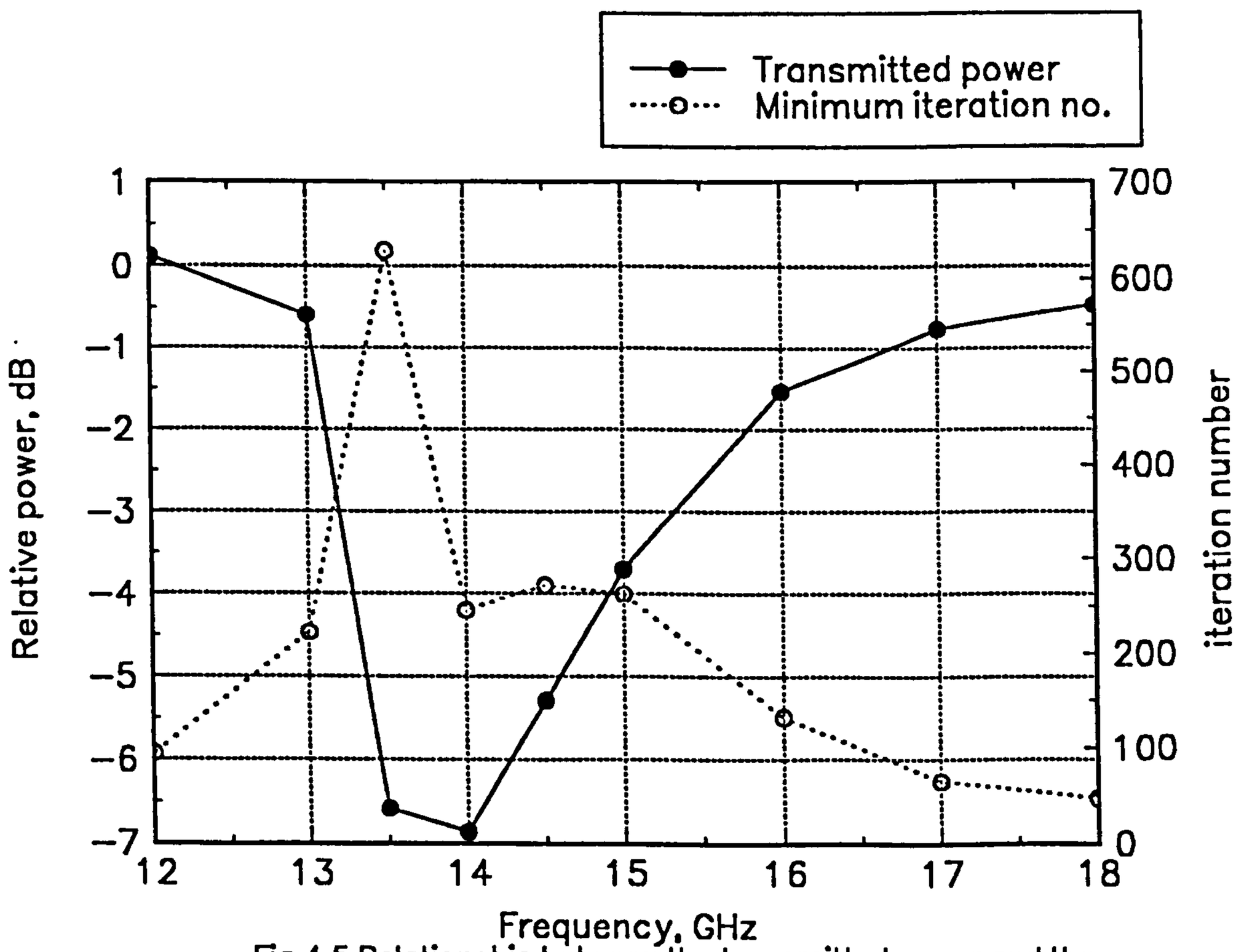

Fig.4.5 Relationship between the transmitted power and the minimum iteration number with frequency.

where the subscript n_i is the number of iteration and the norm is defined as $\|b\|^2 = \langle b,b \rangle = b.b^*$

$$b_{-1} = \left\| \frac{1}{[A]^*[R]_0} \right\|$$

Because of the nature of the derivation obtained from Sarkar [16] the initial coefficient b_{-1} start at iteration number -1, which precedes 0.

$[A]^*$ is the conjugate transpose square matrix of $[A]$.

The algorithm shown here will reduce the error norm $\frac{\|[R]_{n_i}\|}{\|[Y]\|}$ or root mean square (RMS) error after each iteration. The loop of operation will terminate after a certain finite number of iterations with an error criteria e defined by the user. This is a minimum criterion that determines the accuracy of the iterative CG solution.

Both the elimination and CG method lead to the same answer for an error criterion or accuracy e of 0.1% for a 1760x1760 matrix size. The convergence rates for this impedance matrix around the resonant frequencies for a free standing conical FSS are shown in Fig 4.4. The size of the matrix depends on the feed model. In this case the SPS feed model is chosen. It is observed that the convergence rate at 13.5 GHz slows down after about 100 iterations before finally converging after 620 steps. But at 14 GHz, the matrix converges rapidly from the 100th step onwards terminating at 246 steps.

It appears from the results shown in Fig.4.5 that the computational time for the CG method varies with frequency. It changes from 47 steps (1.13 hours) at 18 GHz to 629 steps (6.41hours) at 13.5 GHz, the resonant frequency. This is in contrast to the elimination method, for which the computation time remains constant at about 5.5 hours. Therefore, it is evident that the CG method is superior in speed of computation across the frequency band of the conical FSS except for the resonant frequency. However, it did not converge at all when the quasi-static approximation for the EFIE was used (Sec.4.3.1). This is caused by possible round off errors in the computation of the coupling terms in the impedance matrix. Therefore, the elimination method was adopted in the computer model because it is computationally more stable.

It was also found that when the RAM, which was used to store the impedance matrix, was exceeded by 20%, the CG would slow down considerably. In the SUN workstation, when the storage of the matrix exceeds the RAM, the hard disk is accessed to compensate for the extra memory. Thus, it would appear that the speed of the CG and elimination method is machine dependent. In practice, the RAM is often restricted by the technology of computer hardware. In the present case, the maximum amount of RAM allowed in the SUN SPARC II is 126 Megabytes although there is only 96 Megabytes available in the current workstation. For the small cone FSS that is analysed in this work, a minimum of 97 Megabytes is required. In most practical FSS, the demands are for a much greater memory storage. Thus the elimination method is preferred if the impedance matrix memory storage is much larger than the RAM.

For a $N'XN'$ matrix , the memory storage can be reduced by a factor of about N' times if every matrix element is computed after each iteration. However, the computing time was found to be excessive in the present case because of excessive computations for each matrix element.

4.2.5 Radiated and scattered fields

The radiated fields from the FSS cone can be computed from the surface radiation integral with the surface electric and magnetic current sources enclosed by a closed surface around the cone and feed system. The electric current source on each metallic dipole can be calculated from the solution of the EFIE formulation. The radiated fields from both current sources in the aperture regions of a free standing curved FSS is calculated using the radiated field from the feed aperture. However, for a dielectric FSS, it is an intractable problem to determine these current sources in the dielectric region. Therefore it has been approximated by fields radiated from the feed aperture as well. Thus, the total field radiated from the cone is the sum of the scattered fields from the cone and radiated fields from the feed aperture.

For the conducting segments with $n=1,2..N'$ (N' is the total number of current pulses), the scattered field at a distance Γ_n from the centre of each current pulse to the receive feed is given by:

$$\vec{E}^{scat}(\Gamma_n) = \frac{-j\omega\mu_o}{4\pi}\frac{e^{-jk_o\Gamma_n}}{\Gamma_n}\int_{segment}\left[\vec{I}_n - \left(\vec{I}_n \cdot \hat{\Gamma}_n\right)\right]\hat{\Gamma}_n e^{jk_o\vec{r}_t\cdot\hat{\Gamma}_n} ds$$

$$=\frac{-j\omega\mu_o}{4\pi}\frac{e^{-jk_o\Gamma_n}}{\Gamma_n}.\left[\tilde{I}_n-\left(\tilde{I}_n.\hat{\Gamma}_n\right)\hat{\Gamma}_n\right] \tag{4.24}$$

where

$$\tilde{I}_n = \int_{segment} \vec{I}_n\, e^{jk_o\vec{r}_t.\hat{\Gamma}_n} ds$$

$$= \int_{n-1/2}^{n} I_n\,\hat{s}_{n-1/2}\, e^{jk_o\vec{r}_t.\hat{\Gamma}_n} ds + \int_{n}^{n+1/2} I_n\,\hat{s}_{n+1/2}\, e^{jk_o\vec{r}_t.\hat{\Gamma}_n} ds$$

$$=I_n\hat{s}_{n-1/2}\left(s_n-s_{n-1/2}\right)+I_n\hat{s}_{n+1/2}\left(s_{n+1/2}-s_n\right) \tag{4.25}$$

Therefore, the total scattered field from the FSS cone is the sum of all the current pulses given by,

$$\vec{E}^{scat}_{cone} = \sum_{n=1}^{n=N'} \vec{E}^{scat}(\Gamma_n) \tag{4.26}$$

The total radiated field from the FSS cone is,

$$\vec{E}_{total} = \vec{E}_{feed} + \vec{E}^{scat}_{cone} \tag{4.27}$$

where $\vec{E}_{feed}$ is the field radiated from the feed aperture.

4.3 Dielectric and ferrite coated metallic FSS dipole

Since the width of the FSS element structures is usually thin, an arbitrary geometry can be formed by interconnecting thin metallic segments. This thin segment supported by a thin dielectric substrate can be modelled approximately as a cylindrical metallic segment with dielectric coating. The width of a flat dipole segment can be approximated by the diameter of the cylindrical segment and the thickness of the substrate is equivalent to the thickness of the cylindrical coating. This approximation considers the dielectric acting as a continuous load on the conductor. The analysis was first derived by Popovic [8] for a dielectric and ferrite coated antenna but it has been applied here for dielectric and ferrite coated metallic elements in a finite conical FSS. The quasi static approximation for a dielectric coated antenna, requires the thickness of

the coating should be less than twice the radius of the dipole. The permittivity and permeability of the coating should be less than 10 and is assumed to be homogeneous. One advantage of this method is that memory storage and the computing time is virtually the same as for the free standing case. This is based on a quasi-static approximation of electric and magnetic fields in the transverse plane of the segment axis.

4.3.1 Quasi-static equivalent of dielectric backed FSS

The flat metallic dipole segment of the FSS supported by dielectric substrate is modelled here as a cylindrical dipole segment with dielectric coating. The width of the flat dipole is assumed to be the same size of the diameter of the cylindrical dipole. The thickness of the substrate is approximated by the thickness of the coating. Consider a metallic dipole segment of radius a coated with a layer of dielectric with permitivitty ε where the outer radius is $\rho = b$ as shown in Fig.4.6. Let the electric current flowing in the segment be I. The dipole segment is assumed to be a perfect metallic conductor with infinite conductivity. The dipole segment with a cylindrical coating is approximated as inner and outer cylindrical layers of polarisation charges at $\rho=a$ and b respectively with a current I flowing along the segment axis in the inner radius.

For the static case, the metallic segment with a cylindrical coating is assumed to be infinitely long. The inner cylinder of radius a and outer radius b enclose a line source in the axis with charge per unit length q and length L. According to Gauss's law [17] the total outward flux of the electric displacement $\vec{D}$ over any enclosed surface in a dielectric medium is equal to the total free charge Q enclosed in the surface

Thus, $$\oint_{\substack{cylindrical\\surface}} \vec{D}.\hat{n}dS = Q \tag{4.28}$$

For the cylindrical surface, Eq.(4.28) becomes

$$D_\rho \hat{n}.\hat{n} 2\pi\rho L = qL$$

This implies that $$D_\rho = \frac{q}{2\pi\rho} \tag{4.29}$$

The subscript ρ denotes the radial component of the flux D.

The electric field intensity, $\vec{E}_\rho$, is given by,

$$\vec{E}_\rho = E_\rho \hat{n} = \frac{D_\rho}{\varepsilon}\hat{n} = \frac{q}{2\pi\rho\varepsilon}\hat{n} \tag{4.30}$$

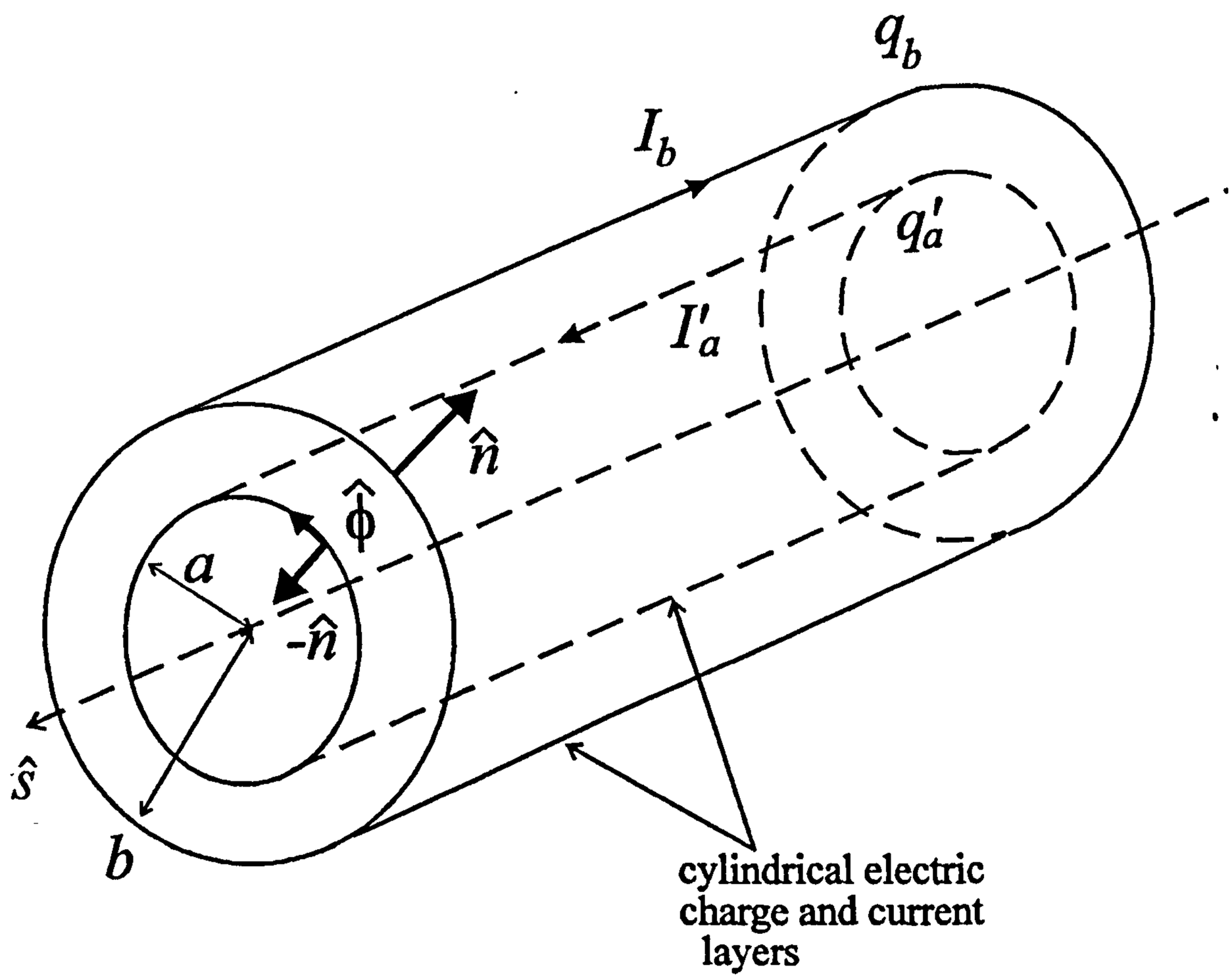

Fig.4.6 Metallic dipole segment with dielectric and ferrite coatings represented by electric charge and current layers.

But the polarisation charge vector $\vec{P}_\rho$ is given by,

$$\vec{P}_\rho = \vec{D}_\rho - \varepsilon_o \vec{E}_\rho \tag{4.31}$$

Substituting Eq.(4.29) and Eq.(4.30) into Eq.(4.31) gives,

$$\vec{P}_\rho = \frac{q}{2\pi\rho}\hat{n} - \frac{q}{2\pi\rho}\frac{\varepsilon_o}{\varepsilon}\hat{n} = \frac{q}{2\pi\rho}\left(1 - \frac{1}{\varepsilon_r}\right)\hat{n} \tag{4.32}$$

Therefore, at the inner radius, $\rho=a$, the polarised charge vector is $\vec{P}_a$,

$$\vec{P}_a = \frac{q}{2\pi a}\left(1 - \frac{1}{\varepsilon_r}\right)\hat{n} \tag{4.33}$$

And, at the outer radius, $\rho=b$,

$$\vec{P}_b = \frac{q}{2\pi b}\left(1 - \frac{1}{\varepsilon_r}\right)\hat{n} \tag{4.34}$$

The polarised charge per unit length q_a at $\rho=a$ is,

$$q_a = \oint_{\substack{cylindrical \\ circumference}} \vec{P}_a.(-\hat{n})dS_c = \int_{-\pi}^{\pi} \frac{q}{2\pi a}\left(1 - \frac{1}{\varepsilon_r}\right)\hat{n}.(-\hat{n})a\,d\phi$$

$$= -q\left(1 - \frac{1}{\varepsilon_r}\right) \tag{4.35}$$

(Note that the integral over the surface S is reduced to a line integral over the circumference S_c because of the charge density q.)

Since the dielectric encloses a line charge per unit length of q at $\rho=a$, the total charge density q'_a at $\rho=a$ is the sum of q and polarised charge density q_a .

$$q'_a = q + q_a = q - q\left(1 - \frac{1}{\varepsilon_r}\right) = \frac{q}{\varepsilon_r} = \frac{1}{\varepsilon_r}\left(\frac{-1}{j\omega}\frac{dI}{ds}\right) \tag{4.36}$$

Similarly, for the polarised charge density q_b at the outer radius $\rho=b$, the normal vector $\hat{n}$ is pointing outwards. So

$$q_b = \oint_{\substack{cylindrical\\circumference}} \vec{P}_b.(\hat{n})dS_c = \int_{-\pi}^{\pi} \frac{q}{2\pi b}\left(1-\frac{1}{\varepsilon_r}\right)\hat{n}.(\hat{n})b\,d\phi$$

$$=\left(1-\frac{1}{\varepsilon_r}\right)q=\left(1-\frac{1}{\varepsilon_r}\right)\left(\frac{-1}{j\omega}\frac{dI}{ds}\right) \tag{4.37}$$

The radial polarisation current density is, $\vec{J}_\rho = j\omega\vec{P}_\rho$ (4.38)

Note that the volume polarisation charges in the coating do not exist because the coating is homogeneous.

4.3.2 Quasi-static equivalent of ferrite backed FSS

The flat dipole segment of the FSS with ferrite substrate is also modelled in a similar way to the dielectric coated segment in the previous section. This is now represented by a cylindrical dipole segment with ferrite coating. It is assumed that the metallic segment and coating is a infinitely long quasi-static structure. Therefore, in a ferrite coating of thickness $(b-a)$, the magnetic field intensity $\vec{H}$ would circulate around the segment of radius a with current I. Ampere's law states that the circulation of the magnetic field intensity around any closed path is equal to the free current flowing through the surface bounded by the path l.

Using the Ampere's law,

$$\oint_{\substack{cylindrical\\circumference}} \vec{H}.d\vec{l} = I \tag{4.39}$$

Therefore, for the cylindrical metallic segment,

$$H_\phi = \frac{I}{2\pi\rho} \tag{4.40}$$

Eq.(4.40) implies that the magnetisation vector is also circulating around the cylindrical surface with the centre at the segment axis.

The ϕ component of the magnetisation vector M_ϕ is given by:

$$M_\phi = (\mu_r - 1)H_\phi \tag{4.41}$$

Substituting Eq.(4.40) into Eq.(4.41) yields,

$$M_\phi = (\mu_r - 1)\frac{I}{2\pi\rho} \tag{4.42}$$

There is also a radial magnetisation current density of $\frac{-\partial M_\phi}{\partial s}$ in the coating .

The magnetisation current density at $\rho = a$ is given by,

$$\vec{J}_a = M_\phi \hat{\phi} \times (-\hat{n}) = M_\phi \hat{s} \tag{4.43}$$

From Eq.(4.42) and Eq.(4.43) it is evident that the surface magnetisation current I_a at $\rho = a$ is,

$$I_a = (\mu_r - 1)I \tag{4.44}$$

However, the total current at $\rho = a$ is the sum of the magnetisation current I_a and the conducting current I. Therefore, the total current I'_a is given by:

$$I'_a = \mu_r I \tag{4.45}$$

At the outer surface, the normal vector $\hat{n}$ is pointing away from the surface. Therefore, the surface magnetisation current density will flow in the reverse direction and is given by,

$$\vec{J}_b = M_\phi \hat{\phi} \times \hat{n} = -M_\phi \hat{s} \tag{4.46}$$

So the surface magnetisation current at $\rho = b$ from Eq.(4.42) and Eq.(4.46) is,

$$I_b = -(\mu_r - 1)I \tag{4.47}$$

In general, for dielectric and ferrite coatings, the quasi-static approximation can be represented by the currents I'_a and I_b and charge densities q'_a and q_b on the two cylindrical surfaces respectively. The total electric field is computed along the segment axis. Here the electric field due to the radial polarisation and magnetisation currents is zero because the radial currents only exist in the coatings. When the electric field due to this coated segment is computed along the axis of any other segment, the field due

to the radial currents can be neglected, because these radial currents are uniformly distributed in all directions in a small area. Thus, the fields due to the metallic segment and the coating are the contributions from a cylindrical layer of charge density q'_a and current I'_a at $\rho=a$, and another layer at q_b and I_b at $\rho=b$ as shown in Fig.4.6.

The EFIE in Eq.(4.7) for a free standing FSS with cylindrical radius a can be rewritten as :

$$\vec{E}_i = \frac{j\omega\mu_o}{4\pi} \int_{segment} I\hat{s}g(R_a)ds + \frac{1}{4\pi\varepsilon_o} \int_{segment} \left(\frac{-1}{j\omega}\frac{dI}{ds}\right)\vec{\nabla}g(R_a)ds \qquad (4.48)$$

Substituting Eqs.(4.36), (4.37), (4.45) and (4.47) into the EFIE in Eq.(4.48) yields,

$$\vec{E}_i = \frac{j\omega\mu_o}{4\pi}\left[\int_{segment} \mu_r I\hat{s}g(R_a)ds - \int_{segment}(\mu_r - 1)I\hat{s}g(R_b)ds\right]$$

$$+\frac{1}{4\pi\varepsilon_o}\left[\int_{segment} \frac{1}{\varepsilon_r}\left(\frac{-1}{j\omega}\frac{dI}{ds}\right)\vec{\nabla}g(R_a)ds + \int_{segment}\left(1-\frac{1}{\varepsilon_r}\right)\left(\frac{-1}{j\omega}\frac{dI}{ds}\right)\vec{\nabla}g(R_b)ds\right]$$

(4.49)

R_a and R_b are the distances from the inner and outer radius to the point of observation P as shown in Fig.4.7.

If the metallic segment is coated by dielectric alone, μ_r =1, the current component in Eq.(4.49) is not dependent on the permeability of a ferrite .
It has been shown in Eq.(4.22) that the impedance matrix elements for a free standing FSS are given by:

$$A_{mn} = \frac{-1}{j\omega 4\pi\varepsilon_o}\left\{\left(k_o^2\psi(m)_{n-1/2}^{n}\hat{s}_{n-1/2} + k_o^2\psi(m)_{n}^{n+1/2}\hat{s}_{n+1/2}\right)\cdot\left(\vec{r}_{m+1/2} - \vec{r}_{m-1/2}\right)\right.$$

$$\left.-\frac{\psi\left(m+1/2\right)_{n}^{n+1}}{(s_{n+1}-s_n)} + \frac{\psi\left(m+1/2\right)_{n-1}^{n}}{(s_n - s_{n-1})} + \frac{\psi\left(m-1/2\right)_{n}^{n+1}}{(s_{n+1}-s_n)} - \frac{\psi\left(m-1/2\right)_{n-1}^{n}}{(s_n - s_{n-1})}\right\} \qquad (4.22)$$

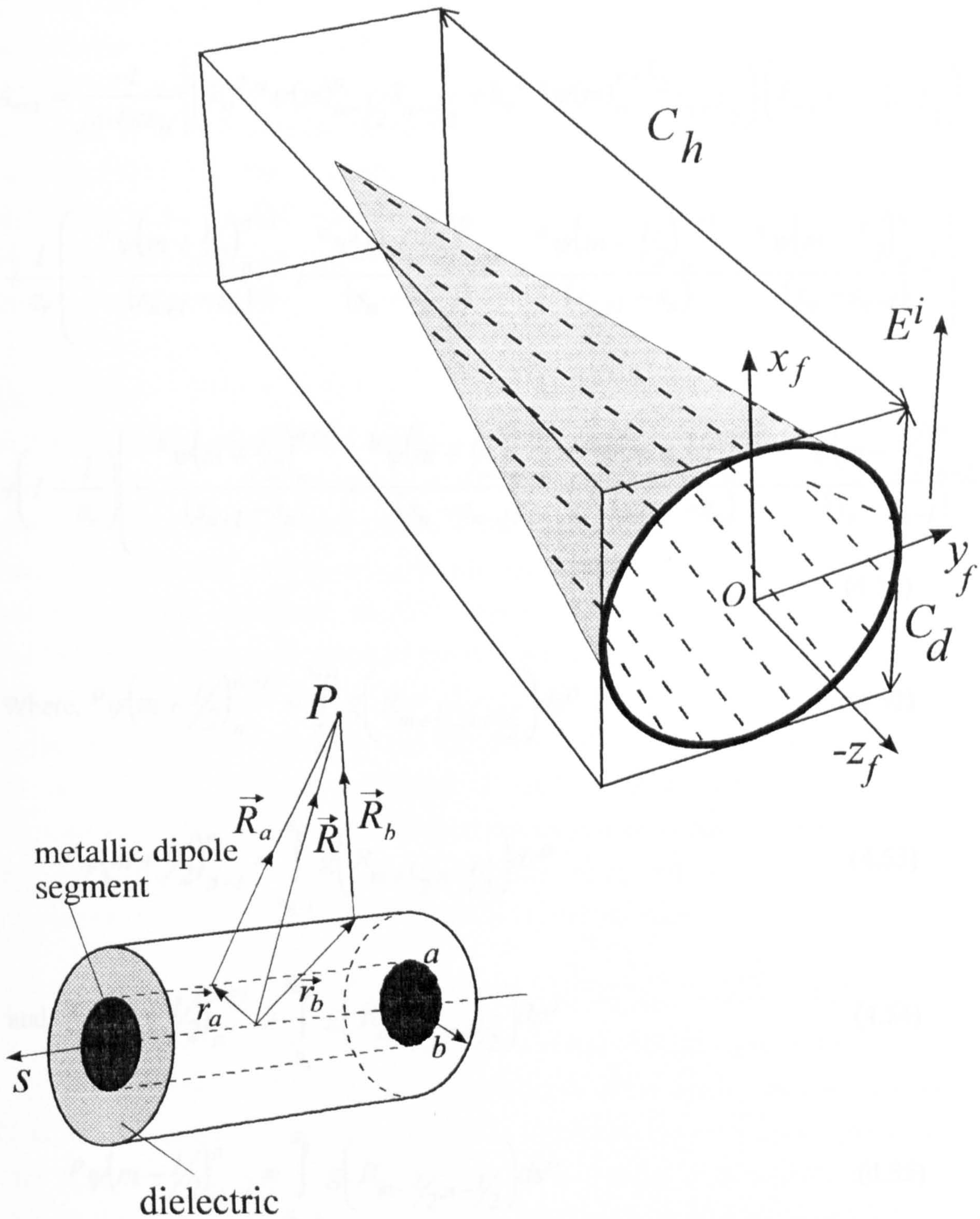

Fig. 4.7 Geometry of the conical FSS and the model of a dielectrically loaded metallic segment.

Therefore, if Eq.(4.48) is compared with Eq.(4.49), it is evident that only a simple modification in the impedance matrix is required to account for the dielectric loading, so the new impedance square matrix $[A_{mn}]$ for the dielectric coating becomes,

$$A_{mn} = \frac{-1}{j\omega 4\pi\varepsilon_o}\left\{\left(k_o^{2\,a}\psi(m)_{n-1/2}^{n}\hat{s}_{n-1/2} + k_o^{2\,a}\psi(m)_{n}^{n+1/2}\hat{s}_{n+1/2}\right)\cdot\left(\vec{r}_{m+1/2} - \vec{r}_{m-1/2}\right)\right.$$

$$+\frac{1}{\varepsilon_r}\left(-\frac{{}^{a}\psi\left(m+1/2\right)_{n}^{n+1}}{(s_{n+1}-s_n)} + \frac{{}^{a}\psi\left(m+1/2\right)_{n-1}^{n}}{(s_n-s_{n-1})} + \frac{{}^{a}\psi\left(m-1/2\right)_{n}^{n+1}}{(s_{n+1}-s_n)} - \frac{{}^{a}\psi\left(m-1/2\right)_{n-1}^{n}}{(s_n-s_{n-1})}\right)$$

$$\left.+\left(1-\frac{1}{\varepsilon_r}\right)\left(-\frac{{}^{b}\psi\left(m+1/2\right)_{n}^{n+1}}{(s_{n+1}-s_n)} + \frac{{}^{b}\psi\left(m+1/2\right)_{n-1}^{n}}{(s_n-s_{n-1})} + \frac{{}^{b}\psi\left(m-1/2\right)_{n}^{n+1}}{(s_{n+1}-s_n)} - \frac{{}^{b}\psi\left(m-1/2\right)_{n-1}^{n}}{(s_n-s_{n-1})}\right)\right\}$$

(4.51)

Where, $${}^{\rho}\psi\left(m+1/2\right)_{n}^{n+1} = \int_{s_n}^{s_{n+1}} g\left(R_{m+1/2,n+1/2}\right)ds^{\rho} \qquad (4.52)$$

$${}^{\rho}\psi\left(m+1/2\right)_{n-1}^{n} = \int_{s_{n-1}}^{s_n} g\left(R_{m+1/2,n-1/2}\right)ds^{\rho} \qquad (4.53)$$

and $${}^{\rho}\psi\left(m-1/2\right)_{n}^{n+1} = \int_{s_n}^{s_{n+1}} g\left(R_{m-1/2,n+1/2}\right)ds^{\rho} \qquad (4.54)$$

$${}^{\rho}\psi\left(m-1/2\right)_{n-1}^{n} = \int_{s_{n-1}}^{s_n} g\left(R_{m-1/2,n-1/2}\right)ds^{\rho} \qquad (4.55)$$

ρ denotes the radius a and b.

The scattered far field from each current pulse across the junction of the segments is computed in the same manner as the free-standing case as described in Sec. 4.2.5. But now the current has been modified by the dielectric effect. This is because at far fields,

Γ_n is large, so the value of the ψ term in Eq.(4.51) at $\rho=a$ and b is numerically the same. Therefore, the scalar potential terms in Eq.(4.51) will cancel each other. Effectively, A_{mn} is dependent on the vector potential which varies with current I only. The total radiated field from the FSS cone is the sum of the scattered fields from each current pulse that has been modified by the dielectric coating, and the radiated field from the feed alone as shown in Eq.(4.27). A computer model was developed using the quasi-static EFIE to predict the far field radiation patterns of a dielectric FSS radome enclosing a feed. This has been called the finite current (FC) model here because the interactions of all the FSS elements are treated in a finite geometrical sense. The predictions were compared against the experimental results from a prototype cone as discussed in the next section.

4.4 Results

In this section, the experimental results are used to validate the predictions obtained from the computer model using the quasi static approximation of the EFIE. The geometry of the cone and feed system is the same as Fig.3.8 in Chapter 3. Fig.4.1 shows the actual FSS cone covering the corrugated conical feed in the experiment. At this stage of the experiment, an ADC (Analogue to Digital Conversion) card was installed in the computer to automate the set-up as described as described in Sec.3.5.2 [18]. This is to convert the analogue signal from the vector network analyser into digital data for storage purposes. The amplitude and phase were measured in the set-up as previously discussed in Chapter 3. But the ADC software enables both measurements at each angle with a frequency scan as well so that the radiation patterns can be taken over a wider frequency range compared to the spot frequency measurements made on the large FSS cone in the earlier work.

The orientation of the FSS elements in relation to the feed electric field is shown in Fig.4.7. A conical FSS was constructed from a planar configuration with two identical half sectors representing the top and bottom parts of the surface on the same sheet. This is then wrapped around with the metallic dipoles on the exterior and glued on one side to ensure symmetry in the cone. Each sector had the array already printed on a 0.1mm thick dielectric substrate with $\varepsilon_r=3$. The length of each flat metallic dipole is 10.0mm, the width 0.5 mm and the element spacing is 12mm arranged in a square lattice. Therefore this is modelled as cylindrical dipole of the same length with radius a=0.25 mm and a coating of 0.1mm (b-a). The cone is just over 30 cm long with a base diameter of 12.6 cm. The feed aperture has a diameter of 9.6 cm. The number of elements falling within the area of illumination in the SPS and PB feed model are 352 and 234 respectively. Each dipole is divided into 6 segments. Therefore, the total

number of matrix elements in the MOM is 1760X1760 for SPS and 1170X1170 for PB feed models.

In Sec.4.4.1, the measured transmission response of an array of metallic dipoles backed by the conical dielectric substrate surface will be compared with the predictions using the FC computer model for the dielectric loaded EFIE formulation. Predictions with modal analysis for a planar infinite array will also be used to check the validity of the dielectric loading. In Sec.4.4.2 the results of the radiation patterns will be discussed. The SPS and PB feed models have been used to compute the fields radiated from the feed aperture.

4.4.1 Transmission response

The predicted transmitted response of the conical FSS is obtained from the total radiated field from the FSS normalised with respect to the radiated field from the feed (Eq.(4.27)) at boresight. The transmitted response was estimated using the modal analysis for an infinite array of the same lattice and element geometry, at TE and TM incidence at 45 degrees. TE is defined as the electric field polarised along the dipole axis and TM with magnetic field orthogonal to it as shown in Fig.4.8a and Fig. 4.8b. respectively. The dielectric cladding for each cylindrical dipole in the conical array FSS is assumed to be the same thickness as the substrate of the planar array. Fig.4.9 shows a comparion of the measured results with the predicted transmission responses from the SPS and PB feed model and the modal analysis. Both feed models predicted a reflection band centre at 13 GHz with the SPS predicting a sharper null up to -19.0 dB. The measured band centre, however, is located at 12.4 GHz a shift of about 0.6 GHz from the predictions with a null of about -12.0 dB. For the planar array, the TE incidence has predicted the band centre at 12.6 GHz which is closer to the measured value whilst TM incidence gives 13.6 GHz. It also predicts a sharper null about -35 dB because the planar array is supposed to be infinite. Therefore, it appears that the curved FSS (FC model) gives an average band centre location between the TE and TM incidences of the infinite planar FSS. A slight kink is observed in the measured response at 12.9 GHz which was predicted by the SPS at 13.6 GHz although the effect is more acute. The quasi-static EFIE was also checked for a free standing conical array using the SPS feed model. Fig.4.10 shows how the predicted band centre is shifted by about 1 GHz from about 14 GHz to 13 GHz of the dielectric case. The predicted transmission response is also shallower and broader than the dielectric case. This confirmed that the quasi static approximation can be used to load the EFIE in order to shift the resonant frequency.

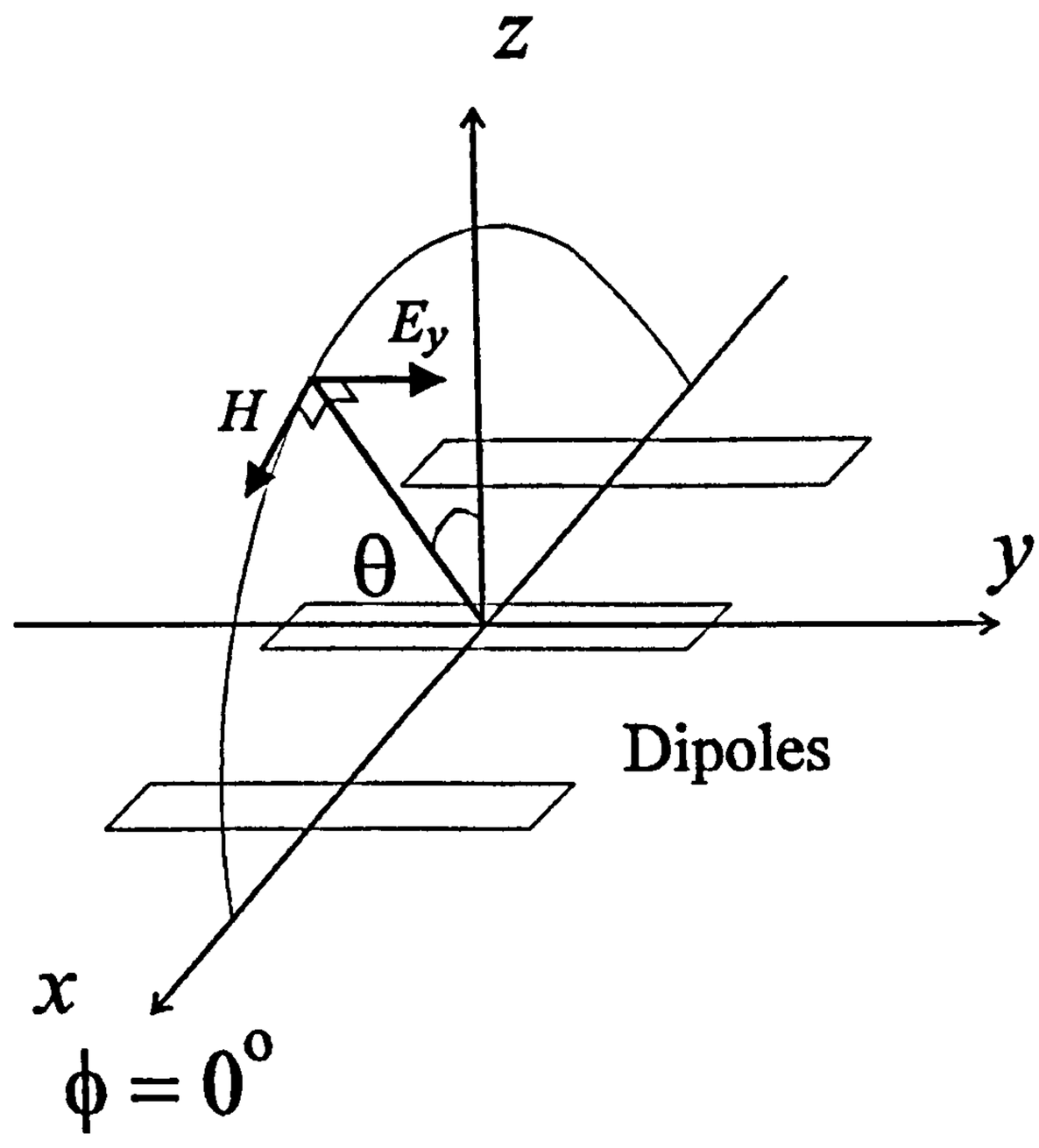

Fig.4.8a TE incidence.

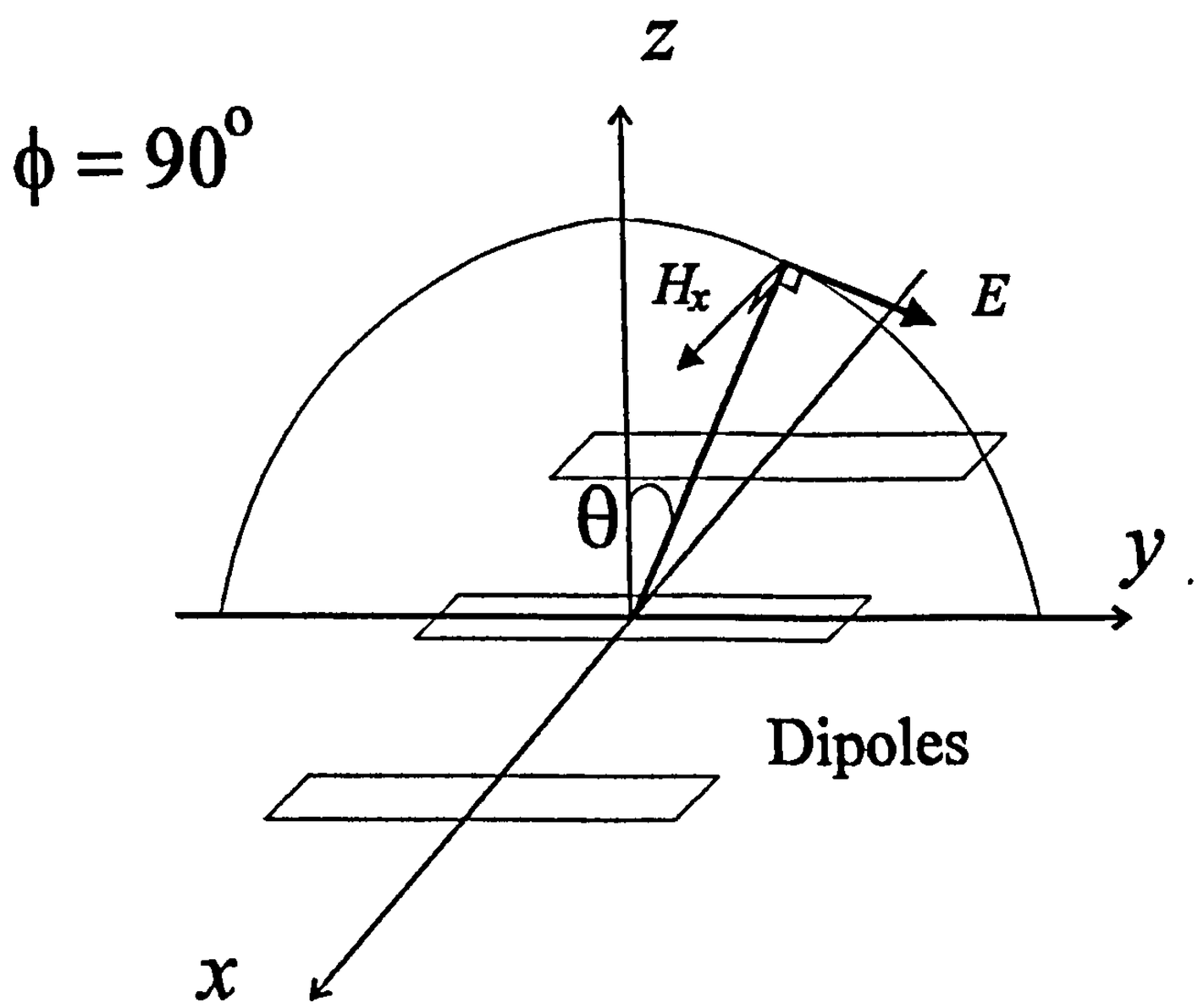

Fig.4.8b TM incidence.

Predictions from the FC model using the SPS feed modelling has been assessed for various thickness of the dielectric. Fig.4.11 shows a shift in resonant frequency from 13.0 GHz, 12.8 GHz to 12.6 GHz as the thickness increases from 0.1mm, 0.15mm to 0.2 mm. The resonance also tends to get shallower as the thickness increases. It appears from the observations, that an equivalent thickness of 0.15 mm gives the best predicted transmission response although there is still a discrepancy of 0.4 GHz in the frequency shift. This could possibly be due to the dielectric regions in the unit cell on the curved surface which have not been taken into consideration. The quasi-static model only accounts for loading from the thickness of the dielectric substrate.

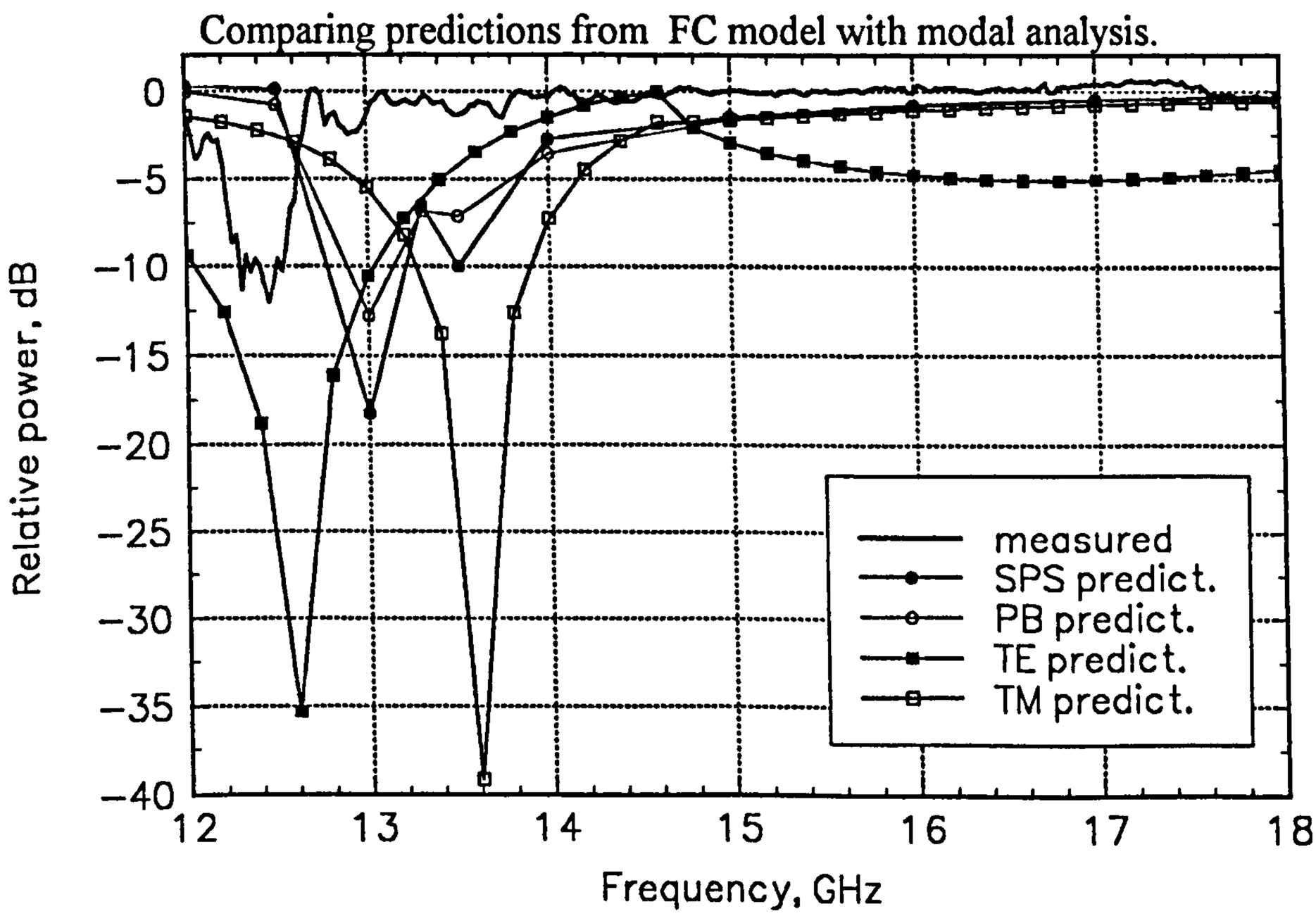

Fig.4.9 Passband response of the conical FSS.

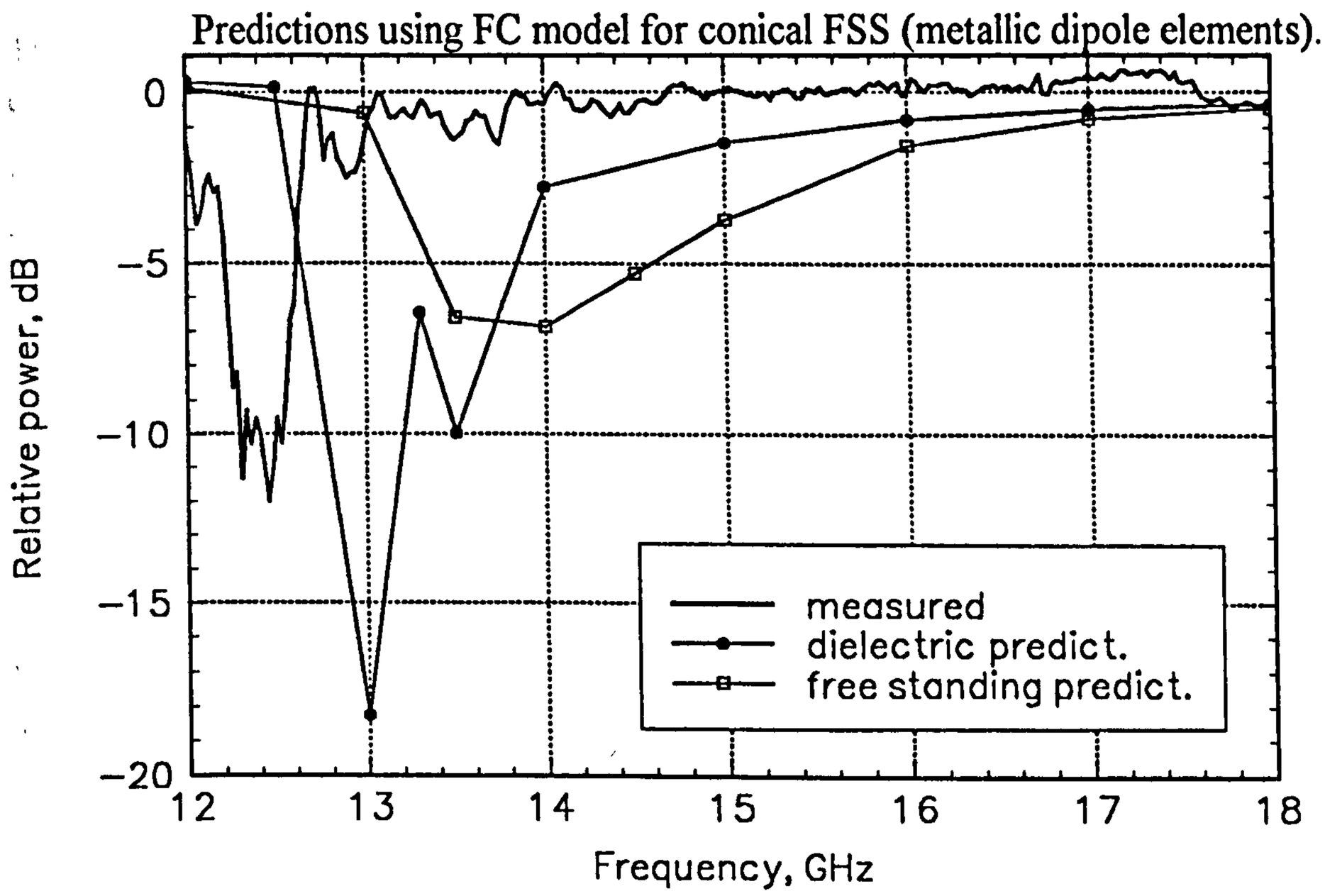

Fig.4.10 Passband response of the conical FSS using the SPS feed model.

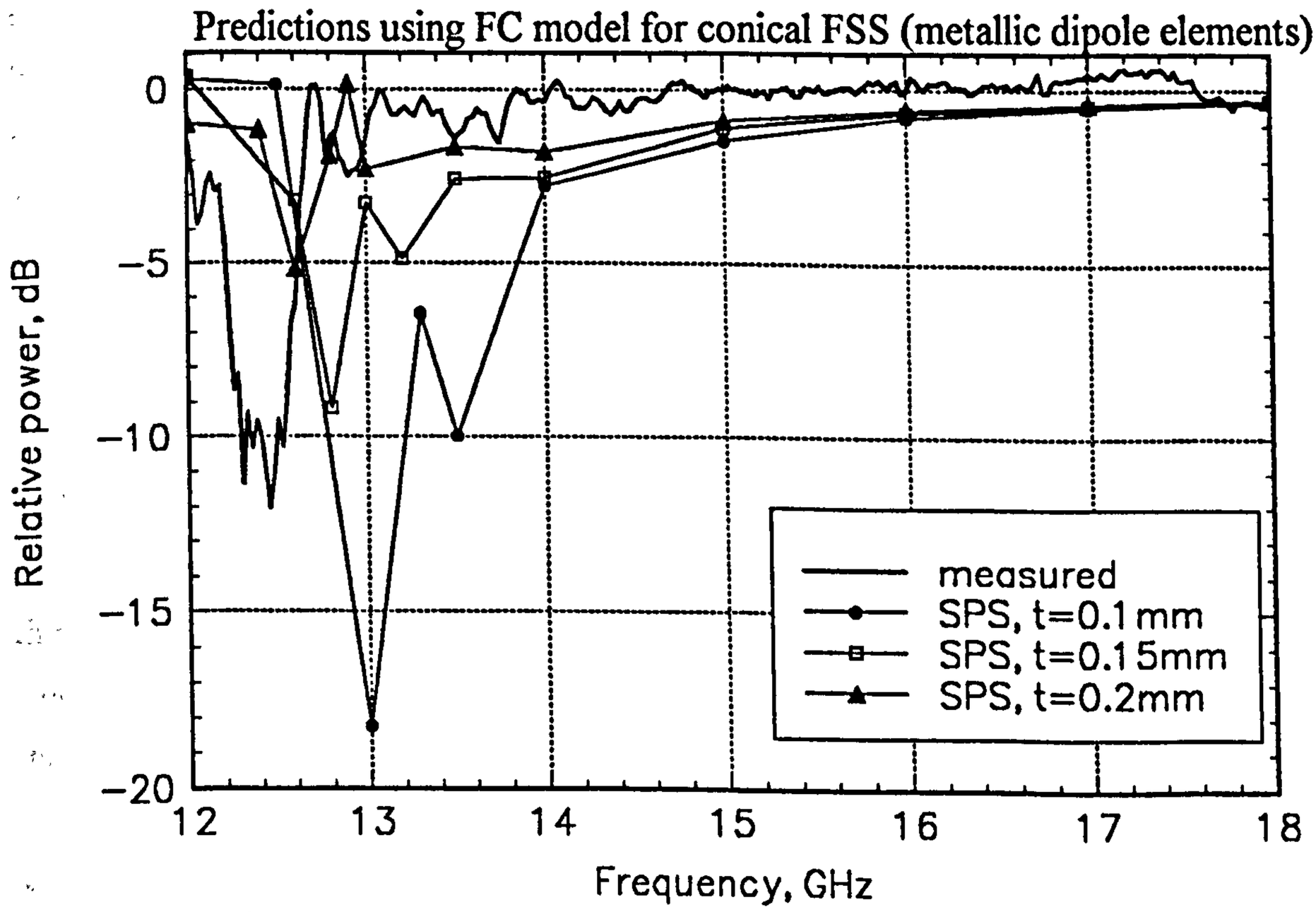

Fig.4.11 Passband response for various dielectric thickness.

4.4.2 Radiation patterns

The following discussion is devoted to the radiation patterns in the transmission band because of their importance in radome designs. The measured reflection band is in the range from about 12.2 to 12.6 GHz as shown in Fig.4.11. The FC model is used to predict the far field radiation pattern for a conical array of metallic dipole elements.

4.4.2.1 H-plane

The H-plane copolar patterns in the transmission band at 12, 15 and 17 GHz can be found in Fig.4.12a to Fig.4.14a with SPS predictions and Fig. 4.12b to Fig.4.14b with PB predictions. It can be seen below the reflection band at 12 GHz, when the FSS is transmitting, the main lobe of the measured feed pattern lobe has been distorted. The SPS and PB predictions also show this distortion and the rise in the sidelobes at $\pm 30^{o}$ scan.

Above the reflection band at 15 and 17 GHz, there is very little distortion in the main lobe of the feed pattern although the sidelobe levels tend to increase in the presence of the conical FSS. It seems to indicate that the effect of scattering within the metallic FSS has been reduced when the frequency is above the resonance region. This is confirmed by both SPS and PB predictions. There is slight discrepancy in the boresight losses about 1.5 dB in the predictions at 15 GHz. The cross polar levels in the H-plane of the conical FSS in the transmission band are very low, about -40 dB which is confirmed by both feed models.

Although the models are not able to locate the measured band centre at 12.4 GHz of the FSS, the resonant pattern can be compared with the predicted copolar patterns at 13 GHz (the band centre for the SPS and PB feed models) as illustrated in Fig.4.15a and 4.15b. The measured results seem to suggest that the fields are scattered to the side walls at about $\pm 12^{o}$ scan, giving a small null at the boresight. It would appear that the electromagnetic energy at the boresight is diverted to the side walls at the resonant frequency. The PB shows better agreement on boresight with side lobes higher than the measurements.

4.4.2.2 E-plane

The E-plane copolar patterns in the transmission band at 12, 15 and 17 GHz are shown in Fig.4.16a to Fig.4.18a with SPS predictions and Fig. 4.16b to Fig.4.18b with PB predictions. At 12 GHz, the main lobe of the measured feed pattern has been made reduced by the presence of the conical FSS. The SPS also predicted a narrower pattern but higher side lobes at $\pm 25^{o}$ scan. The nulls are predicted quite accurately at

$\pm 20^{o}$. The PB model predictions are poorer with a narrower main lobe, and the first pair of nulls are located at $\pm 18^{o}$.

At 15 and 17 GHz, a minor 'shoulder' distortion appears in the main lobe of the feed pattern at $\pm 15^{o}$ with the inclusion of the conical FSS. On the whole, there is lesser scattering within the metallic FSS when the frequency is above the resonance region. Broadly speaking, there is fairly good agreement with both SPS and PB predictions. The cross polar levels in the E-plane of the conical FSS in the transmission band are very low, about -40 dB which is confirmed by both feed models.

The measured copolar pattern at 12.4 GHz, the reflected band centre of the FSS, is compared with the predicted patterns at 13 GHz, the band centre for the SPS and PB feed models, as illustrated in Fig.4.19a and Fig.4.19b. The measured results seems to show that the fields are scattered to the side walls at about $\pm 10^{o}$ scan, giving a small null at the boresight with more energy diverted to the right side. This could be due to the slight misalignment of the feed with respect to the axis of the conical FSS. The PB model seems to show a better prediction compared to the SPS model.

4.4.2.3 45° plane

The 45° copolar patterns show similar trends to the H-plane at the frequency band as mentioned above. Representative copolar results at 17 GHz are compared with the SPS feed model in Fig.4.20a and with the PB model in Fig.4.20b respectively. It is expected that the measured crosspolar levels in the transmission band are higher. Peak crosspolar levels of up to -26 dB at $\pm 12^{o}$ were measured. The SPS predicts slightly higher sidelobe levels generally as compared to the PB model (Fig.4.21a and Fig.4.21b).

Thus, from this above discussions, the predictions from the computer model gave generally good agreements with measured patterns in the transmission band. Both the SPS and PB feed models using the quasi static EFIE approximation gave comparable predictions in the radiation patterns for the principal and 45° planes. The FSS and feed interaction at the transmission band is less acute as compared with those in the reflection band, judging from the copolar patterns. The quasi-static EFIE could account for the shift in resonant frequency which is due to the presence of the substrate. The predicted shift however is less than the measured value because only the thickness of the dielectric substrate is taken into account in the quasi static approximation. The dielectric region in the unit cell area has been neglected in this simple model.

4.5 Conclusions

A quasi-static formulation of the EFIE using MOM has been used to account for the coupling between all the metallic FSS elements on a small cone. Two mathematical techniques were used to solve the matrix system from the MOM method of solution. For a free standing conical FSS, it was discovered that the iterative CG method is faster than the conventional elimination method if the computer RAM is sufficient to cope with the size of the impedance matrix. Moreover, the computation of the CG algorithm is more rapid for frequencies away from the resonant frequency, but the elimination method maintains constant computation time across the frequency band. The speed of computation for both methods is also machine dependent. For a practical conical FSS, however, it is required to model the dielectric backing using a quasi static approximation. Due to computer round-off errors in the calculation of coupling element in the matrix, the CG method did not converge. Thus the elimination method was adopted in this case.

The quasi-static approximation with the EFIE formulation has been applied in the computer model and solved for a conical FSS with metallic dipole elements using MOM. The FC computer model is able to predict the radiation patterns in the transmission band of the conical FSS which encloses a corrugated conical feed. Both PB and SPS feed models give comparable predictions, but the reflection band centre is higher than the measured. This could be due to the size of the dielectric region in the unit cell area which is considerably larger than the thickness. It has been shown that by increasing the theoretical thickness, an equivalent frequency shift is produced in the predictions.

Conical FSS (metallic dipole elements) using FC model.

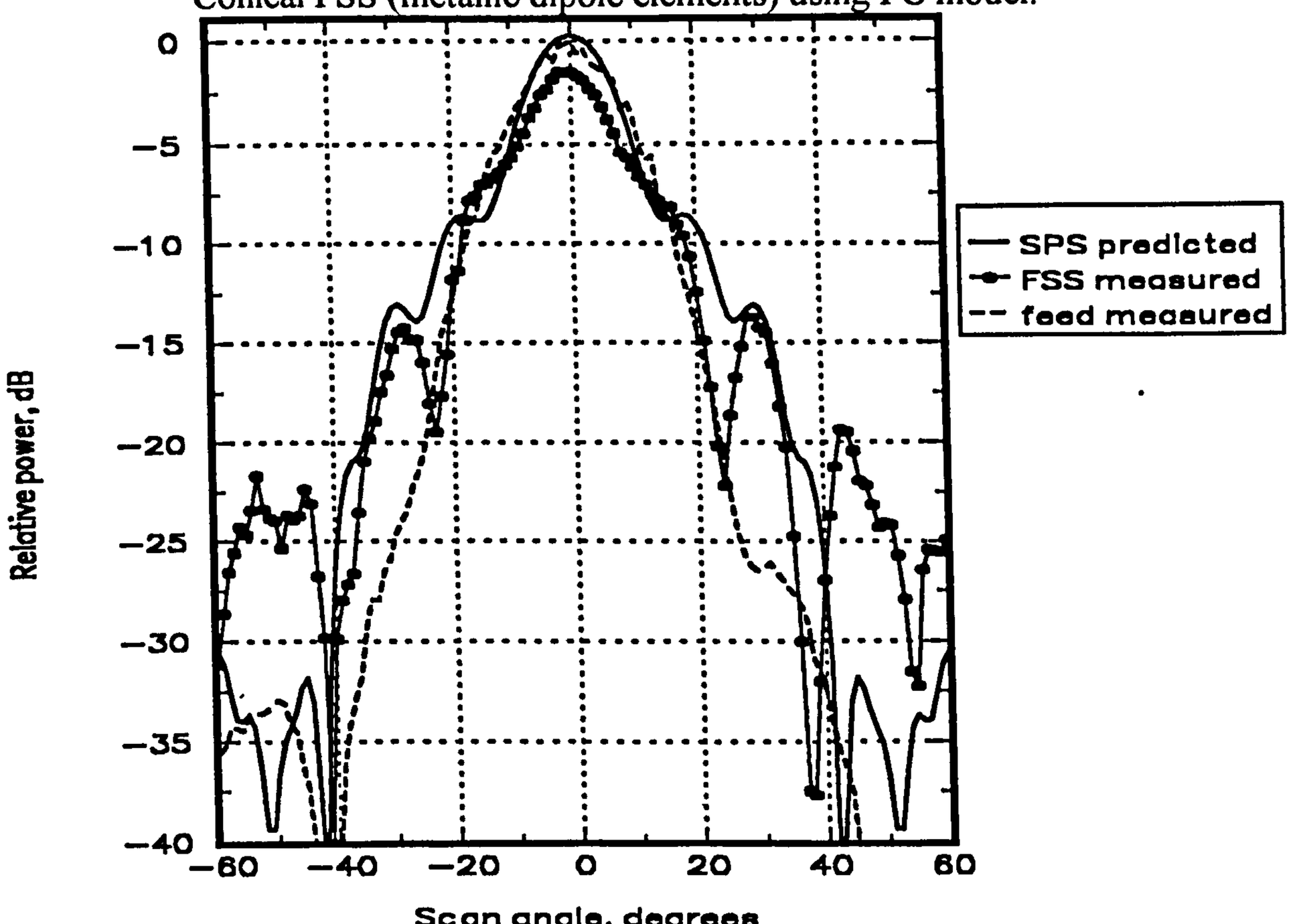

Fig.4.12a H−plane copolar pattern at 12 GHz using the SPS feed model.

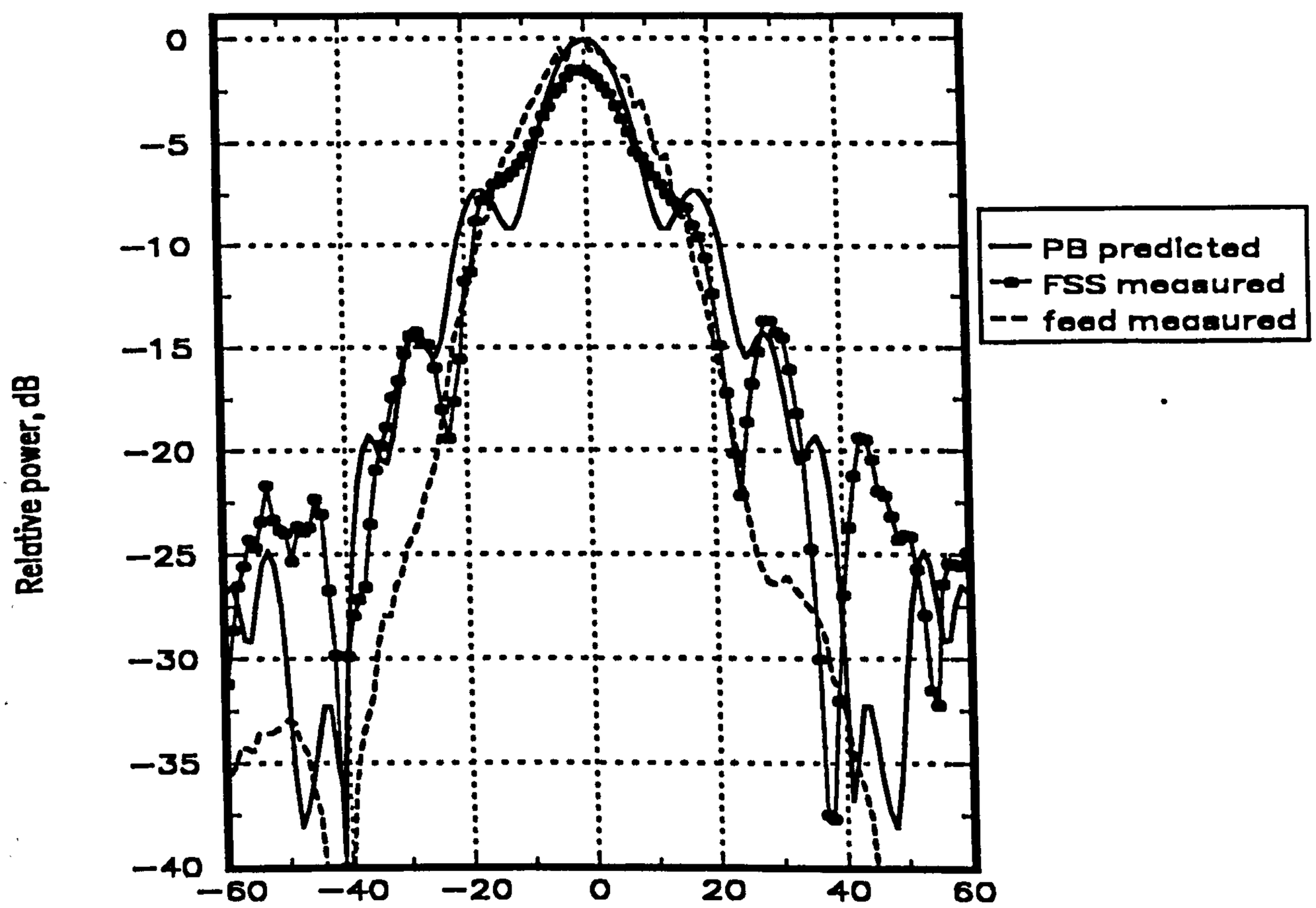

Fig.4.12b H−plane copolar pattern at 12 GHz using the PB feed model.

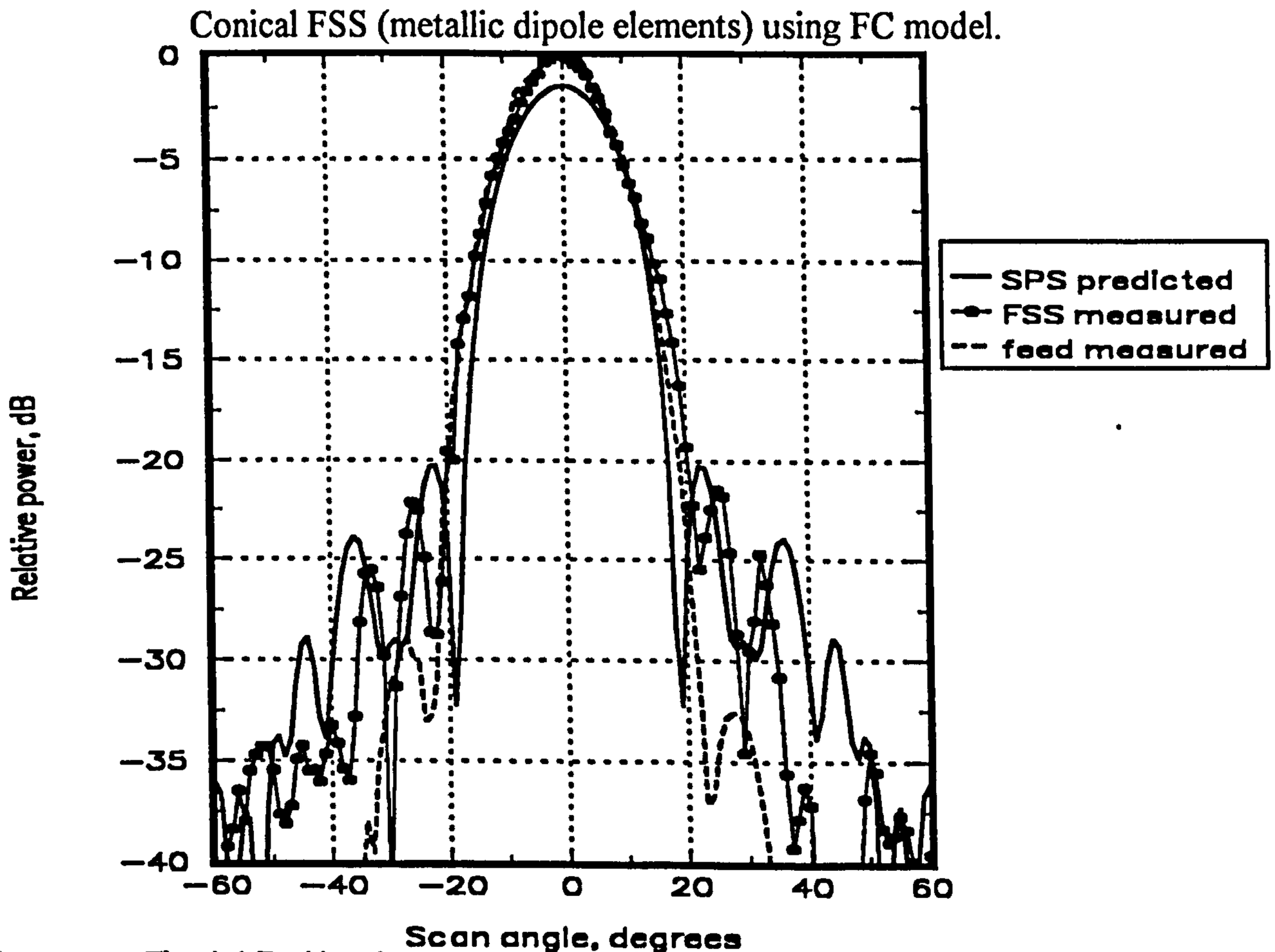

Fig.4.13a H−plane copolar pattern at 15 GHz using the SPS feed model.

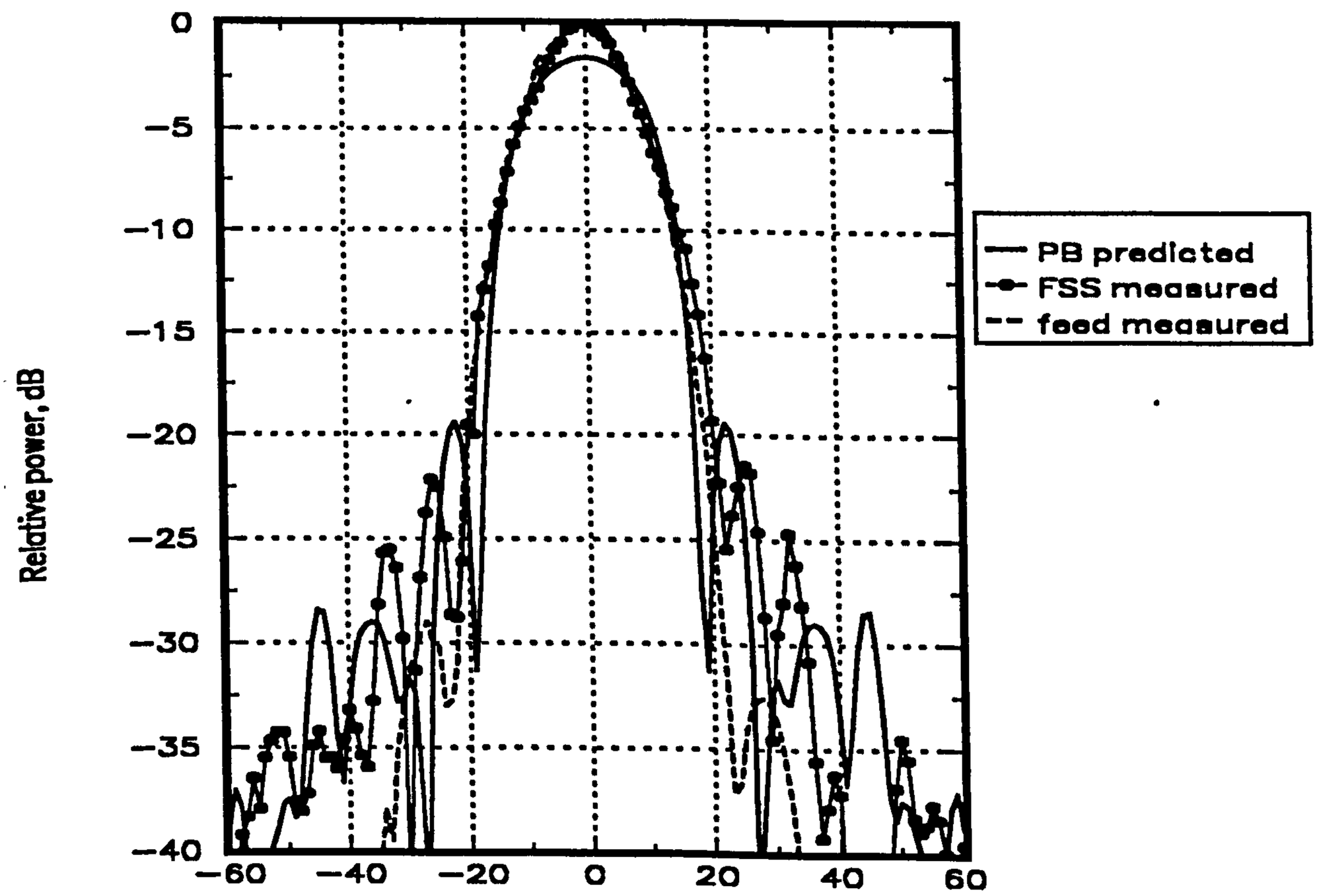

Fig.4.13b H−plane copolar pattern at 15 GHz using the PB feed model.

Conical FSS (metallic dipole elements) using FC model.

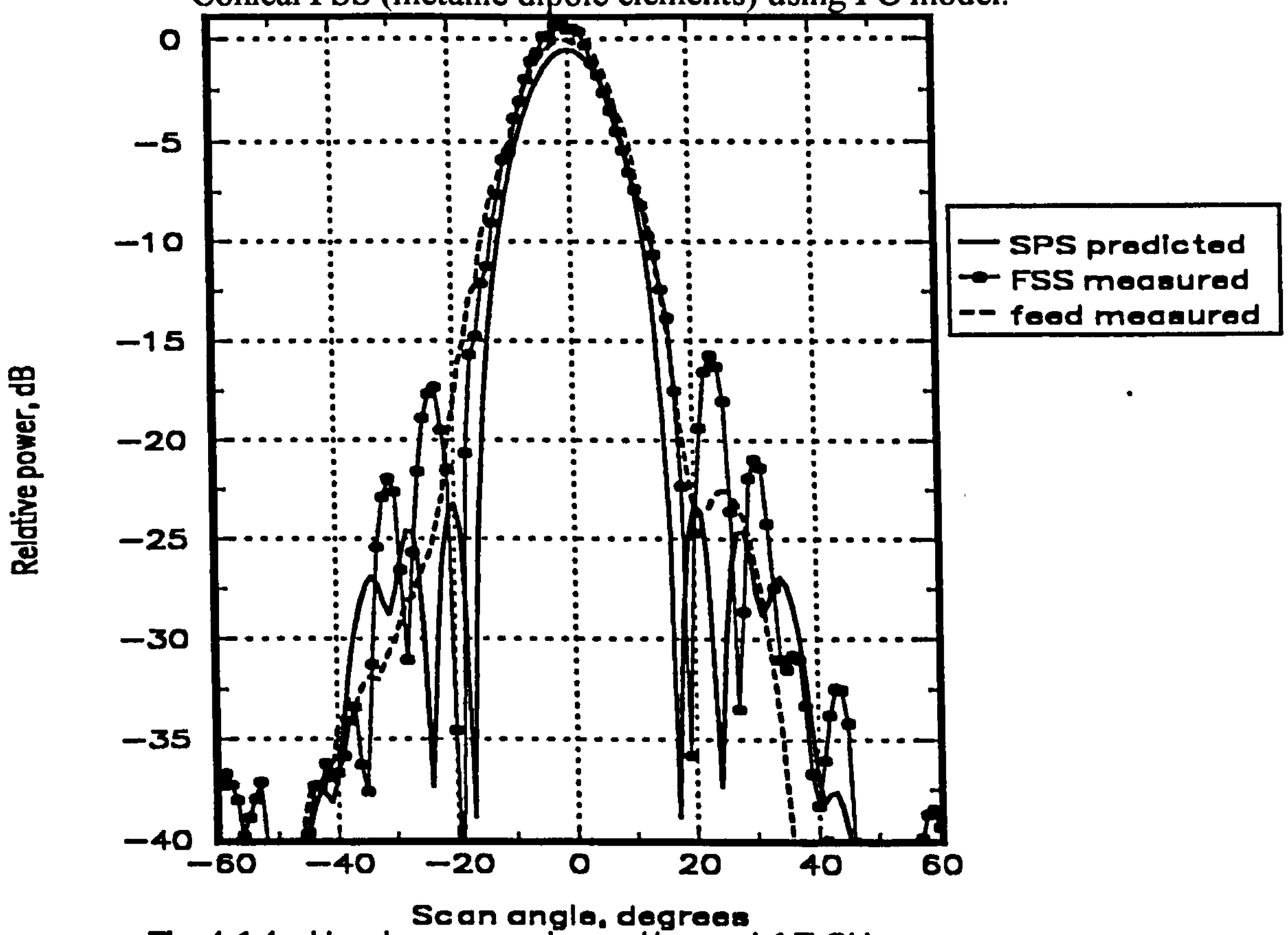

Fig.4.14a H−plane copolar pattern at 17 GHz using the SPS feed model.

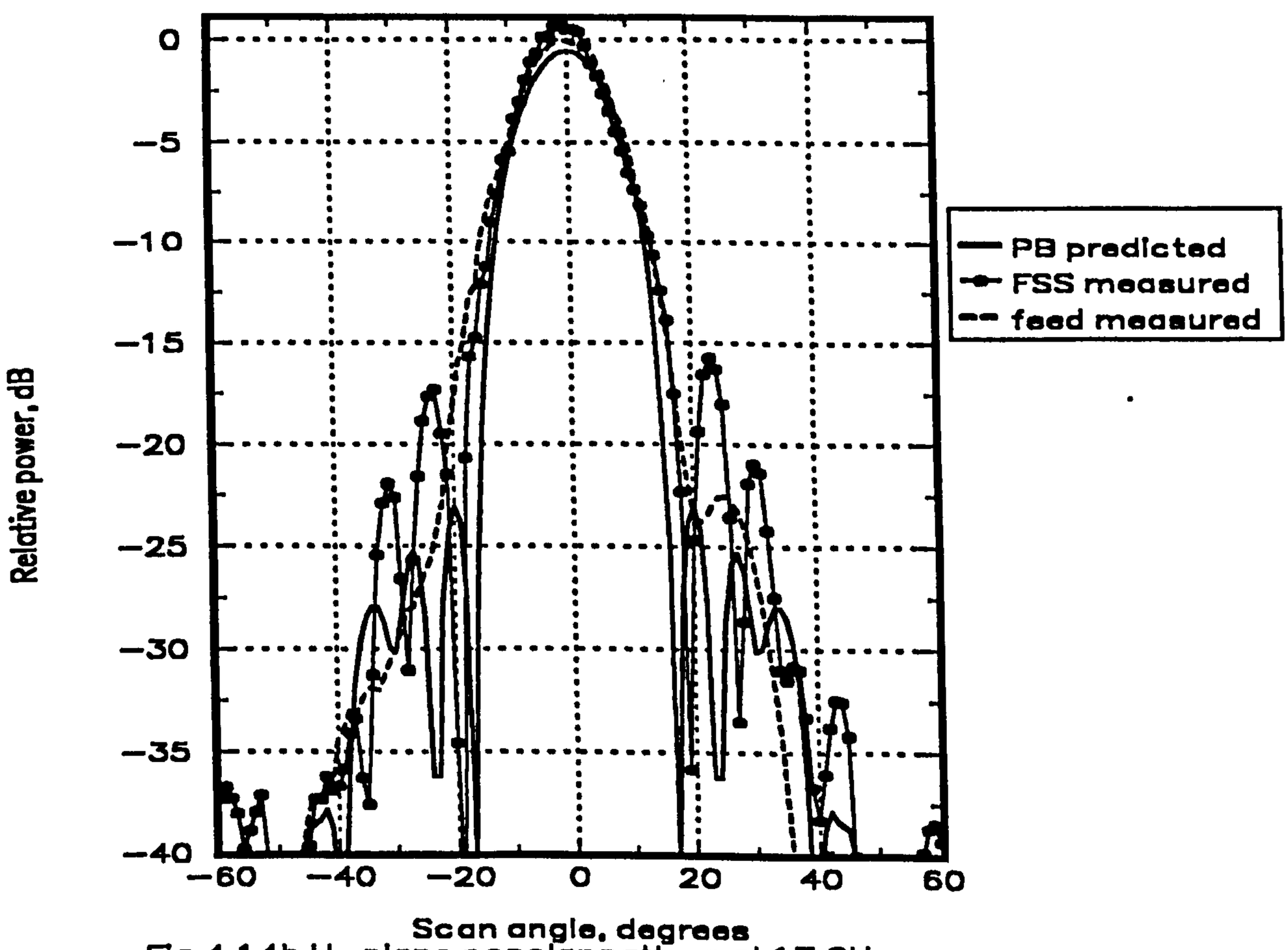

Fig.4.14b H−plane copolar pattern at 17 GHz using the PB feed model.

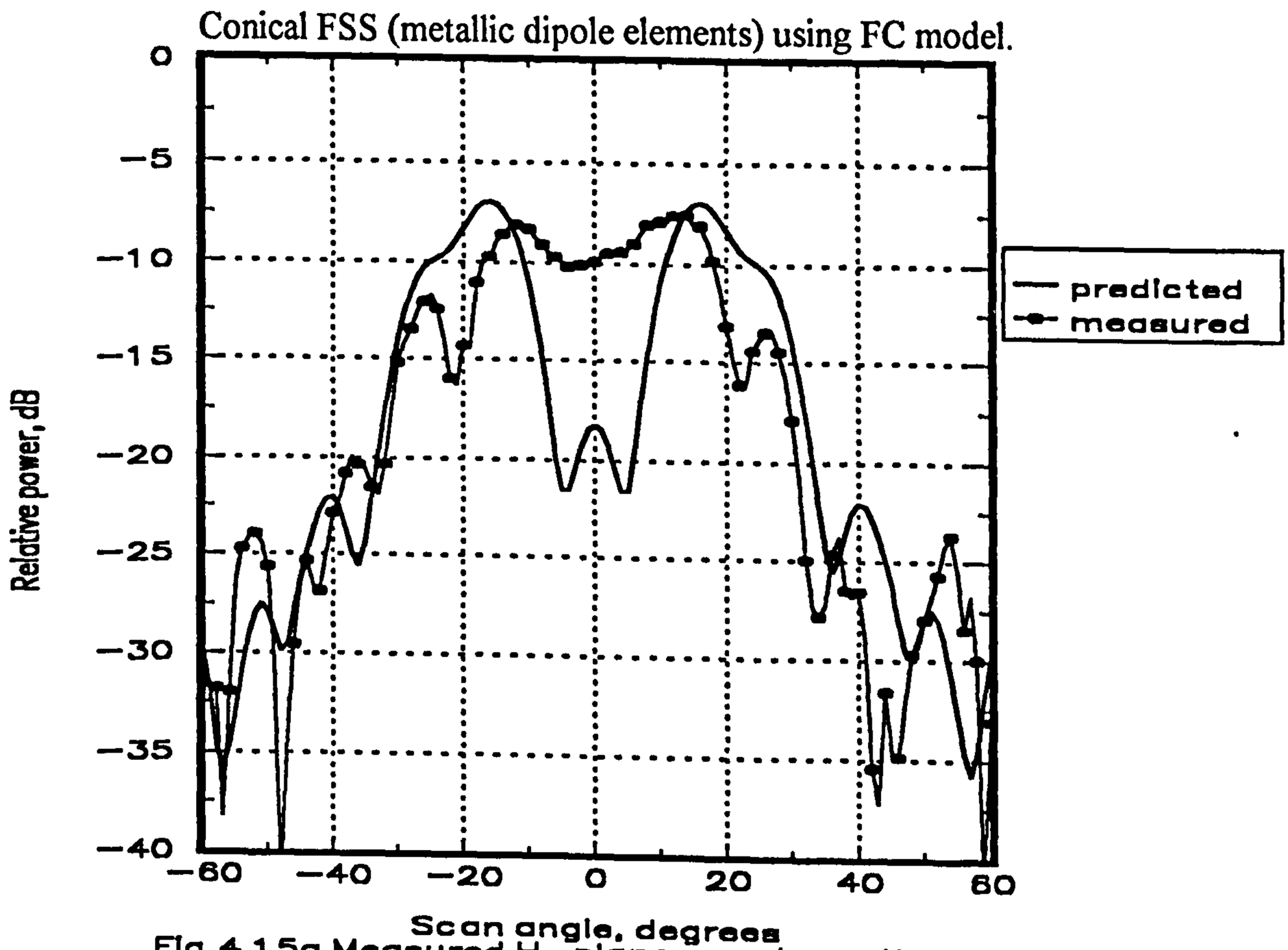

Fig.4.15a Measured H—plane copolar pattern at 12.4 GHz compared with the SPS feed model at 13 GHz.

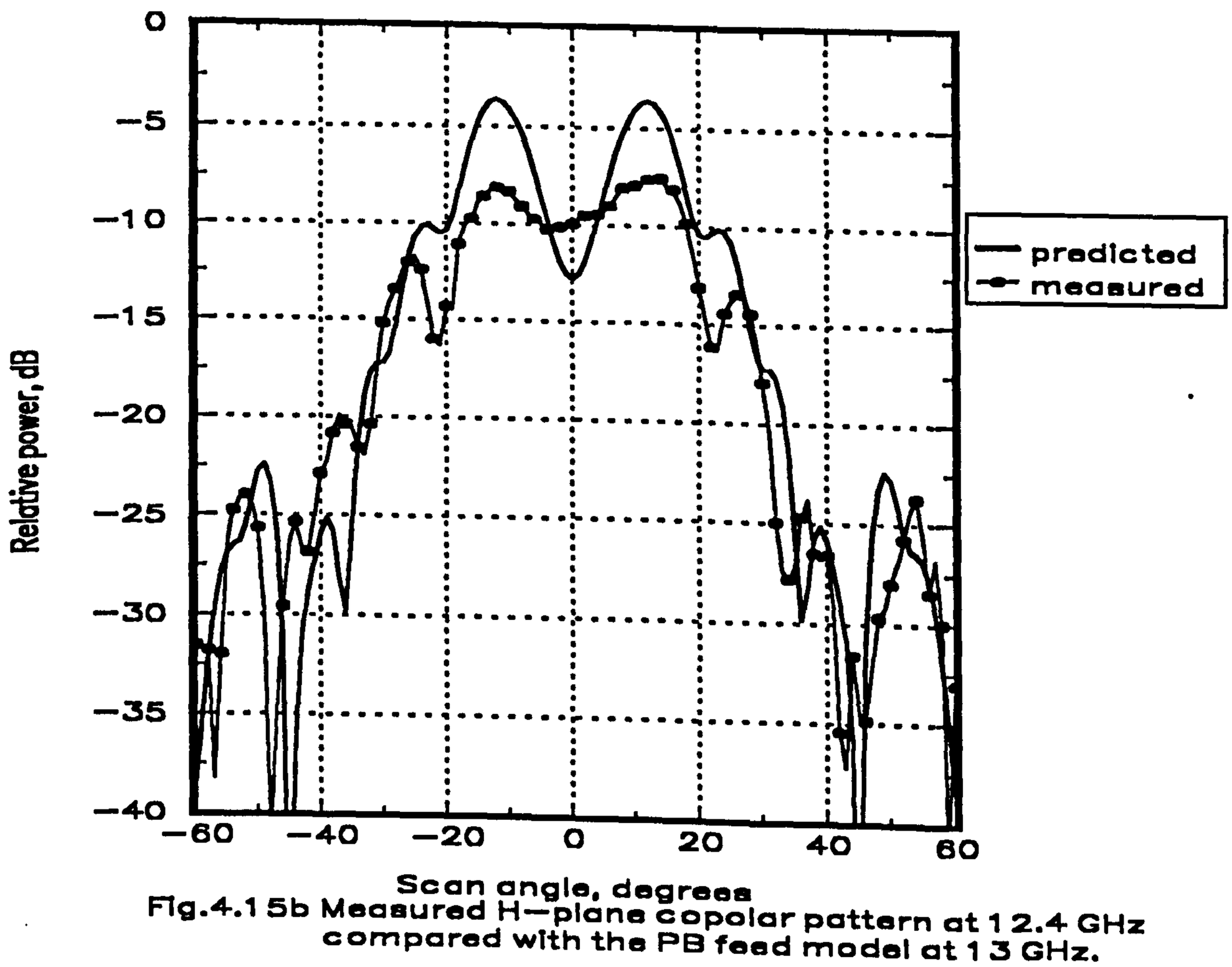

Fig.4.15b Measured H—plane copolar pattern at 12.4 GHz compared with the PB feed model at 13 GHz.

Conical FSS (metallic dipole elements) using FC model.

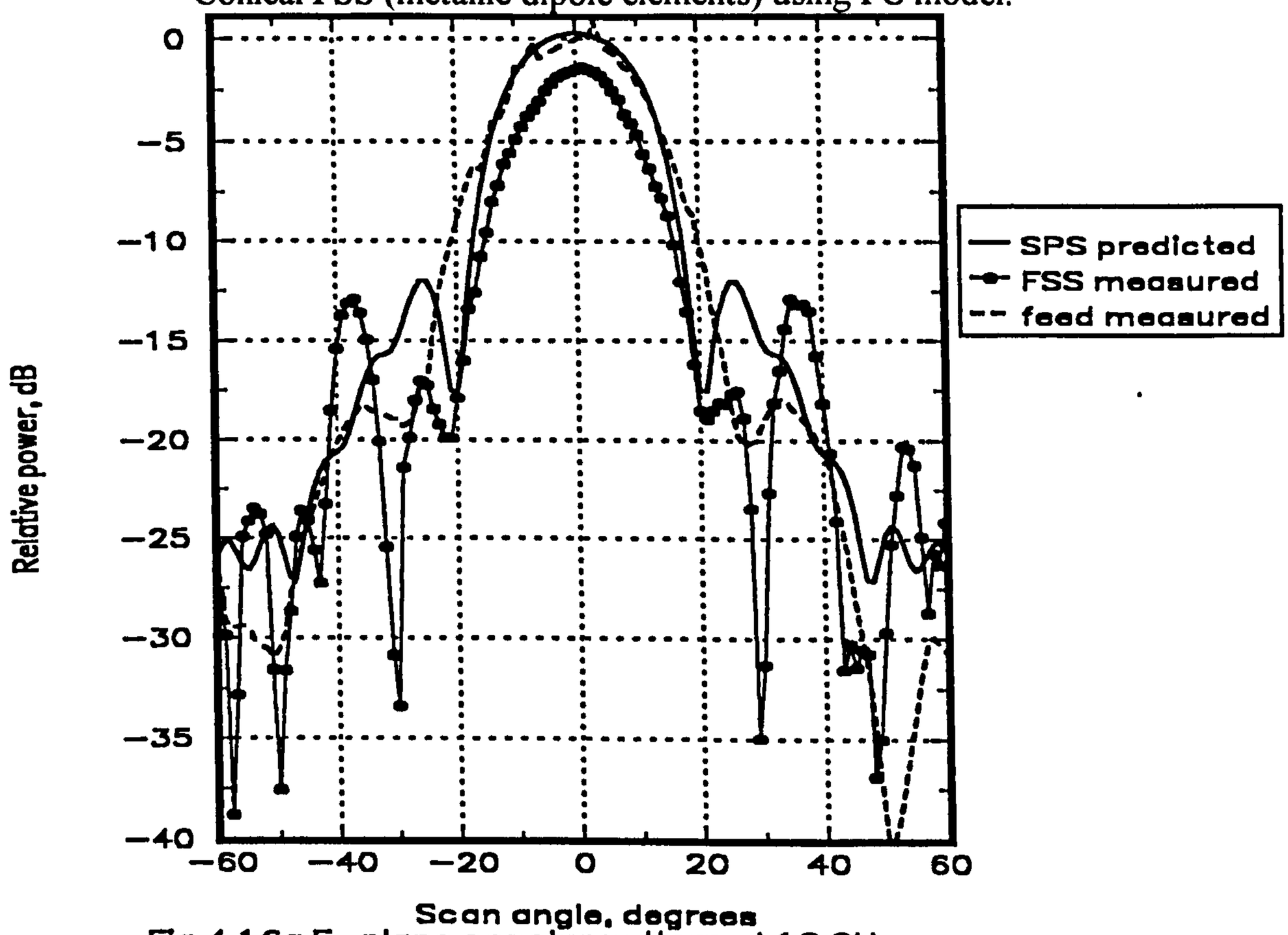

Fig.4.1 6a E—plane copolar pattern at 1 2 GHz using the SPS feed model.

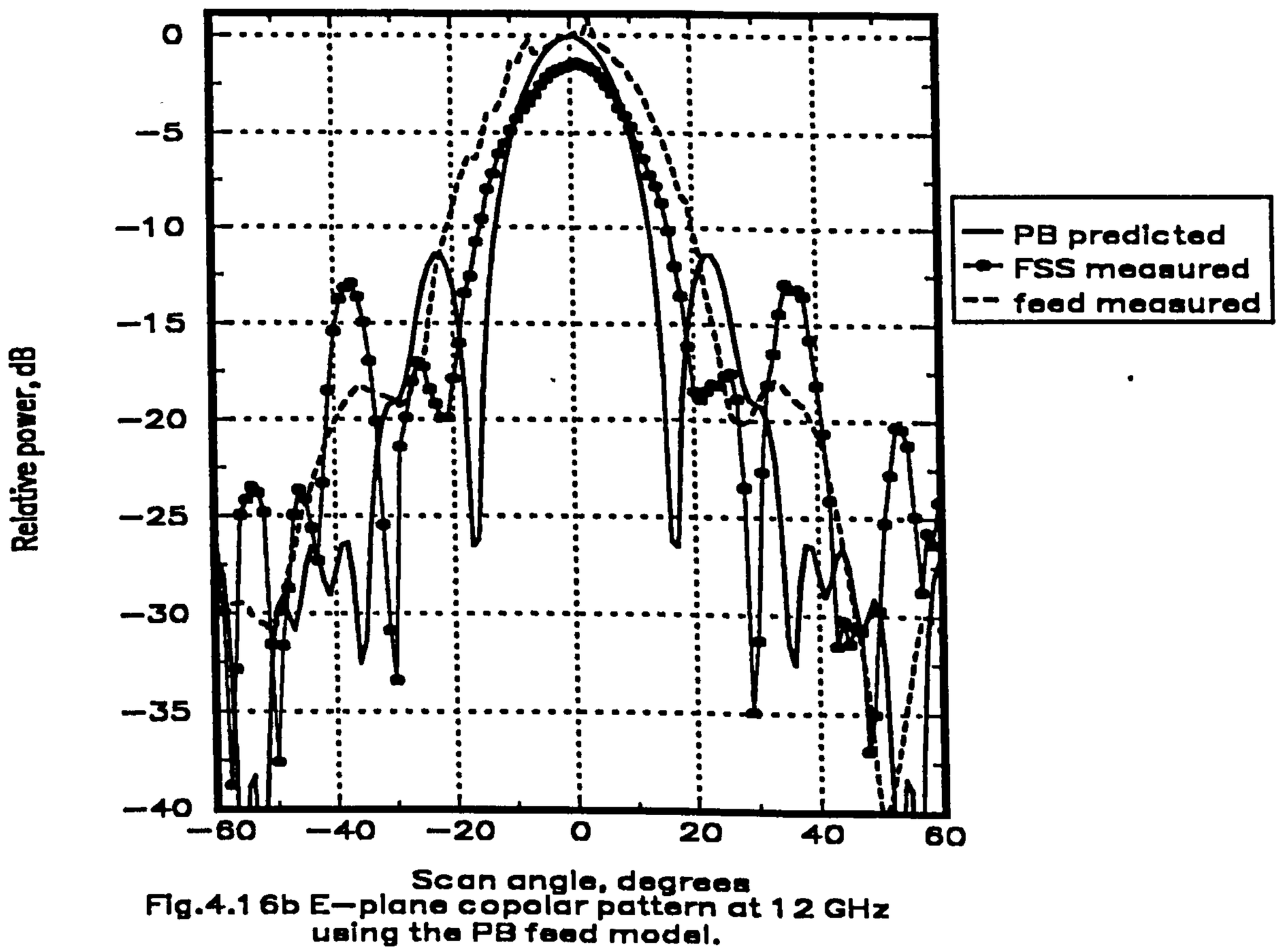

Fig.4.1 6b E—plane copolar pattern at 1 2 GHz using the PB feed model.

Conical FSS (metallic dipole elements) using FC model.

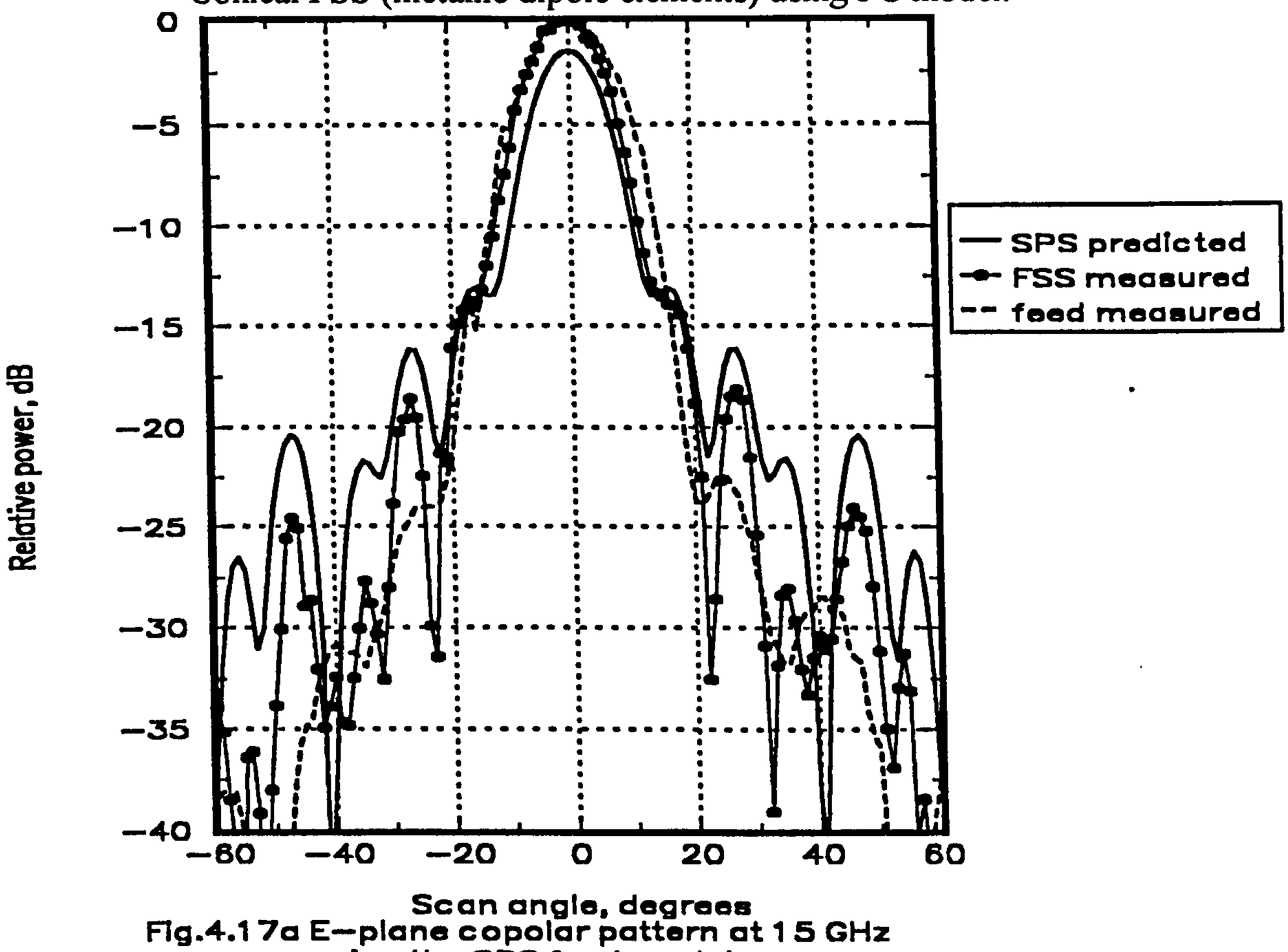

Fig.4.17a E−plane copolar pattern at 1.5 GHz using the SPS feed model.

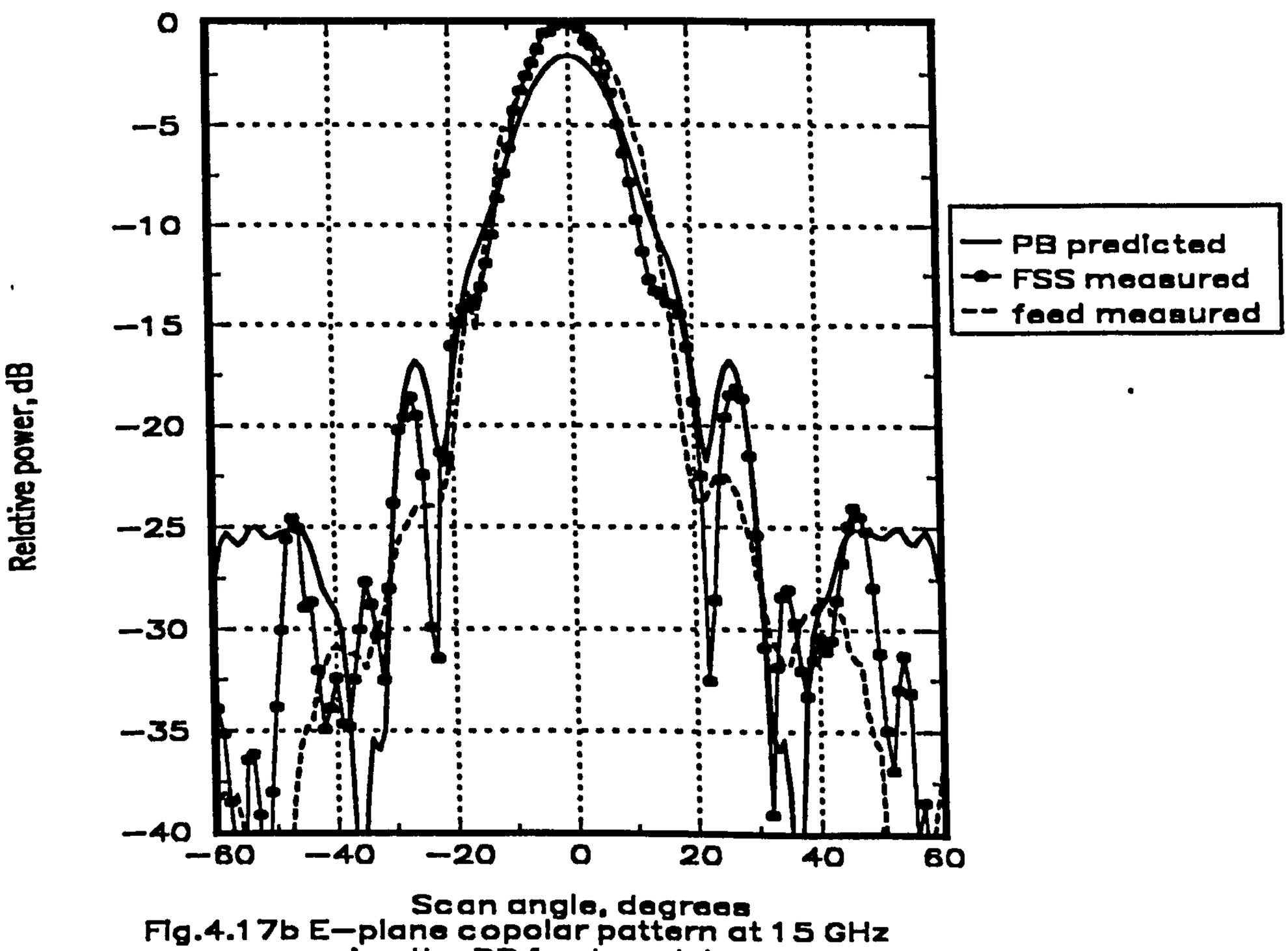

Fig.4.17b E−plane copolar pattern at 1.5 GHz using the PB feed model.

Conical FSS (metallic dipole elements) using FC model.

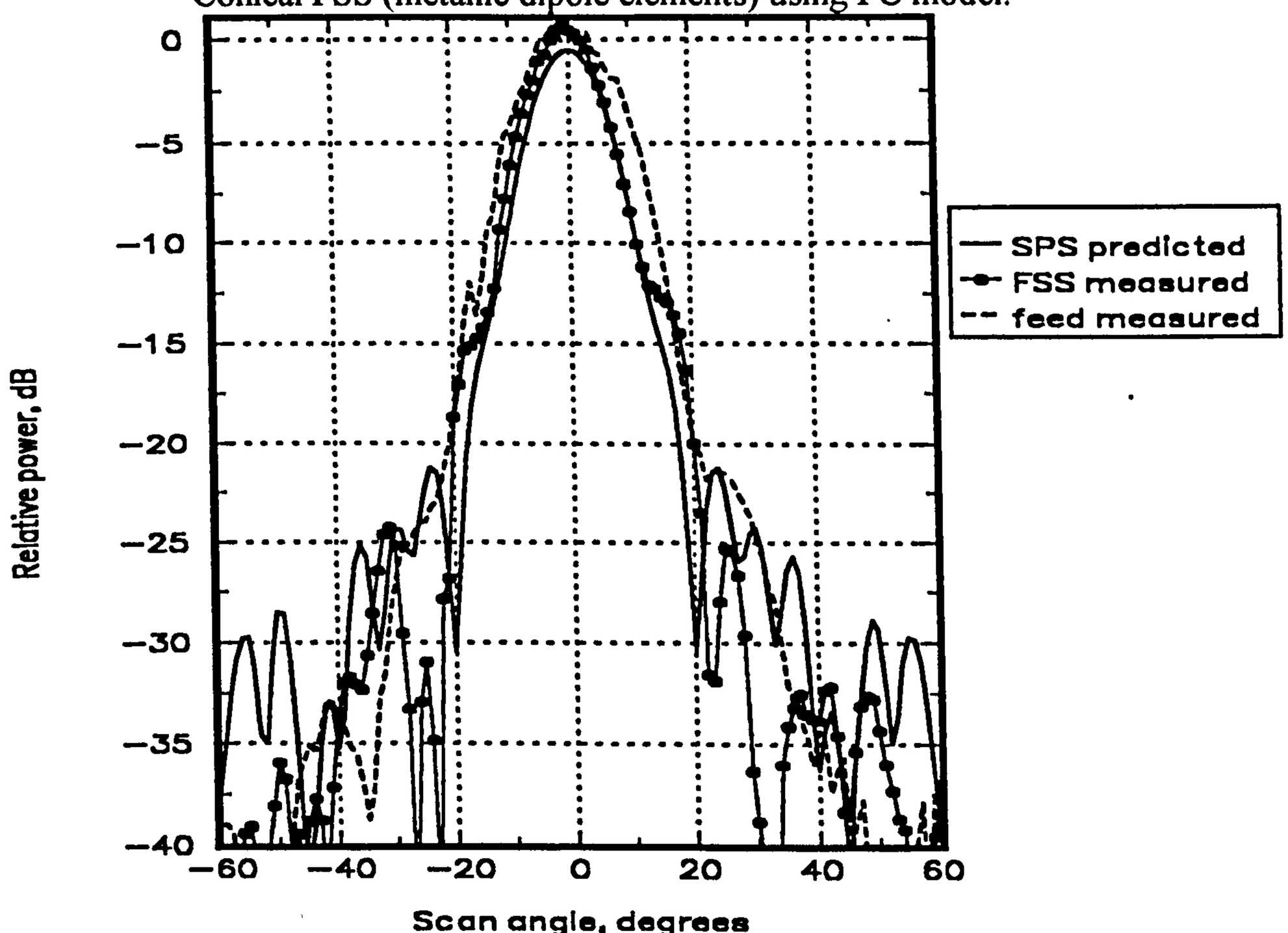

Fig.4.18a E—plane copolar pattern at 17 GHz using the SPS feed model.

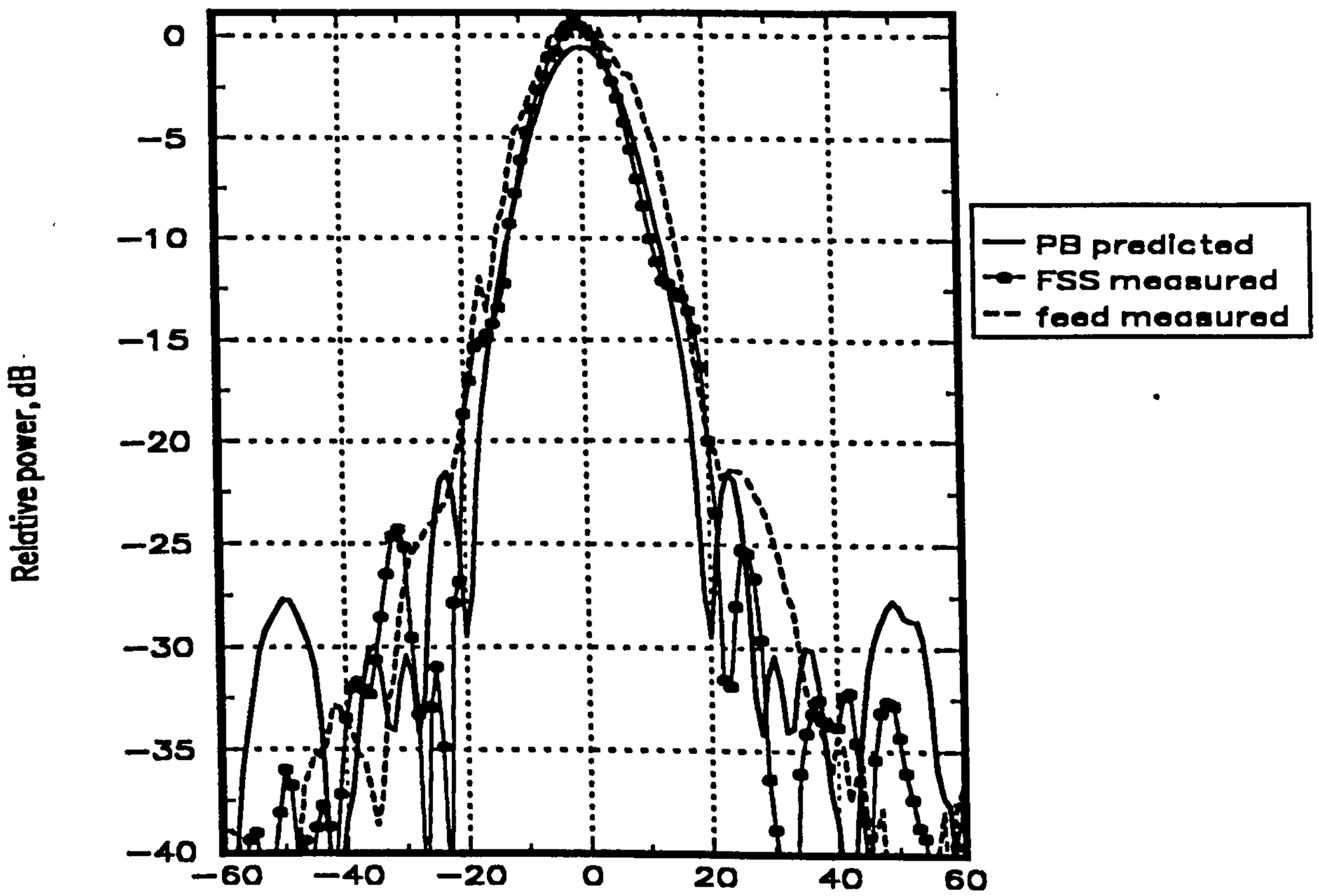

Fig.4.18b E—plane copolar pattern at 17 GHz using the PB feed model.

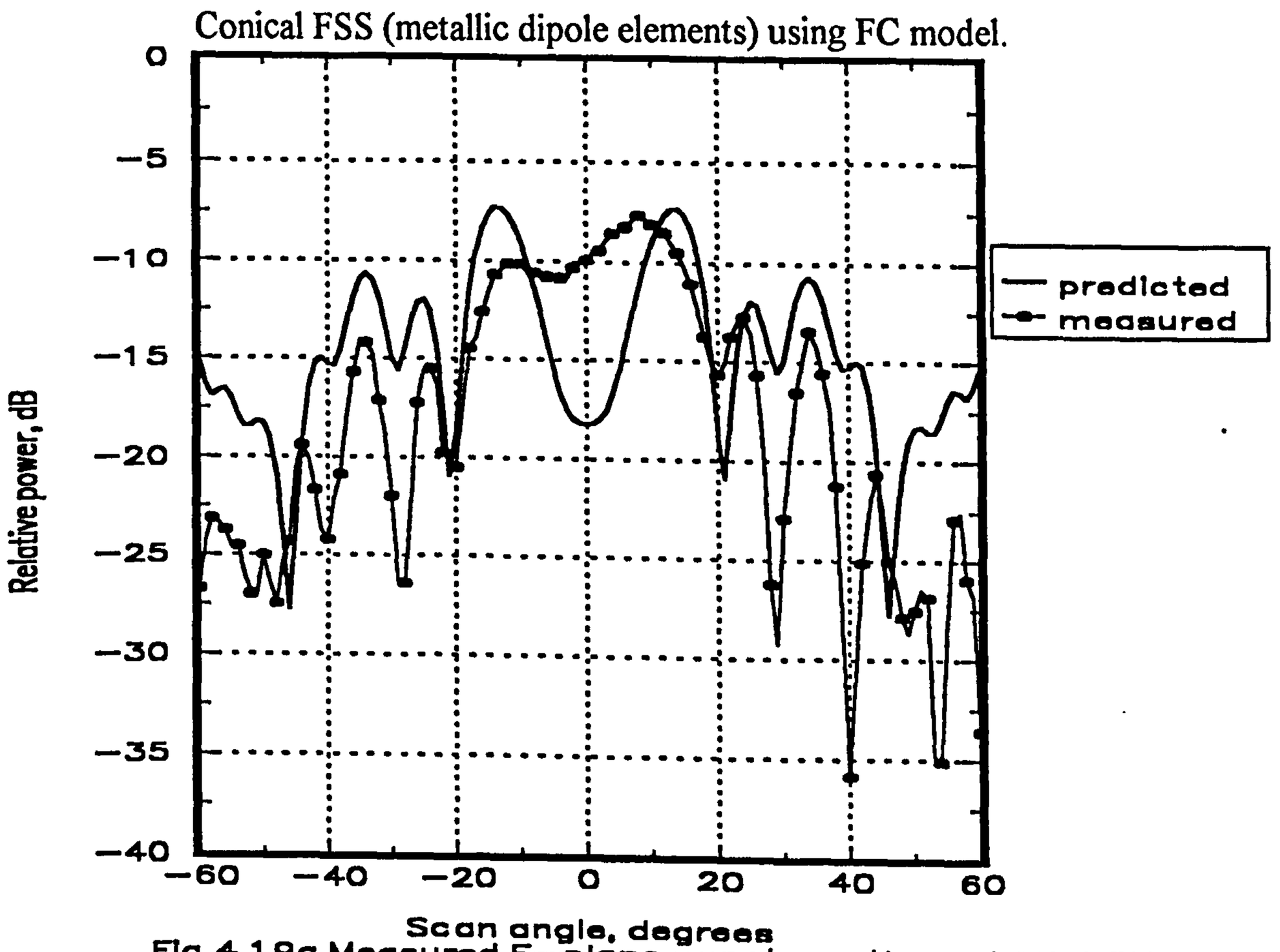

Fig.4.19a Measured E—plane copolar pattern at 12.4 GHz compared with the SPS feed model at 13 GHz.

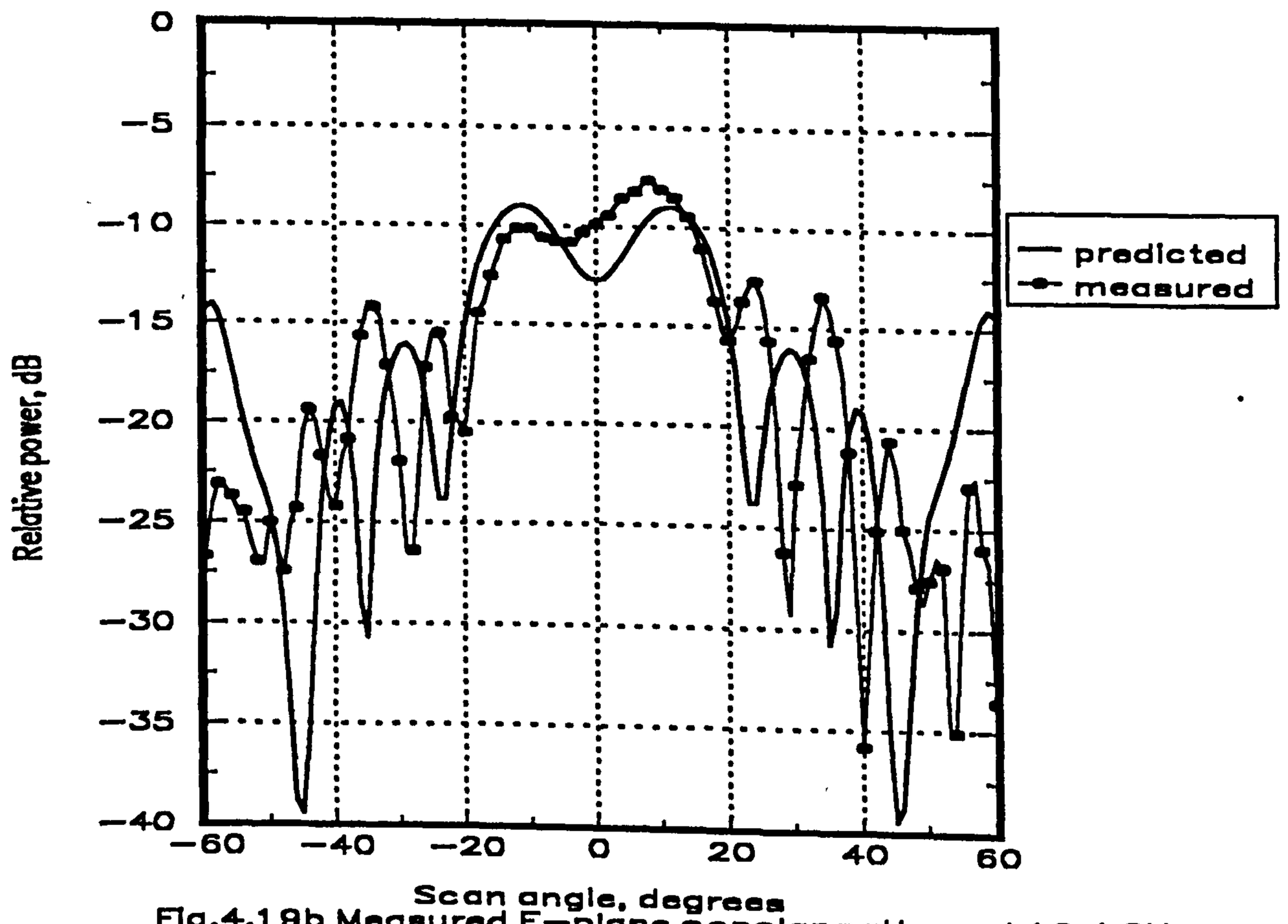

Fig.4.19b Measured E—plane copolar pattern at 12.4 GHz compared with the PB feed model at 13 GHz.

Conical FSS (metallic dipole elements) using FC model.

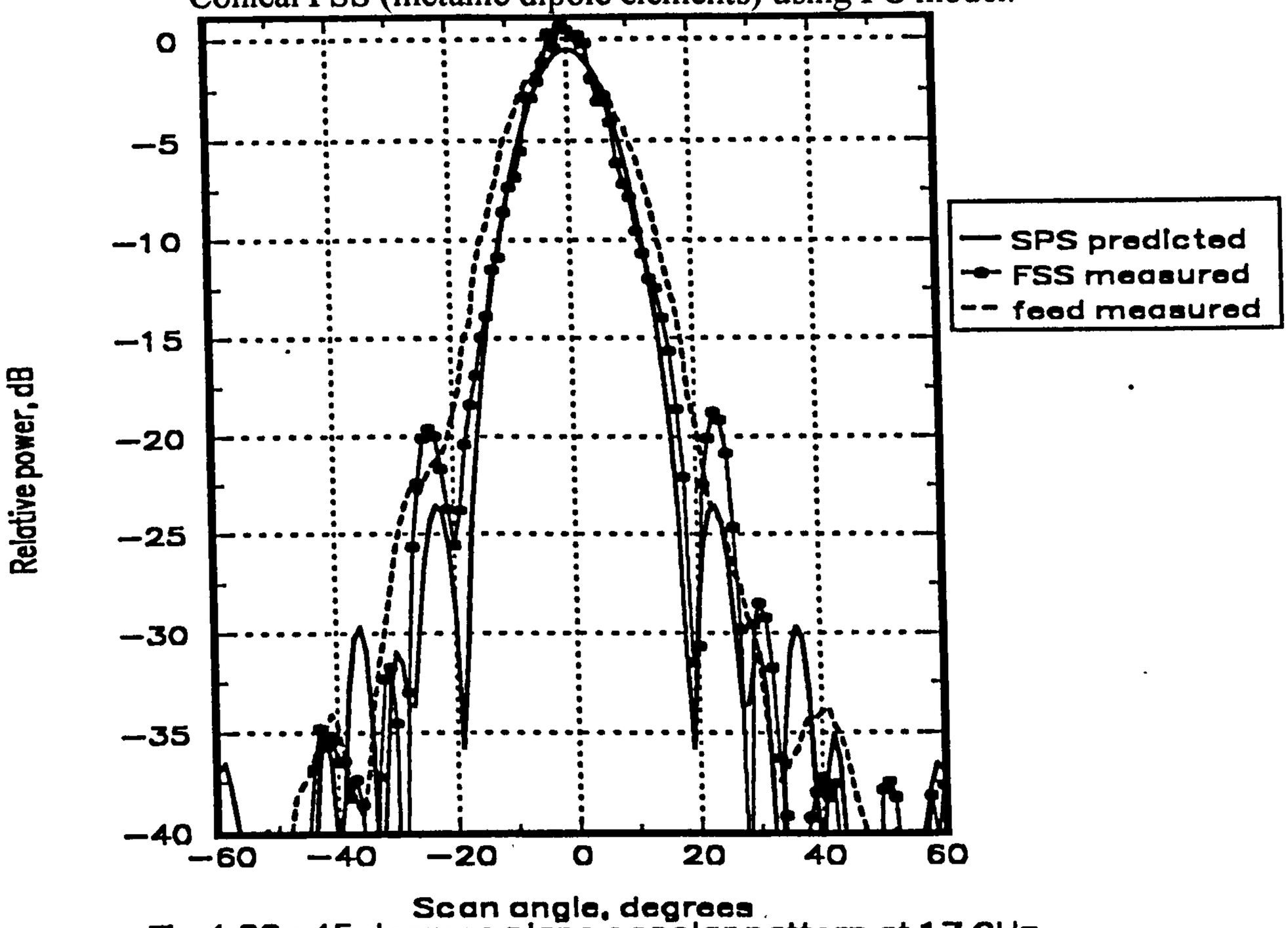

Fig.4.20a 45 degrees plane copolar pattern at 17 GHz using the SPS feed model.

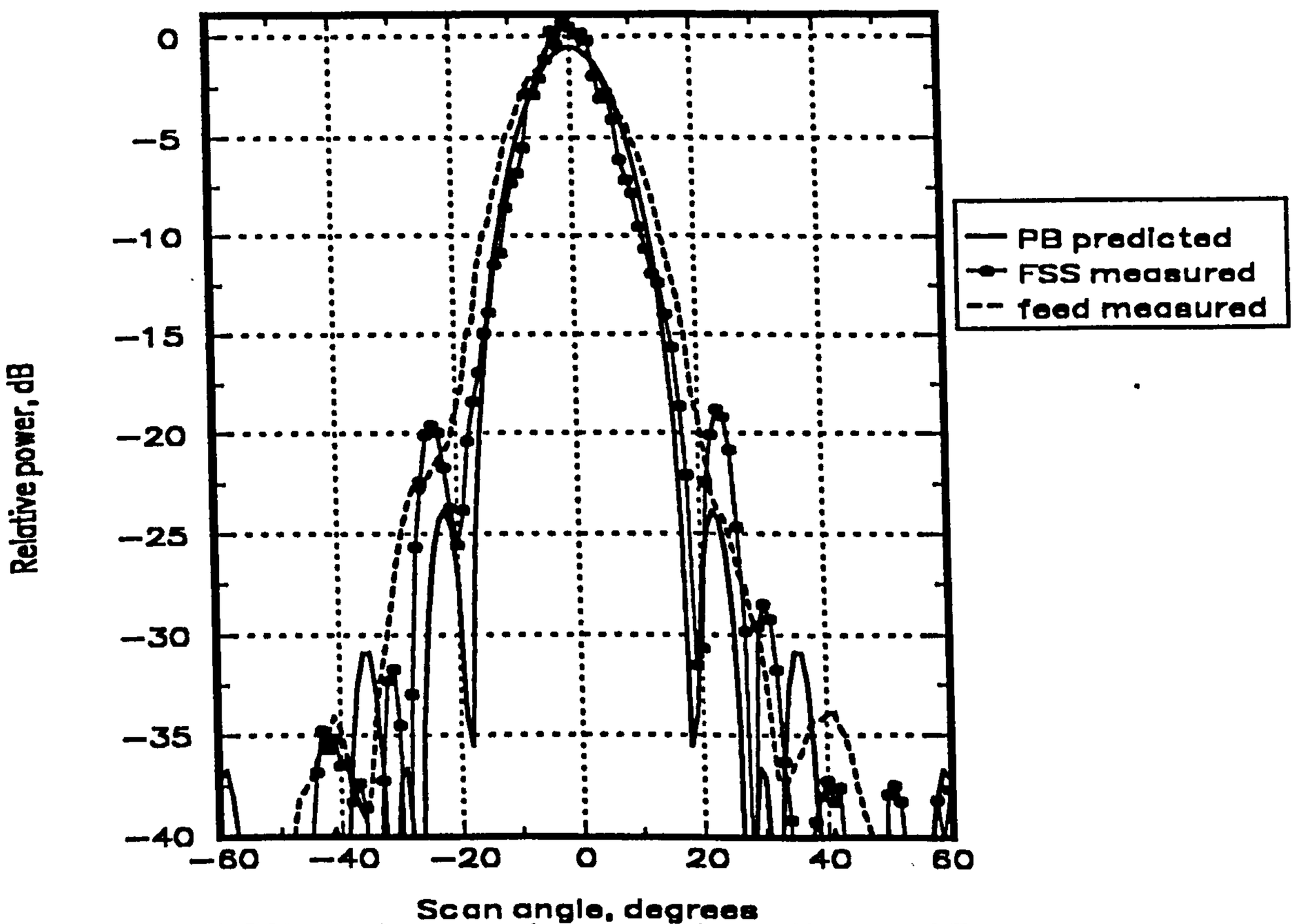

Fig.4.20b 45 degrees plane copolar pattern at 17 GHz using the PB feed model.

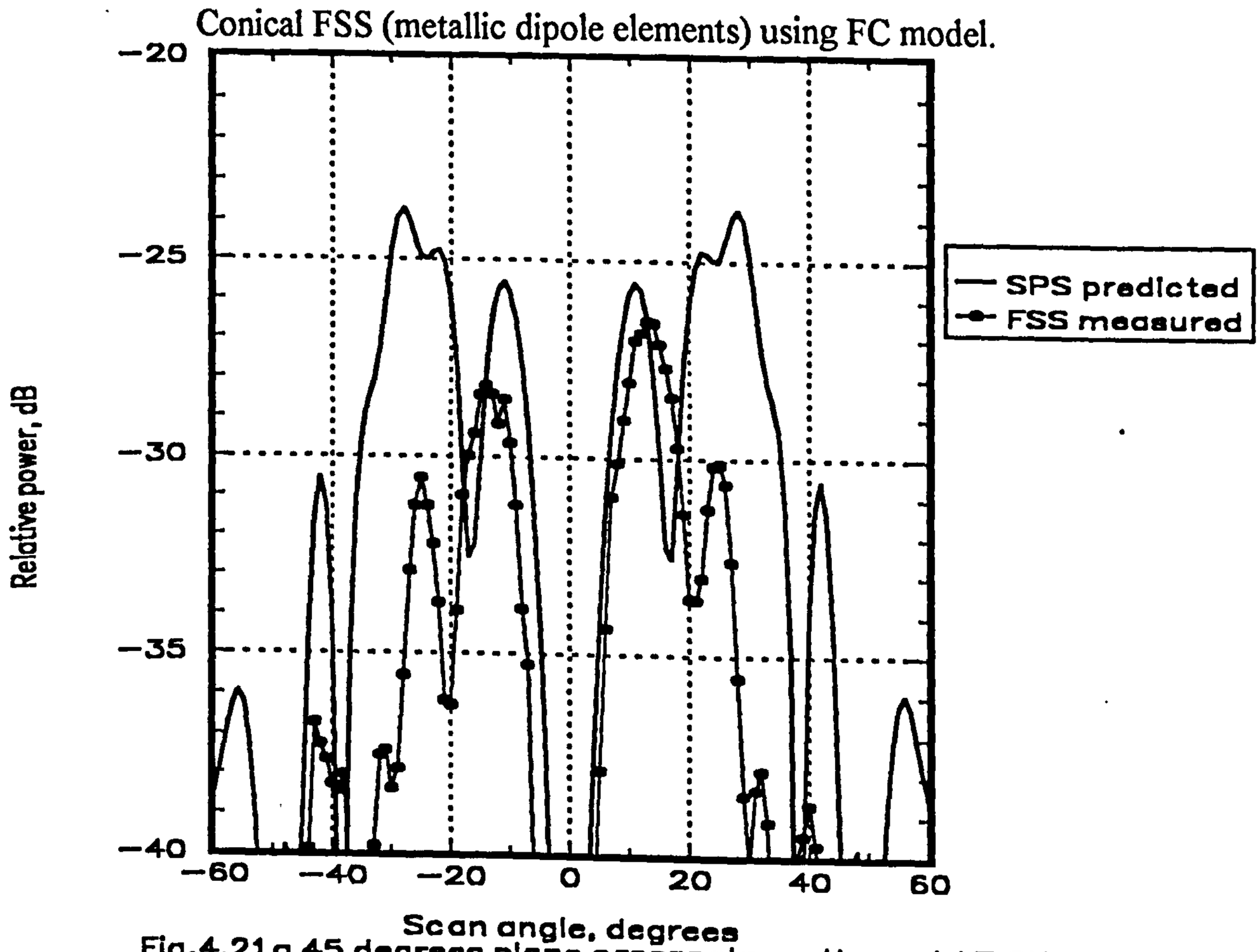

Fig.4.21 a 45 degrees plane crosspolar pattern at 1 7 GHz using the SPS feed model.

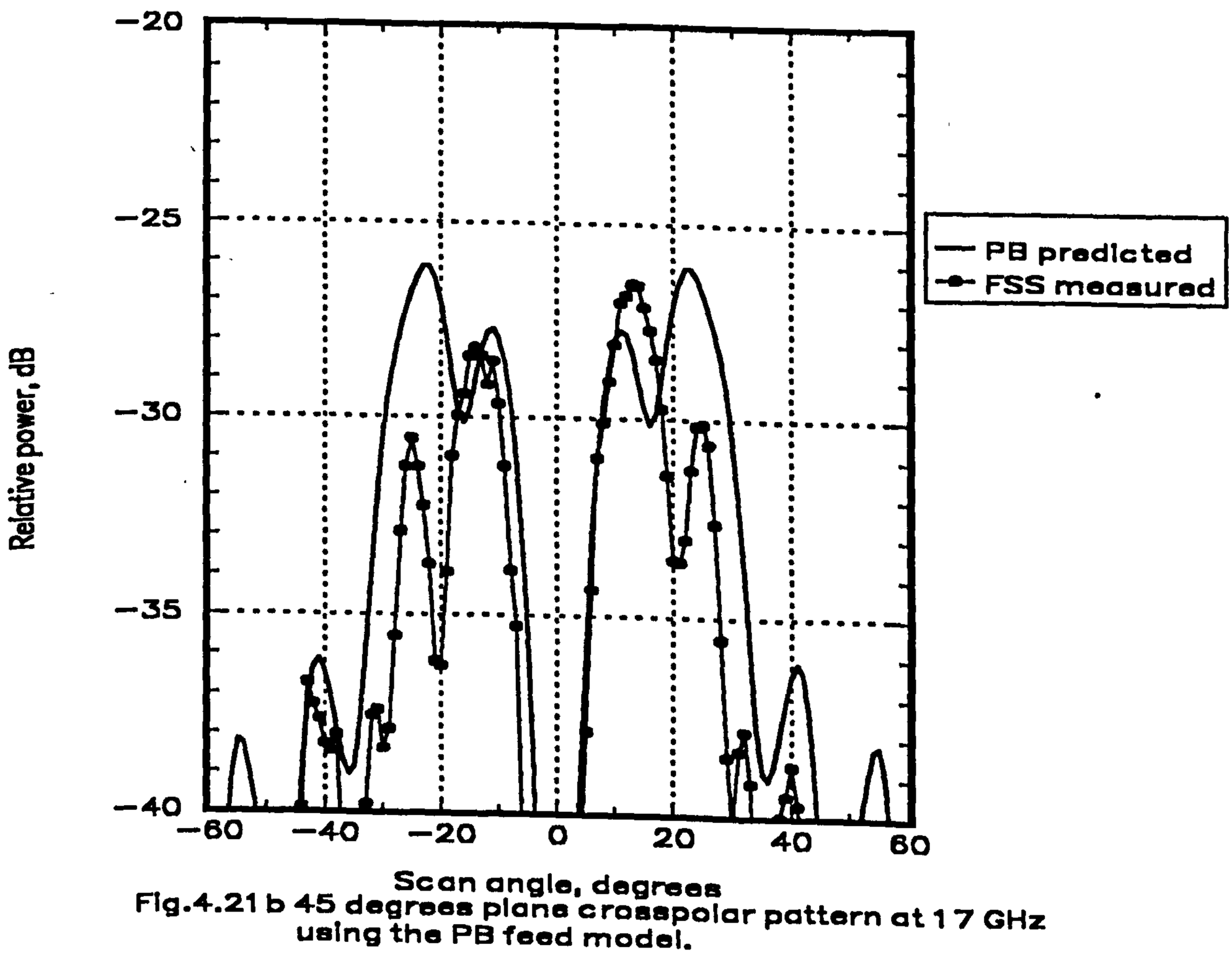

Fig.4.21 b 45 degrees plane crosspolar pattern at 1 7 GHz using the PB feed model.

References

[1] Moore, J. and Pizer, R. (Ed.) :' Moment methods in electromagnetics', Research Studies Press, John Wiley & sons, 1984.

[2] Montgometry, J.P.:'Scattering by an infinite periodic array of thin conductors on a dielectric sheet', IEEE Trans., AP-23, pp.70-75.

[3] Stylianou, A.S. :'Scattering from finite and multilayer FSS using iterative schemes Loughborough Univ. Tech., Ph.D. thesis, 1992.

[4] Harrington, R.F. :'Matrix methods for field problems', IEEE Proc.,1967, pp.136-149.

[5] Jennings, A. :'Matrix Computation for engineers and scientists', John Wiley & sons 1977.

[6] Casey, J.P. and Bansal, R. :'Dielectrically loaded wire antennas', IEE Proc.H, 1988, 135, pp.103-110.

[7] Sarkar, T.K., Rao, S.M. and Djordjevic, A.R. :'Electromagnetic scattering and radiation from finite microstrip structures', IEEE Trans., 1990, AP-38, pp.1568-1574.

[8] Popovic, B.D., Dragovic, M.B. and Djordjevic, A.R. :'Analysis and synthesis of wire antenna', Research Studies Press,1982, pp.100-104.

[9] Glisson, A.W. and Wilton, D.R. :'Simple and efficient numerical methods for problems of electromagnetic radiation and scattering from surfaces', IEEE Trans., 1980, AP-28, pp. 593-603

[10] 'Subroutine F04ADF', Numerical Algorithm Group, NAG, Mk.13.

[11] Canning, F.X. :'Direct solution of the EFIE with half the computation', IEEE Trans. ,1991, AP-1, pp.118-119

[12] Sarkar, T.P. (Ed.) :'Application of conjugate gradient method to electromagnetics and signal analysis', Elsevier Science Pub. Co. 1991, pp. 255-256

[13] Hestenes, M. and Stiefel, E. :' Methods of conjugate gradients for solving linear systems', J. Res. Nat.. Bur. Stand, Vol.49,pp.409-436, 1952.

[14] Su, C.C. :'Calculation of electromagnetic scattering from a dielectric cylinder using the conjugate gradient method and FFT', IEEE Trans., 1987, AP-35,pp.1418-1425.

[15] Catedra, M.F., Gago, E. and Nuno, L. :' A numerical scheme to obtain the RCS of three dimensional bodies of resonant size using the conjugate gradient method and the FFT', IEEE Trans., 1989, AP-37, pp.1418-1425.

[16] Sarkar, T.K. and Rao, S.M. :' The application of the conjugate gradient method to the solution of electromagnetic scattering from arbitrarily oriented wire antennas', IEEE Trans., 1984, AP-32, pp.398-403.

[17] Cheng, D.K. :'Field and wave electromagnetics', Addison-Wesley Pub. Co.,1983, pp.78.

[18] Yuen, K.M. :'Interface of a microwave measure receiver to a microcomputer', BSc. Report, Elec. Dept., Lough. Univ. of Tech. 1993.

CHAPTER 5.0

FINITE CURVED APERTURE FSS

5.1 Introduction

This Chapter deals with the analysis of a finite conical FSS with arbitrarily oriented slotted elements illuminated by the near field of a feed horn. An alternative method is to use the tangential infinite array (TIA) approach in Chapter 3 but the internal reflections in the cone are neglected in that model. These effects however could be a serious problem if the feed is very close to the FSS. Therefore, it is important to take into account the mutual coupling between all the FSS elements using a finite approach. The classical problem of the penetration of time harmonic electromagnetic fields through an aperture in a planar conducting screen has been a on going research for many years and only in the case of diffraction by a circular aperture are analytical results available [1]. Booker was the first to extend Babinet's principle of optics in vector electromagnetic fields to work out the properties of slot antennas from existing knowledge of strip and wire antennas [2]. A tutorial review has been presented by Butler and others [3] on analysing various types of aperture but dielectric backings are not included. Butler has also derived a magnetic field integral equation (MFIE) formulation for an aperture in an infinite screen separating two half spaces of different electromagnetic properties [4]. Recently Singh [5] has used this MFIE and Floquet field expansions to include the effects of multiple layers of dielectric substrate for an infinite planar array of arbitrarily oriented slots.

To the knowledge of the author, there is no published work on finite and curved aperture FSS with dielectric substrate. A novel MFIE has been derived here to account for the dielectric loading of thin slotted dipole elements on a conical FSS. This formulation is based on the original MFIE for an aperture lying in an infinite planar conducting metallic screen in free space. In Sec.5.2. a MFIE separating two half spaces is formulated in terms of an equivalent magnetic current source which replaces the aperture using the equivalence principle [4]. The MFIE is used for a free standing conical FSS later. The curvature of each slotted dipole FSS element on the cone is treated as linear segments which behave like planar apertures. The diffraction effects at the edges of the cone has been neglected. Using MOM, the MFIE is reduced to a linear system of equations to find the magnetic current coefficients. These are solved using the elimination method (Further descriptions can be found in Sec.4.2.3). In the novel MFIE formulation, the dielectric/ferrite substrate for a FSS slotted dipole is modelled as a thin coating on a cylindrical slot. It uses a quasi-static approximation, similar to the approach adopted in Sec.4.3. This new formulation makes use of symmetrical or

dual form in the Maxwell's equations for the static fields. Here the theory of duality is discussed and equations for the magnetic charge in ferrite medium and magnetic current in dielectric medium have been expanded explicitly (Sec.5.3). These are often neglected in current literature because of the fictitious nature of the magnetic charge and current source. In Sec.5.4 these equations are used to form the novel MFIE for a quasi-static approximation of the dielectric and ferrite loading. Computer models have been developed for a conical FSS with slotted dipole elements. SPS and PB feed models (Please refer to Sec.3.3.2 for further descriptions) have been used to calculate the near field illumination from a corrugated conical feed located at the base of the cone. This finite approach is called the finite current (FC) model because it considers the interaction of all the FSS elements in a finite geometrical sense. In Sec.5.5 the predictions obtained from the FC model will be compared with the experimental results from a conical prototype. The performance from the FC model will also be compared with the tangential infinite array (TIA) model (Sec.5.6).

5.2 Free standing finite aperture FSS

This section describes the analysis of an aperture lying in a planar infinite metallic screen separating two half spaces. The analysis is easily reduced to an aperture in free space. In Sec.5.2.1, the MFIE is obtained after the boundary conditions are enforced in the aperture regions. Subsequently, in Sec.5.2.2, the MOM technique is then applied to the MFIE, similar to Chapter 4, to obtain a linear system of equations. These was solved using elimination method [Sec.4.2.3] to find the magnetic current source. The MOM extends the MFIE formulation for a single aperture to a general curved FSS structure by dividing the curved slot into segments of aperture so that it would conform to the curvature of the FSS. The assumption here is that locally at each segment the metallic portions surrounding the aperture is behaving like an infinite planar screen in free space. The radiation from the FSS cone is computed using the total contribution of scattered fields from the magnetic current sources.

5.2.1 Aperture in screen formulation

Consider an aperture lying in an infinite planar metallic conducting screen which is a perfect conductor. The following formulation was derived originally for an aperture of an infinite length but finite width. But here it has been extended to an aperture of finite length [4]. The length of the aperture is l in the y axis and width d in the x axis separating two half spaces with parameters (μ_a, ε_a)on the left and (μ_b, ε_b) on the right as shown in Fig.5.1. The incident fields in the respective medium are $\left(\vec{H}_a^i, \vec{E}_a^i\right)$

and $\left(\vec{H}_b^i, \vec{E}_b^i\right)$. In order to find the MFIE, it is important to find the fields on both sides of the screen. Therefore, this problem is divided to an equivalent left half-space as shown in Fig.5.2 and 5.3 and an equivalent right half space in Fig.5.4 and 5.5. The total fields on each side will be enforced using the boundary conditions for the continuity of fields across the aperture. The objective is to find the aperture field across the width of the slot given by $\vec{E}_{ap}$. Fig.5.1 to Fig.5.3 show a systematic procedure to derive the total magnetic field on the left hand side (LHS). From Fig.5.1, the screen is short-circuited as shown in Fig.5.2 so that it will be continuous with a LHS equivalent magnetic current $\vec{I}_f$ in the region formerly occupied by the aperture where:

$$\vec{I}_f = -\hat{z} \times \vec{E}_{ap} \tag{5.1}$$

This problem is further reduced as shown in Fig.5.3 using the image theory (method of images) [6] to obtain the total magnetic current on LHS. Thus the equivalent magnetic current is doubled, $2\vec{I}_f$ across the former aperture and is pointing in the y direction. The total magnetic field on the LHS is given by:

$$\vec{H}_a = \vec{H}_a^{sc} + \vec{H}_a^{scat} \quad z < 0 \tag{5.2}$$

where the subscript denotes the medium a.

$\vec{H}_a^{sc}$ is the short-circuit magnetic field due to the incident field which is obtained using the image theory where:

$$\vec{H}_a^{sc} = 2\vec{H}_a^i \tag{5.3}$$

$\vec{H}_a^{scat}$ is the scattered fields from the magnetic current source $2\vec{I}_f$ where,

$$\vec{H}_a^{scat} = -\left(j\omega\vec{F}_a + \nabla\Phi_a\right) \tag{5.4}$$

The vector potential $\vec{F}_a$ is given by:

$$\vec{F}_a = \frac{\varepsilon_a}{4\pi} \int_{aperture} 2\vec{I}_f g(R) ds \tag{5.5}$$

where s here denotes the direction of the magnetic current flow. For convenience, this notation is used later for an arbitrarily oriented slotted segment of a FSS dipole. Sec.5.2.2. In the Fig.5.1 to Fig.5.5, s is represented by y axis.

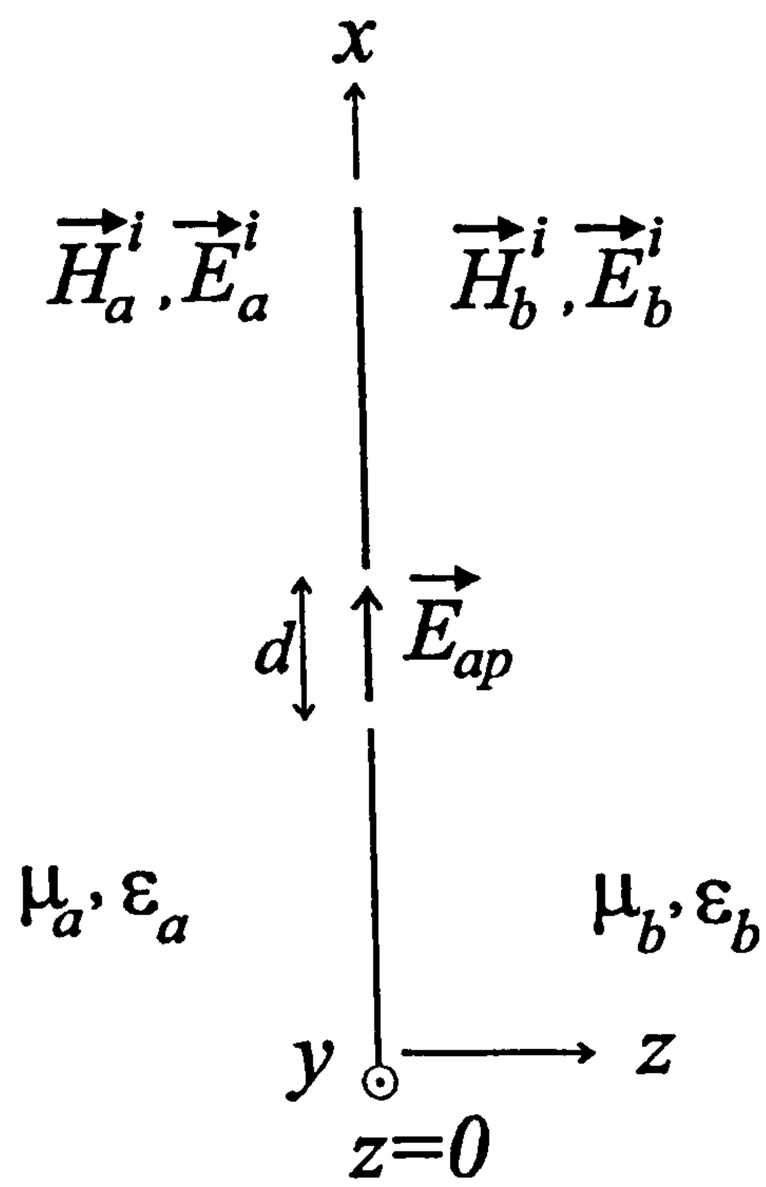

Fig.5.1 Planar aperture in an infinite metallic screen lying in the *x-y* plane.

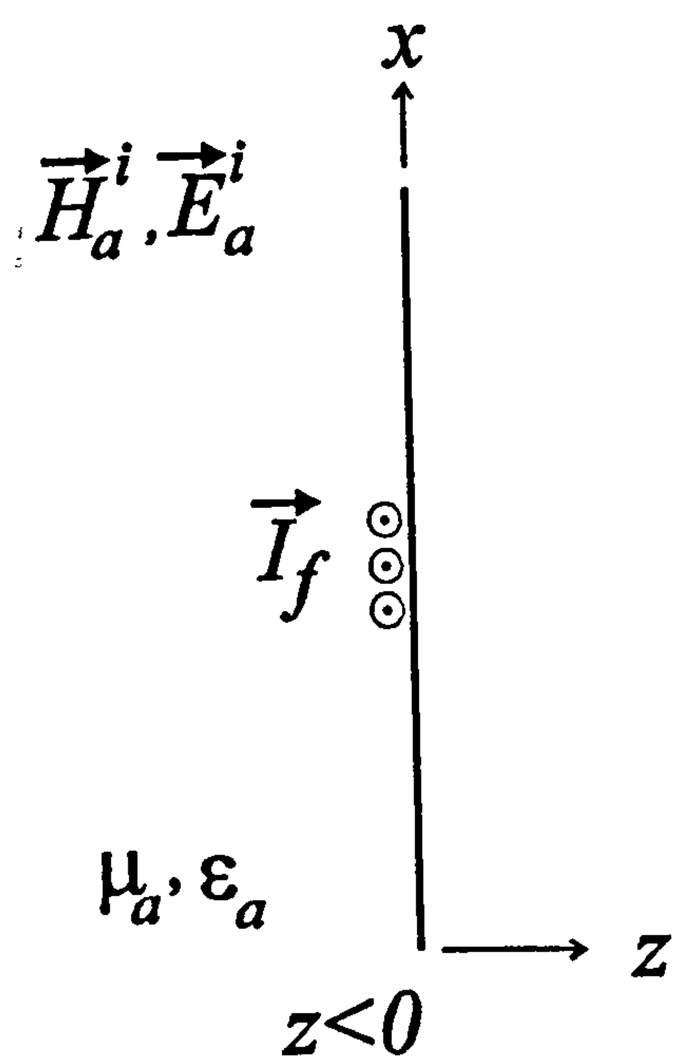

Fig.5.2 Short circuit aperture for *z<0.*

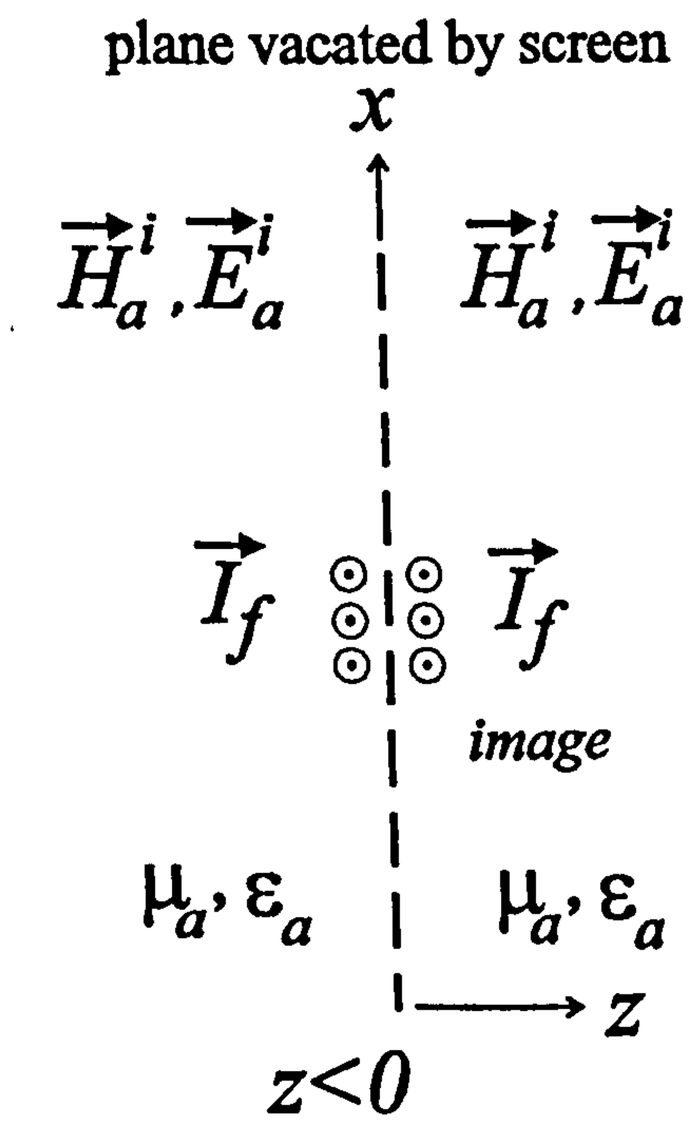

Fig.5.3 Left half equivalence problem. (Valid for *z<0.*)

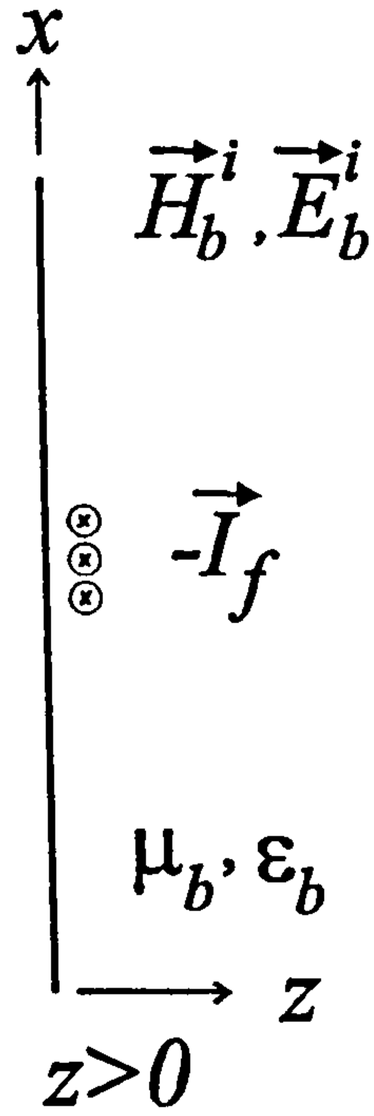

Fig.5.4 Short circuit aperture for $z>0$.

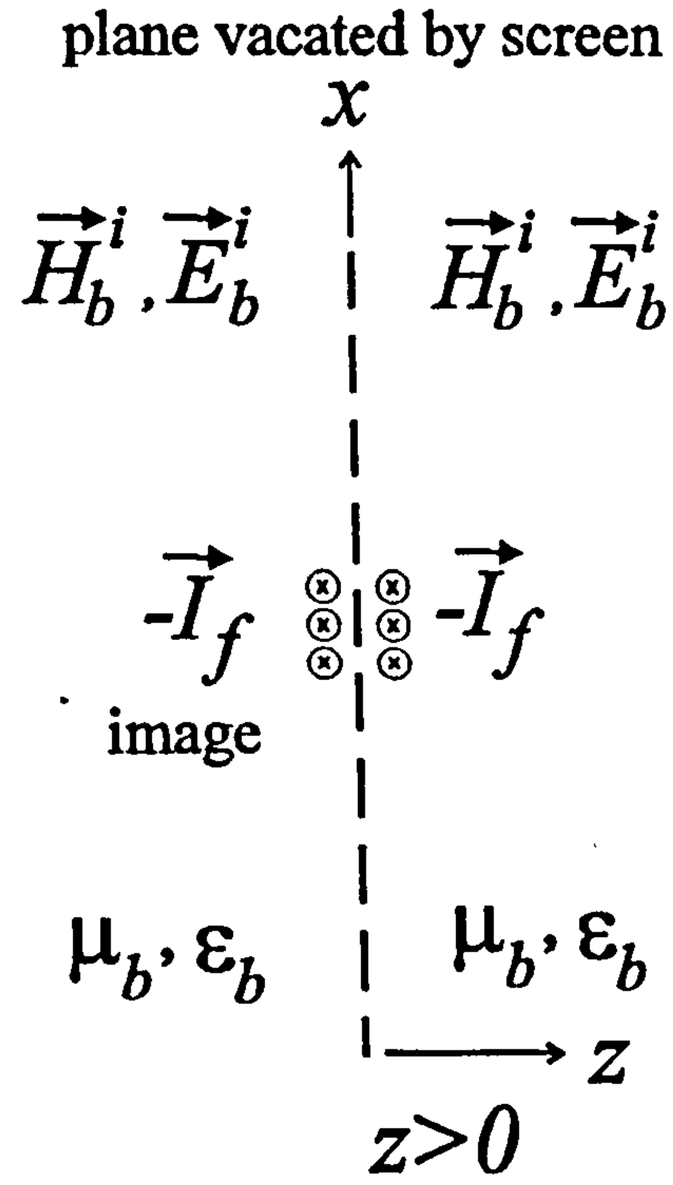

Fig.5.5 Right half equivalence problem (Valid for $z>0$.)

The scalar potential Φ_a is:

$$\Phi_a = \frac{1}{4\pi\mu_a} \int_{aperture} \vec{\nabla}.\left(2\vec{I}_f\right) g_a(R) ds \tag{5.6}$$

The Green's function on side a is given by:

$$g_a(R) = \frac{e^{-jk_a R}}{R} \tag{5.7}$$

where $k_a = k_o\sqrt{\varepsilon_{r_a}}$ and $k_o = \frac{2\pi}{\lambda}$ (ε_{r_a} is the relative permitivitty of medium a). $R = |\vec{r} - \vec{r}'|$ where $\vec{r}$ and $\vec{r}'$ are the positions of the observation and source with respect to an origin. In this case, the origin lies on the planar screen as shown in Fig.5.1 to Fig.5.5. Later, this is extended to a general FSS structure in free space by choosing a global origin.

Similarly, the equivalence principle can be applied to the right hand side (RHS). Since the vector normal is now pointing in the opposite direction, the direction of the magnetic current is now reversed. This is given by:

$$\vec{I}_f^b = \hat{z} \times \vec{E}_{ap} = -\vec{I}_f \tag{5.8}$$

Using the image theory, the right half equivalence current is now $-2\vec{I}_f$. The equivalence problem for the RHS. can be summarised according to the sequence of Fig.5.1, Fig.5.4 and Fig.5.5. Therefore, the total magnetic field on side b is given by:

$$\vec{H}_b = \vec{H}_b^{sc} + \vec{H}_b^{scat} \quad z > 0 \tag{5.9}$$

where $\vec{H}_b^{sc} = 2\vec{H}_b^i$ (5.10)

$$\vec{H}_b^{scat} = \left(j\omega\vec{F}_b + \vec{\nabla}\Phi_b\right) \tag{5.11}$$

Notice that the expression of Eq.(5.11) is positive compared to the negative value of $\vec{H}_a^{scat}$ in Eq.(5.4). This is due to the magnetic current source in Eq.(5.8) which is pointing in the opposite direction.

Enforcing the continuity of the total magnetic field across the aperture area A' in Eq.(5.4) and Eq.(5.11) yields,

$$\vec{H}_a \times \hat{z} = \vec{H}_b \times \hat{z} \tag{5.12}$$

$$\left[\vec{H}_a\right]_{tan} = \left[\vec{H}_b\right]_{tan} \tag{5.13}$$

$$\left[\vec{H}_a^{scat} - \vec{H}_b^{scat}\right]_{tan} = \left[j\omega\vec{F}_a + \vec{\nabla}\Phi_a + j\omega\vec{F}_b + \vec{\nabla}\Phi_b\right]_{tan} \tag{5.14}$$

$$\left[2\vec{H}_a^i - 2\vec{H}_b^i\right]_{tan} = \left[j\omega\vec{F}_a + \vec{\nabla}\Phi_a + j\omega\vec{F}_b + \vec{\nabla}\Phi_b\right]_{tan} \tag{5.15}$$

Let the medium be the same on both half-space denoted by medium a. If the illumination is only on side a only, $\vec{H}_b^i(r) = 0$. So Eq.(5.15) becomes the MFIE given by:

$$\left[\vec{H}_a^i\right]_{tan} = \left[j\omega\vec{F}_a + \vec{\nabla}\Phi_a\right]_{tan} \quad in\ A' \tag{5.16}$$

and Eq.(5.9) becomes,

$$\left[\vec{H}_b\right]_{tan} = \left[j\omega\vec{F}_b + \vec{\nabla}\Phi_b\right]_{tan} \quad in\ A' \tag{5.17}$$

Since, the medium is the same on both sides then Eq.(5.17) becomes,

$$\left[\vec{H}_b\right]_{tan} = \left[j\omega\vec{F}_a + \vec{\nabla}\Phi_a\right]_{tan} \quad in\ A' \tag{5.18}$$

$$\left[\vec{H}_b\right]_{tan} = \left[\vec{H}_a^i\right]_{tan} \quad in\ A' \tag{5.19}$$

5.2.2 MOM using pulses testing and basis functions

The MFIE in Eq.(5.16) is of the same form to the EFIE in Eq.(4.7). The slot has been replaced by an equivalent linear magnetic current source. If the magnetic current

source elements are distributed on a conical surface with respect to a global co-ordinate system as illustrated in Sec.4.2.2, then the MFIE can be written as :

$$\vec{H}_a^i.\hat{s} = j\omega\vec{F}_a.\hat{s} + \vec{\nabla}\Phi_a.\hat{s} \tag{5.20}$$

Note that $\hat{s}$ is a free vector lying along the segment axis therefore, the dot product in Eq.(5.21) gives the tangential field along this axis.

In general, for a free standing medium, let $\mu_a = \mu_o$, $\varepsilon_a = \varepsilon_o$ and $\vec{H}_a^i = \vec{H}^i$. So that Eq.(5.20) can be rewritten as,

$$\vec{H}^i.\hat{s} = j\omega\vec{F}.\hat{s} + \vec{\nabla}\Phi.\hat{s} \tag{5.21}$$

which is similar to the EFIE given by Eq.(4.7) as shown below:

$$\vec{E}^i.\hat{s} = j\omega\vec{A}.\hat{s} + \vec{\nabla}\Phi.\hat{s}$$

If the MOM is applied on the EFIE as previously discussed in Sec.4.2.2, it can be shown that Eq.(4.7) as shown above would yield Eq.(4.19) after using Galerkin's pulse testing and current basis functions. Eq.(4.19) is repeated here for convenience:

$$\vec{E}^i.\left(\vec{r}_{m+1/2} - \vec{r}_{m-1/2}\right)$$

$$= \frac{j\omega\mu_o}{4\pi} I_n\left[\psi(m)_{n-1/2}^{n}\hat{s}_{n-1/2} + \psi(m)_{n}^{n+1/2}\hat{s}_{n+1/2}\right].\left(\vec{r}_{m+1/2} - \vec{r}_{m-1/2}\right)$$

$$+\frac{1}{j\omega 4\pi\varepsilon_o} I_n\left[\frac{\psi\left(m+1/2\right)_{n}^{n+1}}{\left(s_{n+1}-s_n\right)} - \frac{\psi\left(m+1/2\right)_{n-1}^{n}}{\left(s_n - s_{n-1}\right)}\right]$$

$$-\frac{1}{j\omega 4\pi\varepsilon_o} I_n\left[\frac{\psi\left(m-1/2\right)_{n}^{n+1}}{\left(s_{n+1}-s_n\right)} - \frac{\psi\left(m-1/2\right)_{n-1}^{n}}{\left(s_n - s_{n-1}\right)}\right]$$

This process is repeated here for Eq.(5.21) to produce Eq.(5.22) for the curved FSS. If there are m pulse testing functions and n pulse current basis functions, then using MOM on Eq.(5.21), one should arrive at the following expression,

$$\vec{H}^i.\left(\vec{r}_{m+1/2}-\vec{r}_{m-1/2}\right)$$

$$=\frac{j\omega\varepsilon_o}{4\pi}2I_{fn}\left[\psi(m)^n_{n-1/2}\hat{s}_{n-1/2}+\psi(m)^{n+1/2}_n\hat{s}_{n+1/2}\right].\left(\vec{r}_{m+1/2}-\vec{r}_{m-1/2}\right)$$

$$+\frac{1}{j\omega 4\pi\mu_o}2I_{fn}\left[\frac{\psi\left(m+1/2\right)^{n+1}_n}{(s_{n+1}-s_n)}-\frac{\psi\left(m+1/2\right)^{n}_{n-1}}{(s_n-s_{n-1})}\right]$$

$$\frac{1}{j\omega 4\pi\mu_o}2I_{fn}\left[\frac{\psi\left(m-1/2\right)^{n+1}_n}{(s_{n+1}-s_n)}-\frac{\psi\left(m-1/2\right)^{n}_{n-1}}{(s_n-s_{n-1})}\right] \tag{5.22}$$

Notice that the above expression is of the same form as Eq.(4.19) for the EFIE. Eq.(5.22) is expressed as linear matrix system as,

$$[Y_m]=[A_{mn}][I_{fn}] \tag{5.23}$$

$$[Y_m]=\vec{H}^i.\left(\vec{r}_{m+1/2}-\vec{r}_{m-1/2}\right) \tag{5.24}$$

$$A_{mn}=\frac{-2}{j\omega 4\pi\mu_o}\left\{\left(k_o^2\,\psi(m)^n_{n-1/2}\hat{s}_{n-1/2}+k_o^2\,\psi(m)^{n+1/2}_n\hat{s}_{n+1/2}\right).\left(\vec{r}_{m+1/2}-\vec{r}_{m-1/2}\right)\right.$$

$$\left.\frac{\psi\left(m+1/2\right)^{n+1}_n}{(s_{n+1}-s_n)}+\frac{\psi\left(m+1/2\right)^{n}_{n-1}}{(s_n-s_{n-1})}+\frac{\psi\left(m-1/2\right)^{n+1}_n}{(s_{n+1}-s_n)}-\frac{\psi\left(m-1/2\right)^{n}_{n-1}}{(s_n-s_{n-1})}\right\} \tag{5.25}$$

$[I_{fn}]$ and $[Y_m]$ are column matrices of the unknown magnetic current and excitation due to the incident fields respectively. $[I_{fn}]$ represents the nth magnetic current pulse source which has been weighted on I_f after the MOM segmentation scheme. m and $n=1,2,.....N'$, where N' is the total number of current pulses. $[A_{mn}]$ is a square matrix that accounts for the couplings between the segments.

5.2.3 Radiated fields

The radiated fields from the FSS cone can be computed from the radiation integral with the linear magnetic current sources distributed on the conical surface of the FSS. In this case the source is represented by magnetic current pulse. The electric current source is neglected because of the infinite ground plane assumptions at each local segment. Thus, the electric field radiated from the cone is calculated from superposition of the scattered fields from each magnetic current pulse.

The scattered field at a distance Γ_n from the centre of each magnetic current pulse to the receiving feed is given by:

$$\vec{E}^{scat}(\Gamma_n) = \frac{-j\omega\mu_o}{4\pi}\frac{e^{-jk_o\Gamma_n}}{\Gamma_n}\int_{segment}\left[\sqrt{\frac{\varepsilon_o}{\mu_o}}\vec{M}'_n \times \hat{\Gamma}_n\right]e^{jk_o\vec{r}_t\cdot\hat{\Gamma}_n}ds$$

$$= \frac{-j\omega\mu_o}{4\pi}\frac{e^{-jk_o\Gamma_n}}{\Gamma_n}\left[\sqrt{\frac{\varepsilon_o}{\mu_o}}\tilde{M}'_n \times \hat{\Gamma}_n\right] \tag{5.26}$$

where $n=1,2..N'$ (N' is the total number of current pulses),

From Eq.(5.5) and Eq.(5.8), it can be shown that total magnetic current source at each junction of the segment is $\vec{M}'_n = -2\vec{I}_{fn}$, therefore,

$$\tilde{M}_n = \int_{segment}\vec{M}_n\, e^{jk_o\vec{r}_t\cdot\hat{\Gamma}_n}ds$$

$$= \int_{segment}-2\vec{I}_{fn}\, e^{jk_o\vec{r}_t\cdot\hat{\Gamma}_n}ds$$

$$= \int_{n-1/2}^{n} -2I_{fn}\,\hat{s}_{n-1/2}\, e^{jk_o\vec{r}_t\cdot\hat{\Gamma}_n}ds + \int_{n}^{n+1/2} -2I_{fn}\,\hat{s}_{n+1/2}\, e^{jk_o\vec{r}_t\cdot\hat{\Gamma}_n}ds$$

$$= -2I_{fn}\hat{s}_{n-1/2}\left(s_n - s_{n-1/2}\right) - 2I_{fn}\hat{s}_{n+1/2}\left(s_{n+1/2} - s_n\right) \tag{5.27}$$

The total radiated field from the slotted FSS cone is the contribution from all the magnetic current pulses and is given by:

$$\vec{E}_{cone}^{scat} = \sum_{n=1}^{n=N'} \vec{E}^{scat}(\Gamma_n) \tag{5.28}$$

5.3 Magnetic charge and current: theory of static fields

In order to account for the dielectric substrate backing of the slotted FSS on a curved surface, a quasi-static approximation approach analogous to Popovic [7] is used. In Sec.4.3, this quasi-static approximation has been used in the EFIE formulation to account for the effect of a thin dielectric and ferrite coating on a cylindrical wire. This method assumes that the substrate coating should be thin enough. According to Popovic, the thickness should be less than twice the wire radius. He had used the concept of static electric charge and current with the help of Gauss' and Ampere's law to derive the quasi-static version for the EFIE. It has been shown that the inner and outer cylindrical layers of quasi-static electric charges and currents are equivalent to the electric currents and charges flowing in both the wire and dielectric/ferrite coatings as illustrated in Fig.4.5. In this section, a similar quasi-static approach has also been also developed to account for such loading on a thin slot. In the proposed model, the slot with dielectric and ferrite coating is modelled as cylindrical layers of magnetic charge and current. Although, magnetic charge and current are merely formalisms, they have been incorporated in the traditional Maxwell's equations for symmetry and duality [8]. The symmetrical equations of the static fields, complementary version of the Ampere's law for magnetic current and Gauss's law for magnetic charge are derived explicitly here. These laws are fundamental to the development of the quasi-static approximation of the MFIE.

The theoretical basis for the new formulation are based on the following assumptions:
(i) Isolated magnetic charge and magnetic current exist.
(ii)The static electric flux/field due to the fictitious magnetic charge is non-divergent.
(iii)The static magnetic flux/field due to the fictitious magnetic current is non-rotational and conservative.

The above assumptions have often been used in Maxwell's equation to assume a more symmetrical form. But this is not often explicit enough in current literature to be applied for static fields in the ferrite and dielectric medium. Therefore, the following

Sections will attempt to derive and expand on the dual equations here so that they could be used in the quasi-static approximation of the slot later.

The derivation of the static magnetic fields due to magnetic charge source in the ferrite medium is expanded in Sec.5.3.1. Initially, existing equations for the electric field due to electric charge will be derived for a dielectric medium with the help of Gauss' law. These equations will be compared with the derivations for the complementary magnetic field that originates from the magnetic charge source in order to show explicitly the duality. In Sec.5.3.2, the expanded derivations of the static electric fields due to magnetic current source in the dielectric medium will be discussed. Existing equations for the magnetic field from electric current source in a ferrite medium will be derived with the help of Ampere's law. These equations are then compared with the derivations for the complementary electric fields due to the magnetic current source and the complementary Ampere's law. The duality is exploited in a slot to produce a novel formulation of MFIE for dielectric and ferrite loading. This is discussed later in Sec.5.4.

5.3.1 Magnetic charge in ferrite medium

In order to derive the equations for the static magnetic field which is due to the magnetic charge source in a ferrite medium, existing equations for electric field from the electric charge source in a dielectric medium will be derived first. Then the complementary equations for magnetic charge will be expanded and compared with equations from electric charge source in Table 5.1.

The study of static electric field is known as electrostatics. The two fundamental postulates for electrostatics using the static electric field intensity $\vec{E}$ of an electric charge source in free space of permittivity ε_o are given by:

$$\vec{\nabla}.\vec{E} = \frac{q}{\varepsilon_o} \tag{5.29}$$

$$\vec{\nabla}\times\vec{E} = \vec{0} \tag{5.30}$$

where q is the electric charge volume density in free space.
Eq.(5.30) implies that the static electric field is non-rotational which can be shown to be conservative using Stokes' theorem.

When a dielectric body with permittivity ε is placed in an external field it will be polarised. This will give rise to a polarisation electric charge volume density q_p. So Eq.(5.29) becomes

$$\vec{\nabla}.\vec{E} = \frac{1}{\varepsilon_o}\left(q + q_p\right) \tag{5.31}$$

But $-q_p = \vec{\nabla}.\vec{P}$ ($\vec{P}$ is the polarisation vector) (5.32)

If the dielectric medium is linear and isotropic such that the polarisation is directly proportional to the electric field intensity then,

$$\vec{D} = \varepsilon_o\vec{E} + \vec{P} \tag{5.33}$$

or, $\vec{D} = \varepsilon\vec{E}$ (5.34)

where $\vec{D}$ is the electric flux density or electric displacement.

Substituting Eq.(5.32) into Eq.(5.31) and using Eq.(5.33), yields:

$$\vec{\nabla}.\vec{D} = q \tag{5.35}$$

Applying the divergence law (here $\int_{V_d} \vec{\nabla}.\vec{D}\,dV = \oint_{S_d} \vec{D}.\hat{n}dS$) on Eq.(5.35) yields,

$$\oint_{S_d} \vec{D}.\hat{n}dS = Q \tag{5.36}$$

where, Q is the total electric charge in a volume V_d of dielectric medium enclosed in a close surface S_d such that $Q = \int_{V_d} q\,dV$.

Eq.(5.36) is an expression of Gauss's law which states that the total outward flux of the electric displacement over any closed surface is equal to the total free electric charge enclosed in the surface.

Equations for the static magnetic fields due to the magnetic charge will be derived here in parallel. This is to show the duality with the static electric fields from the electric charge. Note that the present derivations are to lay down explicitly the equations of the field for the magnetic charge in a ferrite medium which is normally not discussed in current literature. To extend the theory of static magnetic fields of magnetic charges, it is assumed that the static magnetic field $\vec{H}_f$ due to the magnetic charge is conservative. Thus $\vec{H}_f$ in free space of permeability μ_o are given by the following two fundamental postulates,

$$\vec{\nabla}.\vec{H}_f = \frac{q_f}{\mu_o} \tag{5.37}$$

$$\vec{\nabla}\times\vec{H}_f = \vec{0} \tag{5.38}$$

where q_f is the magnetic charge density in free space.

The subscript f denotes the magnetic charge source. Eq.(5.38) implies that $\vec{H}_f$ is non-rotational which can be shown to be conservative using Stokes' theorem.

The electric polarisation in a dielectric medium has been taken into account by the presence of volume electric charge density q_p as shown in Eq.(5.31) from Eq.(5.29). Applying a similar concept to the magnetic charge in ferrite medium, an equivalent polarisation in the ferrite medium would also require the presence of volume magnetic charge density q_{fp} under the influence of magnetic field. So that for a ferrite case with permittivity μ, Eq.(5.37) becomes

$$\vec{\nabla}.\vec{H}_f = \frac{1}{\mu_o}\left(q_f + q_{fp}\right) \tag{5.39}$$

where q_{fp} is the polarisation magnetic charge density similar in behaviour to a corresponding polarised electric charge density q_p.

But $-q_{fp} = \vec{\nabla}.\vec{P}_f$ ($\vec{P}_f$ is the polarisation magnetic vector) (5.40)

If the ferrite medium is also linear and isotropic such that the polarisation is directly proportional to the magnetic field intensity, then

$$\vec{B}_f = \mu_o \vec{H}_f + \vec{P}_f \tag{5.41}$$

$$\text{or, } \vec{B}_f = \mu \vec{H}_f \tag{5.42}$$

where $\vec{B}_f$ is the magnetic flux due to the magnetic charge.

Substituting Eq.(5.40) into Eq.(5.39) and using Eq.(5.41) yields

$$\vec{\nabla}.\vec{B}_f = q_f \tag{5.43}$$

Applying the divergence law (here $\int_{V_d} \vec{\nabla}.\vec{B}\, dV = \oint_{S_d} \vec{B}.\hat{n} dS$) on Eq.(5.43) yields,

$$\oint \vec{B}_f.\hat{n} dS = Q_f \tag{5.44}$$

where, Q_f is the total magnetic charge in a volume V_d of ferrite medium enclosed in a close surface S_d such that $Q_f = \int_{V_d} q_f dV$.

Eq.(5.44) states that for a ferrite medium, the total outward flux of the magnetic flux or displacement over any closed surface is equal to the total free magnetic charge enclosed in the surface. This is a complementary version of the Gauss's law for electric charge source in a dielectric medium . This implies that the magnetic fields due to magnetic charge in a ferrite medium behaves like the electric fields of electric charge in the dielectric medium. Thus the fundamental postulates for the magnetic charge in a ferrite medium are given by Eq.(5.38) and Eq.(5.43) which is similar in form to Eq.(5.30) and Eq.(5.35) for a electric charge in a dielectric medium.

Table 5.1 below shows a summary of the comparison between the complementary equations.

Electric field due to electric charge.	Magnetic field due to magnetic charge.
$\vec{\nabla}.\vec{E} = \frac{q}{\varepsilon_o}$ (in free space) (5.29)	$\vec{\nabla}.\vec{H}_f = \frac{q_f}{\mu_o}$ (in free space) (5.37)
$\vec{\nabla}\times\vec{E} = \vec{0}$ (5.30)	$\vec{\nabla}\times\vec{H}_f = \vec{0}$ (5.38)
$\vec{\nabla}.\vec{E} = \frac{1}{\varepsilon_o}\left(q + q_p\right)$ (in dielectric) (5.31)	$\vec{\nabla}.\vec{H}_f = \frac{1}{\mu_o}\left(q_f + q_{fp}\right)$ (in ferrite) (5.39)
$-q_p = \vec{\nabla}.\vec{P}$ (5.32)	$-q_{fp} = \vec{\nabla}.\vec{P}_f$ (5.40)
$\vec{D} = \varepsilon_o\vec{E} + \vec{P} = \varepsilon\vec{E}$ (5.33) & (5.34)	$\vec{B}_f = \mu_o\vec{H}_f + \vec{P}_f = \mu\vec{H}_f$ (5.41)& (5.42)
$\vec{\nabla}.\vec{D} = q$ (5.35)	$\vec{\nabla}.\vec{B}_f = q_f$ (5.43)
$\oint_{S_d}\vec{D}.\hat{n}dS = Q$ (5.36) (Gauss's law)	$\oint_{S_d}\vec{B}_f.\hat{n}dS = Q_f$ (5.44) (Complementary Gauss' law)

Table 5.1.

5.3.2 Magnetic current in dielectric medium

Existing equations for static magnetic field from the electric charge source in a ferrite medium will be derived here. This will be followed by the derivations of the static electric field from the magnetic current source in a dielectric medium in order to show the duality with the electric current. A summary of the complementary equations are shown in Table 5.2 to compare the duality..

The study for static magnetic field from electric current source in ferrite medium is known as magnetostatics. The two fundamental postulates for the magnetostatics due to electric current source in free space of permeability μ_o are given by:

$$\vec{\nabla}.\vec{B} = 0 \qquad (5.45)$$

$$\vec{\nabla} \times \vec{B} = \mu_o \vec{J} \tag{5.46}$$

where $\vec{B}$ is the magnetic flux density due to the electric current density $\vec{J}$.
Eq.(5.45) implies that the magnetic flux is non-divergent.
Taking the divergence of Eq.(5.46) and using Eq.(5.45) yields,

$$\vec{\nabla}.\vec{J} = 0 \tag{5.47}$$

which is consistent with the continuity equation when there is no time variation.
The continuity equation with time variation is given by:

$$\vec{\nabla}.\vec{J} = -\frac{\partial q}{\partial t} \tag{5.48}$$

The time t variation of the electric charge density q is shown on the right hand side of the equation.

Taking the volume integral of Eq.(5.45) and applying the Stokes' theorem, gives

$$\oint_{\substack{closed \\ surface}} \vec{B}.\hat{n}dS = 0 \tag{5.49}$$

Eq.(5.49) is an expression for the law of conservation of magnetic flux.

The effect of magnetisation $\vec{M}$ in a ferrite medium can be taken account by incorporating an equivalent volume electric current density $\vec{J}_m$ into Eq.(5.46). Therefore,

$$\frac{\vec{\nabla} \times \vec{B}}{\mu_o} = \vec{J} + \vec{J}_m \tag{5.50}$$

It is known that $\vec{J}_m = \vec{\nabla} \times \vec{M}$ (5.51)

and $\vec{H} = \frac{\vec{B}}{\mu_o} - \vec{M}$ (5.52)

where $\vec{H}$ is the magnetic field intensity.

Substituting Eq.(5.51) into Eq.(5.50) and using Eq.(5.52), yields

$$\vec{\nabla} \times \vec{H} = \vec{J} \quad (5.53)$$

Eq.(5.45) and Eq.(5.53) are the two fundamental postulates of magnetostatics for magnetic flux/field of a electric charge in a ferrite medium .

Let $\vec{B} = \mu \vec{H}$ (5.54)

and substituting Eq.(5.54) into Eq.(5.52) yields,

$$\vec{M} = (\mu_r - 1)\vec{H} \quad (5.55)$$

where relative permeability $\mu_r = \frac{\mu}{\mu_o}$.

The magnetisation vector $\vec{M}$ is also equivalent to the volume current density $\vec{J}_m$ and surface current density $\vec{J}_{ms}$

where $\vec{J}_{ms} = \vec{M} \times \hat{n}$ (5.56)

Taking the surface integral and using the Stokes' theorem, Eq.(5.53) becomes:

$$\oint_C \vec{H}.d\vec{l} = I \quad (5.57)$$

where $\vec{I}$ is the electric current given by $I = \oint_{\substack{closed \\ surface}} \vec{J}.\hat{n}dS$ ($\hat{n}$ is normal to surface S).

Eq.(5.57) is a expression of the Ampere's law which states that the circulation of the magnetic field intensity around any closed path C is equal to the free electric current flowing through the surface bounded by the path.

To extend a similar argument to the magnetic current source the electric flux density $\vec{D}_f$ due to the magnetic current $\vec{J}_f$ is also assumed to be non-divergent. Therefore, the two fundamental postulates of the static electric flux due to magnetic current in free space are given by:

$$\vec{\nabla}.\vec{D}_f = 0 \tag{5.58}$$

$$\vec{\nabla}\times\vec{D}_f = -\varepsilon_o\vec{J}_f \tag{5.59}$$

where $\vec{D}_f$ is the electric flux density or electric displacement due to the magnetic current density $\vec{J}_f$ .The subscript f denotes the magnetic current source.Eq.(5.58) implies that the electric flux is non-divergent.

Taking the divergence of Eq.(5.59) yields,

$$\vec{\nabla}.\vec{J}_f = 0 \tag{5.60}$$

which is consistent with the equation of continuity Eq.(5.61) where there is no time variation magnetic charge density. Thus, the steady magnetic current due to the magnetic charge is non-divergent.

The continuity equation for the magnetic charge is given by:

$$\vec{\nabla}.\vec{J}_f = -\frac{\partial q_f}{\partial t} \tag{5.61}$$

where q_f is the free magnetic charge density.

Taking the volume integral of Eq.(5.58) and applying the Stokes' theorem, gives

$$\oint_{\substack{closed\\surface}} \vec{D}_f.\hat{n}dS = 0 \tag{5.62}$$

Eq.(5.62) is a statement of the law of conservation of electric flux due to the magnetic current. This is because no work is done by the electric flux as it circulates in the close surface.

The effect of magnetisation $\vec{M}$ has been applied in a ferrite medium as discussed before. But, here a similar effect is also produced in the dielectric medium for a volume magnetic current density $\vec{J}_n$. This is called $\vec{N}$ here for convenience. $\vec{N}$ in the dielectric medium is equivalent to a volume magnetic current density $\vec{J}_n$. Therefore, for a dielectric medium Eq.(5.59) becomes,

$$\frac{\vec{\nabla}\times\vec{D}_f}{-\varepsilon_o} = \vec{J}_f + \vec{J}_n \tag{5.63}$$

Let $\vec{J}_n = -\vec{\nabla}\times\vec{N}$ (5.64)

and $-\vec{E}_f = \dfrac{\vec{D}_f}{\varepsilon_o} + \vec{N}$ (5.65)

where $\vec{E}_f$ is the electric field due to the magnetic current.

Substituting Eq.(5.64) into Eq.(5.63) and using Eq.(5.65), yields

$$\vec{\nabla}\times\vec{E}_f = -\vec{J}_f \tag{5.66}$$

Eq.(5.58) and Eq.(5.66) are the two fundamental postulates for static electric flux/field due to the magnetic current in a dielectric medium.

If $\vec{D}_f = \varepsilon\vec{E}_f$ (5.67)

and substituting Eq.(5.67) into Eq.(5.65) yields,

$$\vec{N} = (\varepsilon_r - 1)\vec{E}_f \tag{5.68}$$

The magnetisation vector $\vec{N}$ is also equivalent to the volume current density $\vec{J}_n$ and surface current density $\vec{J}_{ns}$.

where $\vec{J}_{ns} = -\vec{N}\times\hat{n}$ (5.69)

The normal vector $\hat{n}$ is pointing away from the surface.

Taking the surface integral with the help of Stokes' theorem, Eq.(5.66) becomes:

$$\oint_C \vec{E}_f . d\vec{l} = -I_f \tag{5.70}$$

where $\vec{I}_f$ is the magnetic current given by $\vec{I}_f = \oint_{\substack{closed \\ surface}} \vec{J}_f . \hat{n} dS$.

Eq.(5.70) is a expression of a complementary version of the Ampere's law which states that the circulation of the electric field intensity around any closed path C is equal to the free magnetic current flowing through the surface bounded by the path. Table 5.2 compares the equations of the magnetic field due to electric current source with the electric field due to magnetic current source. The complementary equations derived here are summarised in Table 5.1 and Table 5.2. These will be used in the novel formulation of the MFIE for the slot in the next Section.

5.4 Dielectric and ferrite coated FSS slot

The FSS slot supported by a thin dielectric/ferrite substrate can be modelled as a cylindrical dipole slot with the corresponding coatings. This approximation considers the coating acting as a continuous loading on the slot. It will be shown later that the the the dielectric and ferrite coated cylindrical slot is equivalent to the inner and outer cylindrical layers of magnetic currents and charges as illustrated in Fig.5.6. A novel expression is formulated using the MFIE from Eq.(5.21) and the complementary equations from Sec.5.3. This modified MFIE can be easily extended to a curved FSS using the MOM as previously illustrated in Sec.5.2.2.

The quasi-static equations for a dielectric coated cylindrical slot will be discussed in Sec.5.4.1. It is shown that these equations are complementary to those for a ferrite coated metallic dipole element (Sec.4.3.2). The quasi-static approximation for a dielectric and ferrite coated wire antenna was first formulated by Popovic [7]. In Sec.5.4.2, the quasi-static equations for a ferrite coated cylindrical slot will be discussed. Similarly, they are complementary to those for a dielectric coated metallic dipole element (Sec.4.3.1). The modified MFIE for both coatings will be shown in Eq.(5.90). This is in contrast to Popovic's EFIE in Eq.(4.49) as shown in Table 5.3 here to compare the duality of both integral equations.

Magnetic field due to electric current.	Electric field due to magnetic current .
$\vec{\nabla}.\vec{B}=0$ (5.45)	$\vec{\nabla}.\vec{D}_f=0$ (5.58)
$\vec{\nabla}\times\vec{B}=\mu_o\vec{J}$ (in free space) (5.46)	$\vec{\nabla}\times\vec{D}_f=-\varepsilon_o\vec{J}_f$ (in free space) (5.59)
$\vec{\nabla}.\vec{J}=0$ (5.47)	$\vec{\nabla}.\vec{J}_f=0$ (5.60)
$\oint_{\substack{closed\\surface}}\vec{B}.\hat{n}dS=0$ (5.49)	$\oint_{\substack{closed\\surface}}\vec{D}_f.\hat{n}dS=0$ (5.62)
$\frac{\vec{\nabla}\times\vec{B}}{\mu_o}=\vec{J}+\vec{J}_m$ (in ferrite medium) (5.50)	$\frac{\vec{\nabla}\times\vec{D}_f}{-\varepsilon_o}=\vec{J}_f+\vec{J}_n$ (in dielectric medium) (5.63)
$\vec{J}_m=\vec{\nabla}\times\vec{M}$ (5.51)	$\vec{J}_n=-\vec{\nabla}\times\vec{N}$ (5.64)
$\vec{H}=\frac{\vec{B}}{\mu_o}-\vec{M}$ (5.52)	$-\vec{E}_f=\frac{\vec{D}_f}{\varepsilon_o}+\vec{N}$ (5.65)
$\vec{\nabla}\times\vec{H}=\vec{J}$ (5.53)	$\vec{\nabla}\times\vec{E}_f=-\vec{J}_f$ (5.66)
$\vec{B}=\mu\vec{H}$ (5.54)	$\vec{D}_f=\varepsilon\vec{E}_f$ (5.67)
$\vec{M}=(\mu_r-1)\vec{H}$ (5.55)	$\vec{N}=(\varepsilon_r-1)\vec{E}_f$ (5.68)
$\vec{J}_{ms}=\vec{M}\times\hat{n}$ (5.56)	$\vec{J}_{ns}=-\vec{N}\times\hat{n}$ (5.69)
$\oint_C\vec{H}.d\vec{l}=I$ (5.57) Ampere's law	$\oint_C\vec{E}_f.d\vec{l}=-I_f$ (5.70) Complementary Ampere's law

Table 5.2

Types of integral equation	Complementary forms of the integral equation
EFIE (free standing)	$\vec{E}_i = \frac{j\omega\mu_o}{4\pi} \int_{segment} I\hat{s}g(R_a)ds + \frac{1}{4\pi\varepsilon_o} \int_{segment} \left(\frac{-1}{j\omega}\frac{dI}{ds}\right)\vec{\nabla}g(R_a)ds$ (4.48)
Popovic's EFIE	$\vec{E}_i = \frac{j\omega\mu_o}{4\pi}\left[\int_{segment} \mu_r I\hat{s}g(R_a)ds - \int_{segment}(\mu_r - 1)I\hat{s}g(R_b)ds\right]$ $+\frac{1}{4\pi\varepsilon_o}\left[\int_{segment} \frac{1}{\varepsilon_r}\left(\frac{-1}{j\omega}\frac{dI}{ds}\right)\vec{\nabla}g(R_a)ds\right]$ $+\frac{1}{4\pi\varepsilon_o}\left[\int_{segment}\left(1-\frac{1}{\varepsilon_r}\right)\left(\frac{-1}{j\omega}\frac{dI}{ds}\right)\vec{\nabla}g(R_b)ds\right]$ (4.49)
MFIE (free standing)	$\vec{H}_i = \frac{j\omega\varepsilon_o}{4\pi} \int_{segment} 2I_f\hat{s}g(R_a)ds + \frac{1}{4\pi\mu_o} \int_{segment} \left(\frac{-1}{j\omega}\frac{2dI_f}{ds}\right)\vec{\nabla}g(R_a)ds$ (5.89) (Eq.5.21 is rewritten here as Eq.5.89)
New MFIE	$\vec{H}_i = \frac{j\omega\varepsilon_o}{4\pi}\left[\int_{segment} \varepsilon_r 2I_f\hat{s}g(R_a)ds - \int_{segment}(\varepsilon_r - 1)2I_f\hat{s}g(R_b)ds\right]$ $+\frac{1}{4\pi\mu_o}\left[\int_{segment} \frac{1}{\mu_r}\left(\frac{-1}{j\omega}\frac{2dI_f}{ds}\right)\vec{\nabla}g(R_a)ds\right]$ $+\frac{1}{4\pi\mu_o}\left[\int_{segment}\left(1-\frac{1}{\mu_r}\right)\left(\frac{-1}{j\omega}\frac{2dI_f}{ds}\right)\vec{\nabla}g(R_b)ds\right]$ (5.90)

Table 5.3

The duality of both EFIE and MFIE can be seen in the interchange of variables as shown in Table 5.4.

Popovic's EFIE	New MFIE
$\vec{E}_i$	$\vec{H}_i$
I	$2I_f$
μ_o	ε_o
μ_r	ε_r

Table 5.4

The details of the derivation of the new MFIE will be shown in the following sections.

5.4.1 Quasi static equivalent of dielectric coated slot

A segment of thin slot of width $2a$ with dielectric substrate thickness (b-a) is modelled here as inner and outer cylindrical layers of magnetic currents with magnetic charge in the inner layer. This slotted segment can be consider to be similar to a cylindrical slotted segment of radius a coated with a layer of dielectric with permittivity ε where the outer radius is $\rho = b$ as shown in Fig.5.6. Note that the MFIE in a free standing case shows that the magnetic current flowing in the slotted segment is $2I_f$ (Eq.5.89). This cylindrical segment is assumed to behave like a quasi-static infinitely long cylindrical structure. Thus for a dielectric coating of thickness (b-a), the electric field intensity $\vec{E}_f$ would circulate around the cylindrical segment of radius a with current $2I_f$ according to the complementary Ampere's law in Eq.(5.70) in Table 5.2.

Therefore, $$E_{f\phi} = \frac{-2I_f}{2\pi\rho} \tag{5.71}$$

According to Eq.(5.68), the complementary magnetisation vector $\vec{N}$ should be flowing in the same direction of the electric field intensity. Therefore, Eq.(5.71) implies that $\vec{N}$ is also circulating around the cylindrical surface with the centre at the slotted segment axis. So the ϕ component is given by N_ϕ from Eq.(5.68) as:

$$N_\phi = (\varepsilon_r - 1)E_{f\phi} \tag{5.72}$$

Substituting Eq.(5.72) into Eq.(5.71) yields,

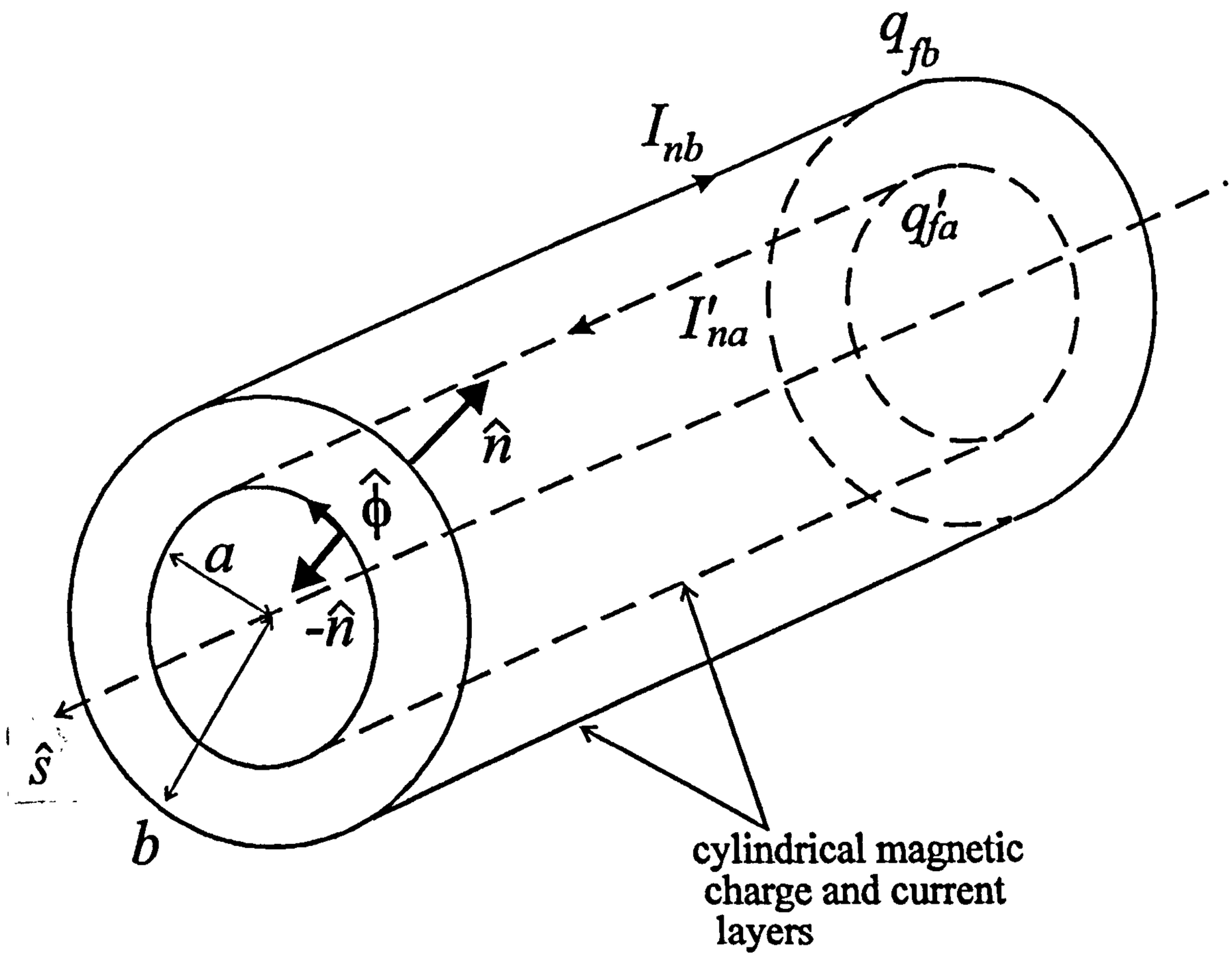

Fig.5.6 Slotted segment with dielectric and ferrite coatings represented by magnetic charge and current layers.

$$N_\phi = -(\varepsilon_r - 1)\frac{2I_f}{2\pi\rho} \tag{5.73}$$

There is also a radial magnetisation magnetic current density of $\frac{-\partial N_\phi}{\partial s}$ in the coating. The normal vector $-\hat{n}$ is pointing inwards from the inner surface $\rho = a$ as shown in Fig.5.6. Therefore, from Eq.(5.69), the complementary magnetisation current density is given by,

$$\vec{J}_{na} = -N_\phi \hat{\phi} \times (-\hat{n}) = -N_\phi \hat{s} \tag{5.74}$$

From Eq.(5.73) and Eq.(5.74), it is evident that the surface magnetisation current I_{na} at $\rho = a$ is,

$$I_{na} = (\varepsilon_r - 1)2I_f \tag{5.75}$$

However, the total current at $\rho = a$ is the sum of the magnetisation current I_{na} and the conducting current $2I_f$. Therefore, the total current I'_{na} is given by:

$$I'_{na} = \varepsilon_r 2I_f \tag{5.76}$$

At the outer surface $\rho = b$, the normal vector $\hat{n}$ is pointing away from the surface. So the surface magnetisation current density should flow in the reverse direction and is given by,

$$\vec{J}_{nb} = -N_\phi \hat{\phi} \times \hat{n} = N_\phi \hat{s} \tag{5.77}$$

Thus the surface magnetisation current at $\rho = b$ from Eq.(5.73) and Eq.(5.77) is,

$$I_b = -(\varepsilon_r - 1)2I_f \tag{5.78}$$

Thus, the dielectric coated cylindrical slotted dipole segment is equivalent to the inner and outer cylindrical layers of magnetic currents I'_{na} and I_{nb} with magnetised charge density $2q_f$ in the inner layer. The effect of the radial current density is negligible

because of the thin coating. Note that the charge is not dependent on the permittivity as shown in the MFIE in Eq.(5.89). The charge per unit length is given by

$$q_f = \frac{-1}{j\omega}\frac{dI_f}{ds}.$$

5.4.2 Quasi static equivalent of ferrite coated slot

The segment of a slot width $2a$ with ferrite substrate thickness $(b\text{-}a)$ is modelled here as a cylindrical dipole segment of radius a with ferrite coating of the same thickness. The cylindrical magnetic charge density of the segment is $2q_f$ at $\rho=a$. The factor of 2 in the charge comes from the derivation of the magnetic current $2I_f$ in the free standing MFIE as shown in Eq.(5.89) The cylindrical coated dipole segment can be approximated as inner cylindrical layer of magnetic charge and magnetic current at $\rho=a$ with outer cylindrical layer of magnetic charge at $\rho=b$. This cylindrical segment is assumed to behave like a quasi-static infinitely long cylindrical structure.

According to the complementary Gauss's law the total outward flux of the magnetic displacement $\vec{B}_f$ over any enclosed surface in the ferrite medium is equal to the total free magnetic charge Q_f enclosed in the surface. Therefore, using Eq.(5.44) for a cylindrical structure gives,

$$B_{f\rho} = \frac{2q_f}{2\pi\rho} \tag{5.79}$$

The subscript ρ denotes the radial component of the flux $\vec{B}_{f\rho}$.

From Eq.(5.42), the magnetic field intensity, $\vec{H}_f$, is given by,

$$\vec{H}_f = H_{f\rho}\hat{n} = \frac{B_{f\rho}}{\mu}\hat{n} = \frac{2q_f}{2\pi\rho\mu}\hat{n} \tag{5.80}$$

From Eq.(5.41) the polarisation charge vector, $\vec{P}_f$,is given by,

$$\vec{P}_f = \vec{B}_f - \mu_o\vec{H}_\rho \tag{5.81}$$

Substituting Eq.(5.79) and Eq.(5.80) into Eq.(5.81) yields,

$$\vec{P}_f = \frac{2q_f}{2\pi\rho}\hat{n} - \frac{2q_f}{2\pi\rho}\frac{\mu_o}{\mu}\hat{n} = \frac{2q_f}{2\pi\rho}\left(1 - \frac{1}{\mu_r}\right)\hat{n} \tag{5.82}$$

Therefore, from Eq.(5.82) at the inner radius, $\rho=a$, the polarised charge vector is ,

$$\vec{P}_{fa} = \frac{2q_f}{2\pi a}\left(1 - \frac{1}{\mu_r}\right)\hat{n} \tag{5.83}$$

And at the outer radius, $\rho=b$, the polarised charge vector is,

$$\vec{P}_{fb} = \frac{2q_f}{2\pi b}\left(1 - \frac{1}{\mu_r}\right)\hat{n} \tag{5.84}$$

The ferrite surface charge density q_{fa} at $\rho=a$ is,

$$q_{fa} = \oint_{\substack{cylindrical\\circumference}} \vec{P}_{fa}.(-\hat{n})dS_c = \int_{-\pi}^{\pi} \frac{2q_f}{2\pi a}\left(1 - \frac{1}{\mu_r}\right)\hat{n}.(-\hat{n})a\,d\phi$$

$$= -2q_f\left(1 - \frac{1}{\mu_r}\right) \tag{5.85}$$

(Note that the integral over the surface S is reduced to a line integral over the circumference S_c because of the charge density $2q_f$.)

Since the ferrite encloses a line magnetic charge density of $2q_f$ at $\rho=a$, the total magnetic charge density, q'_{fa} , at $\rho=a$ is the sum of $2q_f$ and ferrite surface charge density q_{fa}.

$$q'_{fa} = 2q_f + q_{fa} = 2q_f - 2q_f\left(1 - \frac{1}{\mu_r}\right) = \frac{2q_f}{\mu_r} = \frac{1}{\mu_r}\left(\frac{-1}{j\omega}\frac{2dI_f}{ds}\right) \tag{5.86}$$

Similarly, for the surface magnetic charge density q_{fb} at $\rho=b$,the outer radius, the normal vector, $\hat{n}$, is pointing outwards, so,

$$q_{fb} = \oint_{\substack{cylindrical \\ circumference}} \vec{P}_{fb}.\hat{n}dS_c = \int_{-\pi}^{\pi} \frac{2q_f}{2\pi b}\left(1-\frac{1}{\mu_r}\right)\hat{n}.\hat{n}b\,d\phi$$

$$=\left(1-\frac{1}{\mu_r}\right)2q_f=\left(1-\frac{1}{\mu_r}\right)\left(\frac{-1}{j\omega}\frac{2dI_f}{ds}\right) \tag{5.87}$$

The radial polarisation magnetic current density in the coating is,

$$\vec{J}_{f\rho} = j\omega\vec{P}_{f\rho} \tag{5.88}$$

Therefore, for the ferrite coated slot dipole segment, the effect is equivalent to the magnetic charge density q'_{fa} and magnetic current $2\bar{I}_f$ at the inner cylindrical surface and q_{fb} on the outer cylindrical surface. The magnetic current is not changed since the quasi-static approximation is not dependent on the permittivity in the original MFIE in Eq.(5.89). The effect of the radial current density is negligible.

In general, for both dielectric and ferrite coatings, the quasi-static approximation can be represented by the magnetic currents I'_{na} and I_{nb} and magnetic charge densities q'_{fa} and q_{fb} on the two cylindrical surfaces. The magnetic field of the MFIE is computed along the segment axis. Here the magnetic field due to the radial polarisation and magnetisation currents is zero because the radial currents only exist in the coating. When the magnetic field due to this coated segment is computed along the axis of any other segment, the field due to the radial currents can be neglected, because these radial currents are uniformly distributed in all directions in a small area. Thus, the fields due to the slot segment and the coating are the contributions from inner cylindrical layer of magnetic charge density q'_{fa} and magnetic current I'_{na} at ρ=a, and outer layer at q_{fb} and I_{nb} at ρ= b as shown in Fig.5.6

From Eq.(5.21), the MFIE in free space for a slotted dipole segment of radius a can be rewritten as:

$$\vec{H}_l = \frac{j\omega\varepsilon_o}{4\pi}\int_{segment} 2I_f\hat{s}g(R_a)ds + \frac{1}{4\pi\mu_o}\int_{segment}\left(\frac{-1}{j\omega}\frac{2dI_f}{ds}\right)\vec{\nabla}g(R_a)ds \tag{5.89}$$

Substituting Eq.(5.76), Eq.(5.78), Eq.(5.86) and Eq.(5.87) into Eq.(5.89) yields,

$$\vec{H}_i = \frac{j\omega\varepsilon_o}{4\pi}\left[\int_{segment}\varepsilon_r 2I_f\hat{s}g(R_a)ds - \int_{segment}(\varepsilon_r - 1)2I_f\hat{s}g(R_b)ds\right]$$

$$+\frac{1}{4\pi\mu_o}\left[\int_{segment}\frac{1}{\mu_r}\left(\frac{-1}{j\omega}\frac{2dI_f}{ds}\right)\vec{\nabla}g(R_a)ds + \int_{segment}\left(1-\frac{1}{\mu_r}\right)\left(\frac{-1}{j\omega}\frac{2dI_f}{ds}\right)\vec{\nabla}g(R_b)ds\right]$$

(5.90)

R_a and R_b are the distances from the inner and outer radius to the point of observation as shown in Fig.5.7 .

Eq.(5.90) is the novel expression of the MFIE for modelling thin slot with dielectric and ferrite substrate using the concept of magnetic charge and current. This expression is compared with Popovic's EFIE in Eq.(4.19) as shown in Table 5.3 to show the duality. The complementary nature of both integral equations is illustrated by a simple interchange of variables as shown in Table 5.4.

Since the slotted FSS used in the experiment is supported by dielectric substrate, only the dielectric loaded version of Eq.(5.90) is used in the model. Therefore, without the ferrite material, $\mu_r = 1$. Substituting this into Eq.(5.90) confirms that the magnetic current component in the new MFIE is independent of the permeability of the ferrite.

The new impedance square matrix for the new MFIE with dielectric coating becomes,

$$A_{mn} = \frac{-2}{j\omega 4\pi\mu_o}\left\{\varepsilon_r\left(k_o^{2\,a}\psi(m)^n_{n-1/2}\hat{s}_{n-1/2} + k_o^{2\,a}\psi(m)^{n+1/2}_n\hat{s}_{n+1/2}\right)\cdot\left(\vec{r}_{m+1/2} - \vec{r}_{m-1/2}\right)\right.$$

$$-(\varepsilon_r - 1)\left(k_o^{2\,b}\psi(m)^n_{n-1/2}\hat{s}_{n-1/2} + k_o^{2\,b}\psi(m)^{n+1/2}_n\hat{s}_{n+1/2}\right)\cdot\left(\vec{r}_{m+1/2} - \vec{r}_{m-1/2}\right)$$

$$+\left(\frac{{}^a\psi\left(m+\tfrac{1}{2}\right)^{n+1}_n}{(s_{n+1}-s_n)} + \frac{{}^a\psi\left(m+\tfrac{1}{2}\right)^{n}_{n-1}}{(s_n-s_{n-1})} + \frac{{}^a\psi\left(m-\tfrac{1}{2}\right)^{n+1}_n}{(s_{n+1}-s_n)} - \frac{{}^a\psi\left(m-\tfrac{1}{2}\right)^{n}_{n-1}}{(s_n-s_{n-1})}\right)$$

(5.91)

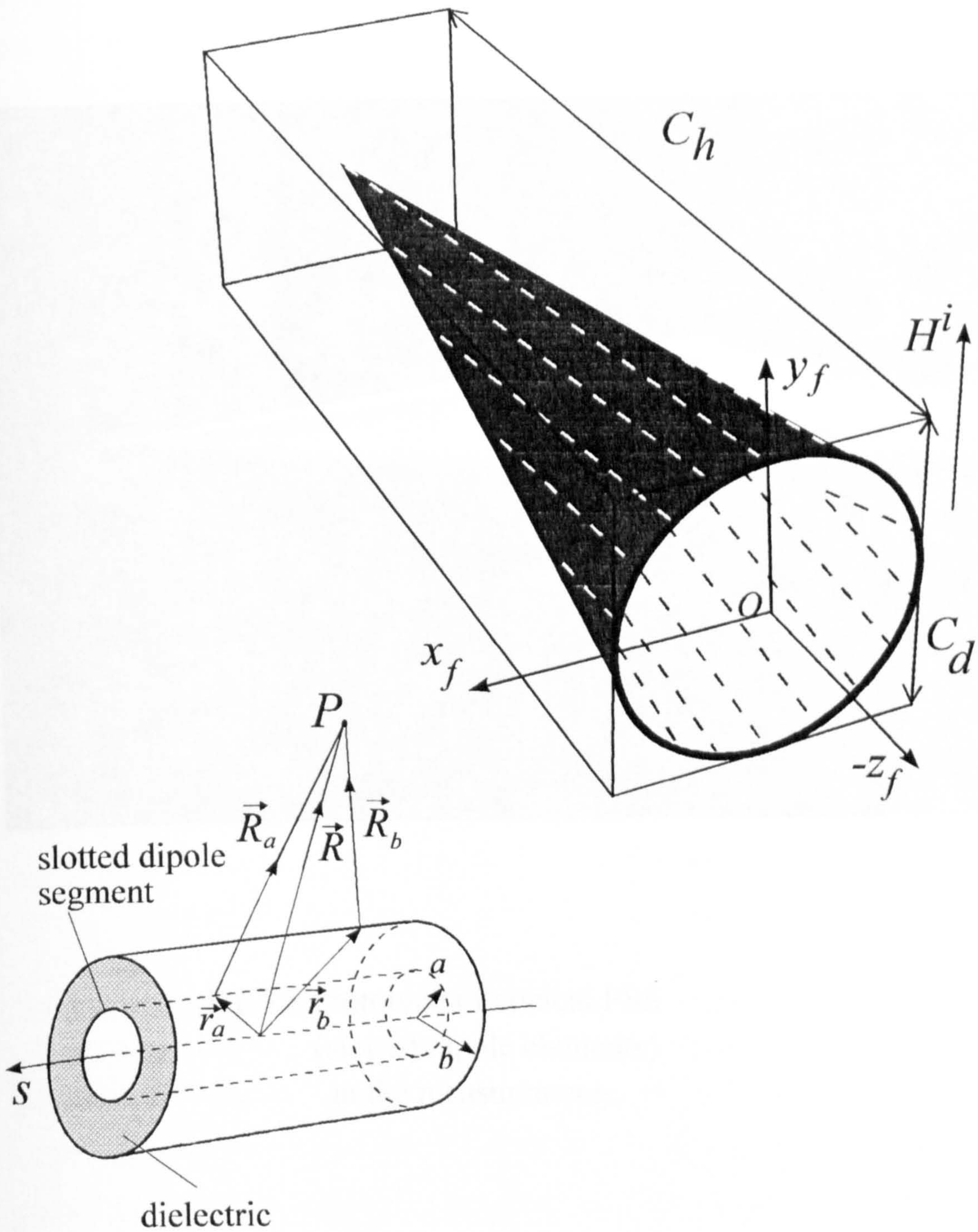

Fig. 5.7 Geometry of the conical FSS and the model of a dielectrically loaded slotted segment.

Fig.5.8 Prototype of conical FSS
(slotted dipole elements)
in the measurements.

The superscript on the top left hand side of ψ denotes the radius of the dipole segment. (Please refer to Eqs.(4.52), (4.63), (4.54) and (4.55) in Chap.4 for further details of the above variables.)

The scattered far fields from each current pulse is computed in the same manner as in the free standing case in Eq.(5.26), with the exception of the dielectric loading effect on the current pulse (For further descriptions please also refer to pp.96-97). The total radiated fields from the slotted FSS with dielectric backing is also given by the same expression in Eq.(5.28).

The above equation can be easily incorporated into the computer model of the former metallic FSS by virtual of the duality with the slotted FSS. A new computer model of the slotted FSS was developed with a view of predicting the radiation patterns and boresight losses. This has been named the finite current model (FC) because it could account for all the couplings of the FSS elements. The predictions were compared with the experimental results of a conical prototype as discussed in the next section.

5.5 Results

In this Section, the experimental results are obtained using a conical slotted FSS supported by dielectric substrate. These are compared with the predictions obtained from the computer model using the quasi static approximation of the MFIE as discussed in the Sec.5.4. The geometry of the cone and feed system is the same as Fig.3.3 in Chap.3. Fig.5.8 shows the actual FSS cone enclosing the corrugated conical feed which is positioned at the base of the cone. The automated set-up as described in Sec.4.4 has been used. .

A corrugated feed whose aperture plane is located at 0 has been used to illuminate the inner area of the cone. The orientation of the FSS elements in relation to the feed magnetic field is shown in Fig.5.7. A conical FSS consists of two identical half sectors on the $z_f - x_f$ plane, representing the top and bottom parts of the surface. Both sectors were initially printed on same sheet of dielectric substrate with ε_r=3 and thickness 0.071mm (*b-a*). This was wrapped into a conical shape and glued on one side. The length of each dipole slot is 8.9mm, the width 0.3 mm (a=0.15 mm) and the element spacing is 12mm arranged in a square lattice in each sector when it was planar. In the FC model, the diameter of a cylindrical slot is the same as the width of a flat dipole FSS element. The cone is just over 30 cm long with a base diameter of 12.6 cm The feed aperture has a diameter of 9.6 cm. The number of elements falling within the area of illumination in the theoretical feed model is 354 for the SPS and 236 for the PB

feed model .Each slot is divided into 6 segments. The total number of matrix elements in the MOM were 1770X1770 for SPS and 1180X1180 for PB.

In Sec.5.5.1 the measured and predicted transmission response for both a free standing and dielectric FSS cone will be discussed and compared using the computer model with the new MFIE formulation. Predictions with modal analysis, from an infinite planar array with the same element and lattice geometry, have been used to compare with the the results from the FC model. In Sec.5.5.2 the predicted radiation patterns, using the novel MFIE with quasi static approximation will be validated. The SPS and PB feed models (For descriptions of feed models please see Sec.3.3.2) have been used to calculate the fields radiated from the feed aperture which is illuminating the conical FSS.

5.5.1 Transmission response

This Section is devoted to the boresight losses in the transmission response of the FSS. Initially, the boresight losses from the modal analysis from a planar array will be compared with the FC model for free standing case as shown in Fig.5.9. Then the new MFIE is assessed for the quasi-approximation of the dielectric coating in Fig.5.10 to compare with amount of frequency shift in the modal analysis. Finally the SPS and PB feed model will be compared in Fig.5.11.

The predicted transmission response from the modal analysis for an infinite array of the same lattice and element geometry, at TE and TM incident at 45° is shown in Fig.5.9. For definition of the incidence state please refer to Fig.4.8a,b in Sec.4.4.1 (The slot dipole is however rotated by 90° and is lying on the x axis in Fig.4.8a and Fig.4.8b). The results are compared with the predictions using the FC model for a free standing slotted cone. Fig.5.9 shows that the SPS predicted pass band centre for a free standing case is about 16 GHz compared to measured value at 13.3 GHz for the slotted FSS dielectric cone. This shows that the conventional MFIE is not sufficient to predict the results for the slotted FSS with dielectric backing. The planar free standing infinite FSS gives a pass band centre at about 15.3 GHz for TE incidence and 14 GHz for TM case.

If the dielectric layer of 0.071 mm thick is included, the predicted bandwidth of the infinite array at TE 45° incidence, is reduced and band centre is shifted by about 0.7 GHz, from 15.3 GHz to 14.6 GHz (Fig.5.10). Very little shift in frequency is observed for TM case. The resonant frequency is expected to decrease because of the dielectric substrate. This shift is even greater for the SPS predictions using the novel MFIE for the FSS cone (Fig.5.10). The reduction in bandwidth is also predicted. The predicted

pass band centre is now shifted by 2.8 GHz, from 16 GHz (free standing case) to about 13.2 GHz for the dielectric case. Although the predicted loss is about -1.53 dB, about 6.37 dB higher than the measured loss, the profile of the transmitted response agrees very well. The location of the passband is clearly reproduced by the predictions except for distinct ripples in the measured results. The discrepancies could be due the mutual coupling between the feed and radome which have not been taken into account. Such coupling is expected to enhance because the cone is relatively small and close to the feed aperture.

The predictions using the PB feed model for the dielectric FSS cone shows that the maximum theoretical transmission loss is about -1.09 dB at 13.2 GHz, about the same value as the SPS feed model. As shown in Fig.5.11, the PB also predicts the profile of the transmission loss although the SPS predictions is slightly better near the pass band centre at 13.2 GHz.

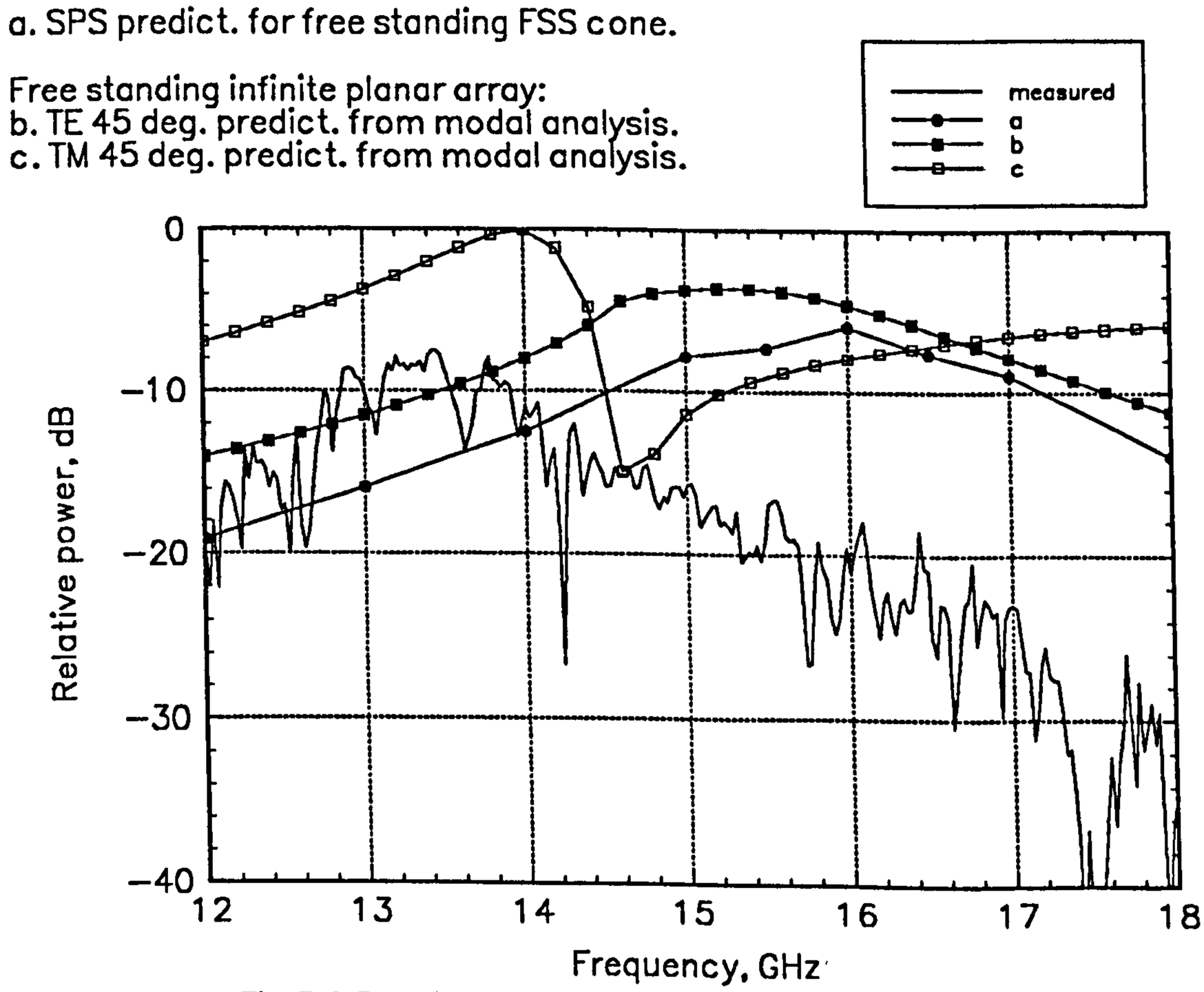

Fig.5.9 Passband response of a slotted conical array.

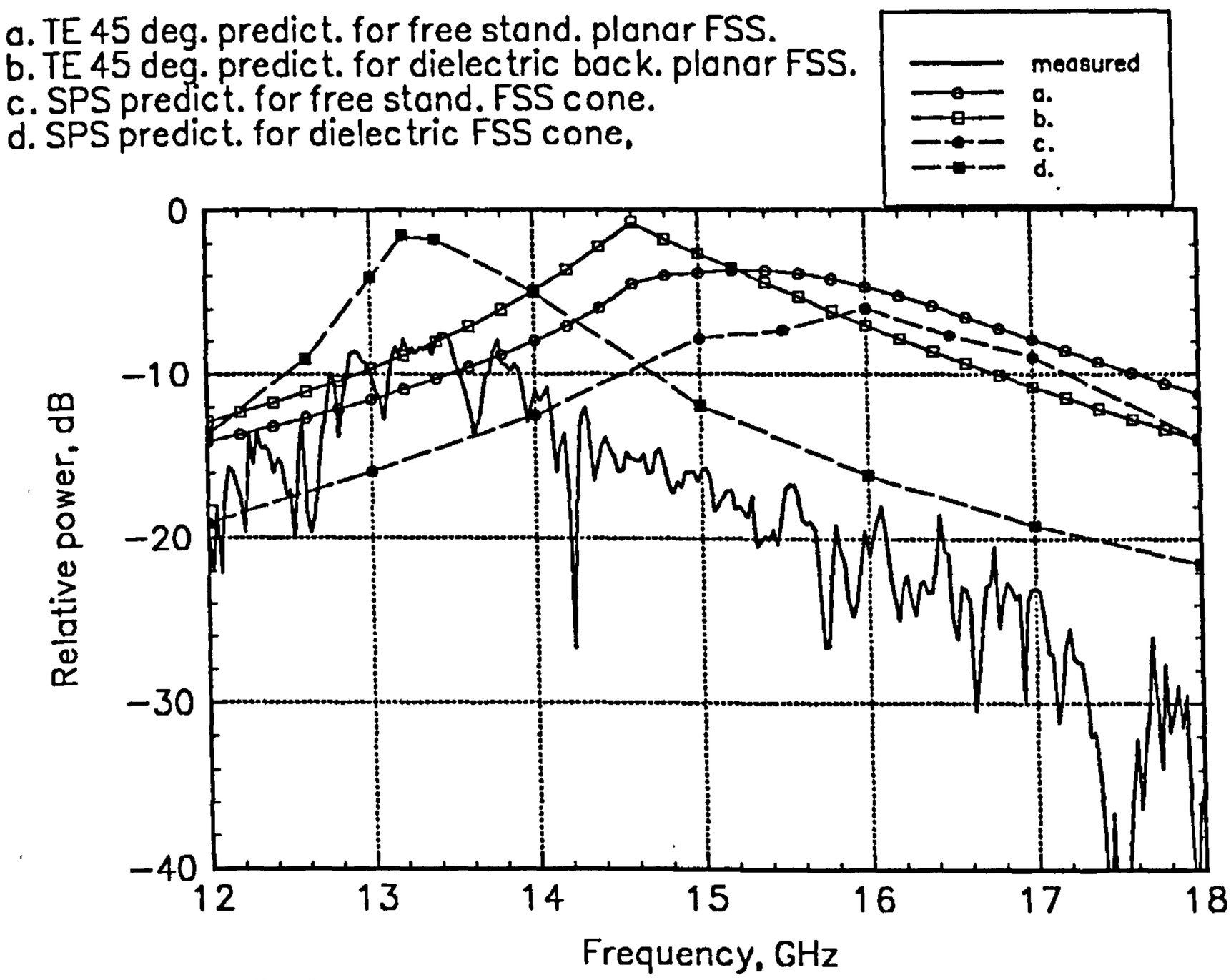

Fig.5.10 Passband response of a slotted conical array

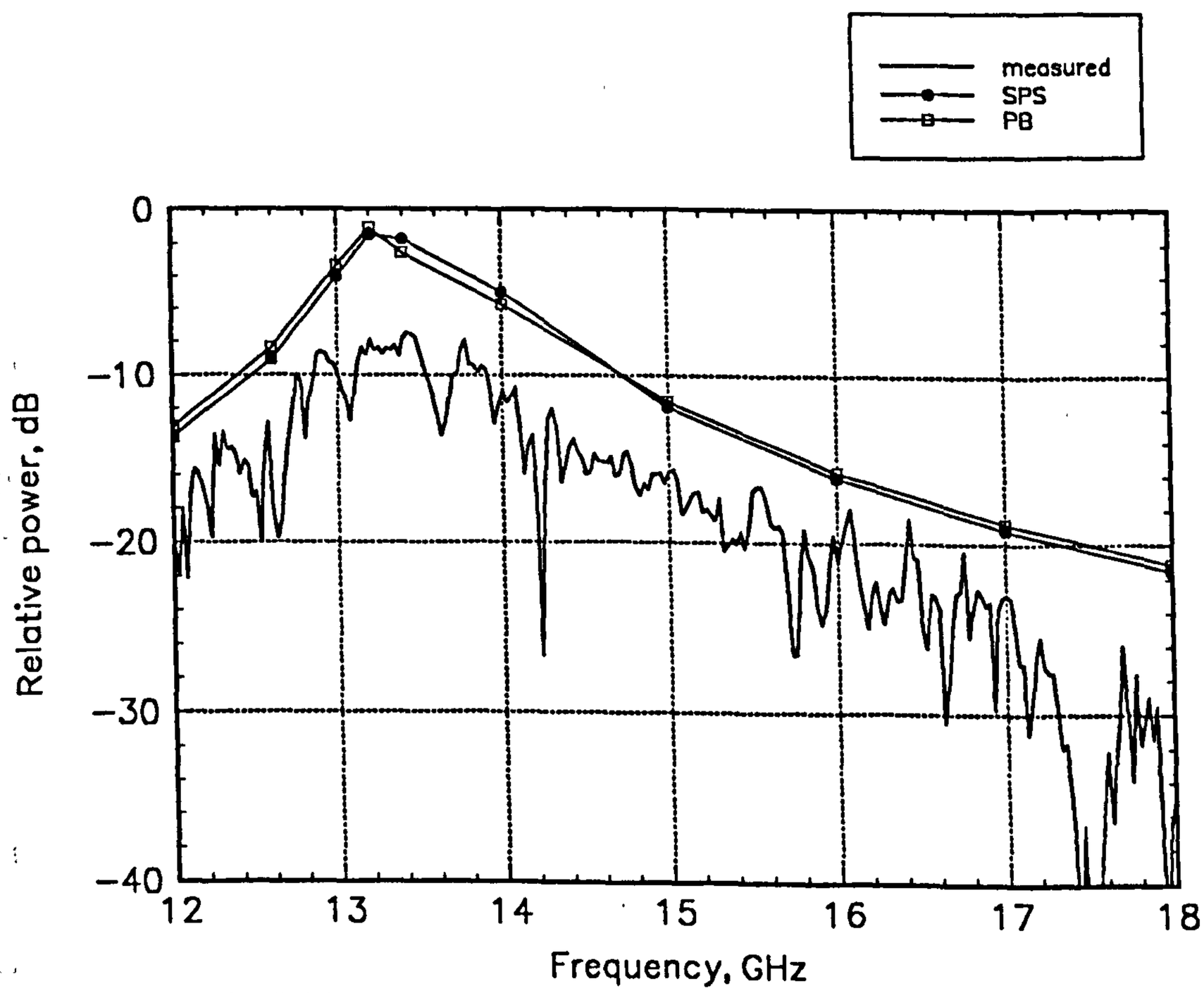

Fig.5.11 Passband response using SPS and PB feed models.

5.5.2 Radiation patterns

5.5.2.1 E -plane

Representative normalised copolar patterns at 13.0 GHz and 13.2 GHz which are near the pass band centre is shown in Fig.5.12a and Fig.5.13a. It is observed that the main lobe and the immediate side lobes are quite dominant in the radiation patterns. As the frequency departs from the passband centre, secondary side lobe levels at $\pm 40^{o}$ to $\pm 60^{o}$ scan would increase rapidly. This could be due to multiple reflections inside the radome and interactions between the feed and FSS since the electromagnetic wave is trapped inside the radome at non-resonant frequencies.

The measured main lobe and the location of the first pair of nulls have been predicted quite accurately by the SPS feed model. At 13.0 GHz and 13.2 GHz, the predicted side lobes are broader. The predictions seems to show a more symmetrical pattern compared to the measured. This could possibly be due to discontinuity at the seam between the top and bottom halves of the FSS array which is formed when the two halves are glued together at one side. This long but thin gap in the cone could have leaked some unwanted electromagnetic radiation when the FSS was excited by the feed.

The measured crosspolar levels at the boresight was very low, nearly -40.0 dB although side lobe levels were as high as -15.0 dB at -50° The SPS predictions are well below these value. When the feed was tilted by 0.5^{o} from the tip of the cone in the $z_f - x_f$ in the model, higher cross polar peaks up to -30.0 dB is predicted. It is very difficult to ensure that the feed axis is aligned along the axis of the cone in the measurements, therefore tilting of feed and slight rotation of the polarised H fields of the feed are inevitable. This misalignment may explain why the measured crosspolar level is higher than expected.

The PB predicts narrower main lobe and higher sidelobe levels as compared to the measurements in the E-plane. The copolar patterns at 13.2 GHz can be found in Fig.5.14a. The predicted nulls are also higher than the measured. As compared to the SPS feed model, the latter gives better predictions.

Fig.5.15a shows effect on the feed pattern at 13.2 GHz (the pass band centre frequency) when the conical FSS was covering the feed. Notice how the main lobe and side lobes of the feed pattern has been made narrower by the FSS. There was a loss of about -7.9 dB. This could be the result of mismatch in the dielectric substrate and coupling between the FSS and feed. The mismatch could potentially be improved if the

dielectric layer is of half wavelength thickness as in the case of pure dielectric radome [9].

5.5.2.2 H-plane

Fig.5.12b and Fig.5.13b show the corresponding normalised copolar patterns at the H-plane. Since the magnetic field is polarised along the same plane as the slot axis (Fig.5.7), the main lobe in the copolar patterns in this plane can be expected to be broader than the E-plane. The immediate and secondary side lobe levels are also higher than those in the E-plane. The SPS predicted the main lobe very well, especially at 13.2 GHz. However, the first side lobe levels are lower than the measured ones. The first pair of nulls is predicted very well at $\pm 20^{o}$. The measured cross-polar levels at the boresight was slightly higher than the E-plane but side lobe levels were generally lower. The SPS feed model however, predicts side lobes levels below -40 dB. This could be due to the misalignment of the feed as discussed in Sec.5.5.2.1.

The PB predictions show narrower main lobe and lower side lobe levels as compared to the measurements in the H-plane. Copolar patterns at 13.2 GHz can be found in Fig.5.14b. The first pair of sidelobes and nulls are not predicted very well as compared to the SPS model.

Fig.5.15b shows how the conical FSS has affected the feed pattern in the H-plane at 13.2 GHz. Notice now the main lobe of the feed pattern has been flatten, leaving a plateau shape up to $\pm 10^{o}$ scan azimuth. Side lobe levels also tends to be higher and oscillates very rapidly in this plane. This could be due to mutual coupling between the feed and FSS in the H-plane.

5.5.2.3 45° plane

The normalised copolar patterns at 45° plane across this frequency band seem to show the same trend as the principal plane except that the size of the main lobe averages between the E and H plane. This can be expected since 45° is diagonally divided between the E and H-planes. Fig.5.16a and Fig.5.16b show the copolar and crosspolar patterns at 13.2 GHz compared with the SPS predictions. It is observed that the profile of the predicted copolar pattern agrees moderately with the measured with the exception of deeper null and slightly narrower main lobe. The crosspolar levels are also reproduced except for the more rapid oscillations in the measured levels. The predictions from the PB model also gives moderate predictions as shown in Fig.5.17a and Fig.5.17b.

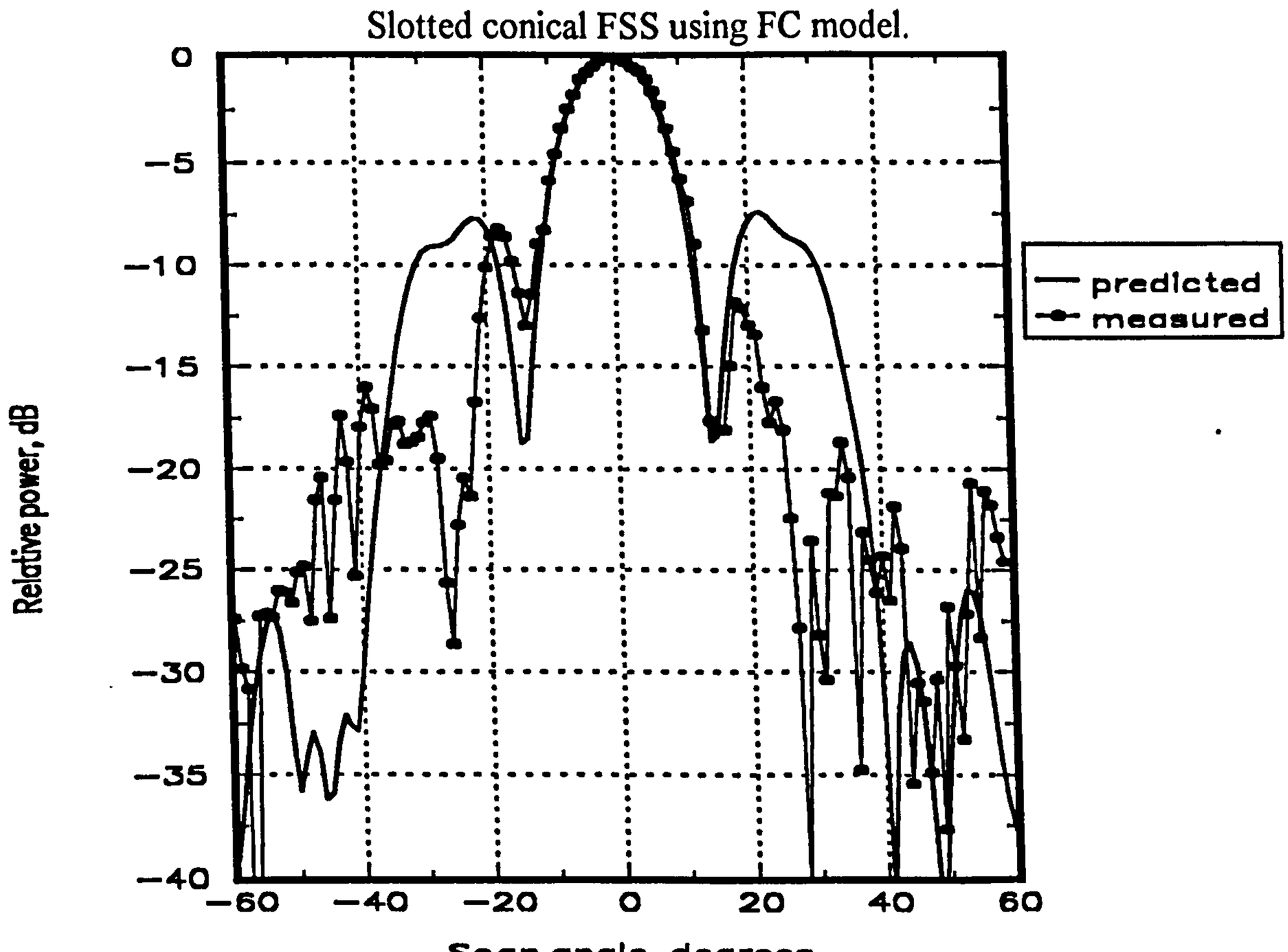

Fig.5.12a E—plane copolar pattern at 13 GHz using the SPS feed model.

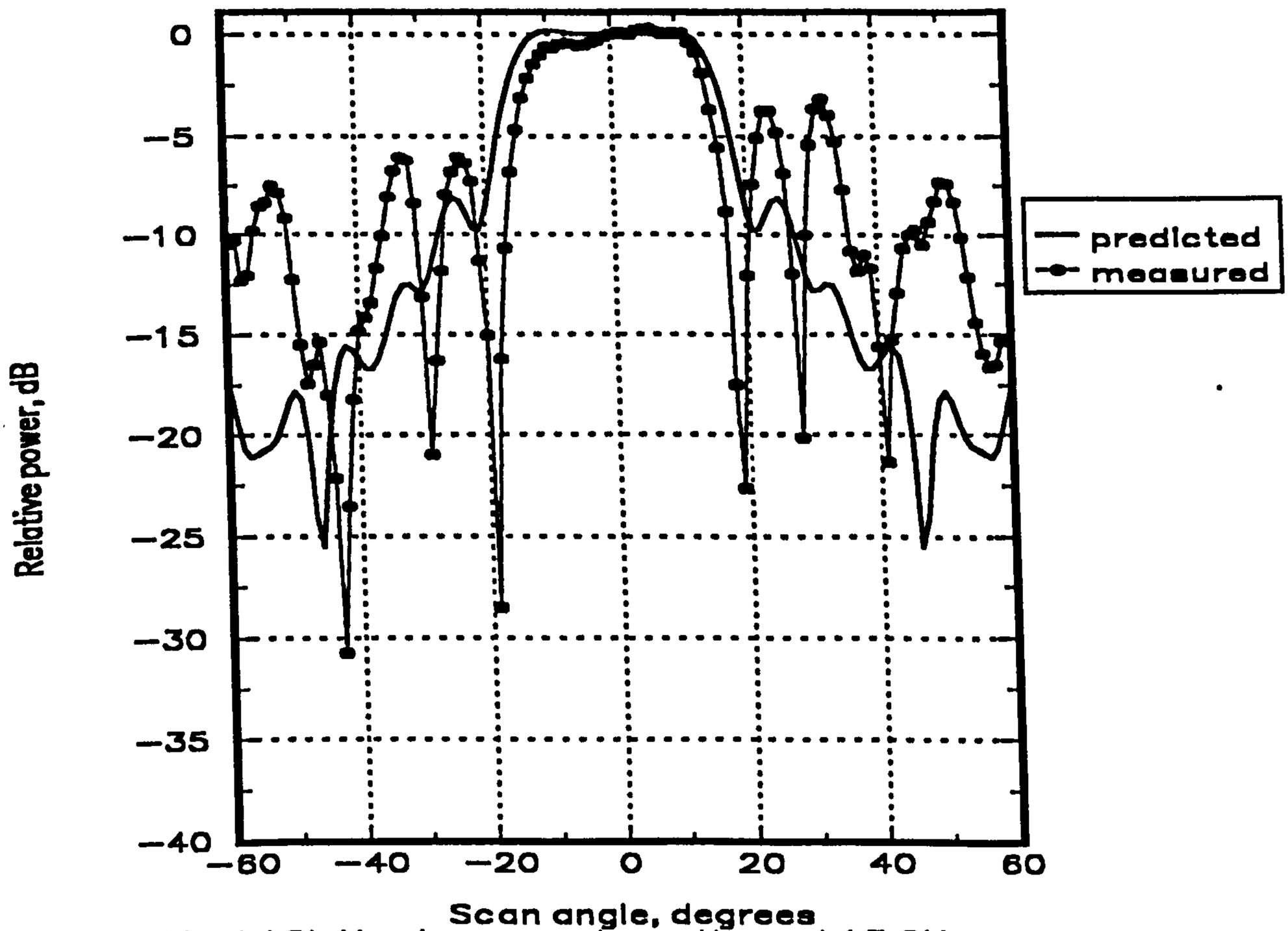

Fig.5.12b H—plane copolar pattern at 13 GHz using the SPS feed model.

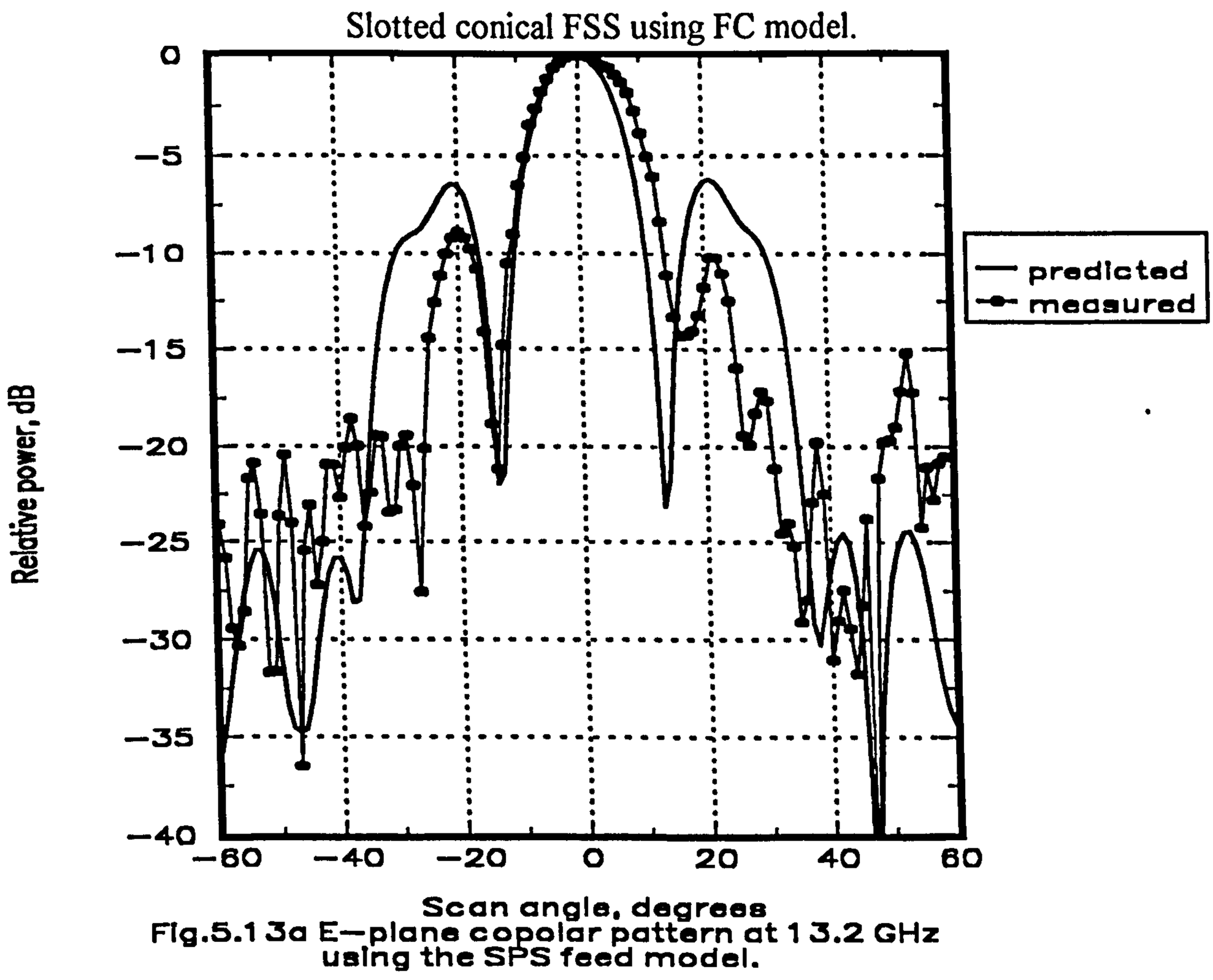

Fig.5.13a E—plane copolar pattern at 13.2 GHz using the SPS feed model.

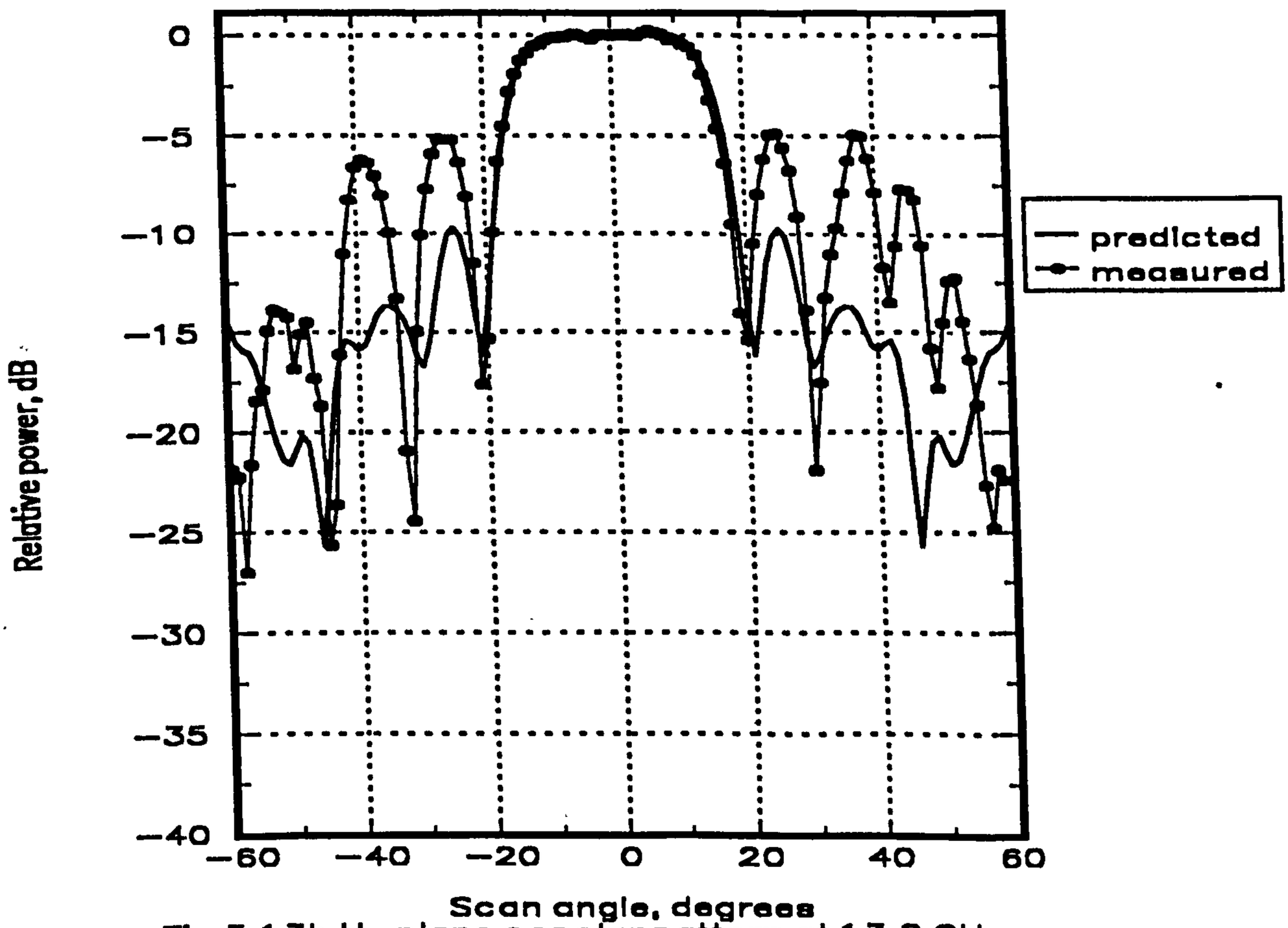

Fig.5.13b H—plane copolar pattern at 13.2 GHz using the SPS feed model.

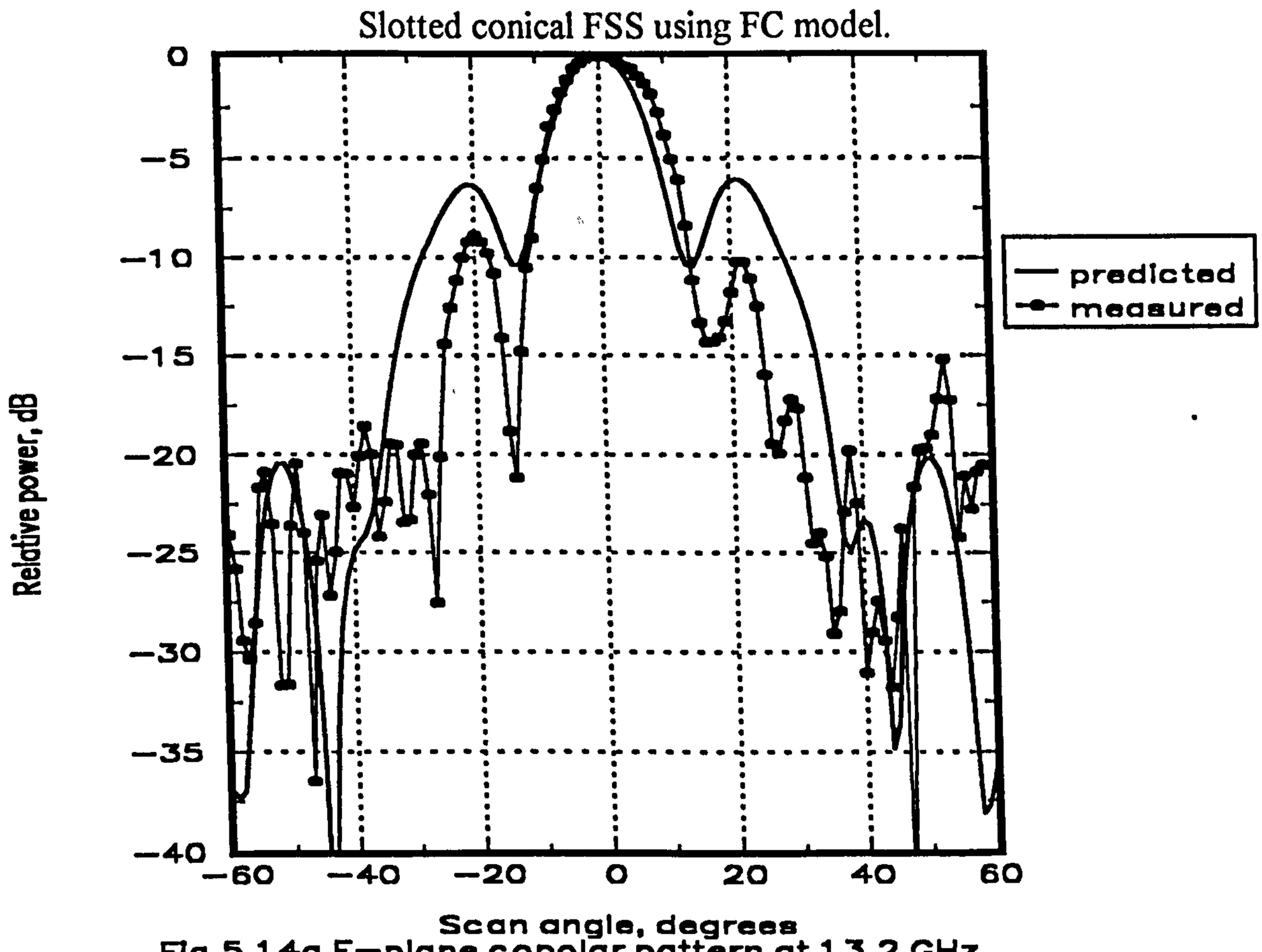

Fig.5.14a E−plane copolar pattern at 13.2 GHz using the PB feed model.

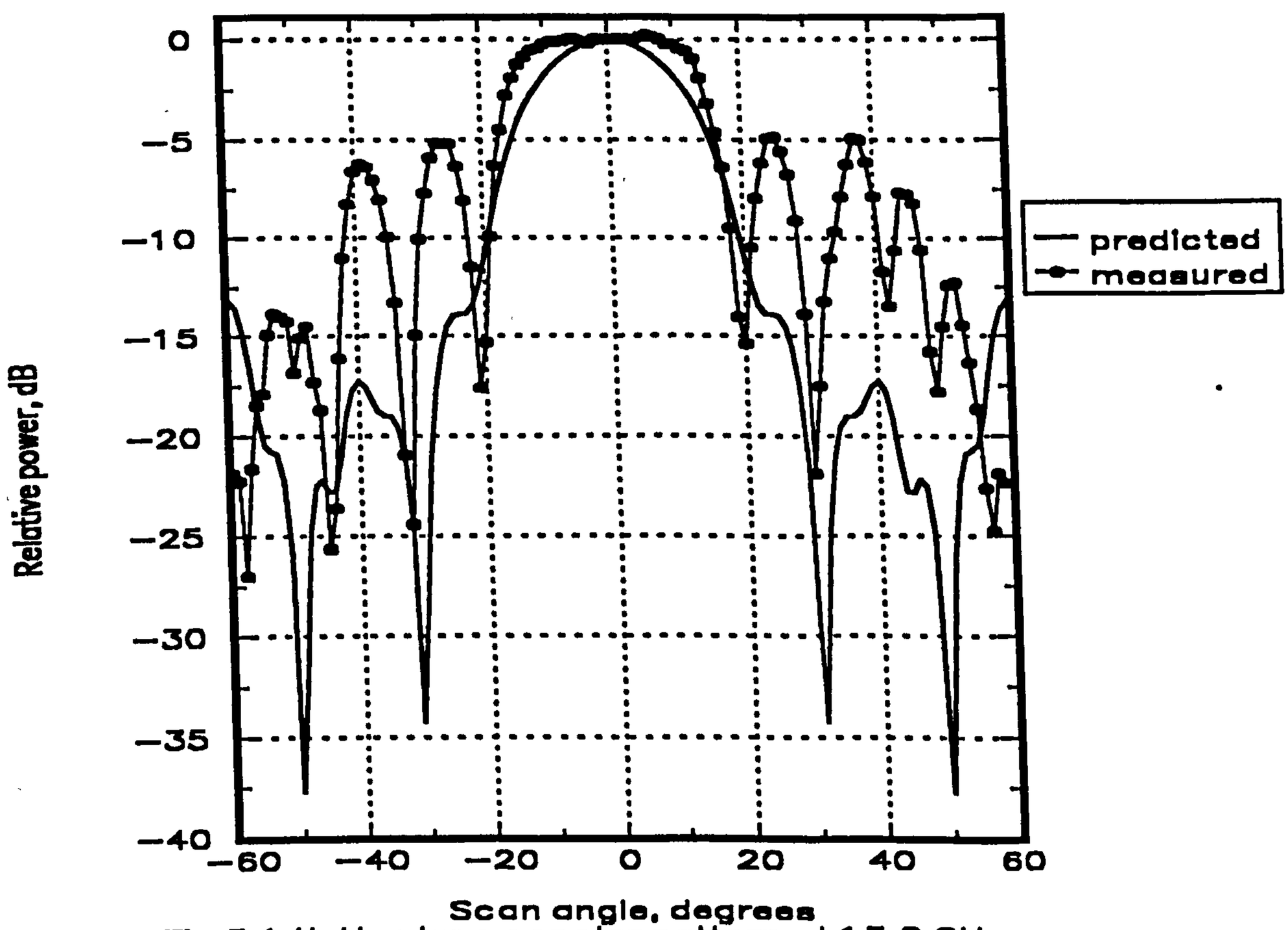

Fig.5.14b H−plane copolar pattern at 13.2 GHz using the PB feed model.

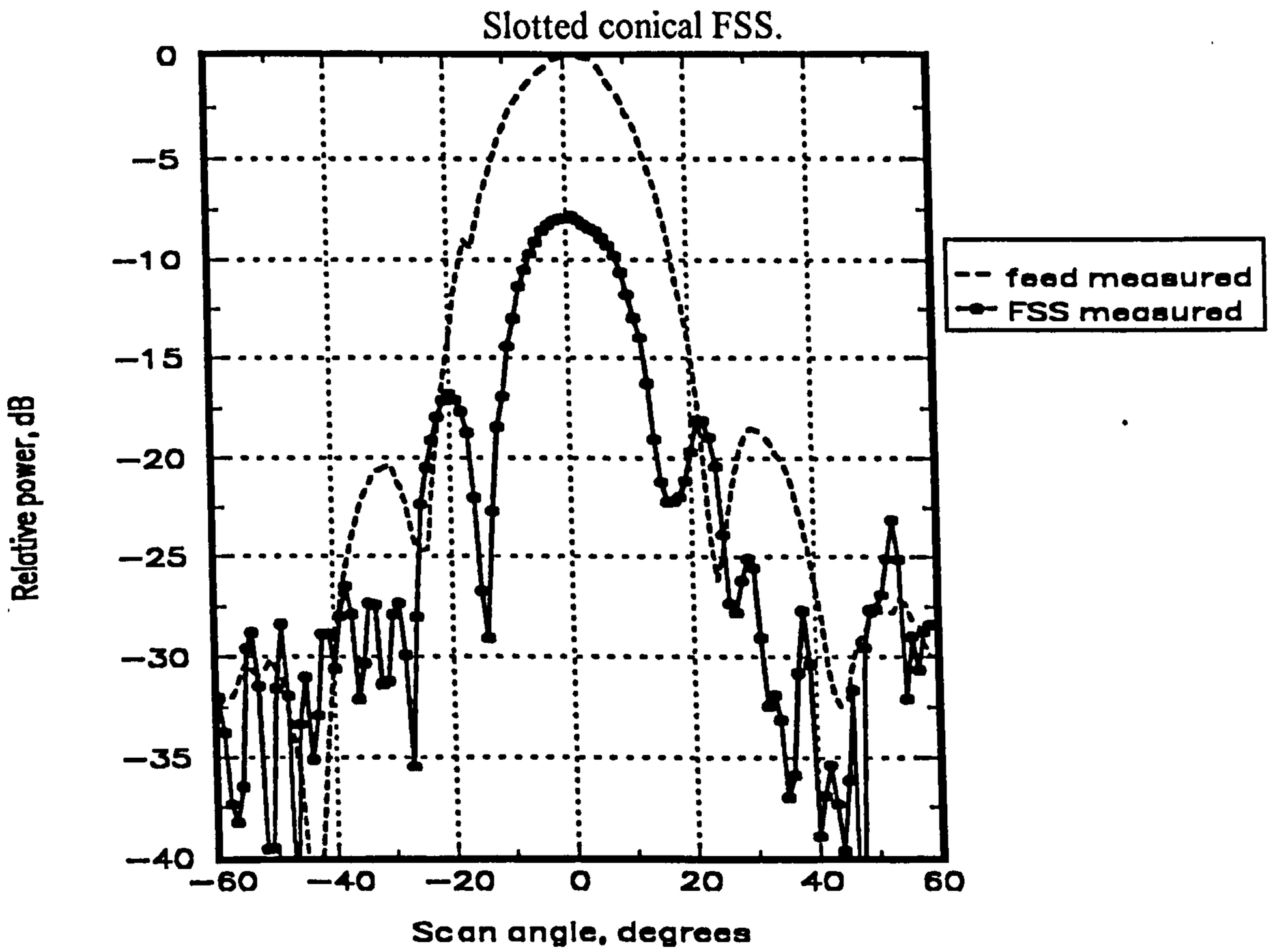

Fig.5.15a E—plane copolar patterns at 13.2 GHz for the feed and FSS.

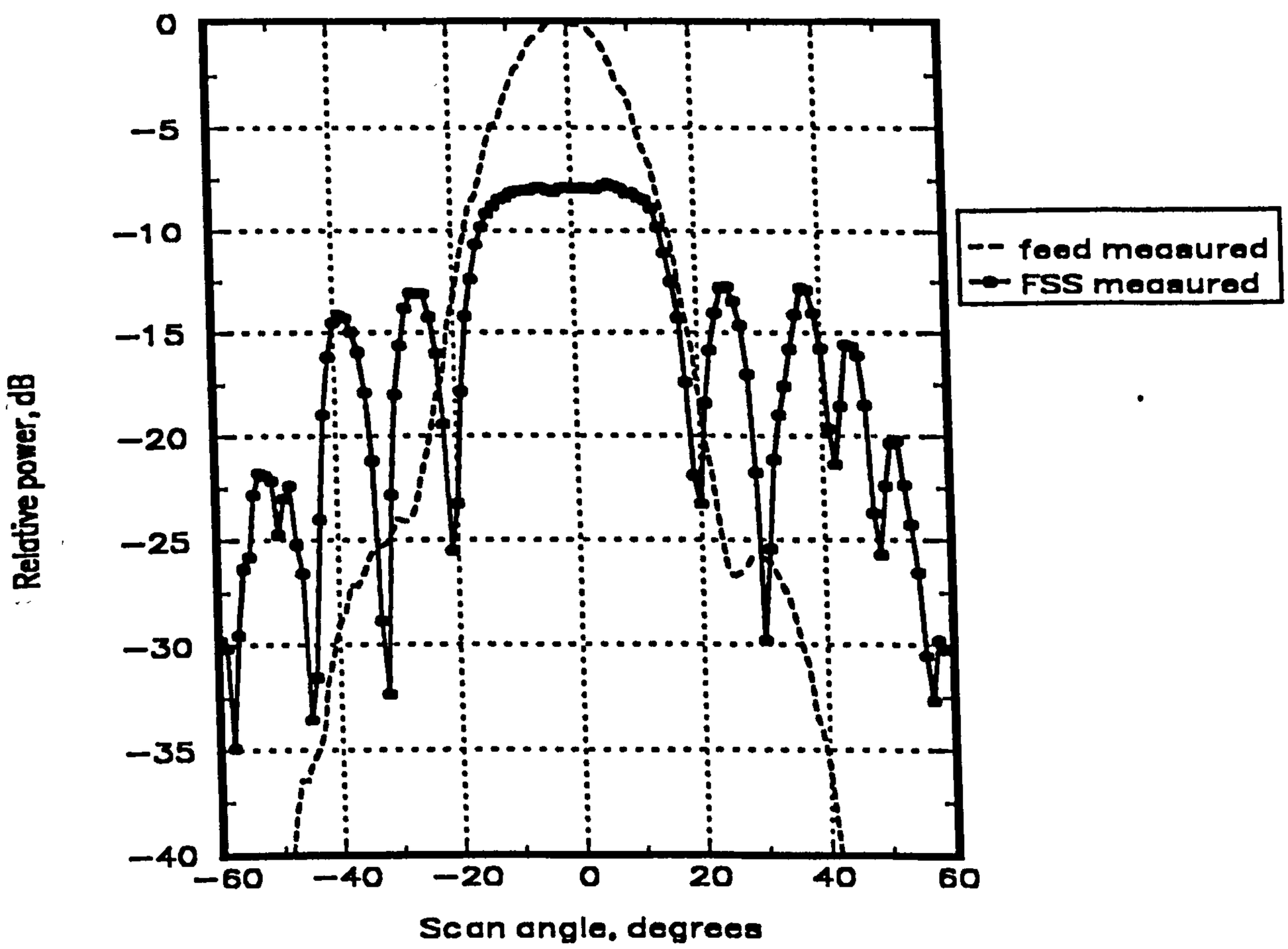

Fig.5.15b H—plane copolar patterns at 13.2 GHz for the feed and FSS.

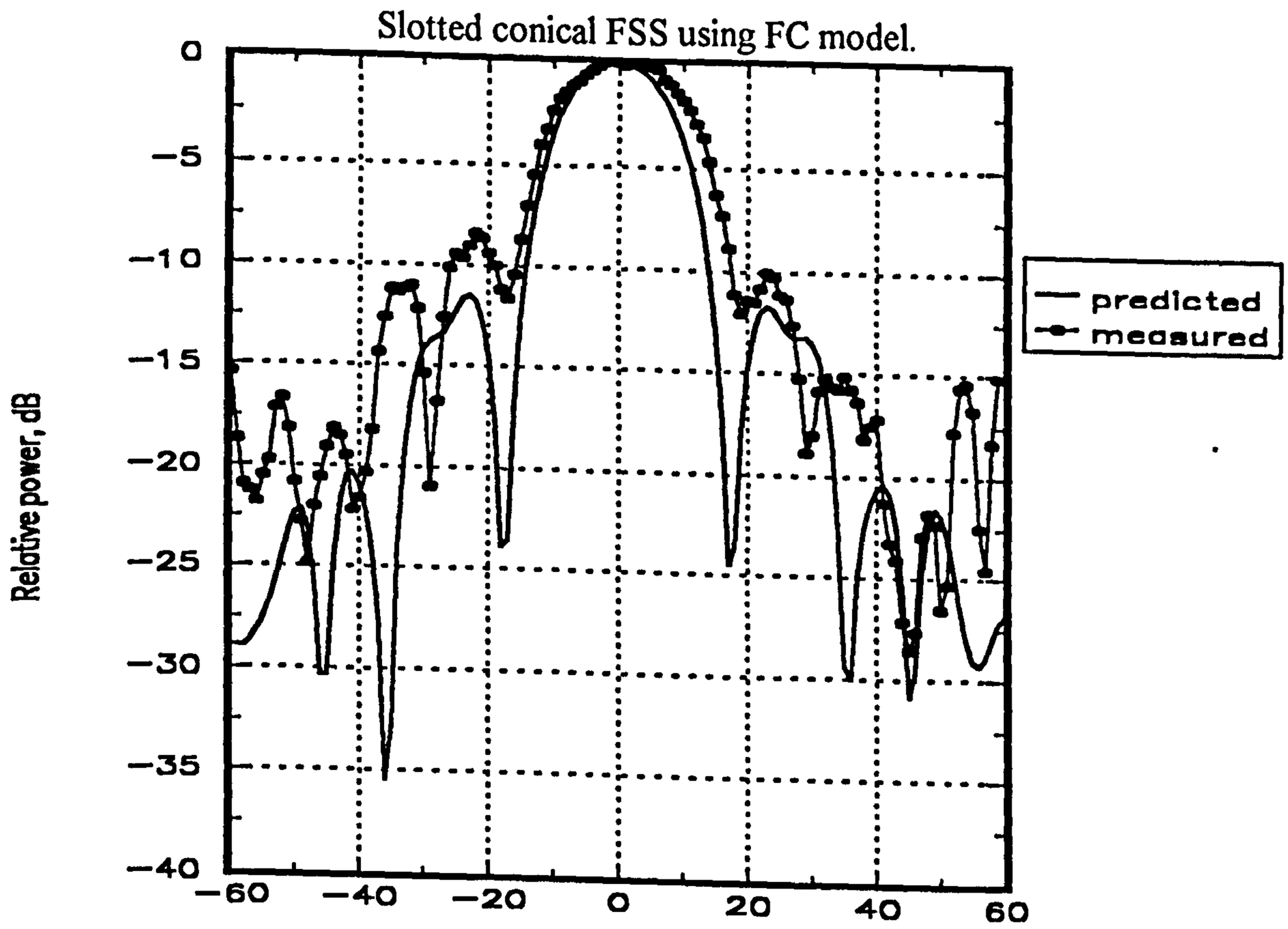

Fig.5.1 6a 45 degrees plane copolar pattern at 13.2 GHz using the SPS feed model.

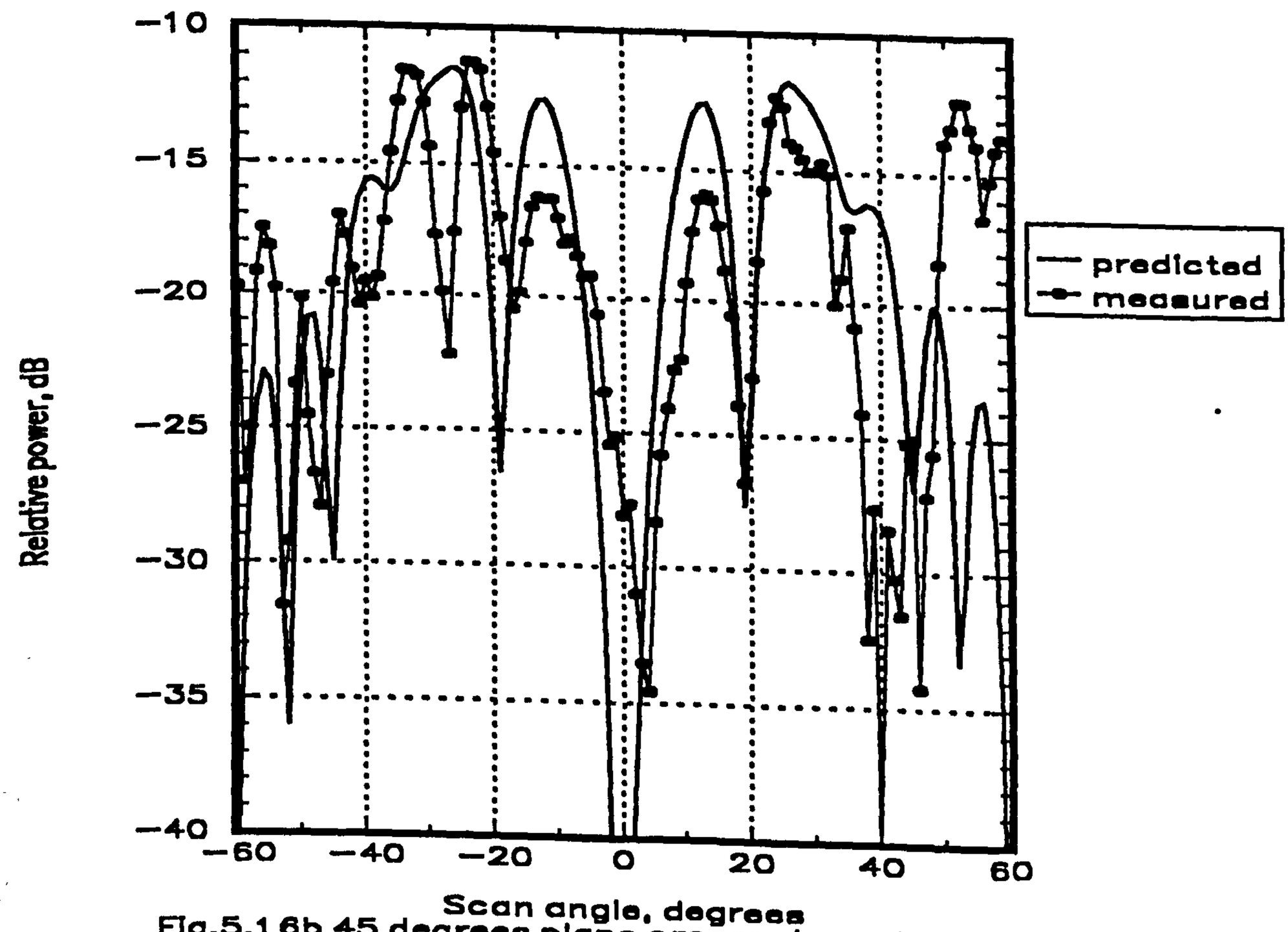

Fig.5.1 6b 45 degrees plane crosspolar pattern at 13.2 GHz using the SPS feed model.

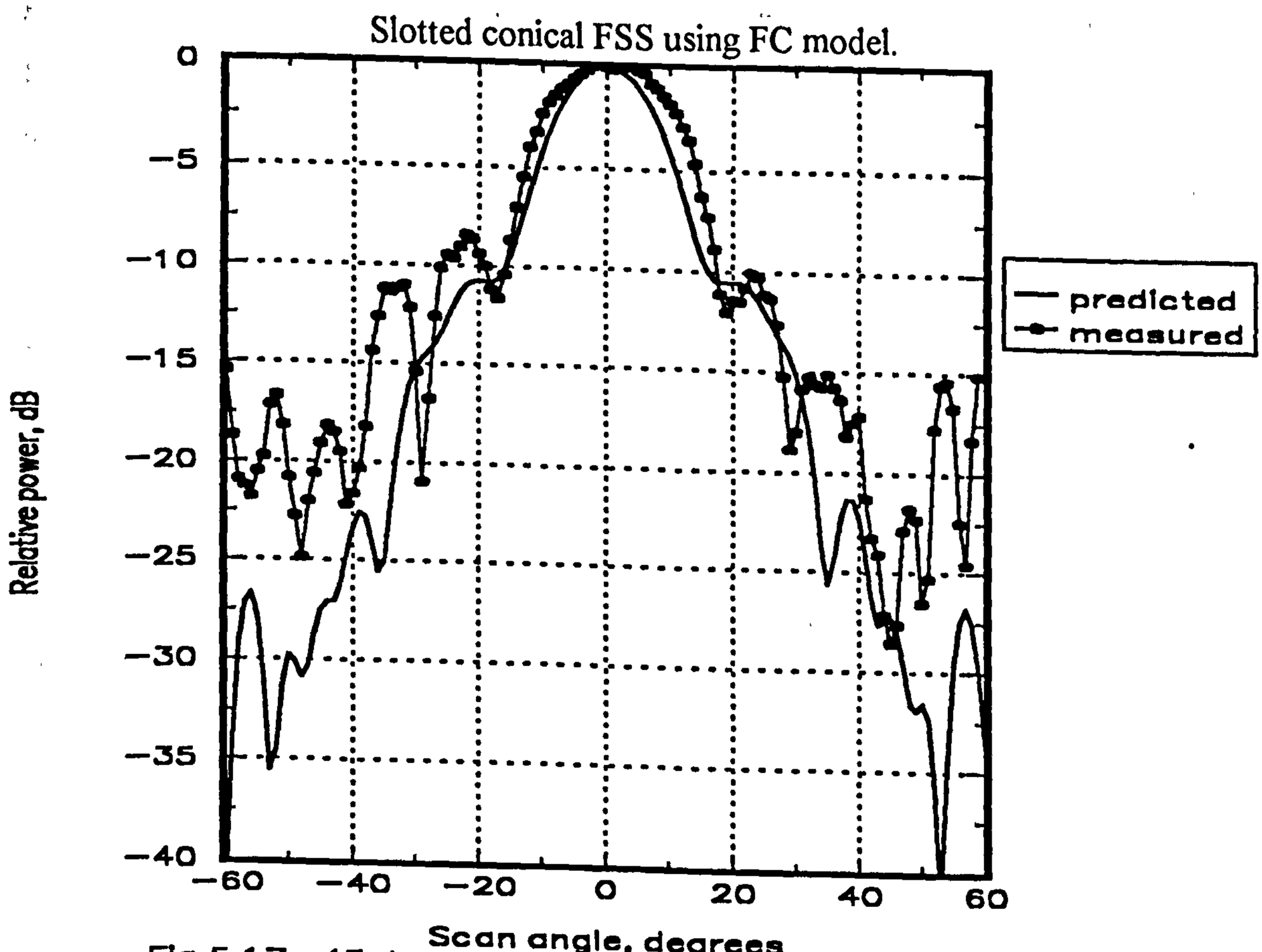

Fig.5.17a 45 degrees plane copolar pattern at 13.2 GHz using the PB feed model.

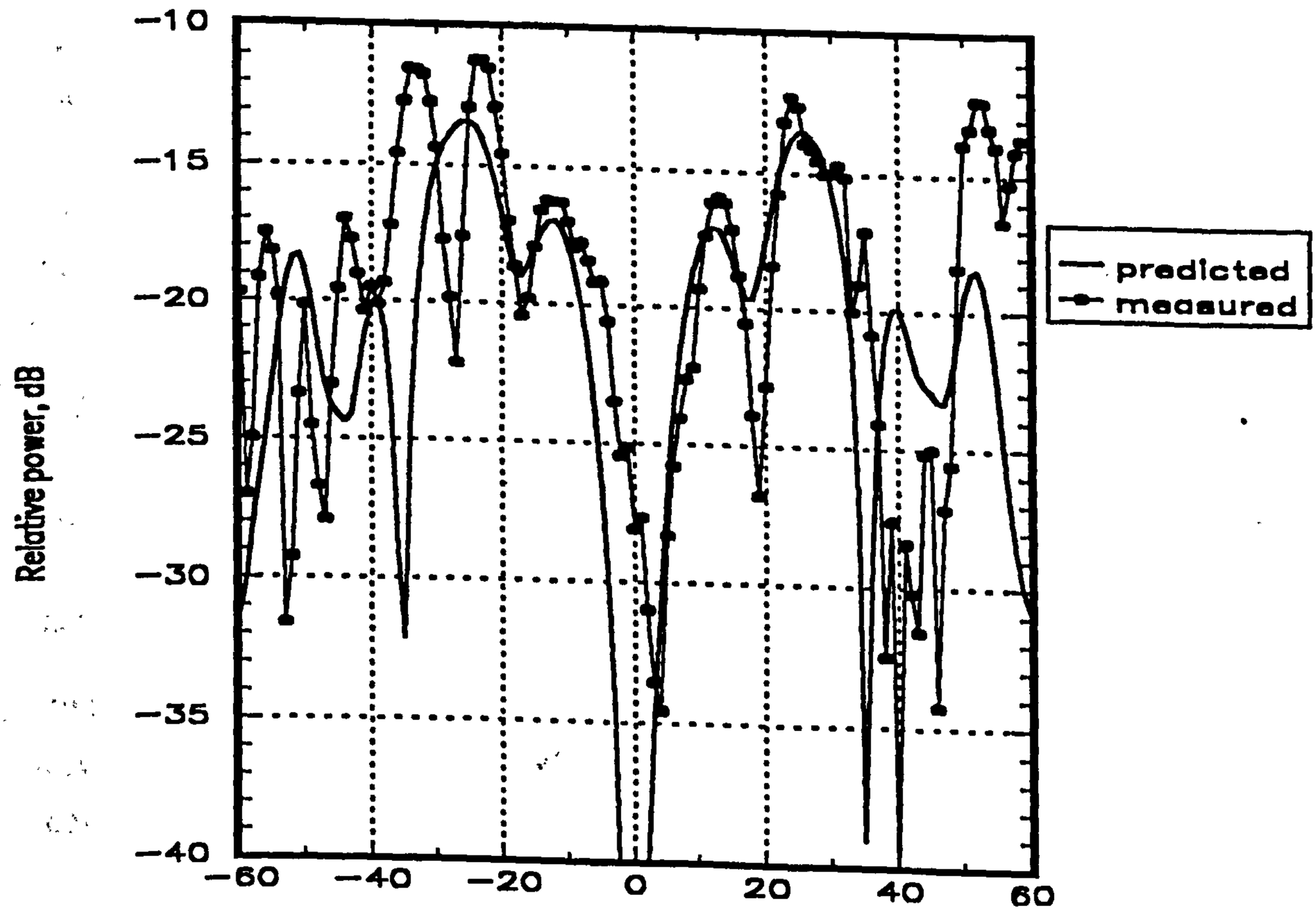

Fig.5.17b 45 degrees plane crosspolar pattern at 13.2 GHz using the PB feed model.

5.6 Comparing the tangential infinite array and finite current models

In this Section, the predictions from the tangential infinite array (TIA) approach are compared with finite current (FC) model using the small conical array of slotted dipoles as discussed previously. Predictions from the TIA and FC models using the three feed models are compared with the measurements. The FN feed model is not suitable here because the feed is located too close to the radome wall. The predicted illumination is expected to be poor because of the inherent far field assumptions. Therefore, this has not been included in the FC model.

The objective here is to test and compare the TIA with the FC model when the internal multiple reflections are expected to be higher especially when the cone is small. The TIA assumes that locally, each FSS element is small relative to the size of the cone so that local interactions of these elements can be approximated by a tangential infinite array. Therefore, the curvature of FSS element is neglected because of the planar assumptions. This is in contrast to the FC model which accounts for the curvature of each FSS element on the conical surface and mutual coupling of all the elements.

5.6.1 Current and modal recipe for a planar array of dipoles

In order to predict the radiation patterns of a conical slotted FSS using the TIA approach, it is required to characterise the current basis functions of each slot in the modal analysis of an infinite planar FSS.

The current expansion for slotted ring element has been previously described in Sec.3.6.1. Using similar convention, the current is expanded in the form of,

$$\vec{M} = \sum_{n_c=1}^{n_c=N_c} c_{n_c} h_{n_c} \hat{v} + \sum_{n_s=1}^{n_s=N_s} c_{n_s} h_{n_s} \hat{v} \tag{5.92}$$

where here $\vec{M}$ is the magnetic current flowing along the length of the slot, L. The slot is lying along the v axis, where $\frac{-L}{2} < v < \frac{L}{2}$. In addition, v can be rotated according to angle ψ as shown in Fig.5.18. This is to facilitate different orientations of the slot with respect to the incident field. Here, ψ=90° when the planar lattice was wrapped on the conical surface. It is assumed that current remains constant across the width, W.

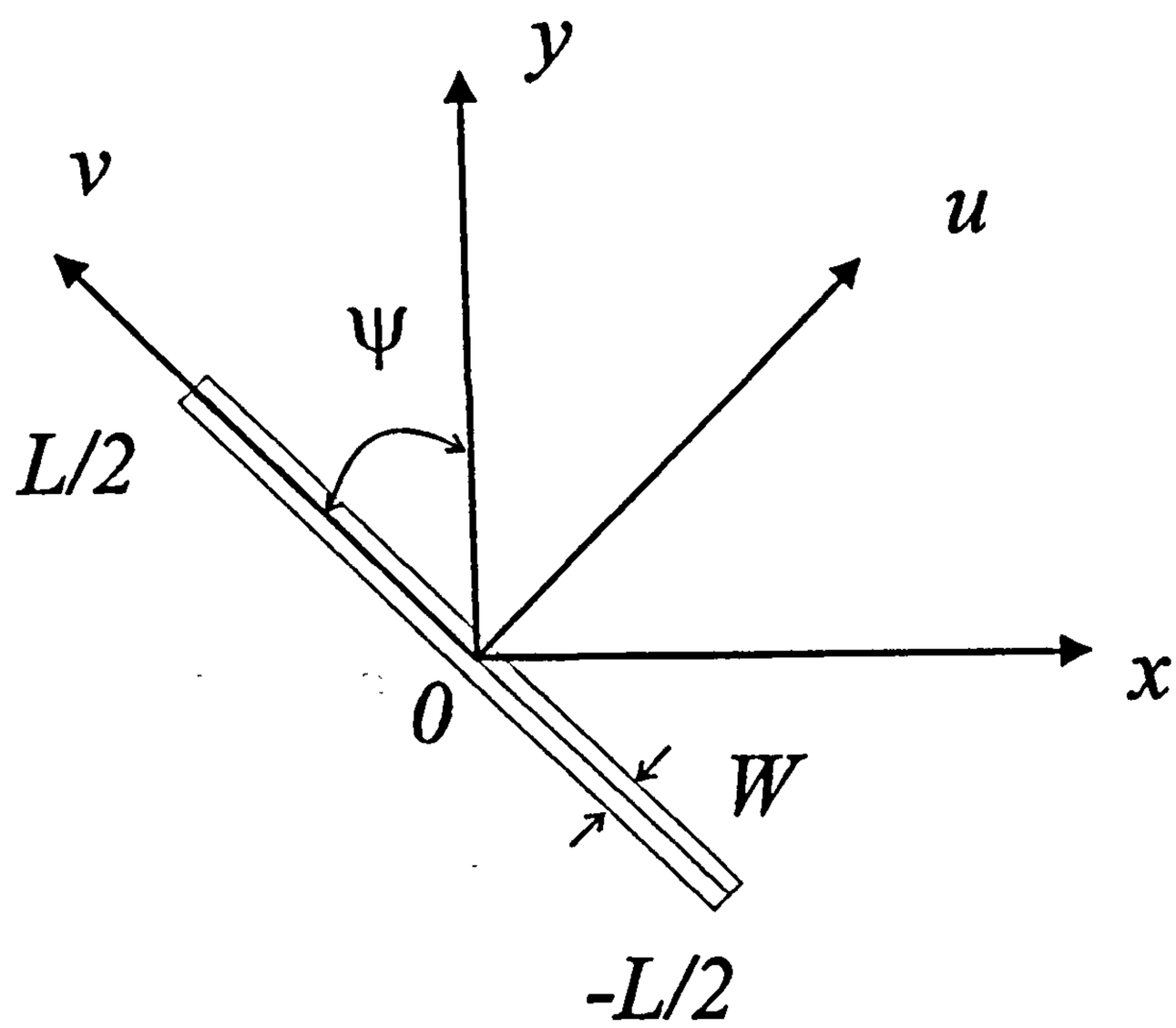

Fig.5.18 Geometry of rotated axis for slotted dipole

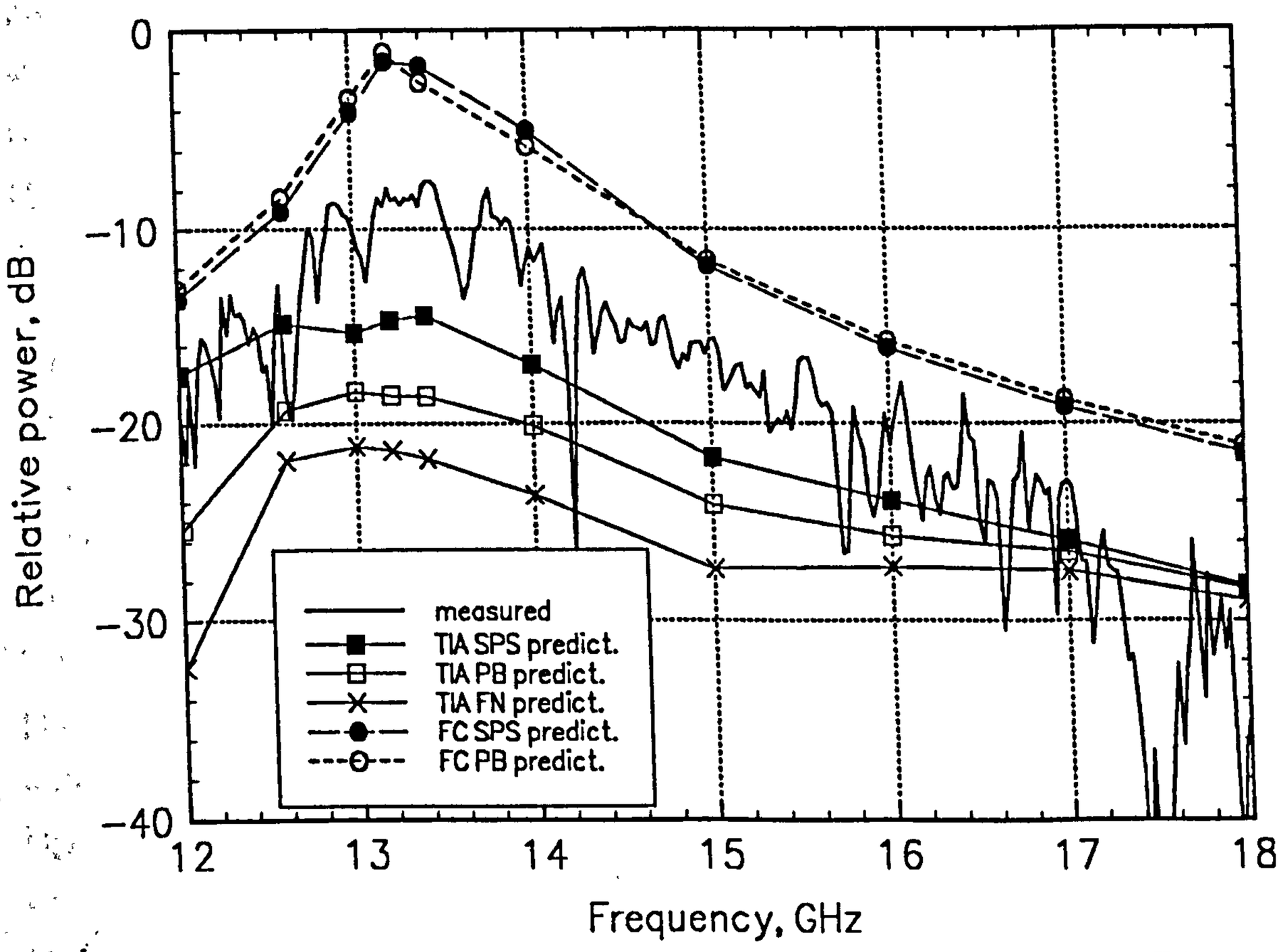

Fig.5.19 Comparing the passband response of the TIA and FC model.

The basis functions defined along the slot axis v are:

$$h_{n_c} = \sqrt{N_a} \cos \frac{(2n_c - 1)\pi v}{L} \quad where\ n_c = 1\ and\ 2. \tag{5.93}$$

$$h_{n_s} = \sqrt{N_a} \sin \frac{2n_s \pi v}{L} \quad where\ n_s = 1, 2\ and\ 3. \tag{5.94}$$

and N_a is a constant normalising factor given by,

$$N_a = \frac{2}{WL} = \frac{2}{A'} \text{ (} A' \text{ is the aperture area of the slot),} \tag{5.95}$$

A minimum of 169 Floquet modes and 5 current modes have been used to expand the tangential fields.

5.6.2. Transmission response

The transmission response of the boresight loss from the predictions of the TIA and FC models are compared with the measured values as shown in Fig.5.19. The TIA model gives a well defined passband using the three types of feed model, although the predicted passband centre is slightly lower at 13 GHz compared to the measured value at about 13.2 GHz. Whereas the FC model has accurately predicted the measured resonant frequency for both the SPS and PB feed models. There is also better agreement in the FC predicted profile with the measurements as compared to the TIA model. However, discrepancies are encountered in the minimum boresight losses of both models. The FC model gives a PB prediction of -1.09 dB and SPS of -1.53 dB as compared to the measured value about -8 dB. The TIA model gives lower value, with the SPS prediction at -14.5 dB, PB at -18.39 dB and FN at -21.2 dB. The difference between measured and FC model is about +6.0 dB for the PB and +6.5 dB for the SPS model. Whereas in the TIA model the descrepancies range from -6.5 dB for the SPS, -10.39 dB for the PB to -13.2 dB for the FN feed model. It is interesting to note that the FC model predictions are higher than the measured values but the TIA model predictions are lower. A possible explanation is that the internal multiple reflections inside the small cone which is modelled in the FC model must have contribute to the higher currents in the FSS elements so that the radiated field is higher. This would lead to a lower boresight loss. But the TIA model only calculates the current from a tangential infinite array approximation which has assumed local interaction of neighbouring elements. Therefore, it has ignored the strong couplings from the other elements when the cone is small.

On the whole, the FC model proves to be more accurate than the TIA model in predicting the passband although there are discrepancies in the boresight losses. Bearing in mind that the TIA model is actually meant for cases where the FSS element is smaller relative to the size of the cone, so that locally the FSS array can be approximated with a tangential infinite array. Previous results from the larger cone using the array of slotted rings (Chapter 3) show that the TIA model is fairly accurate in predicting the transmission response and radiation patterns using the SPS and FN feed models. The internal reflection is probably less serious there because the cone is relatively larger than the feed aperture and also the feed is located further away from the radome wall.

5.6.3 Radiation patterns

The predicted normalised radiation patterns from the TIA model are compared with predictions from the FC models using the SPS and PB feed models. These predictions are also compared with the measurements. For the FN feed modelling, only the predictions from the TIA model are available. The radiation patterns at 13.2 GHz near the pass band centre are used here.

5.6.3.1 The SPS feed model

At 13.2 GHz, the predicted copolar pattern in the principal planes can be seen in Fig.5.20a and Fig.5.20b. In the E-plane, the predicted main lobes of the FC and TIA model agree fairly well with the measured values up to $\pm 15^{o}$ scan. The FC model predicts the first null better but the TIA model gives deeper nulls than the measured values. Asymmetry in the measured main lobe produces a shallower null and broader main lobe near $+15^{o}$. These could be due to the discontinuity on one side of the conical FSS (Please see Sec.5.5.2.1 for further descriptions). The first pair of FC predicted side lobes are broader and the peaks are higher, about -7 dB at $\pm 20^{o}$,as compared to the measured values at -8 dB. The TIA, however, predicts lower peaks in this pair of side lobes down to -16 dB.. The positions of these peaks are located by both FC and TIA models. In the H-plane, it is found that the FC model gives very good agreement in the main lobe but poorer predictions are encountered in the TIA model.

The 45° copolar and crosspolar patterns are shown in Fig.5.21a and Fig.5.12b. For the FC model, there is moderate agreement in the main lobe and side lobe profile with the measurements. The TIA model predictions are poor giving a narrower main lobe and lower side lobe levels. The FC model gives good agreements in the crosspolar levels. But the TIA gives poorer predictions with higher peaks in the crosspolar at $\pm 15^{o}$.

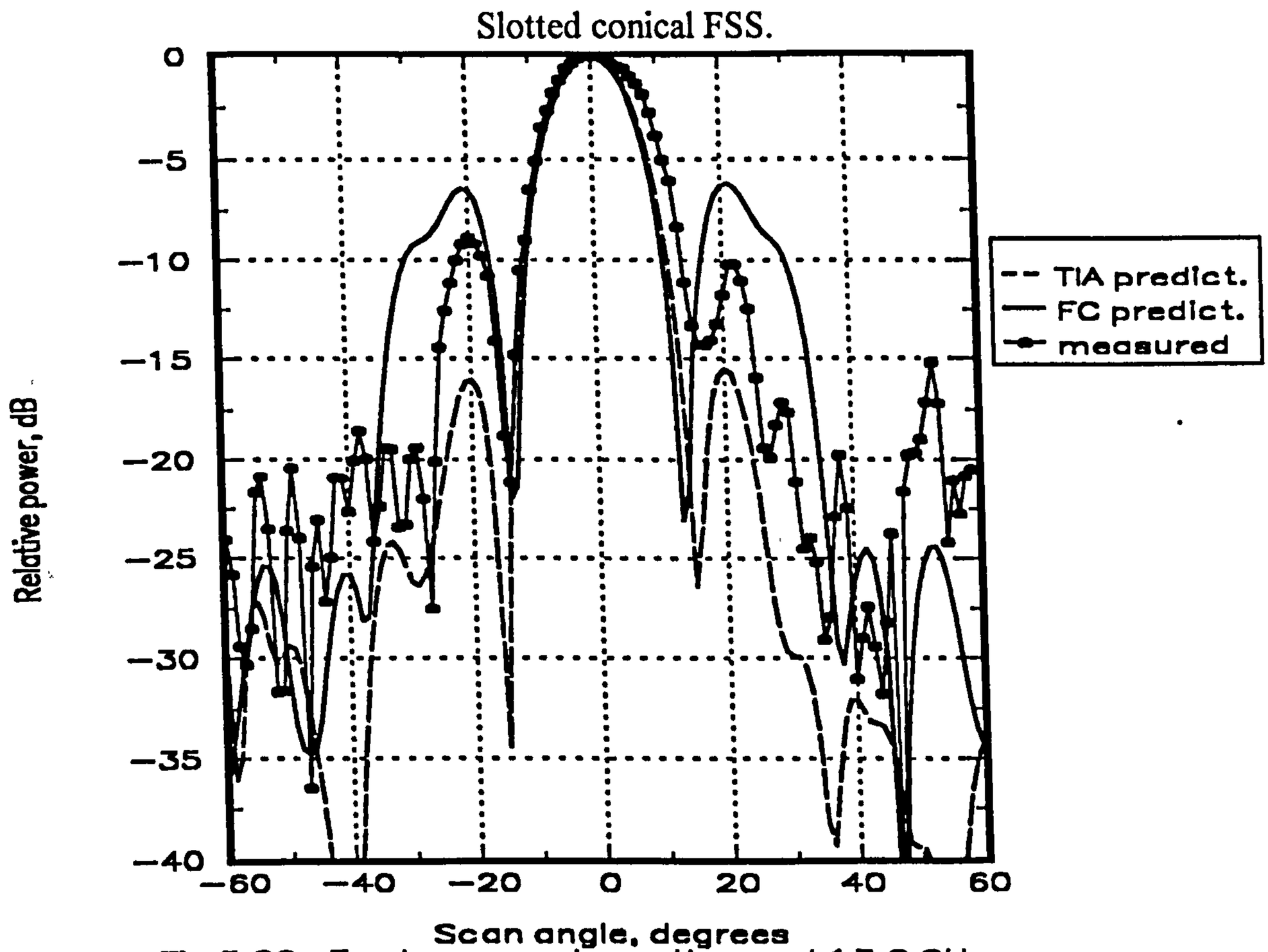

Fig.5.20a E−plane copolar patterns at 13.2 GHz using the SPS feed model.

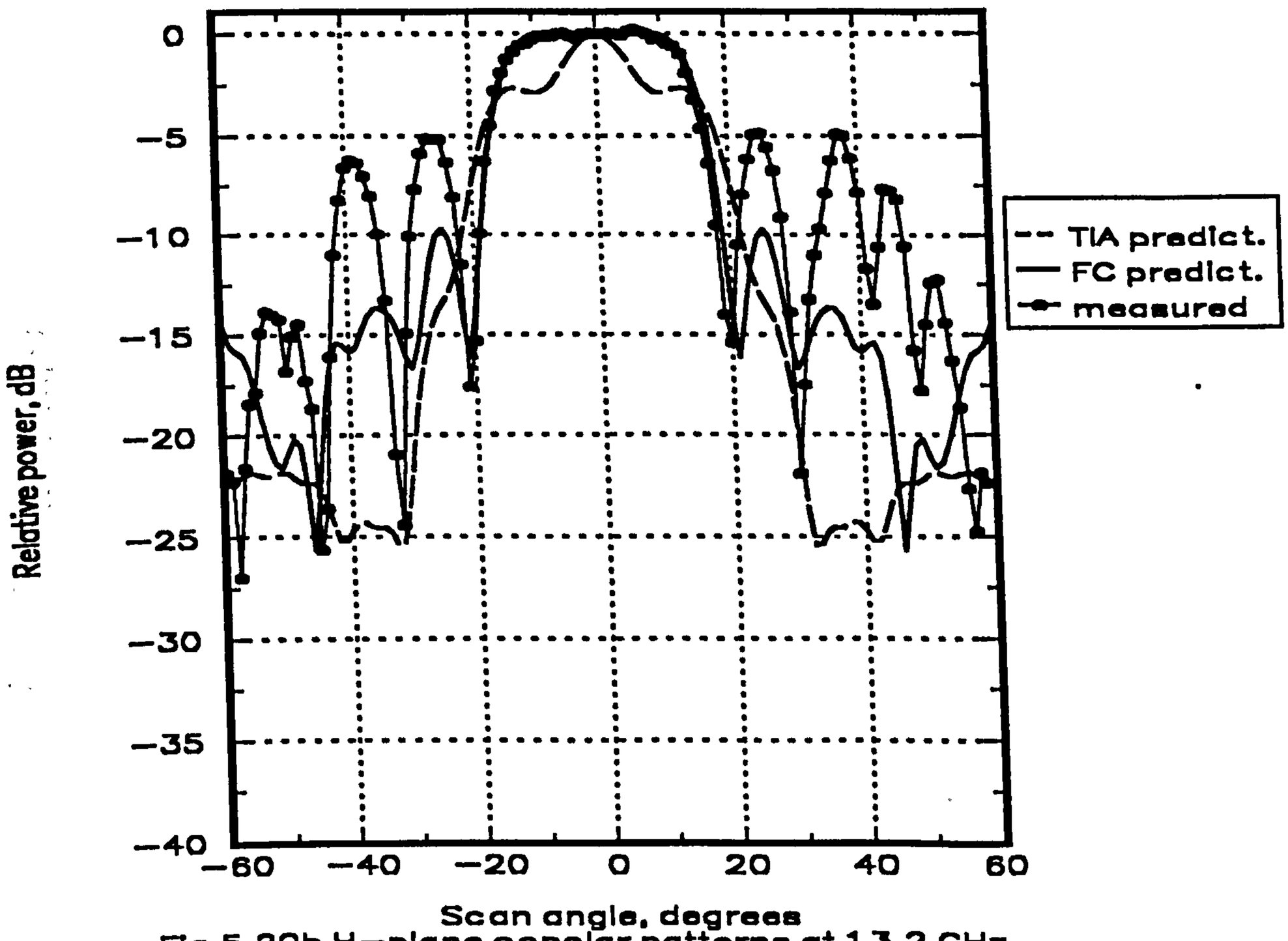

Fig.5.20b H−plane copolar patterns at 13.2 GHz using the SPS feed model.

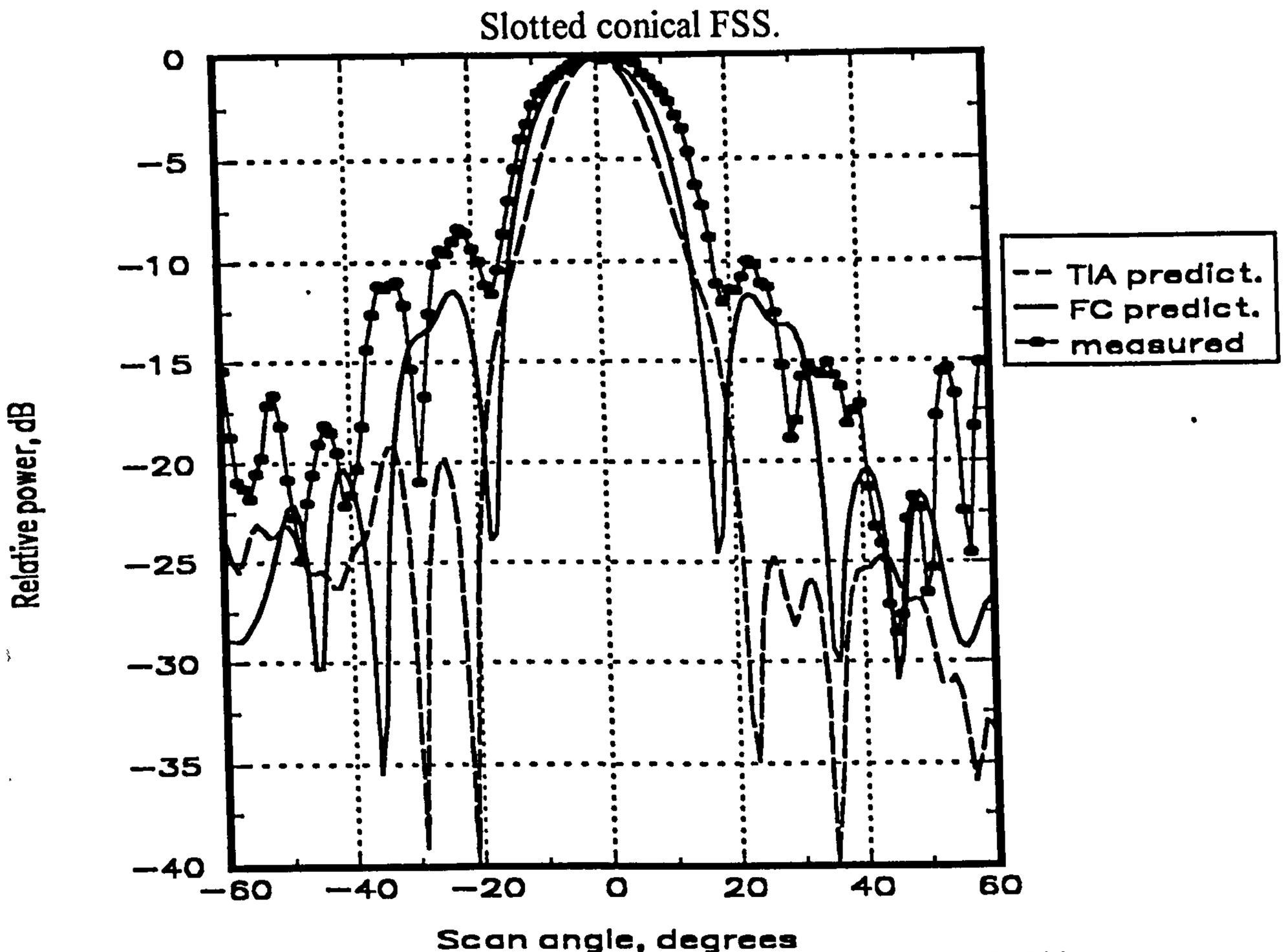

Fig.5.21 a 45 deg. plane copolar patterns at 13.2 GHz using the SPS feed model.

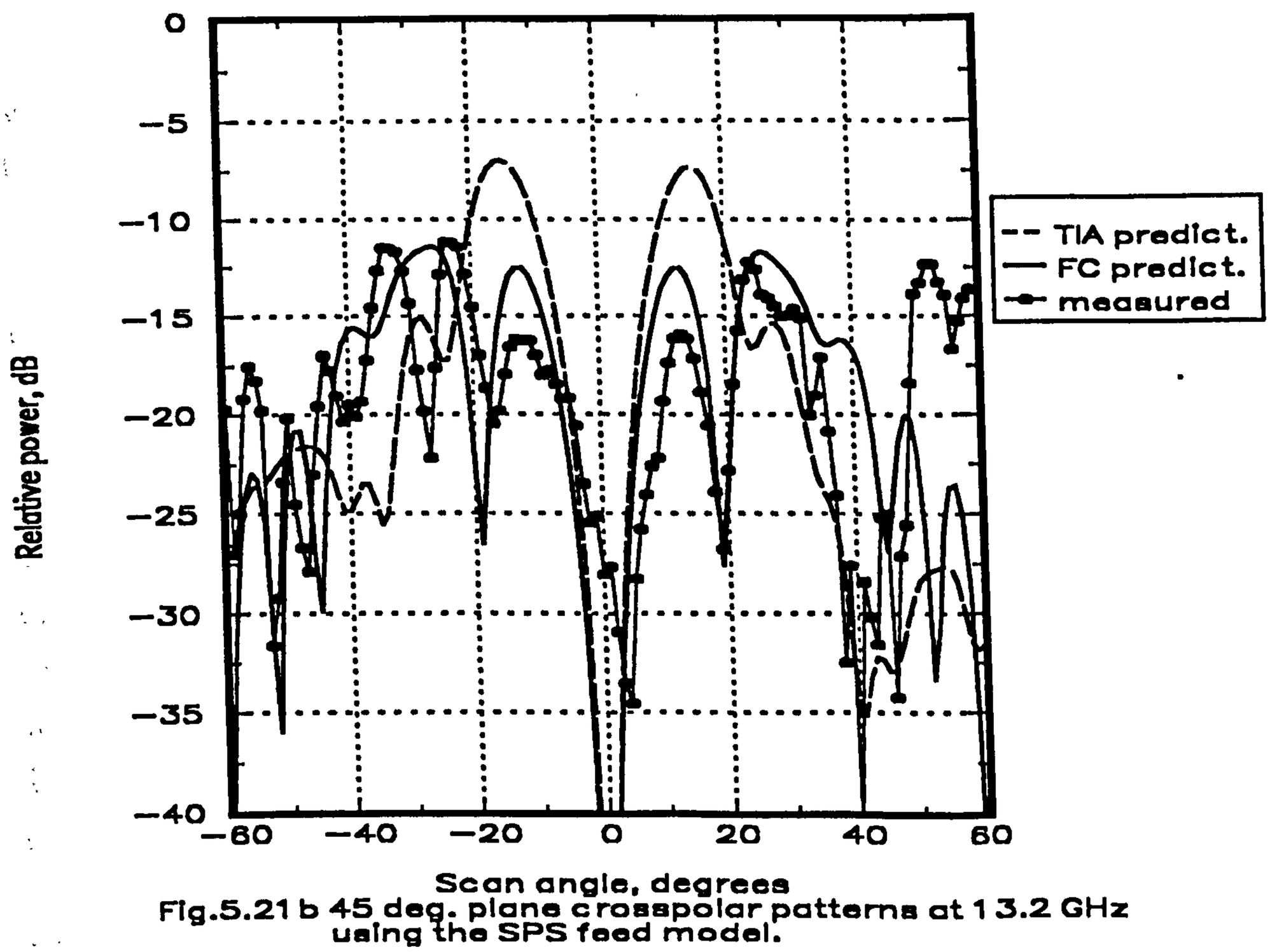

Fig.5.21 b 45 deg. plane crosspolar patterns at 13.2 GHz using the SPS feed model.

5.6.3.2 The PB feed model

The E-plane copolar patterns at 13.2 GHz using the PB feed model with the TIA and FC models are shown in Fig.5.22a. There is agreement in the main lobe of the FC model with the measured patterns up to $\pm 12^{o}$. But the predicted first pair of side lobes are higher and broader. Nevertheless, the position of the measured peak side lobe is predicted at $\pm 20^{o}$. The TIA model gives a much broader pattern overall which does not agree with the measurements. There is also better agreement in the predicted main lobe of the FC model with the measured in the H-plane.(Fig.5.22b). Although the rapid oscillations in the measured side lobe levels is not predicted. In comparison, the TIA model fails even to reproduce the main lobe. Similar predictions were also encountered in the 45° plane with very poor agreement with measurements in the TIA model. The FC model however could predict the general profile of the pattern. Thus, it seems to show that the approximate nature of both the TIA model and the PB feed model would add to the inaccuracies in the predicted patterns. The accuracy of the FC predictions depends mainly on the feed modelling since it could account for all the interaction of the FSS elements and hence the internal multiple reflections.

5.6.3.3 The FN feed model

There were very poor predictions in the radiation patterns of the TIA model using the FN feed modelling. The reason is mainly because the feed is very close to the inner wall of the small conical FSS so that the approximate far field divergent illumination of the FN feed model would not apply at this distance.

Therefore, from the above discussions, it shows the importance of considering the internal multiple reflections within a small conical radome and modelling the near field feed illumination accurately if the feed is very close to the FSS. The simple approximation of a local tangential infinite array is not sufficient to model the currents of the FSS element because it only assumes local interaction of the neighbouring elements. This does not apply here when the element is large relative to the size of the radome and the surface curvature is not taken into account. In this case the cone is small relative to the feed aperture and feed is also very close to the wall of the cone. It was shown that the PB predictions is even better than the FN feed model when the TIA approach was used. This is in contrast to the larger radome of slotted rings when the feed is further away from the FSS. For this case, the FN feed modelling was far superior to the PB. But the SPS is still the best feed model for predicting the near field illumination especially when this fields is required in the proximity of the feed. Using this as a bench mark, it is found that the computation time for the FC and TIA model is about the same with 354 FSS slots on the small cone. Both models took about 5.5

hours to compute. The former model has the advantage of using a general integral equation formulation that does not compute the current for every planar incidence in order to model the non-planar near fields. But it is limited by large computer memory storage for the impedance matrix. Nevertheless, the FC radiation patterns and pass band location agree better with the measurements when compared to the TIA model. Thus, the FC model can provide a viable solution if the patterns are required at the passband centre. Nevertheless, mutual coupling with feed and the FSS is still a major concern especially if the cone is small relative to the feed aperture and the feed is very close to the FSS.

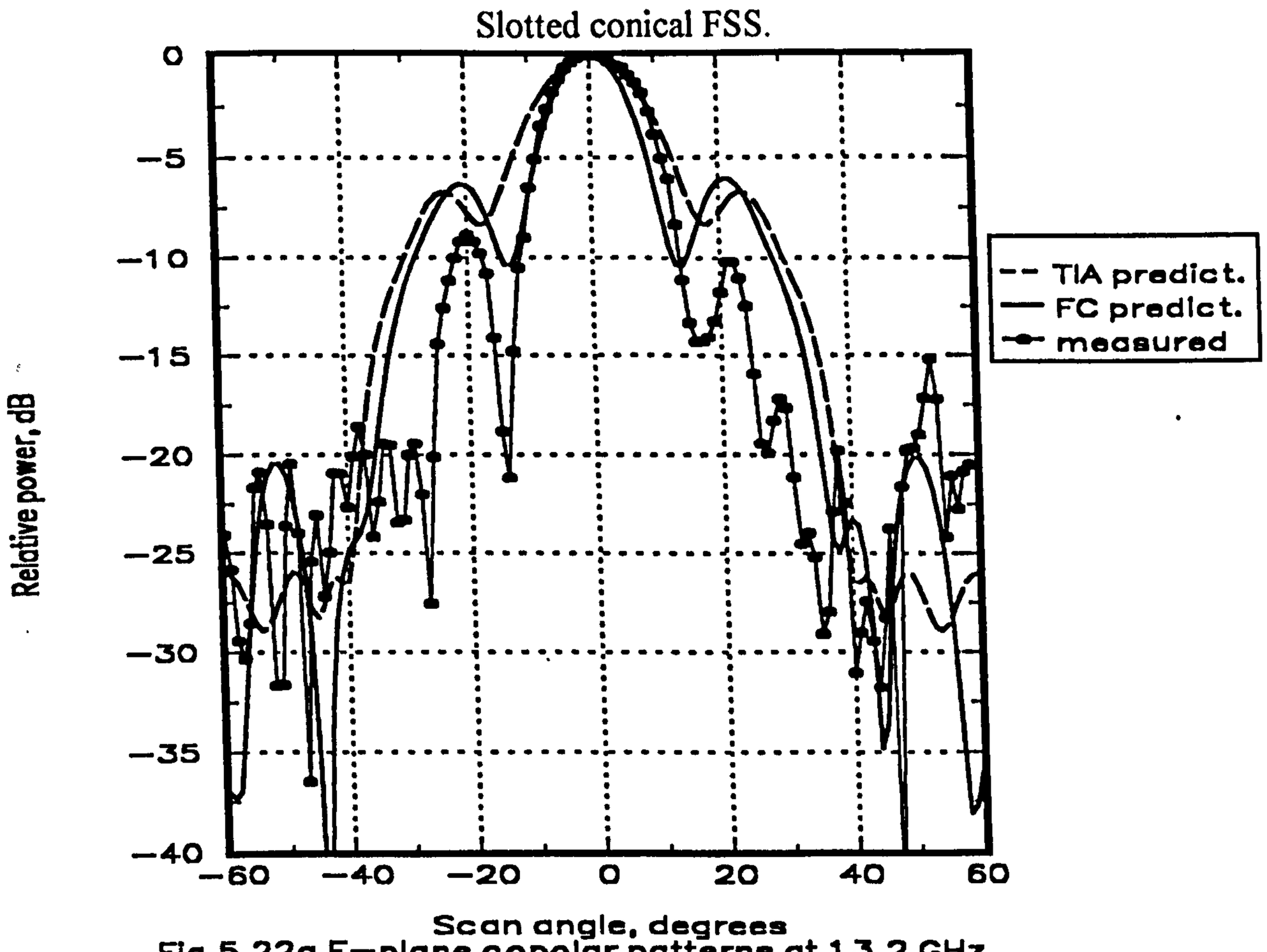

Fig.5.22a E—plane copolar patterns at 13.2 GHz using the PB feed model.

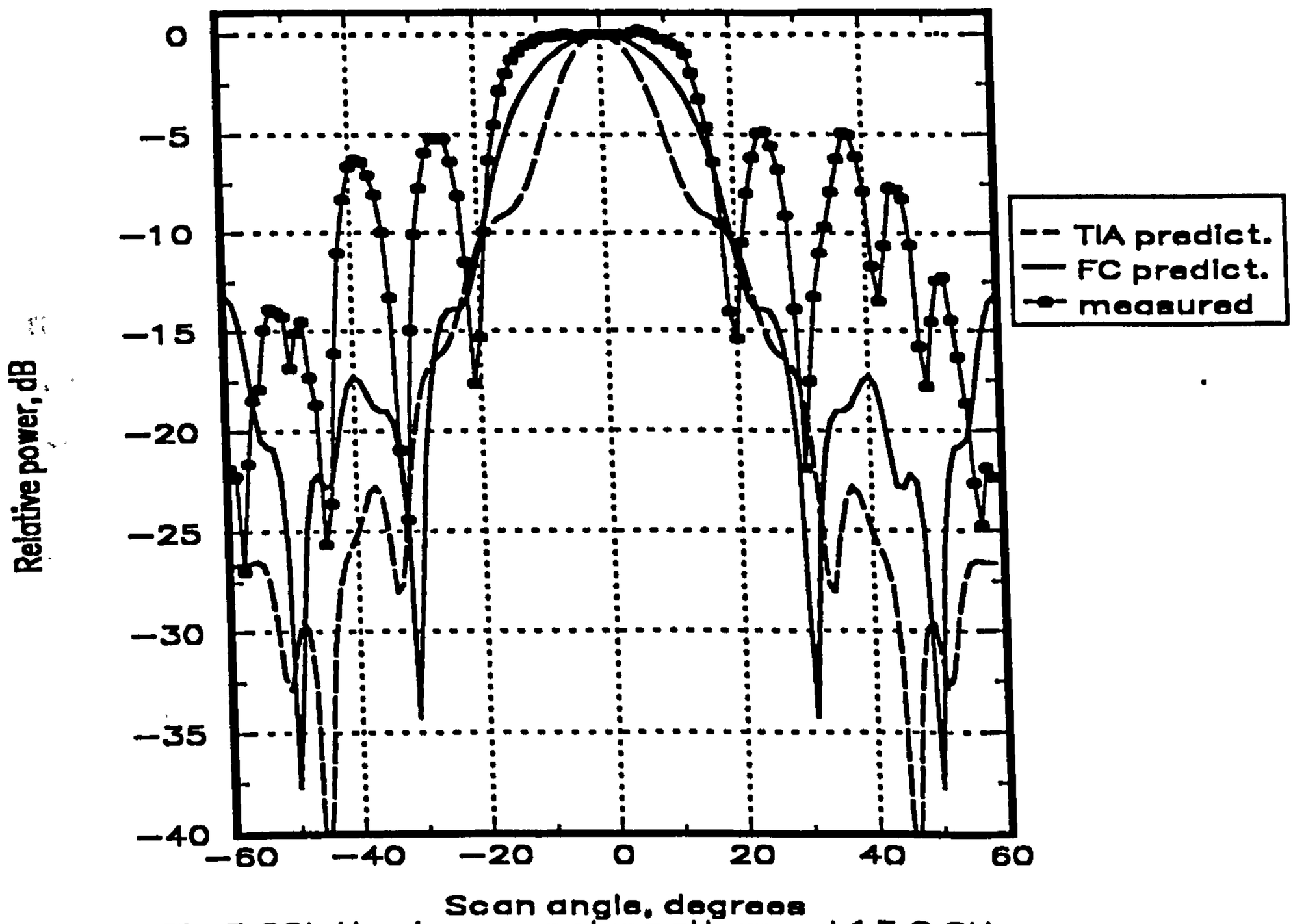

Fig.5.22b H—plane copolar patterns at 13.2 GHz using the PB feed model.

5.7 Conclusions

A novel formulation of the MFIE has been developed to analyse the conical slotted FSS with thin dielectric. Using the duality to electric charge and current, equations for static fields of fictitious magnetic charge in ferrite medium and and magnetic current in dielectric medium were derived and expanded here. These equations has been exploited in a quasi static approximation of the MFIE. Computer models have been developed using the SPS and PB feed models to predict the radiation patterns and transmission response of a slotted FSS cone. A circular corrugated conical horn is positioned at the base of the cone to provide the near field illumination. The SPS gives good agreement in the radiation pattern especially in the main lobe of the H plane at resonant frequency. There are generally better agreements between the predicted and the measured radiation patterns near the pass band centre for the SPS model as compared to the PB. Some discrepancy is observed in the predicted maximum boresight loss but the profile of the predicted transmission response agrees well with measured values. This discrepancy is probably due to close coupling between the feed and the FSS. When the conical FSS was covering the feed, there was substantial boresight losses and the measured main lobe and side lobes of the feed pattern became narrower. This could be due to mismatch in the dielectric substrate and coupling between the FSS and feed. The mismatch could potentially be improved if the dielectric layer is of half wavelength thickness as in the case of pure dielectric radome [9].

The predictions from the FC model was compared with the TIA model. It was shown the importance of considering the coupling of all the FSS elements especially when the radome is small relative to feed aperture and also when the feed is illuminating the radome wall in proximity. In this case, it would appear that the internal multiple reflections strongly affect the radiation patterns. The TIA model is not accurate enough to predict the fields in a small radome. It is also crucial to model the near field using a more rigorous feed model like the SPS feed model. Using this feed model, the computation time between the FC and TIA model is about the same if there are 354 FSS slots on a small cone. The main limitation of the FC model, however, is the computer memory requirement to store the large matrix but this is readily compensated by better accuracy. It has also the advantage of handling arbitrary and different FSS elements on the same cone. The TIA model however requires the same elements on the entire surface. Moreover, the FC model is not restricted by periodic lattice geometry. These features would enhance the capability for solving a general and wider FSS problem compared to the TIA model.

Thus, the FC model can provide a viable solution if the radiation patterns are required at the passband centre. Nevertheless, mutual coupling with feed and the FSS is still a major concern especially if the cone is small relative to the feed aperture and the feed is very close to the FSS. The FC model can be further improved to include the coupling of the feed and FSS if the integral equation formulation incorporates weighting of each point source in the feed aperture as well. This would lead to a slight increase of the impedance matrix size which is proportional to the number of points in the feed aperture used for the SPS feed modelling.

References

[1] Booker, H.G. :'Slot aerials and their relation to complementary wire aerials (Babinet's principle)', Journal IEE, 1946, Vol.93, III-A, pp.620-626.

[2] Bouwkamp, C.J. :'Theoretical and numerical treatment of diffraction through a circular aperture', IEEE Trans., 1970, AP-18, pp.152-176.

[3] Butler, C.M., Rahmat-Samii Y. and Mittra, R. :'Electromagnetic penetration through apertures in conducting surfaces', IEEE Trans., 1978, AP-26, pp.82-93.

[4] Butler, C.M. and Umashankar, K.R. :'Electromagnetic penetration through an aperture in an infinite planar screen separating two half-spaces of different electromagnetic properties', Radio Science, 1976, Vol.11, No.7, pp.611-619.

[5] Singh, S. and Wilton, D.R. :'Analysis of an infinite periodic array of slot radiators with dielectric loading', IEEE Trans., 1991, AP-39, pp.190-196.

[6] Balanis, C.A. :'Antenna theory:analysis and design', John Wiley & Sons, 1982 pp.133-135.

[7] Popovic, B.D., Dragovic, M.B. and Djordjevic, A.R. : 'Analysis and synthesis of wire antenna', Research Studies Press,1982, pp.100-104.

[8] Silver S. (Ed.) :'Microwave antenna theory and design', Peter Peregrinus Ltd., IEE Electromag. Wave Series 19, Chap.3 .

[9] Rudge A.W., Milne K., Olver A.D. and Knight P. (Ed.) :'The handbook of antenna design', Vol.2., Peter Peregrinus Ltd., 1983, pp.457-458.

CHAPTER 6.0

CONCLUSIONS AND SUGGESTIONS FOR FURTHER WORK

Two methods have been used to predict the far field radiation from a conical FSS radome illuminated by a corrugated feed horn. The near field illumination has also been assessed using three types of feed model although mutual coupling between the feed and the FSS radome has not been considered. The first feed model is based on a far field pattern of the feed horn to approximate the near fields and it is denoted as FN. This approximation produces a local plane wave incident field at each element on the cone which is a prerequisite for using the modal analysis for an infinite planar array. The amplitude of the illuminating field is modelled as a Gaussian distribution fitted to the measured far field pattern of the feed. The second one uses a parallel beam (PB) approximation emanating from the feed aperture. The parallel rays are compensated by a phase term due to the ray path difference from the feed aperture to the curved surface. A more rigorous evaluation approximates the near fields of a horn using a superposition of point sources (SPS) from the feed aperture fields.

The first method for analysing the conical FSS is based on a tangential infinite array (TIA) approximation which has assumed the surface is locally flat so that the FSS element current could be calculated using the modal analysis. The location of the passband was predicted by all the three feed models, with some discrepancies in their boresight losses. The SPS is the best feed model for locating the passband centre. Although there are differences in the boresight loss at the band centre, only the SPS predicts a loss, as expected in an antenna/radome system. The other feed models give a slight gain. Generally, there is agreement in the radiation patterns between the predicted and measured values for SPS and FN feed models. However, at wider scan angles, the computer model did not accurately predict the rapid oscillations of the side lobes. Such behaviour can be attributed to multiple reflections within the internal wall of the cone and mutual coupling between the feed and FSS which have not been taken into account in the formulation. The SPS model calls up the modal analysis routine 85 times more for each point on the cone compared to only once per point for the FN model to compute the local fields. This has a profound effect on the computer memory requirements as well as the run time. In the present model only the source fields on the exterior wall of the cone is calculated. One possible way of improving this model is to include the source fields on the interior wall of the cone as well [1].

The accuracy of the scattering from a curved FSS structure was assessed more fully in the second method. Here, the finite size and the curvature of the FSS currents are

tackled using an integral equation formulation which takes into the coupling of all the FSS elements. This has been called a finite current (FC) model here because the interaction of all the FSS elements is treated in a finite geometrical sense. Initially, metallic dipole elements have been used to check the validity of applying the quasi-static approximation in the EFIE formulation for a small conical FSS. This formulation is weighted using the pulse Galerkin's MOM technique to yield a linear system of equations which can be written in matrix form. A small FSS cone is used here because of limitation in computer memory demanded by the impedance matrix. Since the feed is now closer to the radome wall, only the SPS and PB feed models are used to model the illuminations because of their inherent near field assumptions. Both conjugate gradients (CG) and elimination methods are used to solve the matrices for the unknown current coefficients. For the standard EFIE (without dielectric approximation), it was found that the iterative CG method is faster than the conventional elimination method for frequencies away from the resonant frequency if the computer RAM is sufficient to cope with the storage of the impedance matrix. This is in contrast to the constant computation time taken by the latter method. However, when the RAM memory is exceeded substantially and the hard disk is assessed, the elimination method is faster. Therefore, the computational speed of both methods is also machine dependent. For a practical FSS the memory requirement will normally exceed the RAM so the elimination method is preferred. When the quasi-static approximation was incorporated in the EFIE formulation, the CG algorithm did not converge. This could be due to possible round off errors in the computation of the quasi-static approximation. Hence, the elimination method was adopted here.

The computer model based on this quasi-static EFIE is able to predict the radiation patterns in the transmission band of the conical FSS radome. Both PB and SPS feed models give comparable predictions. The predicted reflection band centre frequency is higher than the measured value because the loading effect is also affected by the area in the dielectric portions of the unit cell which is comparatively larger than the FSS element dimensions. The quasi-static approximation here only considers the loading effect of the dielectric thickness around the equivalent cylindrical metallic dipole element. When the dielectric thickness was increased, the resonant frequency and reflection null is shifted closer to the measured values. This quasi-static model, however, is more suitable for the slotted conical FSS case. Although, the actual unit cell of the aperture is now occupied by both the dielectric and metallic screen, it is the slot that is exerting a dominant influence. Thus the narrow slotted region which is supported by the thin dielectric layer can be considered to be equivalent to a cylindrical

slotted dipole with dielectric coating. This quasi-static approximation has been used in a modified version of the MFIE.

A novel formulation of the MFIE has been derived to analyse the slotted dipole FSS elements on thin dielectric conical radome. The equations of the static fields of a fictitious magnetic charge in ferrite medium and magnetic current in dielectric medium have been successfully applied in a new quasi-static approximation of the MFIE. The approximation is based on a set of complementary equations from the duality of the electric to the magnetic charge and current. Basically it is assumed that isolated magnetic charge and current source exist so that the static magnetic fields can be non-rotational and electric field non-divergent. The slotted flat dipole FSS element with dielectric substrate is modelled as a cylindrical slot with dielectric coating. The MFIE has been incorporated in the FC model to account for coupling of a array of slotted FSS element. Predictions from this model has been verified for a slot with dielectric substrate using experimental results. There is generally better agreement between the predicted and the measured radiation patterns, in a narrow scan angle, near the pass band centre for the SPS model as compared to the PB. Some discrepancy is observed in the predicted absolute transmission loss but the frequency profile agrees well with measured values. The differences in the losses and patterns are due to near field coupling because of the feed proximity to the FSS. One way of verifying the new MFIE is to compare the predictions with the measurements of the FSS in the far field of the feed to avoid mutual feed and FSS coupling effect. This could form part of a study for future work to assess the quasi-static approximation of the MFIE.

Results from the FC and TIA models shows that it is important to consider the coupling of all the FSS elements especially when the radome is small and feed is illuminating it in proximity. The TIA model is not sufficient to model the fields in a small radome because it has neglected interaction of all the FSS elements which causes internal multiple reflection. For such a small cone, it is also important to use a accurate feed model like SPS to compute the near field illuminations. Using this feed model to calculate the incidences, the computation time between the FC and TIA model is quite similar because fewer elements are used. This is mainly because the integral formulation in the FC model does not require repeated computations of current for each planar incidences in order to model the non-planar near fields. The main limitation stems from the computer memory requirement to store the large matrix but this is readily compensated by the accuracy. The FC model also has the advantage of analysing arbitrary FSS structures. Moreover, the FSS elements can be positioned anywhere without imposing any periodicity in the lattice. These features would

enhance its capability for solving a general and wider FSS problem compared to the TIA model. Thus, the FC model can provide a viable solution although the coupling with the feed has been neglected.

The FC model can be further improved to include the coupling of the feed and FSS if the integral equation formulation incorporates weighting of each point source in the feed aperture as well. This would lead to a slight increase of the impedance matrix size which is proportional to the number of points in the feed aperture used for the SPS feed modelling. In order to extend the FC model to FSS with thicker dielectric support, mixed integral equations can be coupled to relate the FSS and dielectric portions. This is then solved using the MOM with surface or volume basis functions [2,3]. The main problem in the approach, however, is to constrain the size of the MOM matrix for computer computation. This could potentially be overcome using a sparse matrix which would reduce the memory and computation time if the weaker coupling elements can be identified and ignored.

An alternative method is to employ the Lorentz reciprocity theorem with can account for mutual coupling of electromagnetic structures. The near field interactions between the feed and a purely dielectric radome have been studied by others [4] using the reaction between two structures. This reaction concept is based on Lorentz theorem [5]. The presence of the FSS would require the Lorentz formulation to include the reaction of a third structure in the derivation.

Although the conical radome is fitted with a single layer of FSS, the transmission loss could be improved if it is replaced multi-layer FSS. The presence of cascaded planar FSS has been known to give a broader bandwidth and sharper roll-off [6]. The deterioration in radiation patterns could be altered and improved if the elements are located in a quasi-periodic lattice. Recently, this has also been exploited for frequency scanning purposes [7]. This is achieved by progressive phase shifting through elemental position and size on the curved surface in order to focus the feed pattern to a desired shape. Basically it is acting as an artificial lens antenna [8]. Therefore, the radiation patterns could be tuned according to the arbitrary dimension, element and position of the FSS geometry.

References

[1] Rahmat-Samii, Y. and Tulintseff, A.N. :'Diffraction analysis of frequency selective reflector antennas', IEEE Trans., AP-41, 1993, pp.476-487.

[2] Sarkar, T.K., Rao, S.M. and Djordjevic, A.R. :'Electromagnetic scattering and radiation from finite microstrip structures', IEEE Trans., 1990, AP-38, pp.1568-1574.

[3] Casey, J.P. and Bansal, R. :'Dielectrically loaded wire antennas', IEE Proc.H, 1988, 135, pp.103-110.

[4] Siwiak, K., Dowling T.B. and Lewis L.R. :'Boresight errors induced by missile radomes', IEEE, AP-27,1979, pp.832-841.

[5] Rumsey, V.H. :'Reaction concept in electromagnetic theory', Phy. Rev., Vol.94, Num. 6, 1954, pp.1488-1491

[6] Kraus, J.D. :'Antennas', McGraw-Hill, 1988, pp.603.

[7] Johansson F.S. :'Multibeam satellite antenna using frequency scanned grating reflector', 3rd Int. Conf. on Electomag. in Aerosp. Appl. and 7th Europ. Electromag. Struct. Conf. 1993,.pp.111-114.

[8] Balanis, C.A. :'Antenna theory: analysis and design', 1982, pp. 648-650.

APPENDICES

Appendix 1

Coefficients from the modal analysis

For interfaces at the rear of the screen, $\alpha = 3,4,5,6$ (media notation),

$$\sigma_{\alpha}^{\alpha+1}(m,p,q) = \frac{e^{-j\gamma_{pq}^{\alpha+1} z_{\alpha}} - \rho^{\alpha+1}(m,p,q) e^{j\gamma_{pq}^{\alpha+1} z_{\alpha}}}{e^{-j\gamma_{pq}^{\alpha+1} z_{\alpha}} + \rho^{\alpha+1}(m,p,q) e^{j\gamma_{pq}^{\alpha+1} z_{\alpha}}} \tag{A1.1}$$

$$\rho^{\alpha}(m,p,q) = e^{-j2\gamma_{pq}^{\alpha} z_{\alpha}} \frac{\eta_{mpq}^{\alpha} - \eta_{mpq}^{\alpha+1} \sigma_{\alpha}^{\alpha+1}(m,p,q)}{\eta_{mpq}^{\alpha} + \eta_{mpq}^{\alpha+1} \sigma_{\alpha}^{\alpha+1}(m,p,q)} \tag{A1.2}$$

$$\omega_{\alpha}^{\alpha+1}(m,p,q) = \frac{e^{-j\gamma_{pq}^{\alpha+1} z_{\alpha+1}} + \rho^{\alpha+1}(m,p,q) e^{j\gamma_{pq}^{\alpha+1} z_{\alpha+1}}}{e^{-j\gamma_{pq}^{\alpha+1} z_{\alpha}} + \rho^{\alpha+1}(m,p,q) e^{j\gamma_{pq}^{\alpha+1} z_{\alpha}}} \tag{A1.3}$$

For the interfaces on the illumination side, the coefficients are given:

$$V_{123}(m,p,q) = v_1(m,p,q) v_2(m,p,q) v_3(m,p,q) \tag{A1.4}$$

$$U_{123}(m,p,q) = u_1(m,p,q) v_2(m,p,q) v_3(m,p,q) + u_2(m,p,q) v_3(m,p,q) + v_3(m,p,q) \tag{A1.5}$$

For $\alpha = 1,2,3$ (media notation),

$$v_{\alpha}(m,p,q) = \frac{\eta_{mpq}^{\alpha-1}\left(e^{-j\gamma_{pq}^{\alpha-1} z_{\alpha-1}} + F^{\alpha-1}(m,p,q) e^{j\gamma_{pq}^{\alpha-1} z_{\alpha-1}}\right)}{\eta_{mpq}^{\alpha}\left(e^{-j\gamma_{pq}^{\alpha} z_{\alpha-1}} + F^{\alpha}(m,p,q) e^{j\gamma_{pq}^{\alpha} z_{\alpha-1}}\right)} \tag{A1.6}$$

$$u_\alpha(m,p,q) = \frac{G^\alpha(m,p,q)e^{j\gamma^\alpha_{pq}z_{\alpha-1}} - \frac{\eta^{\alpha-1}_{mpq}}{\eta^{\alpha}_{mpq}} G^{\alpha-1}(m,p,q)e^{j\gamma^{\alpha-1}_{pq}z_{\alpha-1}}}{e^{-j\gamma^\alpha_{pq}z_{\alpha-1}} + F^\alpha(m,p,q)e^{j\gamma^\alpha_{pq}z_{\alpha-1}}} \qquad \text{(A1.7)}$$

For $\alpha = 0,1,2$ (media notation),

$$G^\alpha(m,p,q) = \frac{2\eta^{\alpha+1}_{mpq}e^{j\gamma^{\alpha+1}_{pq}z_\alpha}G^{\alpha+1}(m,p,q)e^{-j\gamma^\alpha_{pq}z_\alpha}}{\eta^{\alpha+1}_{mpq}\left(1+F^{\alpha+1}(m,p,q)e^{j2\gamma^{\alpha+1}_{pq}z_\alpha}\right)+\eta^{\alpha}_{mpq}\left(1-F^{\alpha+1}(m,p,q)e^{j2\gamma^{\alpha+1}_{pq}z_\alpha}\right)} \qquad \text{(A1.8)}$$

$$F^\alpha(m,p,q) = e^{-j2\gamma^\alpha_{pq}z_\alpha}\frac{\eta^{\alpha+1}_{mpq} - \eta^{\alpha}_{mpq}A_\alpha(m,p,q)}{\eta^{\alpha+1}_{mpq} + \eta^{\alpha}_{mpq}A_\alpha(m,p,q)} \qquad \text{(A1.9)}$$

$$A_\alpha(m,p,q) = \frac{1-e^{j2\gamma^{\alpha+1}_{pq}z_\alpha}F^{\alpha+1}(m,p,q)}{1+e^{j2\gamma^{\alpha+1}_{pq}z_\alpha}F^{\alpha+1}(m,p,q)} \qquad \text{(A1.10)}$$

Except for $G^3(m,p,q) = e^{-j\gamma^3_{pq}z_3}$ (A1.11)

and $F^3(m,p,q) = e^{-j2\gamma^3_{pq}z_3}$ (A1.12)

Note,

$$\eta^0_{mpq} = \eta^{air}_{mpq} \qquad \text{(A1.13)}$$

Appendix 2

Feed to surface co-ordinate transformations

Two sets of co-ordinate transformations are required if the feed is allowed to tilt in the y_f-z_f and x_f-z_f planes.

Case(I)

If the feed is tilted in the y_f-z_f plane with θ_o as shown in Fig.3.4a, then the following feed to surface co-ordinate transformation would apply.

$$\begin{bmatrix} \hat{x}_s \\ \hat{y}_s \\ \hat{z}_s \end{bmatrix} = \begin{bmatrix} 1 & 0 & 0 \\ 0 & -\cos\theta_o & -\sin\theta_o \\ 0 & \sin\theta_o & -\cos\theta_o \end{bmatrix} \begin{bmatrix} \hat{x}_f \\ \hat{y}_f \\ \hat{z}_f \end{bmatrix} \tag{A2.1}$$

and

$$\begin{bmatrix} \hat{x}_f \\ \hat{y}_f \\ \hat{z}_f \end{bmatrix} = \begin{bmatrix} 1 & 0 & 0 \\ 0 & -\cos\theta_o & \sin\theta_o \\ 0 & -\sin\theta_o & -\cos\theta_o \end{bmatrix} \begin{bmatrix} \hat{x}_s \\ \hat{y}_s \\ \hat{z}_s \end{bmatrix} \tag{A2.2}$$

Case(II)

If the feed is tilted in the x_f-z_f plane with θ_o as shown in Fig.3.4b, then the following feed to surface co-ordinate transformation would apply.

$$\begin{bmatrix} \hat{x}_s \\ \hat{y}_s \\ \hat{z}_s \end{bmatrix} = \begin{bmatrix} 0 & -1 & 0 \\ -\cos\theta_o & 0 & \sin\theta_o \\ -\sin\theta_o & 0 & -\cos\theta_o \end{bmatrix} \begin{bmatrix} \hat{x}_f \\ \hat{y}_f \\ \hat{z}_f \end{bmatrix} \tag{A2.3}$$

and

$$\begin{bmatrix} \hat{x}_f \\ \hat{y}_f \\ \hat{z}_f \end{bmatrix} = \begin{bmatrix} 0 & -\cos\theta_o & -\sin\theta_o \\ -1 & 0 & 0 \\ 0 & \sin\theta_o & -\cos\theta_o \end{bmatrix} \begin{bmatrix} \hat{x}_s \\ \hat{y}_s \\ \hat{z}_s \end{bmatrix} \tag{A2.4}$$

Appendix 3

FN feed model

The incident fields of the FN feed model can be obtained from Gaussian fittings to the measured copolar and crosspolar feed patterns. These are scaled in the inverse square sense as the field amplitude varies with distance.

The incident fields are firstly expressed in feed co-ordinates as follows:

$$\vec{E}^i = E^i_{xf}\hat{x}_f + E^i_{yf}\hat{y}_f + E^i_{xf}\hat{z}_f \tag{A3.1}$$

The Cartesian components of the fields can be extracted with the help of the Ludwig's third definition vectors[1] using the following equations.

$$\vec{E}^i.\hat{i}_{co} = A_{co}e^{-jk_d r_p}\frac{d_o}{r_p} \tag{A3.2}$$

$$\vec{E}^i.\hat{i}_{cross} = A_{cross}e^{-jk_d r_p}\frac{d_o}{r_p} \tag{A3.3}$$

$$\vec{E}^i.\vec{r}_p = 0 \tag{A3.4}$$

where $\hat{i}_{co}$ and $\hat{i}_{cross}$ are the Ludwig's vectors given in Chapter 2. as Eq.(2.52) and Eq.(2.54). But the polar angles in the vectors here should be in terms of (θ_f, ϕ_f) of the feed co-ordinates. d_o is the intersection of the z_f axis with the cone from the origin of the feed axis and $\vec{r}_p$ is the distance between the feed origin and the surface as shown in Fig3.3.

The copolar pattern is derived from:

$$A_{co} = e^{-\left(\frac{\theta_f}{a_o + a_1\theta_f}\right)^2} \tag{A3.5}$$

where a_o and a_1 are arbitrary constants chosen to fit the desired illumination.

Similarly, the crosspolar pattern can be offset from the boresight according to the peak crosspolar levels at angle θ_p. And it is derived from :

$$A_{cross} = ce^{-\left(\frac{\theta_f - \theta_p}{\sigma}\right)^2} sin2\theta_f \tag{A3.6}$$

where c is the desired peak crosspolar level and σ is a normalisation constant. It is also assumed that the crosspolar is maximum in the diagonal planes i.e. 45 degrees.

Reference

[1] Ludwig, A.C.:'The definition of cross polarisation', IEEE Trans., AP-21, 1973, pp.116-119.

Appendix 4

Aperture fields of a narrow flare circular conical corrugated horn

Details of the derivation of the aperture fields in a circular corrugated waveguide can be found in [1]. The aperture fields in a narrow flare conical corrugated horn can approximated by the fields in a cylindrical waveguide provided that the semi-flare angle does not exceed 15°. The cylindrical components of fields in the hybrid HE_{11} mode are given by in the feed co-ordinates as:

$$E_{\rho_f} = -j\frac{Ak_o}{2k}\left[\left(\Delta+\bar{\beta}\right)J_o\left(k\rho_f\right)+\left(\Delta-\bar{\beta}\right)J_2\left(k\rho_f\right)\right]\cos\phi_f \qquad \text{(A4.1)}$$

$$E_{\phi_f} = j\frac{Ak_o}{2k}\left[\left(\Delta+\bar{\beta}\right)J_o\left(k\rho_f\right)-\left(\Delta-\bar{\beta}\right)J_2\left(k\rho_f\right)\right]\sin\phi_f \qquad \text{(A4.2)}$$

$$H_{\rho_f} = -jy_o\frac{Ak_o}{2k}\left[\left(\bar{\beta}\Delta+1\right)J_o\left(k\rho_f\right)+\left(1-\bar{\beta}\Delta\right)J_2\left(k\rho_f\right)\right]\sin\phi_f \qquad \text{(A4.3)}$$

$$H_{\phi_f} = -jy_o\frac{Ak_o}{2k}\left[\left(\bar{\beta}\Delta+1\right)J_o\left(k\rho_f\right)-\left(1-\bar{\beta}\Delta\right)J_2\left(k\rho_f\right)\right]\cos\phi_f \qquad \text{(A4.4)}$$

ρ_f and ϕ_f denote the radial and phi component of the feed aperture. E and H are the electric and magnetic fields.

Expressing the fields in x_f and y_f feed co-ordinates yields,

$$E^a_{x_f} = -j\frac{Ak_o}{2k}\left[\left(\Delta+\bar{\beta}\right)J_o\left(k\rho_f\right)+\left(\Delta-\bar{\beta}\right)J_2\left(k\rho_f\right)\cos 2\phi_f\right] \qquad \text{(A4.5)}$$

$$E^a_{y_f} = -j\frac{Ak_o}{2k}\left(\Delta-\bar{\beta}\right)J_2\left(k\rho_f\right)\sin 2\phi_f \qquad \text{(A4.6)}$$

$$H^a_{x_f} = -jy_o\frac{Ak_o}{2k}\left(1-\bar{\beta}\Delta\right)J_2\left(k\rho_f\right)\sin 2\phi_f \qquad \text{(A4.7)}$$

$$H^a_{y_f} = -jy_o\frac{Ak_o}{2k}\left[\left(\bar{\beta}\Delta+1\right)J_o\left(k\rho_f\right)-\left(1-\bar{\beta}\Delta\right)J_2\left(k\rho_f\right)\cos 2\phi_f\right] \qquad \text{(A4.8)}$$

J_o and J_1 are Bessel functions of order 0 and 1.

k is the transverse wavenumber given by $k = \frac{U_o}{\rho_a}$ such that $J_o(U_o) = 0$. ρ_a is the inner radius of the feed aperture and A is determined by the power carried by the hybrid mode.

$\overline{\beta} = \frac{\beta}{k_o}$ where $\beta = \sqrt{k_o^2 - k^2}$ and $k_o = \frac{2\pi}{\lambda}$. λ is the wavelength.

$y_o = \sqrt{\frac{\varepsilon_o}{\mu_o}}$ where ε_o and μ_o is the permitivitty and the permeability of free space respectively.

The hybrid mode is balanced (produces a symmetrical pattern) i.e.HE_{11} when the slot depth near the aperture is a quarter wavelength long. For the HE_{11} mode, Δ=1.

Reference

[1] P.J.B Clarricoats and A.D. Olver.:'Corrugated horns for microwave antennas', IEEE Electromagnetic Wave Series:18, Peter Peregrinus, 1984, pp.36 and pp.160-162.

Appendix 5

Parallel Beam (PB) feed model

The PB feed model assumes that the antenna is in the proximity of the FSS so that its near fields can be approximated as a beam of parallel rays illuminating the surface. The rays depend on the aperture fields in the feed therefore the area of illumination is actully a projection of the feed aperture. If the conical FSS has a larger base diameter than the feed aperture, the area illuminated would be smaller than those by the FN and SPS feed model. Hence, fewer FSS elements are excited compared to the other two feed models.

The PB analysis is derived from its fields in the spectral domain i.e. Fourier transfrom. If the radiated electric field $\vec{E}^i(x_f, y_f, z_f)$ is expressed in terms of its Fourier transform $\vec{E}_T(u,v)$, then

$$\vec{E}^i(x_f, y_f, z_f) = \frac{1}{4\pi^2} \int_{-\infty}^{\infty} \int_{-\infty}^{\infty} \vec{E}_T(u,v) e^{-jux_f} e^{-jvy_f} e^{-j\beta z_f} du dv \qquad \text{(A5.1)}$$

where $u = k_o \sin\theta_f \cos\phi_f$ (A5.2)

$v = k_o \sin\theta_f \sin\phi_f$ (A5.3)

$\beta = k_o \cos\theta_f$ (A5.4)

$k_o = \frac{2\pi}{\lambda}$ where λ is the wavelength.

If the beam is parallel, then $\theta_f = 0$, so $\beta = k_o$. So, (A5.1) becomes,

$$\vec{E}^i(x_f, y_f, z_f) = e^{-jk_o z_f} \vec{E}^a(x_f, y_f, 0) \qquad \text{(A5.5)}$$

where

$$\vec{E}^a(x_f, y_f, 0) = \frac{e^{-jk_o z_f}}{4\pi^2} \int_{-\infty}^{\infty} \int_{-\infty}^{\infty} \vec{E}_T(u,v) e^{-jux_f} e^{-jvy_f} du dv \qquad \text{(A5.6)}$$

$\vec{E}^a(x_f, y_f, 0)$ is the aperture fields of the feed.

Therefore, the electric field illuminated on the FSS is obtained from the product of the aperture fields and the parallel phase path difference$(-jk_o z_f)$ from the aperture to the surface.

Since the radiated electric field is planar, its magnetic fields can be calculated using the free space impedance as follows:

$$\vec{H}^i(x_f, y_f, z_f) = \sqrt{\frac{\varepsilon_o}{\mu_o}}\hat{z}_f \times \vec{E}^i(x_f, y_f, z_f) \qquad \text{(A5.7)}$$

Note that $\vec{E}^i(x_f, y_f, z_f)$ lies in the x_f and y_f plane because it depends on the aperture field.

Appendix 6

Scattered fields using Stratton and Chu's formulation

The radiated fields at a observation point P from finite electric current $\vec{J}$ and magnetic current $\vec{J}_m$ sources bounded by surface S is given by the Stratton and Chu [1]. The expressions of the fields are rewritten here as follows:

$$\vec{E}(\vec{r}) = \frac{-j\omega\mu}{4\pi}\iint_S \left[A_1\vec{J} + A_2(\vec{J}.\hat{r})\hat{r} + A_3\sqrt{\frac{\varepsilon}{\mu}}\vec{J}_m \times \hat{r} \right]\frac{e^{-jkr}}{r}dS \qquad \text{(A6.1)}$$

$$\vec{H}(\vec{r}) = \frac{-j\omega\varepsilon}{4\pi}\iint_S \left[A_1\vec{J}_m + A_2(\vec{J}_m.\hat{r})\hat{r} - A_3\sqrt{\frac{\mu}{\varepsilon}}\vec{J} \times \hat{r} \right]\frac{e^{-jkr}}{r}dS \qquad \text{(A6.2)}$$

where

$$A_1 = 1 - \frac{j}{kr} - \frac{1}{k^2r^2} \qquad \text{(A6.3)}$$

$$A_2 = -1 + \frac{3j}{kr} + \frac{3}{k^2r^2} \qquad \text{(A6.4)}$$

$$A_3 = 1 + \frac{1}{jkr} \qquad \text{(A6.5)}$$

and

r is the distance between the current sources and P along vector $\hat{r}$ as shown in Fig.A6.1 such that $r = \left|\vec{R} - \vec{r}'\right|$.

$\vec{r}'$ is position of the current sources and $\vec{R}$ is position of point observation with respect to a arbitrary global origin.

In order to derive the superposition of point source (SPS) feed model, the feed aperture is discretised into small patches where the patch area of the each current sources is reduced to a point. Let the area of the dual current sources be located at the origin in free space (FigA6.1). If this area is shrunk to a small patch, so that distribution of the currents is constant across the patch area, S', then (A6.1) becomes:

$$\vec{E}(\vec{r}) = \frac{-j\omega\mu_o}{4\pi}\frac{e^{-jk_oR}}{R}\left[A_1\vec{J} + A_2(\vec{J}.\hat{R})\hat{R} + A_3\sqrt{\frac{\varepsilon_o}{\mu_o}}\vec{J}_m \times \hat{R} \right]S' \qquad \text{(A6.6)}$$

where $S' = \iint_{s'} dS$ (which gives the area of a small patch). $k_o = \frac{2\pi}{\lambda}$.

The currents' terms are allowed to be extracted from the double integral because the currents is approximated as a point source. The same argument applies to the magnetic fields expression (A6.2).

In the far field, however, the electric fields for a general current sources is approximated as:

$$\vec{E}(\vec{r}) = \frac{-j\omega\mu_o}{4\pi}\frac{e^{-jk_oR}}{R}\iint\left[\vec{J} - \left(\vec{J}.\hat{R}\right)\hat{R} + \sqrt{\frac{\varepsilon_o}{\mu_o}}\vec{J}_m \times \hat{R}\right]e^{jk_o\vec{r}'.\hat{R}}dS \qquad \text{(A6.7)}$$

where the higher order terms in (A6.2), (A6.3) and (A6.4) are removed.
The radiated electric far fields for a point source is also given by (A6.6) except that higher order terms are removed. Thus,

$$\vec{E}(\vec{r}) = \frac{-j\omega\mu_o}{4\pi}\frac{e^{-jk_oR}}{R}\left[\vec{J} - \left(\vec{J}.\hat{R}\right)\hat{R} + \sqrt{\frac{\varepsilon_o}{\mu_o}}\vec{J}_m \times \hat{R}\right]S' \qquad \text{(A6.8)}$$

Reference

[1] Silver, S. (Ed.) :'Microwave Antenna Theory and Design', IEE Electromagnetic Wave Series 19, Peter Perregrinus Ltd, 1986, pp.80-90.

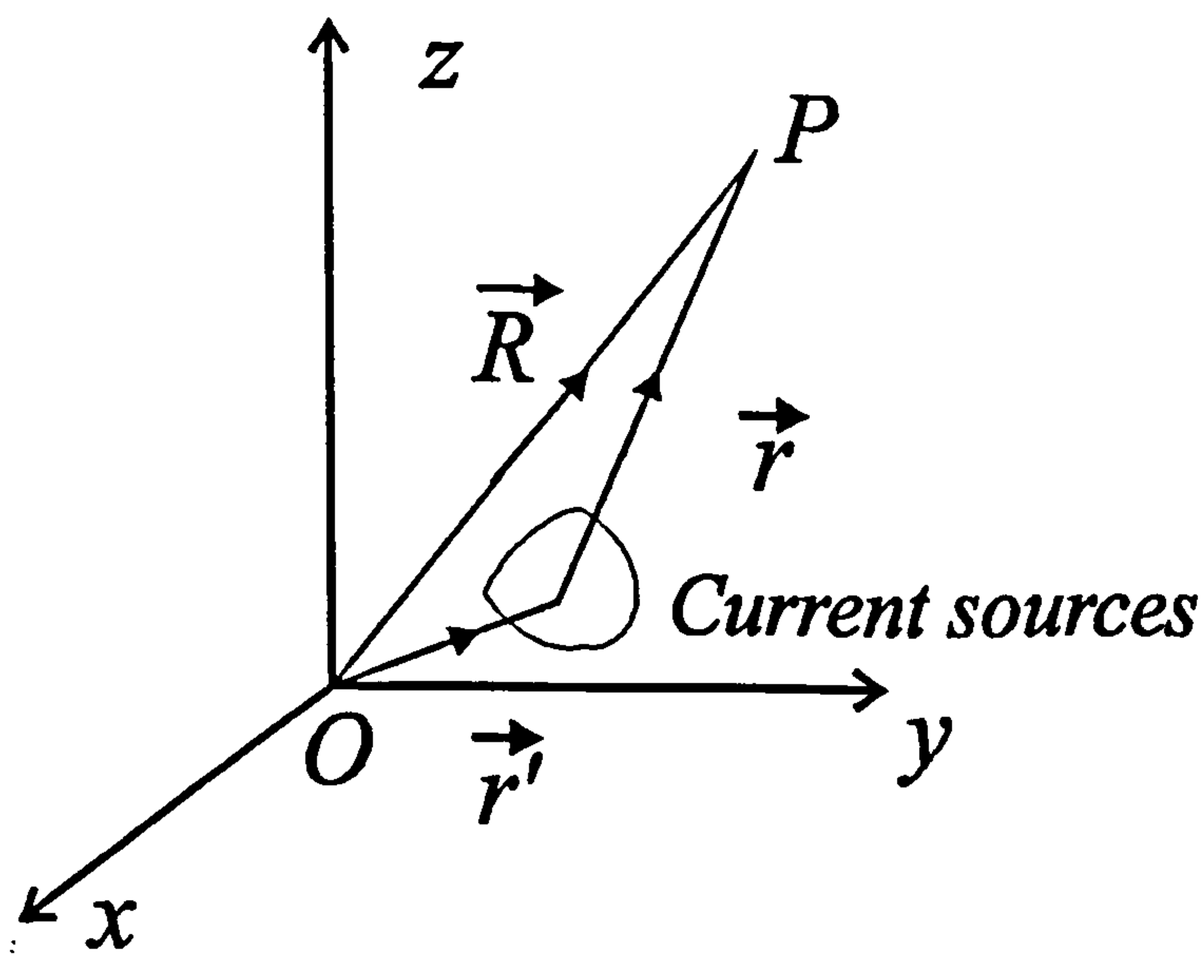

Fig.A6.1 Arbitrary field point P from current sources.